

## Department of Precision and Microsystems Engineering

**Title: Contactless positioning of thin flexible substrates**

**Subtitle: Demonstrator design and validation of opposed air film actuators**

Ruben Salters

Report no : 2019.009  
Coach : Ing. P. J. M. Houben  
Professor : Dr. ir. R. A. J. van Ostayen  
Specialisation : Mechatronic System Design  
Type of report : Master Thesis  
Date : 13 March 2019



# Contactless positioning of thin flexible substrates

## Demonstrator design and validation of opposed air film actuators

by

R.V. Salters

to obtain the degree of Master of Science  
at the Delft University of Technology,  
to be defended publicly on Wednesday March 13, 2019 at 13:00.

Student number:	4150163	
Project duration:	April 1, 2017 – March 13, 2019	
Supervisor:	Dr. ir. R.A.J. van Ostayen,	TU Delft
Thesis committee:	Dr. S.H. HosseinNia,	TU Delft
	Dr. ir. M. Tichem,	TU Delft
	Ing. P.J.M. Houben,	Nexperia

*This thesis is confidential and cannot be made public until March 13, 2024.*

An electronic version of this thesis is available at <http://repository.tudelft.nl/>.



# Summary

At Nexperia in Nijmegen assembly machines are developed for the back-end of the semiconductor production process. At one stage, machines are used to pick dies from a silicon wafer and place them on a flexible web on reel. The web is wrapped on a drum (cylinder) which is rotated by an electric motor. After a die is placed on the web, the web is shifted such that the next die can be placed on the web. The current motion system is able to translate the web with a stroke of 50 mm within 50 ms. This demands large torques and fast response times from the electric motor, resulting in cooling the electric motor and high levels of sophistication on its motion system design.

A possible alternative solution could be to apply contactless air film actuators which make use of air bearing principles. The main advantage of such a technique is that it actuates directly on the web and therefore eliminates the moving mass of the drum. This drastically reduces the actuation force required to accelerate the web, which reduces unwanted deformations and excitations of the machine frame. Because the substrate is not in direct contact with the bearing surface, the web does not experience any wear, stiction or backlash effects. The result could be a cheaper alternative motion system with less components and less disturbances than the current motion system.

The goal of this thesis is to investigate the possibilities of using opposed air film actuators for positioning thin flexible substrates. The aim is to design and build a demonstrator which can actuate a piece of web in one degree of freedom with similar performances as the current motion system. This generates a viscous traction on the substrate that moves it in positive x-direction. During this thesis we want to show if the theoretical model of the motion system complies with the performances of the manufactured demonstrator.

An illustration of opposed air film actuators is shown in figure 1. Here pressurized air is applied at the inlets. This creates an air film on both sides of the substrates which levitates the substrate. At the same time a net flow is generated in positive x-direction. The air flow is shown by the blue arrows. The net flow produces a viscous traction on the substrate which moves the substrate in positive x-direction, shown by the red arrow.

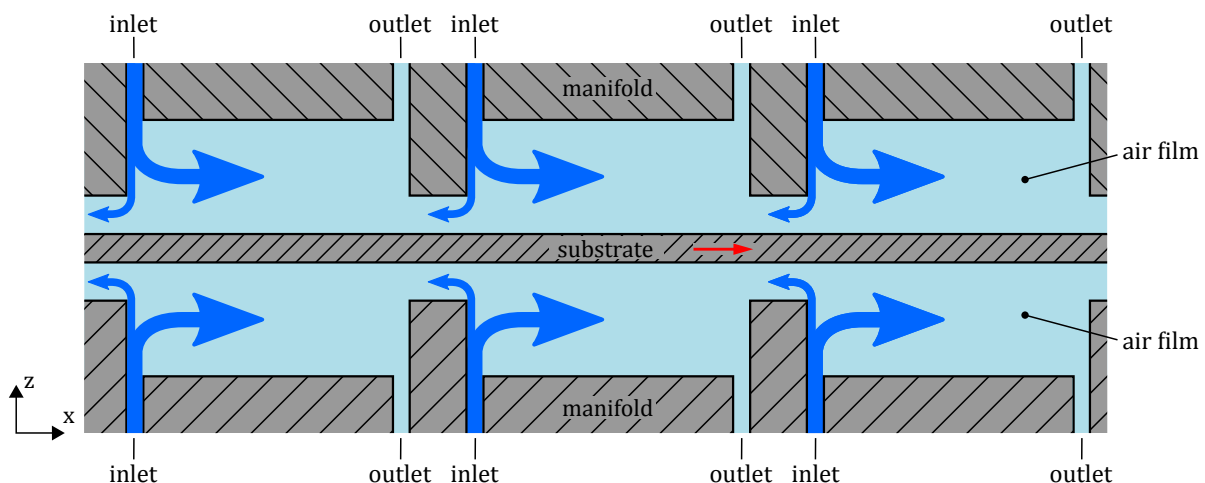


Figure 1: Cross section of opposed air film actuators, where a net flow is realized in positive x-direction shown by the blue arrows. This results in a motion of the substrate in positive x-direction shown by the red arrow.

To predict the performance of the motion system, the air film actuators are modelled with the use of the Reynolds equation for compressible air. With this model properties in-plane and out-of-plane of the fluid can be predicted, such as mass flow through the air film, actuation force applied on the substrate and vertical

stiffness applied on the substrate. The air film actuators are optimized for low air consumption while generating sufficient force to accelerate the substrate with  $160 \text{ m/s}^2$ . As air is a compressible fluid, it takes time to build pressure up in the ducts. Therefore the response of the actuation force on the substrate is dependent on the pressure build up in the system. The transient behaviour of the air flow in the system is described by a pneumatic circuit model with lumped components. For a fast pressure build up in the system, the volumes in the ducts are minimized and proportional valves with a low response time are used.

To verify the theoretical model of the motion system a demonstrator is designed and manufactured. The demonstrator consists of two manifolds with their bearing surfaces facing each other and where the substrate is placed between the two bearing surfaces. A single manifold contains 16 air film actuators in the bearing surface from which 8 are able to actuate the substrate in positive x-direction and the other 8 are able to actuate the substrate in negative x-direction. Three experiments with the demonstrator are described in this thesis.

In the first experiment, measurements were performed on the inlet restrictors to show the relation between flow and pressure. Multiple restrictors showed similar performances which indicated that the inlets were well produced. From the results could be verified that the inlet restrictors behave as orifice restrictors, which agrees with literature.

In the second experiment the behaviour of the air film actuators was measured. Initial tests showed that the substrate was vibrating and did not float fully contactless, as one had to overcome some friction before the substrate moved. This was not expected. The least amount of friction was observed at a fly height of  $17 \mu\text{m}$  at a supply pressure of 5 bar. At this fly height and supply pressure a maximum actuation force of 209 mN was reached in one direction with a total air consumption of 84.4 L/min. Despite the vibration of the substrate, the modelled flow, pressure and actuation force did show good resemblance with the measured results.

In the third experiment the step response of the pressure and the position of the substrate were measured. The theoretical model gave a good approximation of the measured response. However, the plant contained a larger damping constant than predicted. Therefore a lower speed was achieved than initially expected. When all air film actuators were used, a maximum net actuation force of 96.5 mN was reached. With the theoretical model it was determined that the motion system is able to move the substrate 50 mm in 405 ms with a system bandwidth of around 87.0 Hz.

Based on these findings the theoretical models showed good resemblance with the measured results of the demonstrator. Better performances could be achieved by reducing the damping constant in the motion system. Other recommendations for improving the models and the demonstrator can be found in section 5.2.

# Preface

This thesis is the result of my master thesis project, which is the final part of the master Mechanical Engineering and track Precision and Microsystems Engineering (PME) at the Delft University of Technology. During my master courses I became fascinated about the combination of fluid dynamics with mechatronics. At the research group Mechatronic System Design (MSD) within the department of PME, contactless handling systems are developed which features both these subjects. In a meeting with Ron van Ostayen an assignment emerged at Nexperia in Nijmegen that fits well with my field of interest. Jelle Snieder, a former PME student, did a feasibility study at Nexperia about the application of contactless handling systems in one of their positioning machines. This study showed potential benefits and therefore Nexperia gave me the opportunity to create a demonstrator. The possibility to actually manufacture a motion system in collaboration with Nexperia was for me the decisive reason to do this research project.

I would like to thank Ron van Ostayen for being my supervisor and giving me technical guidance during my research. At important moments you helped me making decisions in the right direction. Especially helping me understanding the small details of air bearings and interpreting the measurement results really improved my work. I always appreciated your fast response on my e-mails when I had a question. Thank you for your support and feedback during this research project. Here I also like to thank Hassan HosseinNia and Marcel Tichem for completing my thesis committee.

I also would like to thank Patrick Houben for being my supervisor at Nexperia and coaching me during this research project. Thank you for your advice for improving the design, your guidance in the manufacturing of the demonstrator and helping me contacting suppliers. In addition I would like to thank Gijs van der Veen for also coaching me. The weekly meetings with you and Patrick helped me making progress. Thank you for your advice on the control aspects of the motion system, the search for suitable valves and supporting me during the measurements. The realisation of the demonstrator is also made possible by John Klomp. Thank you for helping me manufacturing detailed features of the design. I also would like to thank Joep Stokkermans for giving me the opportunity of doing my master thesis project at Nexperia and emphasizing the importance of this research. Special thanks to Thijs Kniknie, Ruud de Rooij, Thijs van der Aa and others from the ITEC group of Nexperia for helping me during this project.

Lastly I want to thank my family and friends for providing me support and encouragement during my master thesis project. Thank you for giving me feedback and putting things in perspective. This accomplishment would not have been possible without you.

*R.V. Salters  
Delft, March 2019*



# Contents

<b>1</b>	<b>Introduction</b>	<b>1</b>
1.1	Motivation . . . . .	1
1.2	State of the art air film actuators . . . . .	2
1.2.1	Variable pressure concept . . . . .	3
1.2.2	Deformable surface concept . . . . .	3
1.3	Opposed air film actuators . . . . .	4
1.4	Research goal . . . . .	4
1.5	Outline of this thesis . . . . .	4
<b>2</b>	<b>Theory and working principles of air film actuators</b>	<b>7</b>
2.1	Approach . . . . .	7
2.2	Assumptions . . . . .	8
2.3	Pressure field in thin film fluid . . . . .	8
2.4	In-plane fluid analysis . . . . .	10
2.5	Restrictors . . . . .	11
2.5.1	Capillary restrictor . . . . .	11
2.5.2	Thin film restrictor . . . . .	12
2.5.3	Orifice restrictor . . . . .	12
2.6	Out-of-plane fluid analysis . . . . .	13
2.7	Basic air film actuator . . . . .	15
<b>3</b>	<b>Design</b>	<b>19</b>
3.1	Design requirements . . . . .	19
3.2	Top-down approach . . . . .	19
3.2.1	Trajectory planner . . . . .	20
3.2.2	Required system bandwidth and stability . . . . .	21
3.3	Design concept . . . . .	23
3.4	Actuator cell design . . . . .	24
3.4.1	Actuator cell performance . . . . .	25
3.4.2	Actuator cell stiffness . . . . .	27
3.4.3	Manifold design . . . . .	30
3.5	Pneumatic management . . . . .	32
3.5.1	Tubing . . . . .	32
3.5.2	Pneumatic circuit model . . . . .	32
3.5.3	Valves . . . . .	34
3.6	Control . . . . .	37
3.6.1	Valve pressure control . . . . .	37
3.6.2	Transfer function of the plant . . . . .	38
3.7	Design overview . . . . .	41
<b>4</b>	<b>Experiments and results</b>	<b>43</b>
4.1	Inlets measurement without substrate . . . . .	43
4.2	Measurement with substrate . . . . .	45
4.3	Open-loop response of the motion system . . . . .	48
4.3.1	Results . . . . .	48
4.3.2	Open-loop response . . . . .	51
<b>5</b>	<b>Conclusions and recommendations</b>	<b>55</b>
5.1	Conclusions. . . . .	55
5.1.1	Conclusions regarding design aspects . . . . .	55
5.1.2	Conclusions regarding measurement results. . . . .	56

5.2	Recommendations . . . . .	56
<b>A</b>	<b>Contactless substrate handling systems using air</b>	<b>59</b>
A.1	Air bearings . . . . .	59
A.2	Tilted air jet actuators . . . . .	59
A.3	Squeeze film actuators . . . . .	60
A.4	Air flow actuators . . . . .	61
<b>B</b>	<b>Derivation Reynolds equation</b>	<b>63</b>
B.1	Conservation of mass . . . . .	63
B.2	Conservation of momentum . . . . .	64
B.3	Nondimensionalization: conservation of mass . . . . .	68
B.4	Nondimensionalization: Navier-Stokes momentum equations . . . . .	68
B.4.1	Conservation of momentum in $x$ -direction . . . . .	69
B.4.2	Conservation of momentum in $y$ -direction . . . . .	69
B.4.3	Conservation of momentum in $z$ -direction . . . . .	70
B.4.4	Dominant terms . . . . .	71
B.5	Reynolds equation . . . . .	72
B.5.1	Integrating momentum equations . . . . .	73
B.5.2	Integrating continuity equation . . . . .	74
B.5.3	Volume flow gradients . . . . .	76
B.5.4	Substituting volume flow gradients . . . . .	76
<b>C</b>	<b>Additional design considerations</b>	<b>77</b>
C.1	Substrate . . . . .	77
C.1.1	Web . . . . .	77
C.1.2	Scale . . . . .	77
C.2	Support structure . . . . .	78
C.3	Sensors . . . . .	79
C.3.1	Position sensor . . . . .	79
C.3.2	Pressure sensor . . . . .	79
C.3.3	Flow sensor . . . . .	79
C.4	Numerical analysis . . . . .	79
<b>D</b>	<b>Realisation</b>	<b>83</b>
D.1	Overview design . . . . .	83
D.2	Production of the manifolds . . . . .	84
D.3	End result . . . . .	88
<b>E</b>	<b>Measurement results for different film thicknesses</b>	<b>91</b>
E.1	Results with $h_d = 12\mu\text{m}$ . . . . .	91
E.2	Results with $h_d = 22\mu\text{m}$ . . . . .	93
<b>F</b>	<b>Step responses during pressure rise and pressure fall</b>	<b>95</b>
F.1	Pressure rise of $p_{1,L}$ . . . . .	95
F.2	Pressure fall of $p_{1,R}$ . . . . .	97
F.3	Pressure fall of $p_{1,L}$ . . . . .	99
	<b>Bibliography</b>	<b>101</b>

# Introduction

In this chapter an introduction will be given about air film actuators. First in section 1.1 a motivation will be given for the use of air film actuators to actuate thin flexible substrates. Secondly, in section 1.2 two different basic concepts of air film actuators developed at the Delft University of Technology will be presented to show the state of the art air film actuators. In section 1.3 the advantages of opposed air film actuators are explained. In section 1.4 the focus and research goal of this thesis are presented. Finally, in section 1.5 an overview of the chapters will be given of this thesis.

## 1.1. Motivation

Nowadays semiconductor components are produced at high rates for multiple applications in e.g. the automotive, portable devices, industrial, communication infrastructure, consumer and computing industries. One of the major companies producing these devices is Nexperia in Nijmegen. They are a global leader in Discretes, Logic and MOSFETs devices. Nexperia focuses on the efficient production of reliable semiconductor components at high volume rates. Currently, they are producing 85 billion semiconductor components annually. In order to keep high production rates, they develop assembly machines for the back-end of the semiconductor production process.

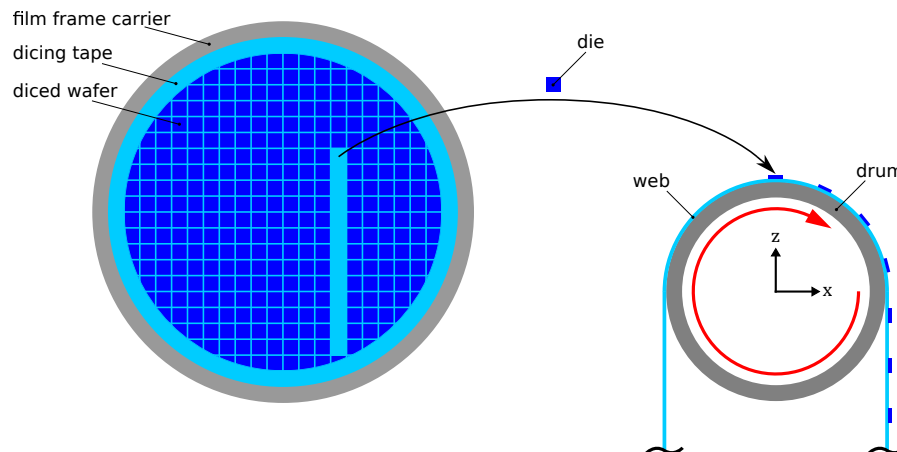


Figure 1.1: Pick and place dies from a diced wafer to a flexible web. The web is wrapped around a drum which rotates to position the web.

One of their machines is to pick dies from a wafer and place them on a flexible web as is schematically shown in figure 1.1. The input to this system is a diced silicon wafer with a diameter of 200 mm or 300 mm which lays on a dicing tape. The dicing tape is attached to a film frame carrier. Each individual device of the wafer is called a die. The typical dimension of a die is between 0.15 mm by 0.15 mm to 5.0 mm by 5.0 mm and has

a thickness between 35 to 600  $\mu\text{m}$ . So a single wafer may contain over 100.000 dies. The dies are picked and placed from the diced wafer to a flexible web on reel. The web is a polymer based foil on which a conducting material can be laminated. By etching the conducting material, antennas can be created on the web which can receive radio waves and conduct electric currents. Therefore the web has the function to be a carrier for both the dies and the antennas. On the web the dies can be further processed depending on the wishes of the customer. The current motion system uses a drum (cylinder) on which the web is wrapped. The drum is rotated by an electric motor to position the web. With this motion system it is possible to position the web with a stroke of 50 mm within 50 ms and ensure a 3  $\mu\text{m}$  ( $1\sigma$ ) die placement accuracy. The motion system has a maximum die placement of 72.000 components an hour, which corresponds to 20 dies per second. For this performance the drum needs to be accelerated with at least 80  $\text{m/s}^2$  for the long stroke of 50 mm. This demands large torques and fast response times from the electric motor, resulting in cooling the electric motor and high levels of sophistication on its motion system design.

A possible alternative actuation solution, for a more elegant design, could be to apply contactless air film actuators which make use of air bearing principles. Such a technique actuates directly on the web and therefore eliminates the moving mass of the drum. This greatly reduces the required actuation forces and reaction forces, which reduces unwanted deformations and excitations of the machine frame. Furthermore, the air film provides a zero in-plane stiffness connection between the substrate and the fixed world. Therefore, the substrate is less affected by in-plane disturbances. Both the lower reaction forces and reduced disturbances are beneficial for positioning the substrate. The result could be a cheaper alternative motion system with less components and less disturbances than the current motion system.

## 1.2. State of the art air film actuators

Since the start of 2006 the Mechatronic System Design group at the Delft University of Technology conducts research on contactless air film based actuators that generate viscous forces on a thin substrate. Such air film actuators have been used for transporting or positioning silicon wafers or glass substrates. The developed actuators are based on air bearing principles. Air bearings are particularly useful when applied for precision applications. This is due to low noise because the substrate is not in direct contact with the bearing surface. The substrate does not experience direct disturbances of surface imperfections. Because there is no friction the bearing surface does not experience any wear, stiction or backlash effects. Through the years the Mechatronic System Design group developed two different basic concepts of air film actuators: the variable pressure concept and the deformable surface concept. These concepts are briefly discussed in subsections 1.2.1 and 1.2.2. An overview of four other contactless substrate handling systems with the use of air are described in appendix A.

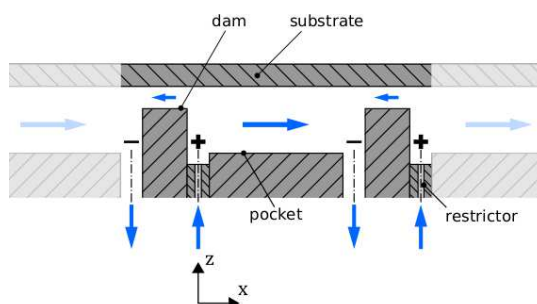


Figure 1.2: Cross section basic air film actuator of the variable pressure concept. The plus symbols indicate areas of high pressure and the minus symbols indicate areas of low pressure. The blue arrows indicate the direction of the air flow.

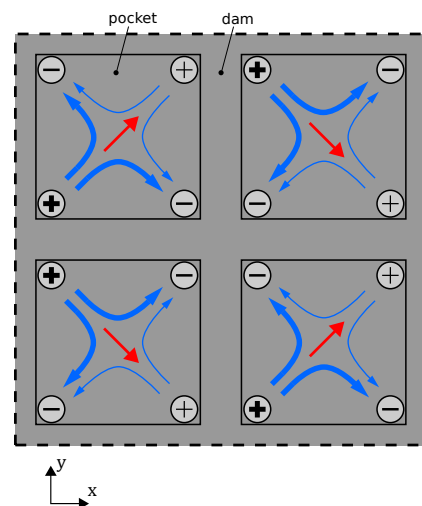


Figure 1.3: Top view of four air film actuators of the variable pressure concept with substrate removed. Blue arrows indicate the air flow and red arrows indicate the viscous traction force generated in each pocket acting on the substrate. For example, the shown flow results in a motion of the substrate in positive x-direction.

### 1.2.1. Variable pressure concept

The first concept was developed by Wesselingh [31]. The main goal of his research was to investigate the properties and applicability of an air film based actuator for precision positioning tasks of thin substrates. The used substrate was a wafer with a diameter of 100 mm and a thickness of 525  $\mu\text{m}$ , resulting in a mass of 9.5 g. Pressurised air was used to provide the bearing functionality while the air flow generated was also used to drive the substrate. Both this bearing and motor function were realised in a single unit, the so-called actuator. Each actuator cell had dimensions of 10 mm by 10 mm consisting of a dam area and pocket area as shown in figure 1.2. The pocket area had dimensions 8 mm by 8 mm with a recess of 20  $\mu\text{m}$ . Each pocket contained two inlets with gauge pressure and two outlets with vacuum pressure. The air film thickness between the dams and the substrate was 15  $\mu\text{m}$ . Each four neighbouring actuator cells formed a group, as is depicted in figure 1.3. In such a group the pressure at each of the eight inlets, indicated with a plus symbol, can be controlled independently by valves. With this the air flow in each actuator cell generates a viscous force on the substrate. In total 36 actuator cells were used which covered 50 % of the substrate area and which could actuate the substrate in every planar direction. In point-to-point positioning, accelerations were reached up to 0.600  $\text{m/s}^2$ . Also a 50 Hz position control bandwidth and 6 nm ( $1\sigma$ ) servo error were achieved.

### 1.2.2. Deformable surface concept

The second concept was developed by Vuong [30]. He created an air film based actuator with a deformable surface to actuate and levitate a thin substrate. The used substrate was a wafer with a diameter of 200 mm and a mass of 58 g. Each air actuator consists of a hollow tube with an outer diameter of 5 mm and a length of 13 mm. On top is a hexagon actuator head that acts as the bearing surface. Each hexagon has a width of 14 mm (distance between two opposite sides). The gap between two neighbouring hexagons has a width of 1 mm. Because of the shape, a single air actuator is called a 'flower' (see figure 1.4). That is why the total system is called the 'Flowerbed'. In total 61 flowers are used. Each flower is connected to a stationary top membrane and a movable bottom membrane. Both membranes are made from spring steel with a thickness of 50  $\mu\text{m}$ . Both membranes have the function to act as rotational hinges, such that a flower can rotate. Here the top membrane is the pivot point as shown in figure 1.4. Whereas the bottom membrane moves horizontally by a piezo actuator. The force generated by the piezo actuator is shown with green arrows. The top membrane has the additional function to seal off the vacuum chamber. With this a vacuum pressure can be created beneath the actuator heads of the flowers. A gauge pressure of 2.50 bar is supplied beneath each flower such that there is a high pressure from the middle of each flower head. In figure 1.4 areas with high pressure are indicated with a plus symbol. Furthermore, a vacuum pressure of  $-0.1$  bar was supplied via a side port. With this a vacuum pressure is created in the gaps between the flowers. Areas with vacuum pressure are indicated with a minus symbol. Therefore air flowed from the middle of the flower to the gaps.

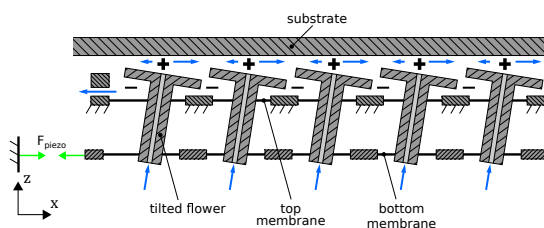


Figure 1.4: Cross section of the deformable surface concept called the "Flowerbed". In this example, each flower head is slightly tilted in positive x-direction due to a piezo actuator. The plus symbols indicate areas of high pressure and the minus symbols indicate areas of low pressure. The blue arrows indicate the direction of the air flow.

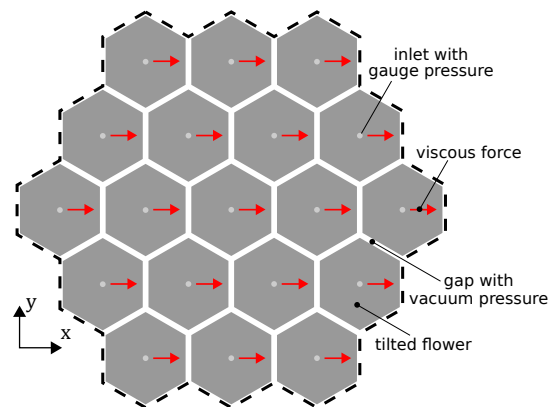


Figure 1.5: Top view of nineteen flowers of the deformable surface concept with substrate removed. In this example, each flower head is slightly tilted in positive x-direction which results in a motion of the substrate in positive x-direction. The red arrows indicate the viscous traction force generated by each flower acting on the substrate.

When a flower is tilted air will flow mainly in the direction with the least amount of flow resistance. For

example, the heads of the flowers in figure 1.4 and 1.5 are slightly tilted in positive x-direction. Therefore the air film thickness on the right side of the actuator head is larger than the air film thickness on the left side of the actuator head. This results in a lower flow resistance to the right than to the left. Thus a larger flow is generated to the right than to the left as indicated by the blue arrows. Because the flow is larger to the right than to the left, a net viscous force is generated on the substrate in positive x-direction. These viscous forces are shown in figure 1.4 by the red arrows for each individual flower. In the work of Krijnen [12] control has been applied to the Flowerbed. From his work the motion system was able to reach a maximum force of 70 mN, resulting in a maximum acceleration of  $1.2 \text{ m/s}^2$  of the wafer. Also a 60 Hz control bandwidth and 104 nm ( $2\sigma$ ) positioning error have been achieved.

### 1.3. Opposed air film actuators

In the past researches, air film actuators have seen promising results for handling thin substrates. These air film actuators have been used on one side of the substrate. An alternative configuration would be to use air film actuators on both sides of the substrate, as suggested by Vuong [30] and Snieder [26]. Such a configuration is similar to conventional opposed pad bearings. Double sided substrate actuation has four advantages over single sided substrate actuation:

1. The air film actuators do not need vacuum pressure to achieve a steady fly height. This because the substrate is preloaded between the opposed air film actuators. Therefore the substrate finds an equilibrium position between the opposed air film actuators.
2. Opposed air film actuators can use gauge pressures above 1 bar downstream the inlet, such that larger traction forces and thus larger substrate accelerations can be achieved. In previous research projects vacuum pressure was needed to preload the substrate. As vacuum pressures cannot go below  $-1$  bar, the gauge pressures downstream the inlets were limited to about 1 bar.
3. On both sides of the substrate similar pressure profiles are applied. Therefore deformations and pitching rotations of the substrate are eliminated (theoretically).
4. With double sided substrate actuation, traction forces are generated on both sides of the substrate. Therefore twice the amount of traction is generated on the substrate compared to single sided substrate actuation with similar conditions

These advantages are beneficial for actuating thin flexible substrates. As explained in section 1.1, for Nexperia air film actuators could be an alternative solution for positioning their webs. Therefore, the focus of this thesis is to exploit the use of opposed air film actuators for positioning thin flexible substrates.

### 1.4. Research goal

The goal of this research project is to investigate the possibilities of using opposed air film actuators for positioning thin flexible substrates. The aim is to design and built a demonstrator to show if the theoretical model of the motion system complies with the manufactured demonstrator. Therefore, the research goal of this thesis is stated as follows:

*"Demonstrator design and validation of opposed air film actuators for contactless positioning of thin flexible substrates, to be applied in the semiconductor industry."*

The demonstrator should be designed that it can reach similar performances for the long stroke as the current motion system from Nexperia. The demonstrator should be able to actuate a piece of web in one degree of freedom, namely in x-direction. The motion system should move the substrate with 50 mm in x-direction within 50 ms. Here the substrate is at standstill at the start and end of the displacement. For this translation a  $\pm 1$  mm positioning accuracy is chosen.

### 1.5. Outline of this thesis

Now that the research goal is defined an overview will be given for the coming chapters of this thesis. In chapter 2 the theoretical working principles of an air film actuator using compressible air will be explained. At the end of the chapter the performance of a basic air film actuator will be evaluated. Next in chapter 3 the theory is used to design a demonstrator which can actuate a piece of flexible substrate with the use of air film

---

actuators. Thereafter, in chapter 4 three different experiments are explained and the results are compared to the theoretical model. With this the performance of the demonstrator can be determined. In chapter 5 the conclusions and recommendations for future work are described. In appendices A to F additional information is given for specific subjects, such as the derivation of the Reynolds equation, realisation of the design and additional measurements.



# 2

## Theory and working principles of air film actuators

In this chapter the theoretical working principles of an air film actuator will be explained. First in section 2.1 the approach to find solutions for the fluid flow fill will be explained. Secondly in section 2.2 the main assumptions used to model the fluid will be discussed. In section 2.3 the Reynolds equation will be presented and simplified to calculate the pressure field in a compressible fluid film. In section 2.4 the in-plane fluid properties will be evaluated which describes the motor function of an air film actuator. In section 2.5 formulas will be derived for restrictors, which are important for describing the mass flow through different sections. In section 2.6 the out-of-plane fluid properties are discussed, which explains the bearing function of an air film actuator. Finally, in section 2.7 the performance of a basic air film actuator will be evaluated with the theory developed in the sections before.

### 2.1. Approach

As described in section 1.2 several concepts have been made for an air actuator which can move a thin substrate by manipulating the flow of an air film. In order to know the performance of the actuator, one needs the velocity field of the fluid. As in many other fluid problems, from the velocity field the other properties are directly derived. Any fluid problem in general must satisfy the three basic conservation laws of mechanics plus a thermodynamic state relation and associated boundary conditions:

1. Conservation of mass (continuity).
2. Conservation of momentum (Newton's second law).
3. Conservation of energy (first law of thermodynamics).
4. A state relation like  $\rho = \rho(p, T)$ .
5. Appropriate boundary conditions at interfaces, inlets and outlets.

As can be found in literature [32] these equations can be solved by two different methods. The first method is to use a control volume approach where a finite region is defined. With this, a flow balance can be made for the flow 'in' and flow 'out' of the region, which is based on the 'Reynolds transport theorem'. But by doing so, the properties at the boundaries are often averaged or one-dimensional values. Control volume analysis is accurate for any flow distribution and lead to useful estimates of gross effects (such as mass flow and energy change) for the given problem. However, this method is not suited for describing the detailed flow pattern at every point  $(x, y, z)$  in the field.

The second method is to use a differential approach for seeking the point-by-point details of a flow pattern. This approach is based on the basic conservation laws which are, in this case, applied to an infinitesimal control volume (or infinitesimal fluid system). From this results the basic differential equations of fluid motion where appropriate boundary conditions can be applied to. These differential equations of motion are quite

difficult to solve and analytical techniques are limited to simple geometries and uniform boundary conditions. But with the use of numerical methods, more complex geometries and boundary conditions, can be solved to an approximated solution. This second method is well suited for describing the pressure field and velocity field in the air film from which the performance of the actuator can be deduced. That is the reason the differential approach is used in this thesis for solving the conservation of mass and momentum equations.

## 2.2. Assumptions

In order to solve the differential equations one needs to make assumptions on how the fluid model behaves. These assumptions simplifies some equations which become easier to solve, while the accuracy of the physics which the equations try to capture do not suffer. The list below explains the chosen fluid model with associated assumptions and properties of the fluid.

1. The used fluid is assumed to be compressible clean air.
2. The fluid is modelled as an ideal gas. Thereby the equation of state is given by the ideal gas law  $\left(\rho = \frac{p}{R_g \cdot T}\right)$ .
3. The fluid viscous forces dominate the fluid inertial forces. This implies that the flow is laminar with the Reynolds number less than 2300.
4. There are 'no slip' conditions at the boundaries. The fluid and boundary surface have the same velocity at the interface ( $u_{\text{fluid}}(@\text{surface}) = u_{\text{surface}}$ ).
5. The fluid behaves as an isotropic Newtonian fluid where the shear stress is linearly proportional with the velocity gradient  $\left(\tau_{xz} = \mu \cdot \frac{\partial u}{\partial z}\right)$ .
6. Stokes' hypothesis applies: isotropic dilatations do not produce viscous stresses ( $\lambda + \frac{2}{3} \cdot \mu = 0$ ).
7. There is no heat transfer across the fluid boundaries ( $\dot{Q} = 0$ , adiabatic process). Furthermore, any adiabatic expansion/cooling is compensated by viscous heating, so the temperature is assumed not to change much.
8. Because the viscosity of air is slightly dependent on temperature, the fluid viscosity is considered constant. This is also known as an isoviscous fluid ( $\mu(T) = \mu$ ).
9. Because the specific heats of air are slightly dependent on temperature, the specific heats of the fluid are considered constant  $\left(c_p(T) = c_p, c_v(T) = c_v, \kappa = \frac{c_p}{c_v} = 1.4\right)$ .
10. The fluid film thickness is much less than the fluid film length and width ( $H \ll L$ ). The dimensions in  $x$ - and  $y$ -direction are of the same order.

## 2.3. Pressure field in thin film fluid

Pressure is the compressive stress at a point in a hydrostatic fluid. As explained in appendix B it is the pressure gradient which drives the fluid flow. The pressure distribution in the fluid can be described by a scalar field. This pressure distributing can be determined with the 'Reynolds equation' which is shown in equation 2.1. A full derivation of equation 2.1 is shown in appendix B.

$$\frac{\partial}{\partial x} \left( \frac{\rho \cdot h^3}{12 \cdot \mu} \cdot \frac{\partial p}{\partial x} \right) + \frac{\partial}{\partial y} \left( \frac{\rho \cdot h^3}{12 \cdot \mu} \cdot \frac{\partial p}{\partial y} \right) - \frac{\partial}{\partial x} \left( \frac{\rho \cdot h \cdot (u_1 + u_2)}{2} \right) - \frac{\partial}{\partial y} \left( \frac{\rho \cdot h \cdot (v_1 + v_2)}{2} \right) = \frac{\partial}{\partial t} (\rho \cdot h) \quad (2.1)$$

Here  $\rho$  is the density,  $h$  is the film height,  $\mu$  the fluid dynamic viscosity,  $p$  the pressure,  $u_1$  the velocity of the lower surface in  $x$ -direction,  $u_2$  the velocity of the upper surface in  $x$ -direction,  $v_1$  the velocity of the lower surface in  $y$ -direction and  $v_2$  the velocity of the upper surface in  $y$ -direction. The modelling of an air film actuator can be explained by a simple flow in two dimensions ( $x$  and  $z$ ) between two surfaces. In this model it is assumed that the flow has infinite width in  $y$ -direction and that there is only a pressure gradient in  $x$ -direction. Therefore the terms in  $y$ -direction in equation 2.1 are omitted for this model. An illustration of this model is shown in figure 2.1 (a). Here the lower surface (manifold) supports the upper surface (substrate) by

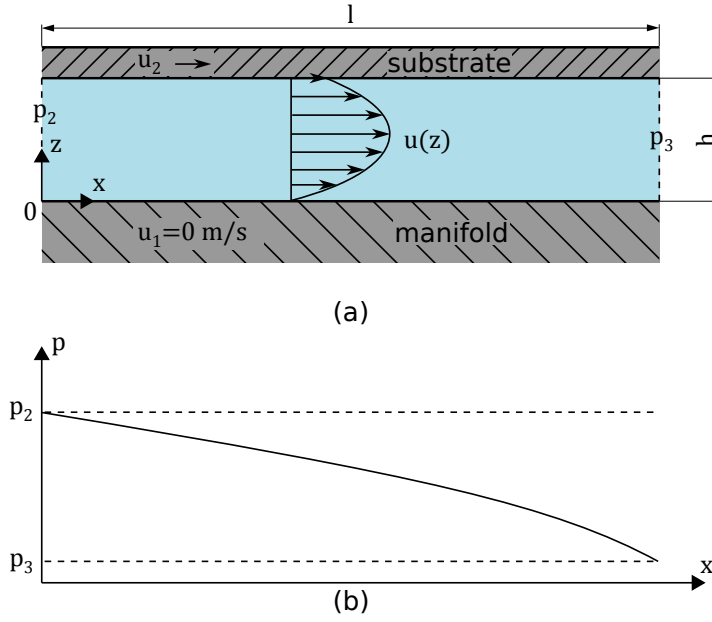


Figure 2.1: Section of a manifold which supports a substrate by a thin film of compressible air.  
 (a) a flow is generated by a pressure difference  $p_2 - p_3$  and by the velocity of the substrate of  $u_2$ .  
 (b) pressure distribution in the fluid between  $p_2$  and  $p_3$ .

a thin film of air with height  $h$ . As explained in appendix B, the pressure is uniform in  $z$ -direction. But there can be a pressure difference between  $p_2$  and  $p_3$ . Also the substrate could have a velocity of  $u_2$  in  $x$ -direction. This pressure gradient and substrate movement may drive a flow in the fluid, which results in a velocity profile  $u(z)$  across the film height.

Furthermore, the compressible fluid can be modelled by the ideal gas law (assumption 2), therefore the density in equation 2.1 can be replaced by  $\rho = \frac{p}{R_g \cdot T}$ . Here  $p$  is the fluid pressure,  $R_g$  is the specific gas constant of air and  $T$  the temperature of the fluid. By also omitting the terms in  $y$ -direction equation 2.1 results in equation 2.2.

$$\frac{\partial}{\partial x} \left( \frac{h^3 \cdot p}{12 \cdot \mu \cdot R_g \cdot T} \cdot \frac{\partial p}{\partial x} \right) - \frac{\partial}{\partial x} \left( \frac{h \cdot (u_1 + u_2) \cdot p}{2 \cdot R_g \cdot T} \right) = \frac{\partial}{\partial t} \left( \frac{h \cdot p}{R_g \cdot T} \right) \quad (2.2)$$

Because it is assumed that the temperature does not change much (assumption 7),  $T$  can be assumed constant in the fluid. Therefore the term  $T$  can be brought out of each partial derivative. Therefore both  $R_g$  and  $T$  can be divided from equation 2.2 because they are both constants. This results in equation 2.3.

$$\frac{\partial}{\partial x} \left( \frac{h^3 \cdot p}{12 \cdot \mu} \cdot \frac{\partial p}{\partial x} \right) - \frac{\partial}{\partial x} \left( \frac{h \cdot (u_1 + u_2) \cdot p}{2} \right) = \frac{\partial}{\partial t} (h \cdot p) \quad (2.3)$$

Furthermore by assuming the flow is steady, the partial derivative with respect to  $t$  becomes zero. Also, it is assumed that the second term of equation 2.3 is negligible compared to the first term. This is because the substrate velocity  $u_2$  is either zero or very small. Also the manifold is not moving, thus  $u_1 = 0$  m/s at all time. This simplifies equation 2.3 to equation 2.4.

$$\frac{\partial}{\partial x} \left( \frac{h^3 \cdot p}{12 \cdot \mu} \cdot \frac{\partial p}{\partial x} \right) = 0 \quad (2.4)$$

In equation 2.4 there are two dependent variables  $h(x)$  and  $p(x)$ . For a section of length  $l$  where  $h(x)$  is constant and where  $p_2 > p_3$  (see figure 2.1 (a)), one can integrate equation 2.4 twice with respect to  $x$ . Subsequently, by filling in the boundary conditions results in equation 2.5 which is plotted in figure 2.1 (b).

$$p(x) = \sqrt{-\frac{p_2^2 - p_3^2}{l} \cdot x + p_2^2} \quad \text{for } 0 \leq x \leq l \quad (2.5)$$

## 2.4. In-plane fluid analysis

Now that the pressure field is defined, other important fluid parameters can be derived. In this section parameters that are accompanied with motion of the substrate in  $x$ -direction will be discussed. As explained in section B.5.1 the velocity profile in  $x$ -direction between two parallel surfaces can be described by equation 2.6.

$$u = \underbrace{\frac{1}{2} \cdot \frac{1}{\mu} \cdot (z^2 - h \cdot z) \cdot \frac{\partial p}{\partial x}}_{\text{Poiseuille flow}} + \underbrace{(u_2 - u_1) \cdot \frac{z}{h} + u_1}_{\text{Couette flow}} \quad (2.6)$$

The first term in equation 2.6 describes a Poiseuille flow. This is a flow that is driven by a pressure gradient, while the top and bottom surfaces are stationary. This is shown by  $u(z)$  in figure 2.2. The second term in equation 2.6 describes a Couette flow. This is a flow that is driven by motion of the top surface and/or bottom surface. For example, in case the bottom surface is stationary ( $u_1 = 0$  m/s) and when the pressure gradient is zero ( $\frac{\partial p}{\partial x} = 0$  N/m<sup>3</sup>), the Couette flow is driven by the top surface ( $u_2$ ). This is shown by  $u(z)$  in figure 2.3.

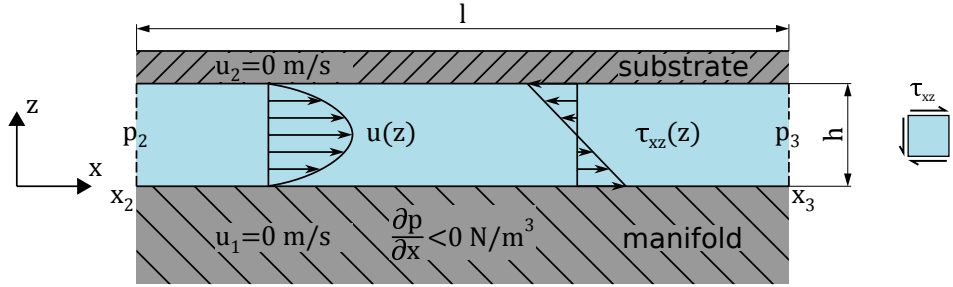


Figure 2.2: Poiseuille flow in  $x$ -direction. Here  $\frac{\partial p}{\partial x} < 0$  N/m<sup>3</sup>,  $u_2 = 0$  m/s and  $u_1 = 0$  m/s. The left graph shows the velocity profile and the right graph shows the shear stress profile.

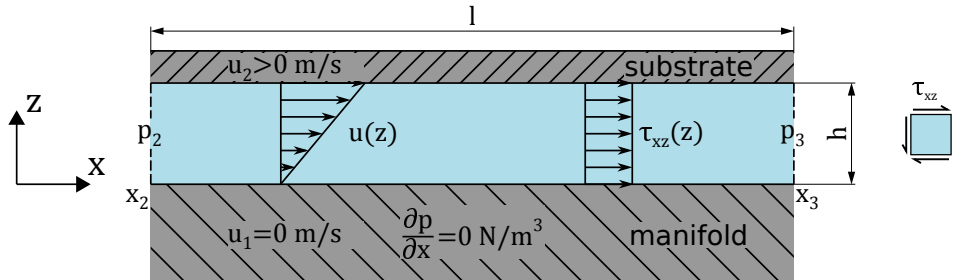


Figure 2.3: Couette flow in  $x$ -direction. Here  $\frac{\partial p}{\partial x} = 0$  N/m<sup>3</sup>,  $u_2 > 0$  m/s and  $u_1 = 0$  m/s. The left graph shows the velocity profile and the right graph shows the shear stress profile.

The pressure gradient can be derived by differentiating equation 2.5 with respect to  $x$ . This is shown in equation 2.7. For  $p_2 > p_3$  the pressure gradient is minimum for  $\frac{\partial p}{\partial x}(x=l) = -\frac{p_2^2 - p_3^2}{2 \cdot l \cdot p_3}$ .

$$\frac{\partial p}{\partial x} = -\frac{p_2^2 - p_3^2}{2 \cdot l \cdot \sqrt{-\frac{p_2^2 - p_3^2}{l} \cdot x + p_2^2}} \quad \text{for } 0 \leq x \leq l \quad (2.7)$$

Next, one can determine the volume flow in  $x$ -direction per unit depth by integrating equation 2.6 across the fluid height. This results in equation 2.8.

$$q_{x,y} = \int_0^h u(z) \cdot dz = \underbrace{-\frac{h^3}{12 \cdot \mu} \cdot \frac{\partial p}{\partial x}}_{\text{Poiseuille flow}} + \underbrace{\frac{u_1 + u_2}{2} \cdot h}_{\text{Couette flow}} \quad (2.8)$$

Furthermore, the fluid can be assumed to behave as a Newtonian fluid (assumption 5 from section 2.2). This means that by definition the shear stress in the fluid is proportional to the velocity gradient. The proportionality constant which relates the two is the viscosity:  $\tau_{xz} = \mu \cdot \frac{\partial u}{\partial z}$ . From this and by substituting the derivative of equation 2.6 follows equation 2.9.

$$\tau_{xz} = \underbrace{\left(z - \frac{1}{2} \cdot h\right) \cdot \frac{\partial p}{\partial x}}_{\text{Poiseuille flow}} + \underbrace{\mu \cdot \frac{u_2 - u_1}{h}}_{\text{Couette flow}} \quad (2.9)$$

To illustrate this, the shear stress profile for a Poiseuille flow is shown in the right graph of figure 2.2. Here the shear stress is linear with the fluid height. Furthermore, the shear stress profile for a Couette flow is shown in the right graph of figure 2.3. Here the shear stress is constant across the fluid height. In both figures on the far right side, the shear stresses are drawn on a fluid element in positive sign convention. This shows that the faster moving fluid pulls the slower moving fluid forward. While the slower moving fluid pulls the faster moving fluid backward.

Finally, one can determine the viscous force in  $x$ -direction per unit depth acting on the substrate ( $F_{f_{x,y}}$ ). This viscous force can be obtained by integrating the viscous shear stress in  $x$ -direction between  $p_2$  and  $p_3$ . Because the shear stress on the top of a fluid element is defined in positive  $x$ -direction, the shear stress acting on the substrate is defined in negative  $x$ -direction (third law of Newton). Therefore a minus sign is in the integral. The result is shown in equation 2.10. Note that  $h$  is taken constant between  $p_2$  and  $p_3$ .

$$F_{f_{x,y}} = \int_{x_2}^{x_3} -\tau_{xz}(h) \cdot dx = - \left[ \frac{1}{2} \cdot h \cdot p(x) + \mu \cdot \frac{u_2 - u_1}{h} \cdot x \right]_{x_2}^{x_3} = \underbrace{\frac{1}{2} \cdot h \cdot (p_2 - p_3)}_{\text{Poiseuille flow}} + \underbrace{\mu \cdot \frac{u_1 - u_2}{h} \cdot l}_{\text{Couette flow}} \quad (2.10)$$

## 2.5. Restrictors

For air to enter the air film and to limit the air flow, a restrictor is added to the manifold. There are various restrictors which can be used. Three basic restrictor elements will be discussed in this section.

For further analysis a similar model is used as in section 2.4, except now the model has a finite width of  $b$  in  $y$ -direction. Also an inlet restrictor is added for air to enter the fluid film. An illustration is shown in figure 2.4 (a). Here  $p_1 > p_2 > p_3$  such that the air flows from  $p_1$  to  $p_2$  to  $p_3$ . Note that in the model a wall is added on the left side so that the fluid can only flow to the right. This system can be viewed as two resistances connected in series. Such an analogy is similar to an electric circuit. This is shown in figure 2.4 (b). The mass flow through the inlet restrictor must be equal to the mass flow through the air film, in order to have mass continuity. Let us now express the mass flow for three different restrictors: capillary restrictor, thin film restrictor and orifice restrictor.

### 2.5.1. Capillary restrictor

The first restrictor to discuss is the capillary restrictor shown in figure 2.5 (a). The mass flow through a capillary restrictor is defined in equation 2.11. This equation is similar to the Hagen-Poiseuille equation, but then for compressible flow. This equation holds only under the conditions that the flow is laminar ( $Re < 2300$ ) and that the tube has a large length to diameter ratio ( $l/d > 20$ ) [28] [32]. The mass flow through a restrictor can be defined by the local density  $\rho$  divided by a resistance term  $R$  and multiplied by the pressure difference over the restrictor ( $p_1 - p_2$ ). Here the local density can be substituted by the averaged ideal gas law  $\rho = \frac{p_1 + p_2}{2 \cdot R_g \cdot T}$ .

$$\dot{m} = \rho \cdot \underbrace{\frac{\pi \cdot d^4}{128 \cdot \mu \cdot l}}_{R^{-1}} \cdot (p_1 - p_2) = \frac{\pi \cdot d^4}{256 \cdot \mu \cdot l \cdot R_g \cdot T} \cdot (p_1^2 - p_2^2) \quad (2.11)$$

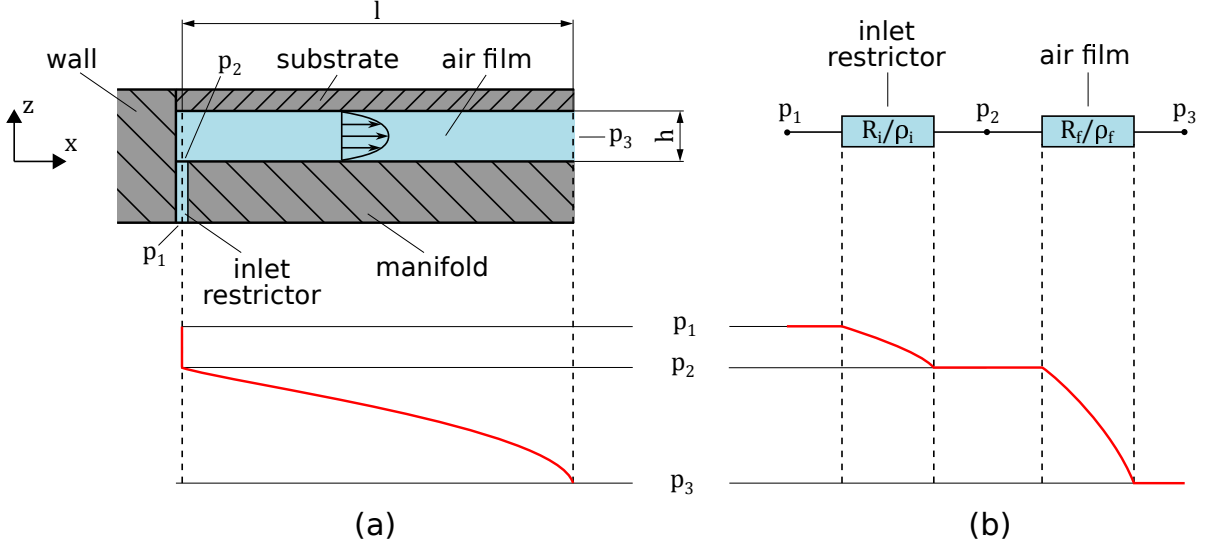


Figure 2.4: (a) flow between substrate and manifold parallel to each other with an inlet restrictor for air to enter the air film. A wall is added to the model to constrain only a flow to the right. The model has a finite width of  $b$  in  $y$ -direction. (b) equivalent model by using a schematic overview.

### 2.5.2. Thin film restrictor

The second restrictor to discuss is the thin film restrictor which is shown in figure 2.5 (b). The mass flow for such a restrictor can be derived by multiplying the volume flow (from equation 2.8) with the local density in the restrictor. Here it is assumed that only a Poiseuille flow dominates in the restrictor. Furthermore the thin film restrictor has a finite width of  $b$ . This results in equation 2.12. Note that assumptions 3 and 10 from section 2.2 must hold. This means that equation 2.12 is only valid when the flow is laminar ( $Re < 2300$ ) and when the restrictor height is much less than the restrictor length ( $h \ll l$  and  $h \ll b$ ).

$$\dot{m} = \rho \cdot \underbrace{\frac{b \cdot h^3}{12 \cdot \mu \cdot l}}_{R^{-1}} \cdot (p_1 - p_2) = \frac{b \cdot h^3}{24 \cdot \mu \cdot l \cdot R_g \cdot T} \cdot (p_1^2 - p_2^2) \quad (2.12)$$

### 2.5.3. Orifice restrictor

The third and last restrictor to discuss is the (inherent) orifice restrictor which is shown in figure 2.5 (c). The mass flow for such a restrictor is shown in equation 2.13 [24] [25] [28] [32].

$$\dot{m} = \begin{cases} C_d \cdot A_{\text{ori}} \cdot p_1 \cdot \sqrt{\frac{2}{R_g \cdot T} \cdot \frac{\kappa}{\kappa-1} \cdot \left[ \left( \frac{p_2}{p_1} \right)^{\frac{2}{\kappa}} - \left( \frac{p_2}{p_1} \right)^{\frac{\kappa+1}{\kappa}} \right]} & \text{if } \frac{p_2}{p_1} \geq \left( \frac{2}{\kappa+1} \right)^{\frac{\kappa}{\kappa-1}} \\ C_d \cdot A_{\text{ori}} \cdot p_1 \cdot \sqrt{\frac{2}{R_g \cdot T} \cdot \frac{\kappa}{\kappa-1} \cdot \left[ \left( \frac{2}{\kappa+1} \right)^{\frac{2}{\kappa-1}} - \left( \frac{2}{\kappa+1} \right)^{\frac{\kappa+1}{\kappa-1}} \right]} & \text{if } \frac{p_2}{p_1} < \left( \frac{2}{\kappa+1} \right)^{\frac{\kappa}{\kappa-1}} \end{cases} \quad (2.13)$$

Here  $C_d$  is the coefficient of discharge which accounts for vena contracta<sup>1</sup> effects at the entrance to the fluid film and for effects such as the sharpness of corners which the flow passes. The value of  $C_d$  can range between 0 and 1, but is often around 0.9. Furthermore  $A_{\text{ori}}$  is the smallest passage area of the orifice which the fluid has to flow through. For an inherent orifice restrictor this is often either the circular cross section area of the orifice hole ( $\pi \cdot d^2/4$ ) indicated in red or the cylindrical area ( $\pi \cdot d \cdot h$ ) in the fluid film connected to the orifice indicated in green. The flow in the orifice restrictor is assumed to be isentropic, with  $\kappa$  the ratio of the specific heats ( $\kappa = \frac{c_p}{c_v} = 1.4$  for air). The pressure ratio  $\frac{p_2}{p_1}$  is limited at the lower end. If the ratio is smaller than the critical ratio  $\left( \frac{p_2}{p_1} \right)_{\text{crit}} = \left( \frac{2}{\kappa+1} \right)^{\frac{\kappa}{\kappa-1}} = 0.528$ , then the orifice is said to be choked. This means that the flow reaches the speed of sound  $v_{\text{sound}} = \sqrt{\kappa \cdot R_g \cdot T}$  and the maximum possible mass flow passes through

<sup>1</sup>Vena contracta is the point in the fluid where the flow diameter is at its minimum. For orifices this point is located slightly downstream the orifice and results in an increase in velocity. This increase in velocity lowers the pressure.

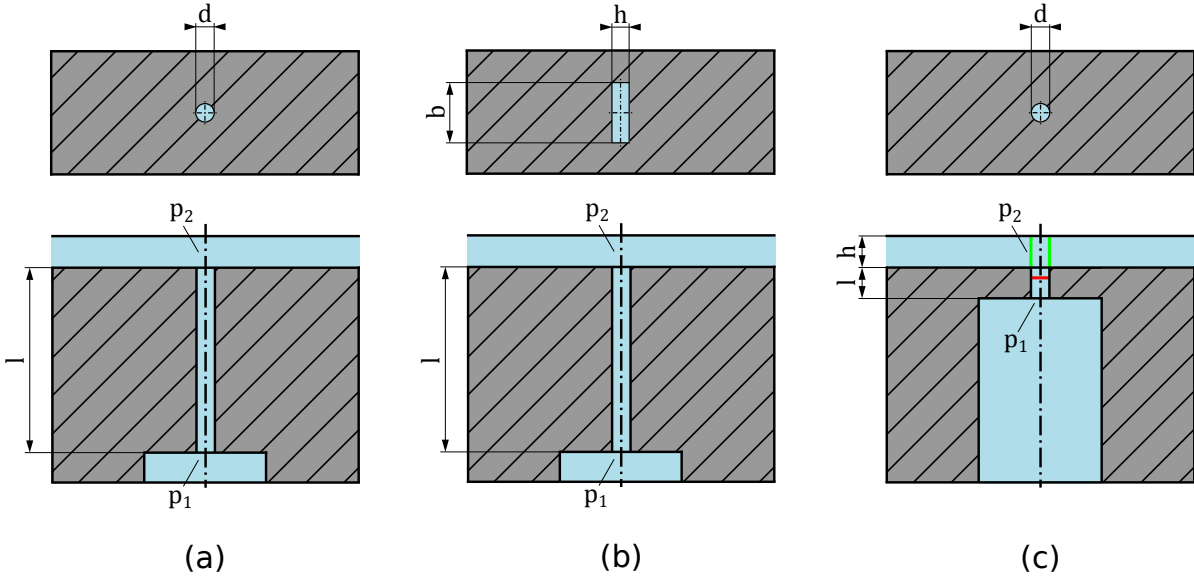


Figure 2.5: Top view and cross section view for various restrictors: (a) capillary restrictor where  $Re < 2300$  and  $l/d > 20$ , (b) thin film restrictor where  $Re < 2300$ ,  $h \ll l$  and  $h \ll b$ , (c) orifice restrictor where the smallest passage area  $A_{ori}$  is either the circular area ( $\pi \cdot d^2/4$ ) indicated in red or the cylindrical area ( $\pi \cdot d \cdot h$ ) indicated in green.

the orifice. The orifice can carry no additional mass flow, unless either  $A_{ori}$  or  $p_1$  is increased. At choked conditions  $p_2$  is linearly dependent on  $p_1$  by the critical ratio. Important to emphasize is that equation 2.13 holds for turbulent flow of a compressible fluid.

## 2.6. Out-of-plane fluid analysis

With the in-plane parameters defined and expressions given for various restrictors, one can now determine the out-of-plane parameters. With these parameters, insight can be obtained of forces in vertical direction which act on the substrate and manifold.

In figure 2.4 the pressures at  $p_1$  and  $p_3$  are predefined values, which only leaves  $p_2$  to be unknown. In order to determine  $p_2$  one applies the conservation of mass. Therefore the mass flow through the inlet restrictor needs to be equal to the mass flow through the air film. The mass flow can be determined by multiplying the local density with the local volume flow. This is shown in equation 2.14 between  $p_1$  and  $p_3$ . In equation 2.15 this is shown between  $p_2$  and  $p_3$ . The volume flow term can be further expressed by a resistance term  $R$  and a pressure difference, as is explained in section 2.5. Here  $R_i$  is the resistance in the inlet restrictor and  $R_f$  the resistance in the air film as is shown in figure 2.4 (b).

$$\dot{m}_{13} = \rho_{13} \cdot q_{13} = \rho_{13} \cdot \frac{p_1 - p_3}{R_i + R_f} \quad (2.14)$$

$$\dot{m}_{23} = \rho_{23} \cdot q_{23} = \rho_{23} \cdot \frac{p_2 - p_3}{R_f} \quad (2.15)$$

Next, one can set  $\dot{m}_{13} = \dot{m}_{23}$ . Here the densities are computed with the ideal gas law and by linearly averaging the pressure.

$$\frac{p_1 + p_3}{2} \cdot \frac{1}{R_g \cdot T} \cdot \frac{p_1 - p_3}{R_i + R_f} = \frac{p_2 + p_3}{2} \cdot \frac{1}{R_g \cdot T} \cdot \frac{p_2 - p_3}{R_f} \quad (2.16)$$

From equation 2.16 the value of  $p_2$  can be determined which is shown in equation 2.17.

$$p_2 = \sqrt{\frac{R_f}{R_i + R_f} \cdot (p_1^2 - p_3^2)} + p_3 \quad (2.17)$$

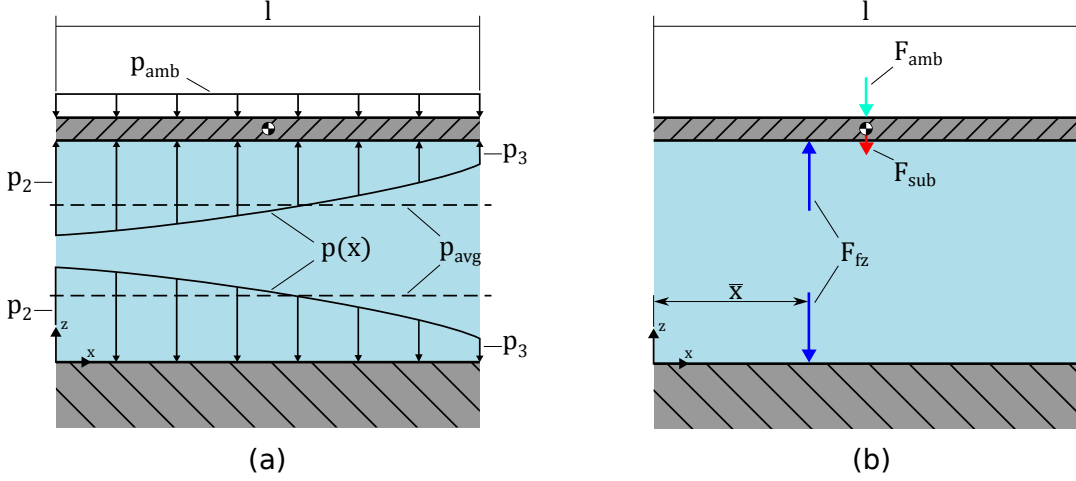


Figure 2.6: (a) pressure profiles acting on substrate and manifold. (b) resultant forces in  $z$ -direction acting on substrate and manifold.

Now that  $p_2$  is defined, one can compute the pressure profile described in equation 2.5. This pressure profile acts on the substrate and manifold, as is shown in figure 2.6 (a). Furthermore, one can obtain the resultant force of the air film pressure acting on the substrate and manifold in vertical direction. For this one can integrate equation 2.5 in  $x$ - and  $y$ -direction. The result is shown in equation 2.18. The resultant forces on the substrate are the pressure force by the fluid film ( $F_{fz}$ ), the pressure force by the ambient pressure ( $F_{amb}$ ) and the weight of the substrate ( $F_{sub}$ ). These forces are shown in figure 2.6 (b).

$$F_{fz} = \int_0^l \int_0^b p(x) \cdot dy \cdot dx = b \cdot \int_0^l \sqrt{-\frac{p_2^2 - p_3^2}{l} \cdot x + p_2^2} \cdot dx = \frac{2}{3} \cdot b \cdot l \cdot \frac{p_2^3 - p_3^3}{p_2^2 - p_3^2} = \frac{2}{3} \cdot b \cdot l \cdot \frac{p_2^2 + p_2 \cdot p_3 + p_3^2}{p_2 + p_3} \quad (2.18)$$

The location of the force  $F_{fz}$  can be determined by equation 2.19

$$\bar{x} = \frac{\int_0^l \int_0^b x \cdot p(x) \cdot dy \cdot dx}{\int_0^l \int_0^b p(x) \cdot dy \cdot dx} = \frac{\frac{2}{15} \cdot b \cdot l^2 \cdot \frac{2 \cdot p_2^5 - 5 \cdot p_2^2 \cdot p_3^3 + 3 \cdot p_3^5}{(p_2^2 - p_3^2)^2}}{\frac{2}{3} \cdot b \cdot l \cdot \frac{p_2^3 - p_3^3}{p_2^2 - p_3^2}} = l \cdot \frac{2 \cdot p_2^3 + 4 \cdot p_2^2 \cdot p_3 + 6 \cdot p_2 \cdot p_3^2 + 3 \cdot p_3^3}{5 \cdot (p_2^2 + p_2 \cdot p_3 + p_3^2) \cdot (p_2 + p_3)} \quad (2.19)$$

By dividing equation 2.18 by its surface ( $b \cdot l$ ) follows the average pressure in the fluid film as is shown in equation 2.20.

$$p_{avg} = \frac{2}{3} \cdot \frac{p_2^3 - p_3^3}{p_2^2 - p_3^2} = \frac{2}{3} \cdot \frac{p_2^2 + p_2 \cdot p_3 + p_3^2}{p_2 + p_3} \quad (2.20)$$

For static equilibrium the forces on the substrate in  $z$ -direction should balance one another, which results in equation 2.21. The weight of the substrate is negligible compared to the pressure forces. Therefore the pressure force below and above the substrate must be in equilibrium.

$$\sum F_z = 0 \quad \xrightarrow{\text{follows}} \quad F_{fz} = F_{amb} + F_{sub} \approx 0 \quad \xrightarrow{\text{follows}} \quad p_{avg} = p_{amb} \quad (2.21)$$

Furthermore, due to the asymmetric pressure profile in the fluid the substrate experiences a pitching torque. This pitching torque is computed for the moments about the centre of mass. This results in equation 2.22.

$$\sum M_y = -F_{fz} \cdot \left( \frac{l}{2} - \bar{x} \right) \quad (\text{counter-clockwise is defined positive}) \quad (2.22)$$

Finally, the stiffness of the fluid film can be determined. The stiffness is defined as the negative derivative of the vertical force on the substrate with respect to the fluid height. This is shown in equation 2.23. Here  $p_2$  is substituted by equation 2.17.

$$\begin{aligned} k_z(h) &= -\frac{dF_{fz}}{dh} = -\frac{2}{3} \cdot b \cdot l \cdot \frac{d}{dh} \cdot \left( \frac{p_2^2 + p_2 \cdot p_3 + p_3^2}{p_2 + p_3} \right) \\ &= -\frac{2}{3} \cdot b \cdot l \cdot \frac{d}{dh} \left( \frac{(p_1^2 - p_3^2) \cdot \frac{R_f}{R_i + R_f} + p_3^2 + \left( \sqrt{(p_1^2 - p_3^2) \cdot \frac{R_f}{R_i + R_f} + p_3^2} \right) \cdot p_3 + p_3^2}{\sqrt{(p_1^2 - p_3^2) \cdot \frac{R_f}{R_i + R_f} + p_3^2} + p_3} \right) \end{aligned} \quad (2.23)$$

Interestingly, in equation 2.23 only  $R_i$  and  $R_f$  are dependent on  $h$ . If  $R_i = 0 \text{ (N/m}^2\text{)/(m}^3\text{/s)}$  the stiffness becomes zero for every value of  $h$ . So, in order to have stiffness the inlet restrictor needs to be taken into account in the design. But the derivatives of  $R_i$  and  $R_f$  with respect to  $h$  are highly non-linear. An alternative way is to approximate the stiffness with a Taylor series using a first order central finite difference. This is shown in equation 2.24.

$$k_z(h) \approx -\frac{F_{fz}(h + \Delta h) - F_{fz}(h - \Delta h)}{2 \cdot \Delta h} \quad (2.24)$$

## 2.7. Basic air film actuator

The previous sections describe the flow between two parallel surfaces which are separated by a height  $h$ . By using sections with different values of  $h$  and by placing inlets and outlets at beneficial places, one can manipulate the applied force  $F_{fx}$  on the substrate. This may result in a net force which can actuate the substrate. Let us demonstrate this with a basic air film actuator which is covered by a substrate. In figure 2.7 the layout is shown for a single actuator cell. In figure 2.7 (a) the top view is shown of the actuator with the substrate removed. The manifold consists of three sections: pocket, dam and side. In this example, the pocket contains four inlets with pressure  $p_2$  and four outlets with pressure  $p_3$ . For this model the pressure in  $y$ -direction is assumed to be uniform.

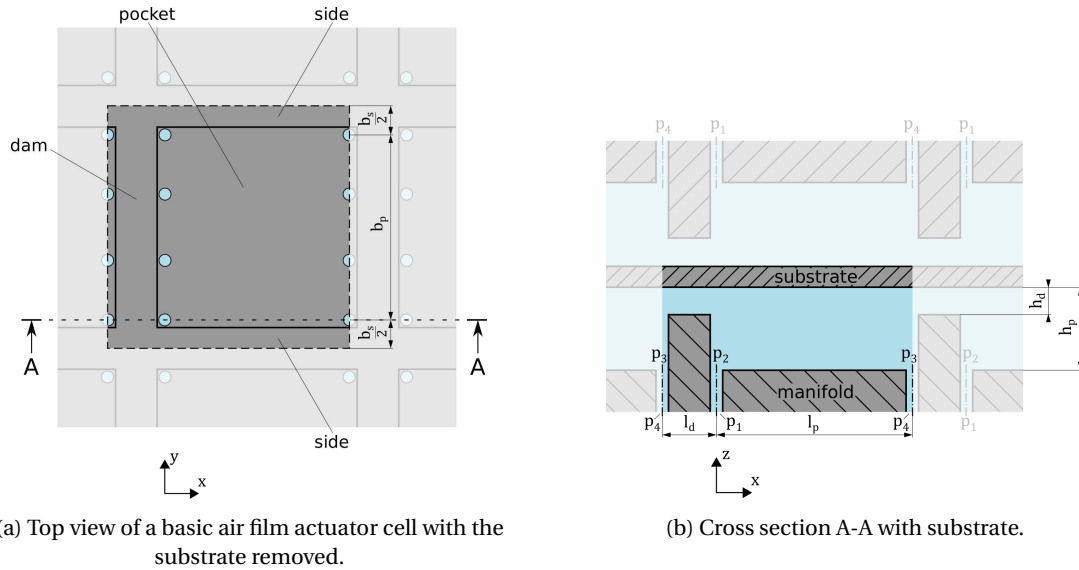


Figure 2.7: Basic air film actuator cell. Only the air film above one actuator cell and below the substrate is analysed.

In figure 2.7 the fluid above the pocket has a length  $l_p$ , a width  $b_p$  and a height  $h_p$ . The fluid above the dam has a length  $l_d$ , a width  $b_d = b_p + b_s$  and a height  $h_d$ . The fluid above the side has a length  $l_s = l_p$ , a width  $b_s$  and a height  $h_s = h_d$ .

Now with the geometry described, one can calculate the performance of the actuator. Let us first calculate the velocity profiles for each section. These can be computed by equation 2.6. The velocity profiles above the pocket, dam and side are shown respectively in equations 2.25, 2.26 and 2.27.

$$u_p = \frac{1}{2} \cdot \frac{1}{\mu} \cdot (z^2 - h_p \cdot z) \cdot \frac{\partial p}{\partial x} + (u_2 - u_1) \cdot \frac{z}{h_p} + u_1 \quad \text{for } 0 \leq x \leq l_p \quad (2.25)$$

$$u_d = \frac{1}{2} \cdot \frac{1}{\mu} \cdot (z^2 - h_d \cdot z) \cdot \frac{\partial p}{\partial x} + (u_2 - u_1) \cdot \frac{z}{h_d} + u_1 \quad \text{for } -l_d \leq x \leq 0 \quad (2.26)$$

$$u_s = \frac{1}{2} \cdot \frac{1}{\mu} \cdot (z^2 - h_s \cdot z) \cdot \frac{\partial p}{\partial x} + (u_2 - u_1) \cdot \frac{z}{h_s} + u_1 \quad \text{for } 0 \leq x \leq l_s \quad (2.27)$$

Secondly, let us calculate the viscous force in  $x$ -direction generated by each section, acting on the substrate. This is done by using equation 2.10 and applying a finite width. The viscous force for the pocket ( $F_p$ ), dam ( $F_d$ ) and side ( $F_s$ ) are shown respectively in equations 2.28, 2.29 and 2.30.

$$F_p = \frac{1}{2} \cdot b_p \cdot h_p \cdot (p_2 - p_3) + \mu \cdot \frac{u_1 - u_2}{h_p} \cdot l_p \cdot b_p \quad (2.28)$$

$$F_d = -\frac{1}{2} \cdot b_d \cdot h_d \cdot (p_2 - p_3) + \mu \cdot \frac{u_1 - u_2}{h_d} \cdot l_d \cdot b_d \quad (2.29)$$

$$F_s = \frac{1}{2} \cdot b_s \cdot h_s \cdot (p_2 - p_3) + \mu \cdot \frac{u_1 - u_2}{h_s} \cdot l_s \cdot b_s \quad (2.30)$$

The total viscous force generated by the actuator cell is the sum of the viscous forces. This is shown in equation 2.31. Here it can be seen that the force is linearly proportional to an actuation constant  $f_a$  times the pressure difference ( $p_2 - p_3$ ), plus a viscous damping constant  $c_{\text{visc}}$  times ( $u_1 - u_2$ ). Note that the manifold is stationary, thus  $u_1 = 0$  m/s at all time. The maximum velocity that the substrate can get is when the force due to the Poiseuille flow balances with the force due to the Couette flow. This is equivalent of setting equation 2.31 equal to zero, which results in  $u_{2,\text{max}} = \frac{f_a}{c_{\text{visc}}} \cdot (p_2 - p_3)$ .

$$F_{\text{fx}} = F_p + F_d + F_s = \underbrace{\frac{1}{2} \cdot b_p \cdot (h_p - h_d)}_{f_a} \cdot (p_2 - p_3) + \underbrace{\left( \frac{l_p \cdot b_p}{h_p} + \frac{l_d \cdot (b_p + b_s) + l_p \cdot b_s}{h_d} \right)}_{c_{\text{visc}}} \cdot \mu \cdot (u_1 - u_2) \quad (2.31)$$

Next, let us now calculate the mass flow through the air film. For this one needs to know the resistances in the system. In figure 2.8 all resistances of the actuator are visualized in a schematic overview. Here the total resistance of the inlet restrictors for one actuator cell is presented by  $R_i$ . The resistance through the pocket, dam and side are respectively  $R_p$ ,  $R_d$  and  $R_s$ . Finally, the total resistance of the outlet restrictors for one actuator cell is presented by  $R_o$ .

Often the resistance of an outlet restrictor is small compared to the other resistances in the system, because of two reasons. The first reason of having a low resistance at the outlet restrictor is that  $p_3 \approx p_4$ , this results in a maximum pressure difference between  $p_2$  and  $p_3$ . The second reason for a low resistance at the outlet restrictor is because the resistance of the outlet restrictor has an adverse influence on the vertical stiffness of the air film. Therefore  $R_o = 0$  (N/m<sup>2</sup>)/(m<sup>3</sup>/s).

The resistances in the air film are calculated by equation 2.12. The resistance for the air film above the pocket, dam and side are given respectively in equations 2.32, 2.33 and 2.34.

$$R_p = \frac{12 \cdot \mu \cdot l_p}{b_p \cdot h_p^3} \quad (2.32)$$

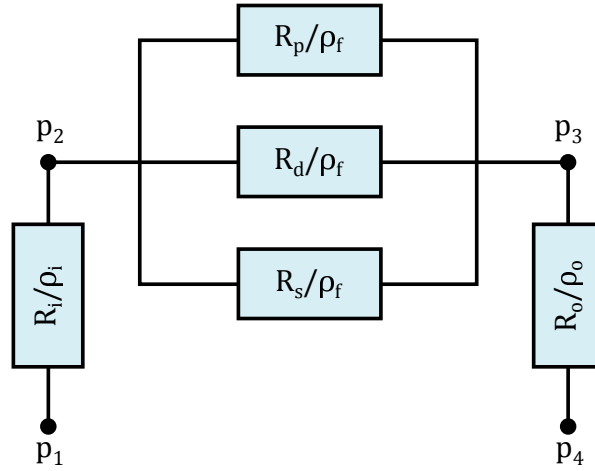


Figure 2.8: Schematic overview of all resistances of a basic air film actuator.

$$R_d = \frac{12 \cdot \mu \cdot l_d}{b_d \cdot h_d^3} = \frac{12 \cdot \mu \cdot l_d}{(b_p + b_s) \cdot h_d^3} \quad (2.33)$$

$$R_s = \frac{12 \cdot \mu \cdot l_s}{b_s \cdot h_s^3} = \frac{12 \cdot \mu \cdot l_p}{b_s \cdot h_d^3} \quad (2.34)$$

These three air film restrictors are connected to each other in parallel. The equivalent restrictor for the total air film in the actuator is given in equation 2.35.

$$R_f = \frac{1}{\frac{1}{R_p} + \frac{1}{R_d} + \frac{1}{R_s}} = \frac{12 \cdot \mu \cdot l_p \cdot l_d}{(b_p \cdot h_p^3 + b_s \cdot h_s^3) \cdot l_d + (b_p + b_s) \cdot l_p \cdot h_d^3} \quad (2.35)$$

When an operation pressure  $p_2$  is known, one can calculate the associate mass flow between  $p_2$  and  $p_3$ . This mass flow is shown in equation 2.36 and is equal to the mass flow which is needed to supply the actuator cell ( $\dot{m} = \dot{m}_{23}$ ).

$$\dot{m} = \dot{m}_{23} = \rho_f \cdot \frac{p_2 - p_3}{R_f} = \frac{1}{2 \cdot R_g \cdot T} \cdot \frac{p_2^2 - p_3^2}{R_f} \quad (2.36)$$

Finally, one can determine the ratio between the viscous force and the mass flow:  $F_{ix}/\dot{m}$ . It is beneficial to design an air film actuator with a large  $F_{ix}/\dot{m}$ , this minimizes the air consumption of the system.

To conclude this chapter, we have now described and explained the most important parameters for designing an air film actuator. The insights will be used in chapter 3 for designing a realistic air film actuator.



# 3

## Design

In this chapter the theory from chapter 2 is used to design a demonstrator which can actuate a piece of flexible substrate with the use of air film actuators. First in section 3.1 the design requirements will be explained. Secondly in section 3.2 a top-down approach will be used to translate the abstract requirements into concrete requirements, which are traceable to design parameters. In section 3.3 a conceptual design is made. This conceptual design explains what the layout will be for the motion system. Thereafter, in section 3.4 the design and analytical performance of each individual actuator cell are determined. Also is explained how the actuator cells are integrated in the design. Subsequently in section 3.5 the pneumatic components are described and modelled. In section 3.6 the control and response of the motion system are determined. Finally, in section 3.7 a brief overview is given of the final design.

### 3.1. Design requirements

As mentioned in section 1.1, a contactless air film actuator could provide an alternative solution for the current motion system. One of the main benefits is that a contactless air film actuator has only the substrate as moving mass which results in lower required actuation forces. Furthermore, there is no horizontal stiffness between the actuator and the substrate which reduces external horizontal disturbances to interfere with the substrate position. Lastly, no cooling is required to operate the valves which may simplify the design. This could result in less components and a cheaper design. To compete with the current motion system the following three design requirements are made:

1. The current motion system from Nexperia is capable of moving the substrate with 50 mm in x-direction within 50 ms. Here the substrate is at standstill, at the start and end of the displacement. To compete with the performance of the current motion system these parameters must be the same.
2. In the current motion system from Nexperia the substrate is mainly translated in x-direction and is able to make small corrections in y-direction. For simplicity of the air flow and the design, it is chosen to limit the demonstrator to only have one degree of freedom which is in x-direction.
3. One of the main disadvantages of the current motion system from Nexperia is that the relative large translations of 50 mm require large torques from the electric motors to accelerate and decelerate the mass of the drum. The main goal of this thesis is to come up with an alternative solution which can perform these relative large translations. For this research the substrate translations are more important than the position accuracy. Therefore, it is aimed to have an accuracy of  $\pm 1$  mm rather than  $\pm 3\mu\text{m}$  which is the capability of the current motion system.

### 3.2. Top-down approach

Before dimensioning a motion system, one can break down the abstract requirements from section 3.1 by a top-down approach. The abstract requirements can be translated into concrete requirements, which are traceable to design parameters. First, in section 3.2.1 the required displacement is translated into a realistic trajectory, which is determined with a trajectory planner. This results in a trajectory with a maximum acceleration of  $160 \text{ m/s}^2$ . Secondly, in section 3.2.2 the required positioning accuracy is translated into a minimum

required bandwidth of 56 Hz. The maximum acceleration and minimum bandwidth will be used in following sections to design the motion system.

### 3.2.1. Trajectory planner

To determine the maximum needed acceleration (and thus actuator force), which provides the desired motion of 50 mm within 50 ms of the substrate, a 3rd order trajectory planner is used. A trajectory planner is an algorithm to calculate an allowable trajectory in time for an unconstrained degree of freedom. In our case we are looking for the trajectory of the substrate in x-direction with the lowest bound on the acceleration and which has a realistic rise time behaviour. Subsequently, with feedforward control a force can be generated to perform an acceleration of the mass in accordance with the desired trajectory, determined with the trajectory planner. Any disturbance or unmodelled behaviour, which varies from this desired trajectory, is compensated with feedback control.

There exist different types of trajectory planners. The bound on the highest order derivative term with respect to the associated degree of freedom, determines the type of trajectory planner. So, a 2nd order trajectory planner has a bound on the acceleration and could have bounds on its lower order derivative terms. While a 3rd order trajectory planner has a bound on the jerk (derivative of acceleration) and could have bounds on its lower order derivative terms. Interestingly, 3rd and higher order trajectory planners include rise/fall time behaviour of the plant. In this thesis we will limit ourselves to 3rd order trajectory planners, because higher order trajectory planners may lead to a considerable increase in execution time of the trajectory, often without a clear mechanism for finding a time optimal solution.

A trajectory planner adds three benefits to the controller. The first benefit of a trajectory planner is that it provides an approach for designing an appropriate trajectory, which complies with the behaviour of the plant. Such an approach is not provided by feedforward control. The second benefit of a trajectory planner is that it lowers the position error. This reduces the feedback control actions, which provide less chance of demanding a motion which is physically impossible or dangerous to perform by the given motion system. The third benefit is that the settling time is reduced when arriving at the desired endpoint, because the dynamics of the controlled system are reduced.

Now let us explain the chosen trajectory with a 2nd and 3rd order trajectory planner. For a 2nd order trajectory planner the lowest bound on the acceleration is an acceleration profile which accelerates at maximum acceleration in the first half of the period and thereafter brakes at maximum deceleration in the second half of the period. Here it assumed that  $a_{\min} = -a_{\max}$ . This acceleration profile also ensures that the velocities at the begin position and end position are 0 m/s. The needed constant acceleration  $a_{\max}$  can be calculated by knowing that during the acceleration period, half of the total displacement has been travelled. This results in:

$$a_{\max} = \frac{2 \cdot (x_{\text{tot}}/2)}{(t_{\text{tot}}/2)^2} = \frac{2 \cdot (0.050/2)}{(0.050/2)^2} = 80 \text{ m/s}^2.$$

Now the acceleration profile for the 2nd order trajectory planner is determined as is shown with the blue line in figure 3.1 where  $a_{\max} = 80 \text{ m/s}^2$  and  $a_{\min} = -80 \text{ m/s}^2$ . By integrating once one can obtain the velocity profile and by integrating twice one can obtain the position profile, which are shown also in figure 3.1. This results in a displacement of 50 mm within 50 ms as desired with a maximum velocity of 2 m/s. Note that the associated jerk profile is zero everywhere, except for  $t = 0 \text{ s}$  or  $t = 0.05 \text{ s}$  where the jerk is  $+\infty \text{ m/s}^3$  and for  $t = 0.025 \text{ s}$  where the jerk is  $-\infty \text{ m/s}^3$ . Because 2nd order trajectory planners have inherently a jerk that is unbounded, the acceleration profile is discontinuous.

Lets move on to 3rd order trajectory planners. For this we are looking for a trajectory which results in a displacement of 50 mm within 50 ms with the lowest maximum jerk. This is the case where the change in acceleration is the slowest (worst case scenario). The result is a triangular acceleration profile. The required jerk has a square shaped profile, which can be divided into four sections with constant jerk. Here it is assumed that  $j_{\min} = -j_{\max}$ . The needed constant jerk  $j_{\max}$  can be calculated by:  $j_{\max} = \frac{x_{\text{tot}}}{2 \cdot (t_{\text{tot}}/4)^3} = \frac{0.050}{2 \cdot (0.050/4)^3} = 1.28 \cdot 10^4 \text{ m/s}^3$ .

The corresponding jerk profile is shown with the red line in figure 3.1. By integration one can obtain the associated acceleration, velocity and position profiles which are also plotted in figure 3.1. This results in a displacement of 50 mm within 50 ms as desired with a maximum acceleration of  $160 \text{ m/s}^2$ . One could increase the value of  $j_{\max}$ , which results in a truncated triangular acceleration profile and lowers the maximum acceleration. An example is shown by the yellow line in figure 3.1, which has a maximum jerk of  $2 \cdot 10^4 \text{ m/s}^3$ .

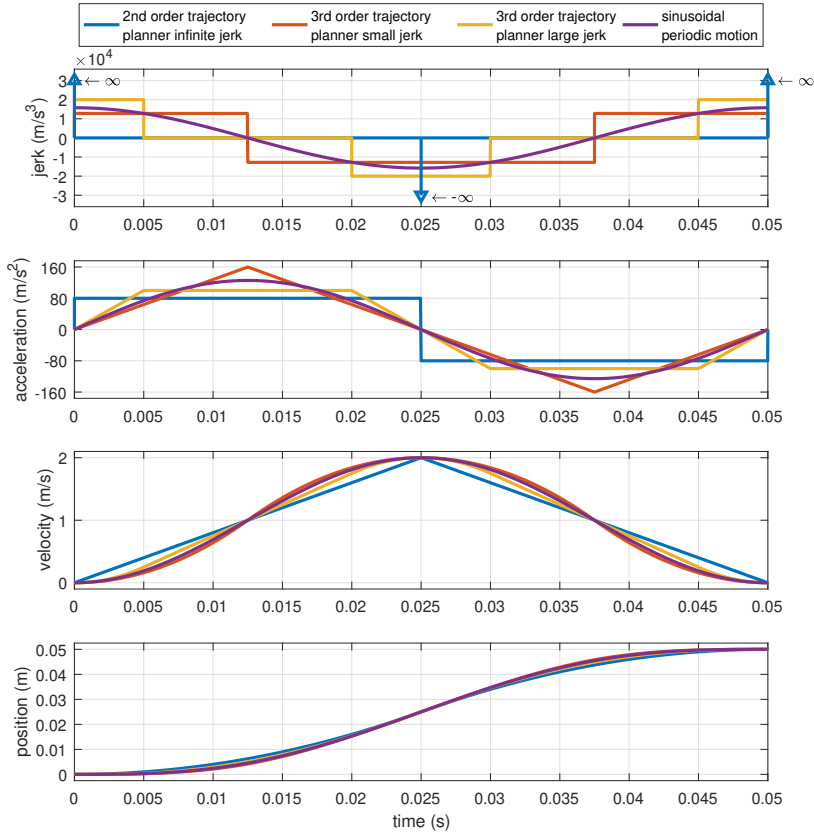


Figure 3.1: Second and third order trajectory profiles.

and a maximum acceleration of  $100 \text{ m/s}^2$ . Using even a higher maximum jerk will approximate the blue line. But a large jerk demands a fast rise time effect (change of acceleration) of the motion system. Therefore it is chosen to use the red line in figure 3.1 for the design process. This states that the motion system we are designing should have a maximum acceleration of at least  $160 \text{ m/s}^2$ . More information and a derivation of 3rd order trajectory planners is shown in [14].

### 3.2.2. Required system bandwidth and stability

A specification of the system performance in terms of frequency response is the bandwidth. In the context of precision positioning systems the term bandwidth is defined as the range from 0 Hz until the unity-gain cross-over frequency ( $f_c$ ), where the amplitude of the open-loop frequency response passes a value of one. For most common situations, this is the point where the amplitude of the frequency response traverses from amplification to attenuation (from low to high frequency). It is this open-loop gain that determines the suppression of output disturbances. Thus a high bandwidth indicates a large suppression of output disturbances and thus relates to a high accuracy performance of the total system.

$$\ddot{x}_{\text{ref}} = 1600 \cdot \pi^2 \cdot \cos(40 \cdot \pi \cdot t) \quad (3.1)$$

$$\dot{x}_{\text{ref}} = 40 \cdot \pi \cdot \sin(40 \cdot \pi \cdot t) \quad (3.2)$$

$$\dot{x}_{\text{ref}} = -\cos(40 \cdot \pi \cdot t) + 1 \quad (3.3)$$

$$x_{\text{ref}} = -\frac{1}{40 \cdot \pi} \sin(40 \cdot \pi \cdot t) + t \quad (3.4)$$

To estimate the required bandwidth, a contactless positioning model is used. The motion system has to follow a reference trajectory of 50 mm within 50 ms within  $\pm 1 \text{ mm}$  accuracy as mentioned in section 3.1. This

reference trajectory can be modelled as a sinusoidal periodic motion with a velocity profile which has an amplitude of 1 m/s, an offset of 1 m/s and a frequency of  $(\frac{1}{0.050} =)$  20 Hz which the substrate has to follow (see equation 3.3). By integrating and differentiating the associated jerk, acceleration and position profiles can be calculated. These are listed in equations 3.1, 3.2 and 3.4 respectively. These equations are also plotted by the purple lines in figure 3.1.

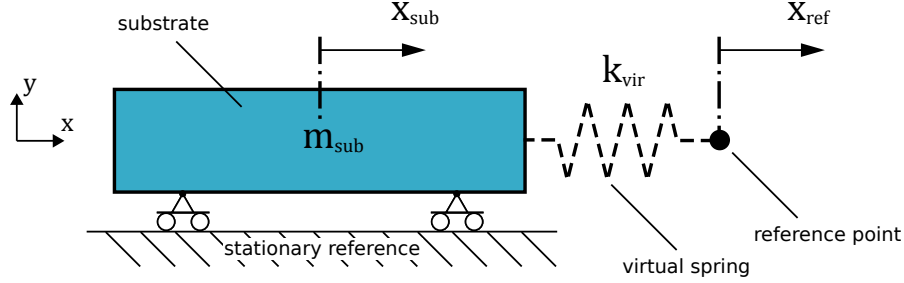


Figure 3.2: Virtual spring between substrate and reference point.

The substrate has to follow a virtual reference point in time which is equal to  $x_{ref}$ . This is visualized by the model in figure 3.2 where there is a virtual spring between the the reference point and the substrate. When the mass of the substrate is 1.058 g (see appendix C.1), the peak amplitude of the force ( $F_{peak}$ ) that corresponds to the peak acceleration equals to  $(1.058 \cdot 10^{-3} \cdot 40 \cdot \pi =)$  133 mN. The maximum allowable error ( $\delta_{error}$ ) between the reference point and the substrate position is 1 mm. The minimum required stiffness of the virtual spring  $k_{vir}$  to stay within the maximum allowable error is calculated in equation 3.5.

$$k_{vir} \geq \frac{F_{peak}}{\delta_{error}} = \frac{133 \cdot 10^{-3}}{1 \cdot 10^{-3}} = 133 \text{ N/m} \quad (3.5)$$

Finally, the undamped natural frequency ( $f_0$ ) of the substrate mass with the virtual spring is calculated in equation 3.6.

$$f_{BW} = f_0 = \frac{1}{2 \cdot \pi} \cdot \sqrt{\frac{k_{vir}}{m_{sub}}} = \frac{1}{2 \cdot \pi} \cdot \sqrt{\frac{133}{1.058 \cdot 10^{-3}}} \approx 56 \text{ Hz} \quad (3.6)$$

Connecting the substrate to a virtual reference point by a physical spring is not possible. Therefore a virtual spring is created. For the motion system this is achieved by the proportional part of a feedback controller, which creates a proportional counteracting force. This force is generated by air film actuators which are controlled by the feedback controller. For this active system  $f_0$  represents the maximum tracking frequency, called bandwidth ( $f_{BW}$ ). When the reference point frequency is above this bandwidth frequency the active system is not able to track the reference point within the accuracy range of  $\pm 1$  mm.

Aside from bandwidth, feedback controlled systems also have to consider the stability of the motion system. Closed-loop stability can be determined by the character of the open-loop frequency response. The stability condition states that the total phase of the open-loop system must be larger than  $-180^\circ$  in the frequency region of the unity-gain cross-over frequency ( $f_c$ ). In equation 3.7 this is shown in mathematical terms.

$$\angle(C(j \cdot \omega_c) \cdot G(j \cdot \omega_c)) > -180^\circ \quad (3.7)$$

Here  $C$  is the transfer function of the controller,  $G$  the transfer function of the plant,  $j$  the imaginary number (not to be confused with the jerk) and  $\omega_c (= 2 \cdot \pi \cdot f_c)$  the unity-gain cross-over frequency in radians. Designing a motion system which has a phase close to  $-180^\circ$  (for example  $-179^\circ$ ) at  $f_c$  is not practical. Because a small additional time-delay or phase-lag would decrease the phase below  $-180^\circ$  which makes the closed-loop system unstable. That is why we use a phase margin ( $\theta_{margin}$ ) of  $35^\circ$  to prevent this situation from happening. Furthermore, it is known from PID-controllers that they can add a maximum phase of  $90^\circ$ . With these stated, one can reformulate equation 3.7 as a design criteria for stability which is given in equation 3.8. By

substituting the variables this results in equation 3.9.

$$\angle C(j \cdot \omega_c) + \angle G(j \cdot \omega_c) > -180^\circ + \theta_{\text{margin}} \quad (3.8)$$

$$\angle G(j \cdot \omega_c) > -235^\circ \quad (3.9)$$

From equation 3.9 it can be seen that the plant should have at least  $-235^\circ$  at  $f_c$  in order to have a stable system. Now one can compare  $f_{BW}$  with  $f_c$  from equations 3.6 and 3.9. From this one can state a more general design criteria which includes the required performance and ensures that the motion system is stable. This is shown in equation 3.10. This equation states that the plant should be designed to have a phase more than  $-235^\circ$  at 56 Hz to meet the required accuracy of  $\pm 1$  mm and have a stable closed-loop system.

$$\angle G(j \cdot 2 \cdot \pi \cdot 56) > -235^\circ \quad (3.10)$$

### 3.3. Design concept

Now that the required performances are described, one can come up with a concept for the design. Using air film actuators, it is chosen to actuate the substrate on both sides of the substrate as will be explained in this section.

As is shown in section 1.2 a substrate can be actuated by using air film actuators on one side of the substrate. This concept is shown in figure 3.3. Within the air film actuators gauge pressure is used at the inlets and vacuum pressure is used at the outlets. With this a vertical force equilibrium is established on the substrate, such that the substrate is kept at a steady fly height. As is shown in previous work [26], when a flexible substrate is used it gets pressed to the surface at the outlets where the pressure is vacuum. So unless the substrate behaves rigid (or at least very stiff), this concept will not work contactless.

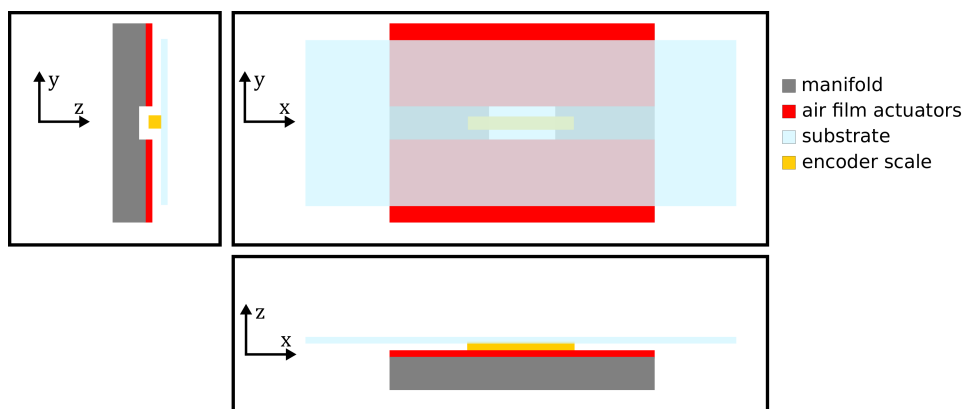


Figure 3.3: Single sided substrate actuation concept. Here the thickness of the air film actuators, substrate and encoder scale are exaggerated to visualise the components.

Another concept would be to actuate the substrate on both sides. This concept is shown in figure 3.4. Such an idea was also mentioned in [26] and [30]. The concept shows much resemblance with opposed pad bearings. An advantage of actuating the substrate on both sides is that it does not need vacuum pressure at the outlets. Instead it uses the pressure profiles on both sides of the substrate to keep the substrate at a steady fly height. Ideally when the pressure profiles are identical, there is no substrate deformation. Furthermore, in contrast to a single sided actuated substrate, the stiffness and horizontal force can be increased much further by simply increasing the inlet pressure. Therefore it is decided to actuate the substrate on both sides.

For the placement of the air film actuators three things should be taken into account. First of all, the actuators should cover as much as possible of the substrate. With this the substrate is evenly supported as much as possible, which prevents the substrate from touching the manifold surfaces. Secondly, the mid section of the motion system should be accessible for a linear encoder system. For this a readhead should be able to be placed under the substrate. Also a scale must be able to be placed on the substrate. The readhead

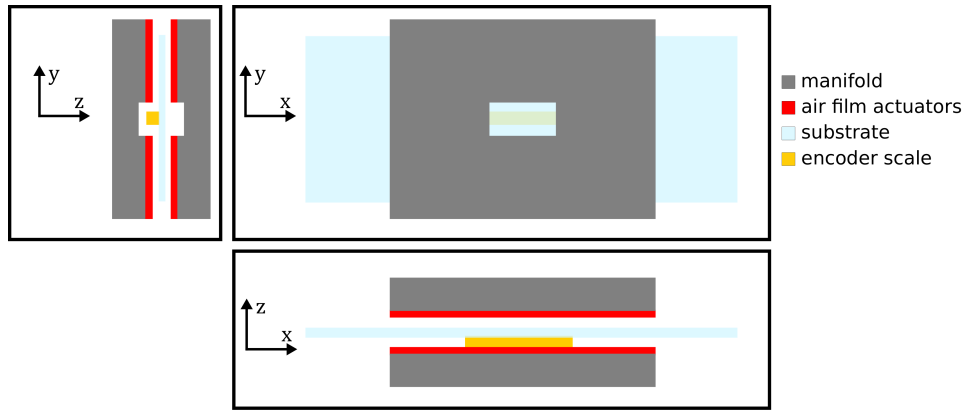


Figure 3.4: Double sided substrate actuation concept. Here the thickness of the air film actuators, substrate and encoder scale are exaggerated visualise the components.

can measure the position of the substrate. Thirdly, there should be enough dam area near the edges of the substrate. Because in previous work [31] it is encountered that at the edges the substrate tends to vibrate the most. Also the dams prevent large flows from the inlets to the edges.

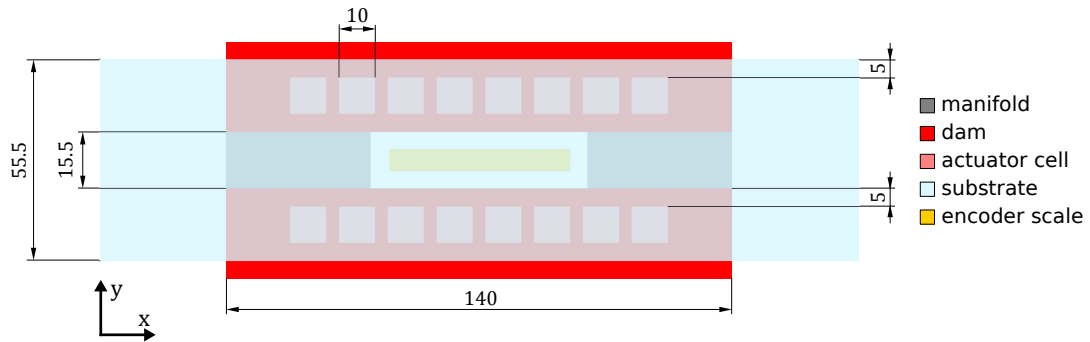


Figure 3.5: Layout of the actuators cells. Top view of the double sided substrate actuation concept with the upper manifold removed. The dimensions are in millimetres.

Based on this reasoning the placement of the actuator cells is determined. In appendix C.3.1 is explained that the readhead of the encoder system has a width of 13.5 mm. Thus it is decided to have a gap in the middle of the manifold with a width of 15.5 mm to place the readhead. Furthermore, it is chosen to use a substrate with a width of 55.5 mm. Therefore an actuator cell with a width of 10 mm can be placed on either side of the encoder scale. With this each actuator cell has a dam area which has a distance of 5 mm before reaching a substrate edge or an unsupported substrate section. At last the length of the dam is chosen to be 140 mm. With this the encoder scale can travel a distance of 50 mm to the left or to the right, while the substrate sections alongside the encoder scale are always supported by an air film above a dam. This results in having space for sixteen 10 mm by 10 mm actuator cells per manifold. The actuator cells layout is shown in figure 3.5.

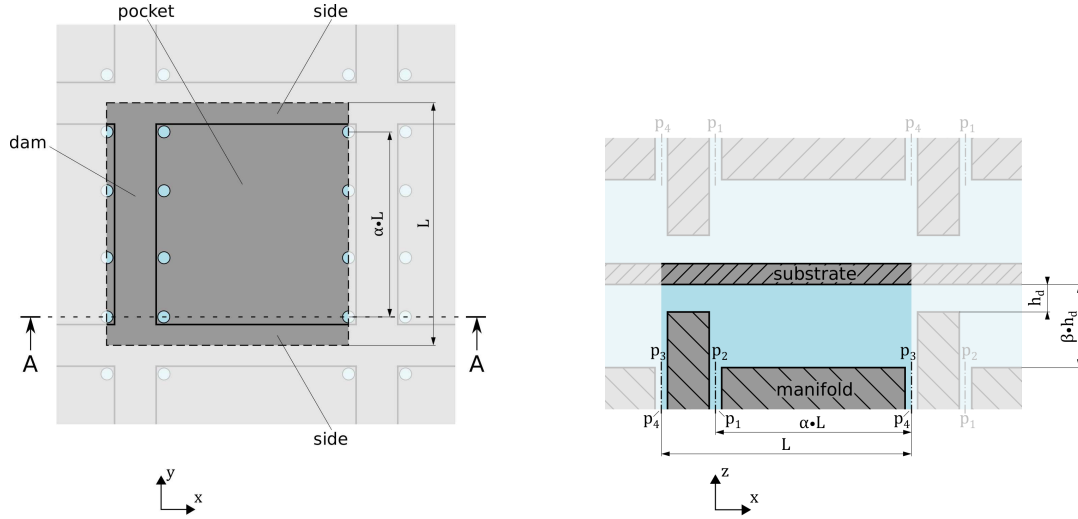
### 3.4. Actuator cell design

In this section the design of a single air film actuator cell will be shown. The goal is to design an efficient actuator cell which can generate a force that can accelerate the substrate with  $160 \text{ m/s}^2$ . This will be explained in section 3.4.1 Furthermore, the actuator cell should be able to provide a significant vertical stiffness to reduce vibrations of the substrate. This will be discussed in section 3.4.2. Lastly, the integration of the actuator cells in the manifold is shown in section 3.4.3.

### 3.4.1. Actuator cell performance

As mentioned in section 3.2, the substrate needs to be accelerated with a maximum acceleration of  $160 \text{ m/s}^2$ . Also as explained in appendix C.1 the substrate has an estimated mass of  $1.058 \text{ g}$ . That is why the maximum force required on the substrate is  $169 \text{ mN}$ .

As mentioned in section 3.3 the design space for each actuator cell is  $10 \text{ mm}$  by  $10 \text{ mm}$ . In total there are 16 actuator cells on each side of the substrate. So in total there are 16 actuator cells for generating a force in the negative x-direction (left) and there are 16 actuator cells for generating a force in the positive x-direction (right). Therefore each actuator cell should at least generate a maximum force of  $169 \text{ mN}/16 = 10.6 \text{ mN}$ . Instead of  $10.6 \text{ mN}$  it is chosen to generate at least  $16.5 \text{ mN}$  per actuator cell, for additional safety margin.



(a) Top view of a square air film actuator cell with substrate removed.

(b) Cross section A-A with substrate.

Figure 3.6: Air film actuator cell with a square geometry. Only the air film above one square actuator cell and below the substrate and is analysed as indicated in the figure.

Let us first look at a square geometry design, because it reduces the number of variables and simplifies the equations. The geometry of a square actuator cell is similar to figure 2.7, only now the geometry is strictly square with length  $L$  as shown in figure 3.6. Here the pocket has a length of  $l_p = \alpha \cdot L$  and the dam has a length  $l_d = (1 - \alpha) \cdot L$ , where  $\alpha$  can vary between 0 and 1. Lastly the film height between the pocket and the substrate is defined by  $h_p = \beta \cdot h_d$  and the substrate speed in positive x-direction as  $u_2 = u_{\text{sub}}$ . With these new parameters the force generated by the actuator cell from equation 2.31 can be simplified to equation 3.11. Also the mass flow through the air film from equation 2.36 can be simplified to equation 3.12.

$$F_{\text{fx}} = \frac{1}{2} \cdot \alpha \cdot (\beta - 1) \cdot h_d \cdot L \cdot (p_2 - p_3) - \left( \left( \frac{1}{\beta} - 1 \right) \cdot \alpha^2 + 1 \right) \cdot \frac{L^2}{h_d} \cdot \mu \cdot u_{\text{sub}} \quad (3.11)$$

$$\dot{m}_f = \frac{h_d^3}{12 \cdot \mu} \cdot \underbrace{\left( \beta^3 - 1 + \frac{1}{\alpha - \alpha^2} \right)}_{R_f^{-1}} \cdot \frac{1}{2 \cdot R_g \cdot T} \cdot (p_2^2 - p_3^2) \quad (3.12)$$

Now with equations 3.11 and 3.12 the actuator cell force and mass flow can be determined. For this the following model design considerations are made:

- The target film height is  $h_d = 10 \mu\text{m}$ , because the air flow scales with  $h_d^3$ . So it is desired to have a film height between the dam and the substrate to be as small as possible.
- The pressure at the inlet  $p_2$  is 3 bar and at the outlet the pressure  $p_3$  is 1 bar, because there is at least 5 bar supply pressure available and the outlet restrictor is assumed to be  $R_o = 0 \text{ (N/m}^2\text{)/(m}^3\text{/s)}$ . So it is

expected there is a total pressure drop of 4 bar between  $p_1$  and  $p_3$ . From previous work [30] [31] it is shown that often an inlet restrictor is chosen where half of the pressure drop is over the inlet restrictor and the other half of the pressure drop is over the air film restrictor, because then the stiffness is optimal in case the air is incompressible. Therefore the design target for  $p_2$  is 3 bar.

- The design space for a single actuator cell is 10 mm by 10 mm, therefore  $L = 10$  mm
- The actuation force per actuator cell should be at least 16.5 mN in order to accelerate the substrate with  $160 \text{ m/s}^2$ .
- The speed of the substrate is 1 m/s when it has an acceleration of  $160 \text{ m/s}^2$  (see figure 3.1). Therefore  $u_{\text{sub}} = 1 \text{ m/s}$ .

With these design considerations, values can be chosen for  $\alpha$  and  $\beta$ . These are varied in the range:  $0 < \alpha < 1$  and  $1 \leq \beta \leq 4$ . With these equations 3.11 and 3.12 can be substituted.

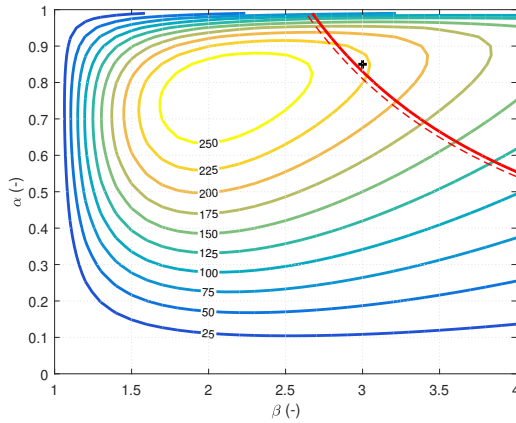


Figure 3.7: The actuation force over mass flow ratio  $F_{\text{fx}} / \dot{m}_f$  in  $\text{N}/(\text{kg/s})$ . The red line indicates where  $F_{\text{fx}} = 16.5 \text{ mN}$ . The black plus symbol indicates the chosen value of  $228 \text{ N}/(\text{kg/s})$  at  $\alpha = 0.85$  and  $\beta = 3.0$ .

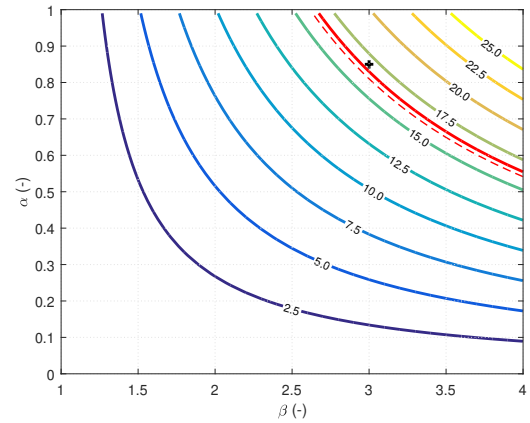


Figure 3.8: The actuation force  $F_{\text{fx}}$  in mN. The red line indicates where  $F_{\text{fx}} = 16.5 \text{ mN}$ . The black plus symbol indicates the chosen value of  $16.9 \text{ mN}$  at  $\alpha = 0.85$  and  $\beta = 3.0$ .

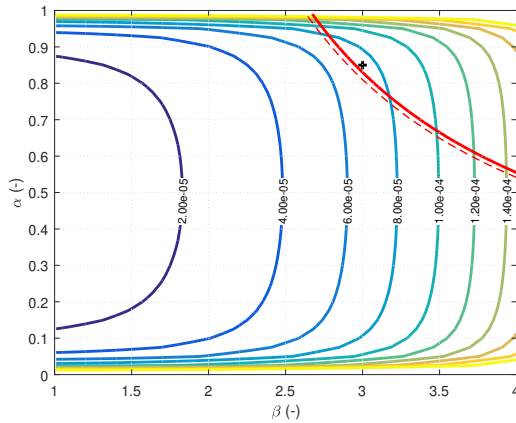


Figure 3.9: The air mass flow  $\dot{m}_f$  in  $\text{kg/s}$ . The red line indicates where  $F_{\text{fx}} = 16.5 \text{ mN}$ . The black plus symbol indicates the chosen value of  $7.41 \cdot 10^{-5} \text{ kg/s}$  at  $\alpha = 0.85$  and  $\beta = 3.0$ .

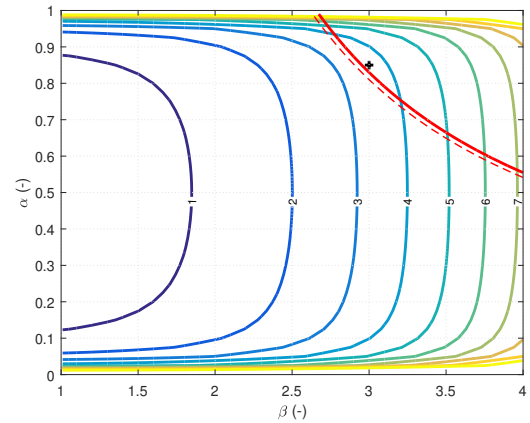


Figure 3.10: The air volume flow  $q_f$  in  $\text{L/min}$  at atmospheric pressure. The red line indicates where  $F_{\text{fx}} = 16.5 \text{ mN}$ . The black plus symbol indicates the chosen value of  $3.63 \text{ L/min}$  at  $\alpha = 0.85$  and  $\beta = 3.0$ .

First lets us look at the performance ratio. This is the ratio between  $F_{\text{fx}}$  and  $\dot{m}_f$  and determines how much force the actuator cell generates per unit mass flow of air. This ratio is also described in previous work [25] [30] and indicates how efficient a design is. This performance ratio is plotted in figure 3.7. For an efficient design

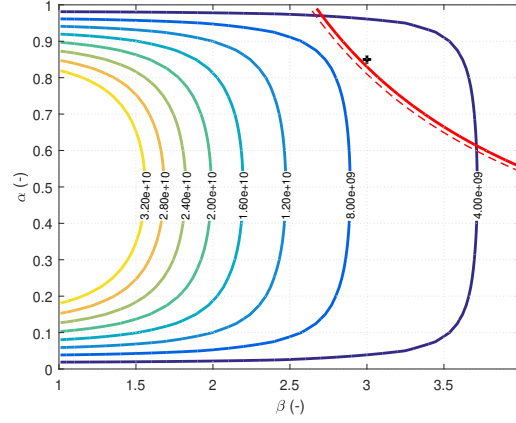


Figure 3.11: The air film resistance  $R_f$  in  $(\text{N}/\text{m}^2)/(\text{m}^3/\text{s})$ . The red line indicates where  $F_{fx} = 16.5 \text{ mN}$ . The black plus symbol indicates the chosen value of  $6.42 \cdot 10^9 (\text{N}/\text{m}^2)/(\text{m}^3/\text{s})$  at  $\alpha = 0.85$  and  $\beta = 3.0$ .

it is desired to have a high performance ratio. The red line indicates for what values of  $\alpha$  and  $\beta$  the actuation force is equal to 16.5 mN. The red dashed line indicates in which direction the actuation force decreases. An overview of the actuation force is shown in figure 3.8. To meet the required actuation force of 16.5 mN and have an efficient actuator cell the values  $\alpha = 0.85$  and  $\beta = 3.0$  are chosen for the design which results in a performance ratio of 228 N/(kg/s) with an actuation force of 16.9 mN. The chosen values are indicated by a black plus symbol.

Next let us look at the mass flow through a single actuator cell. The mass flow is plotted in figure 3.9 with the chosen value of  $7.41 \cdot 10^{-5} \text{ kg/s}$ . The same air flow is also plotted in figure 3.10, but then in L/min at atmospheric pressure. The actuator cell design consumes 3.63 L/min of air. At this point it is good to check the Reynolds number for the flow over the actuator cell, because the equations for the thin film restrictor only hold when the flow is laminar ( $Re < 2300$ ). The Reynolds number is given in equation 3.13 as derived in appendix B.4.4. Note that  $u_{\text{avg}} \cdot \rho = \dot{m} / (b \cdot h)$ . Here  $u_{\text{avg}}$  is the average velocity across the fluid height,  $h$  the film height and  $b$  the film width.

$$Re = \frac{u_{\text{avg}} \cdot \rho \cdot h}{\mu} = \frac{\dot{m}}{b \cdot \mu} \quad (3.13)$$

The Reynolds number for the pocket, dam and side section are respectively  $Re_p$ ,  $Re_d$  and  $Re_s$ . These are calculated in equation 3.14. Here the largest Reynolds number is 384, which is at the pocket section. Thus the flow is laminar for all fluid film sections.

$$Re_p = \frac{\dot{m}_p}{b_p \cdot \mu} = \frac{5.91 \cdot 10^{-5}}{8.50 \cdot 10^{-3} \cdot 1.81 \cdot 10^{-5}} = 384 \quad (3.14a)$$

$$Re_d = \frac{\dot{m}_d}{b_d \cdot \mu} = \frac{1.46 \cdot 10^{-5}}{10.0 \cdot 10^{-3} \cdot 1.81 \cdot 10^{-5}} = 81 \quad (3.14b)$$

$$Re_s = \frac{\dot{m}_p}{b_s \cdot \mu} = \frac{3.86 \cdot 10^{-7}}{1.50 \cdot 10^{-3} \cdot 1.81 \cdot 10^{-5}} = 14 \quad (3.14c)$$

Lastly, the flow resistance of the air film ( $R_f$ ) is plotted in figure 3.11 with the chosen value of  $6.42 \cdot 10^9 (\text{N}/\text{m}^2)/(\text{m}^3/\text{s})$ . In section 3.5.2 it will be shown that a low flow resistance is desired in order to build up pressure quickly in the air film. But the mass flow is inversely proportional to the flow resistance as shown in equation 3.12. So one has to balance between mass flow and flow resistance.

### 3.4.2. Actuator cell stiffness

Now that the geometry of an actuator cell is specified, one can choose the inlets for the actuator cell. These inlets supply air to the air film. The inlets inherently have a flow resistance which has two purposes. The first

purpose is that it partly determines the vertical stiffness of the air film. The second purpose is that it partly determines how fast the pressure builds up in the air film. The effect of the vertical stiffness is discussed in this subsection. The effect of the pressure build up will be explained in section 3.5.2.

First let us look at how the flow and flow resistance of the air film change when  $h_d$  is varied for the chosen geometry. For this analysis the actuator dimensions are kept constant, which were determined in section 3.4.1. Also  $p_2 = 3 \text{ bar}$  and  $p_3 = 1 \text{ bar}$  as before. The film thickness above the dam is varied in the range  $0 \mu\text{m} < h_d \leq 30 \mu\text{m}$ . The resulting mass flow and volume flow are shown in figure 3.12 and 3.13 respectively. This shows that the flow increases exponentially when the film height increases. Figure 3.12 or figure 3.13

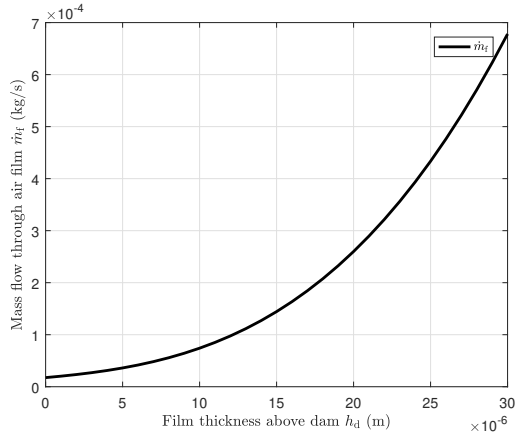


Figure 3.12: Mass flow through the air film above the actuator cell. Here the design operating fly height is  $h_d = 10 \mu\text{m}$  where  $\dot{m}_f = 7.41 \cdot 10^{-5} \text{ kg/s}$ .

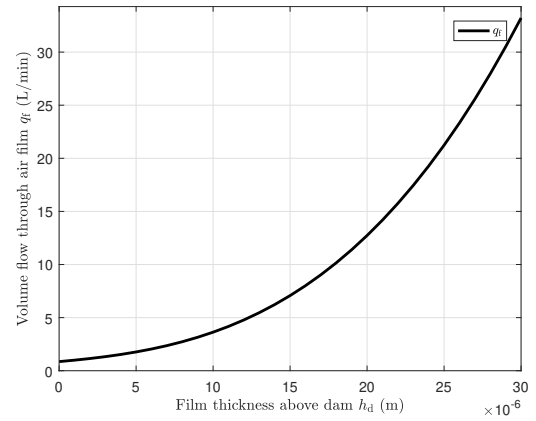


Figure 3.13: Volume flow through the air film above the actuator cell. Here the design operating fly height is  $h_d = 10 \mu\text{m}$  where  $q_f = 3.63 \text{ L/min}$  at atmospheric pressure.

emphasises why it is important to operate at low fly heights, otherwise a large flow is required to maintain a pressure of  $p_2 = 3 \text{ bar}$ . Furthermore, the air film resistance is shown in figure 3.14. Here is shown that  $R_f$  decreases exponentially when the film height increases.

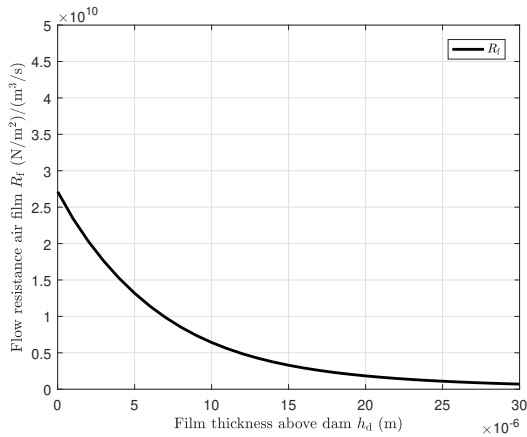


Figure 3.14: Flow resistance of the air film above the actuator cell. Here the design operating fly height is  $h_d = 10 \mu\text{m}$  where  $R_f = 6.42 \cdot 10^9 \text{ (N/m}^2\text{)/(m}^3\text{/s)}$ .

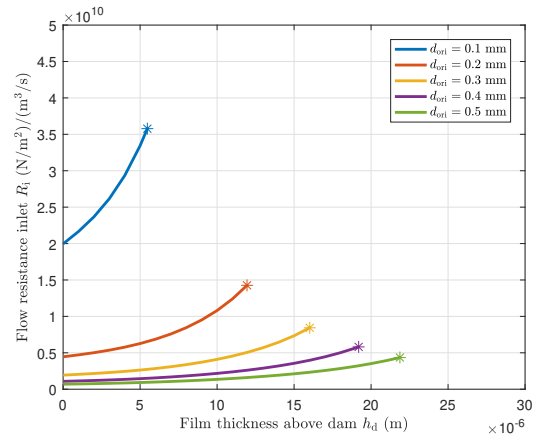


Figure 3.15: Flow resistance of the inlet of an actuator cell. The inlet resistance ( $R_i$ ) is modelled by 4 orifice restrictors ( $R_{ori}$ ) connected in parallel. Each orifice restrictor has a diameter  $d_{ori}$ . Here the design operating fly height is  $h_d = 10 \mu\text{m}$  where  $R_i = 4.10 \cdot 10^9 \text{ (N/m}^2\text{)/(m}^3\text{/s)}$ .

Secondly let us look at the inlet restrictors. It is chosen to use orifice restrictors instead of capillary restrictors because of the following two reasons:

1. Orifice restrictors ensure larger stiffness and lower flow resistance than capillary restrictors [31].

- Capillary restrictors are only predictable when the length over diameter ratio is large ( $l/d > 20$ ) and the flow is laminar ( $Re < 2300$ ). In previous projects [9] [30] the manufacturing and integrating of these restrictors into a design have been challenging. It is also encountered that inlet restrictors often have turbulent flow when working with pressure drops of a few bar over the inlet restrictor. While orifice restrictors do not need large length over diameter ratio and can be modelled for turbulent flows.

The mass flow through the inlet restrictor has to be equal to the mass flow through the air film. An inlet restrictor can consist of multiple orifice restrictors in parallel. With this said, one can solve equation 2.13 for  $p_1$ . Here pressure  $p_2 = 3$  bar and the mass flow through a single orifice restrictor is  $\dot{m}_{\text{ori}} = \dot{m}_f/n$ , where  $n$  is the number of orifice restrictors for the inlet of an actuator cell. Also it is assumed that  $C_d = 0.9$ . The smallest passage for the fluid to go through has an area  $A_{\text{ori}} = \pi \cdot d_{\text{ori}} \cdot h_p$ , which is true for  $h_p \leq d_{\text{ori}}/4$ . Where  $d_{\text{ori}}$  is the orifice diameter and  $h_p$  the film height in the pocket. When solved for  $p_1$ , one can determine the flow resistance for one orifice restrictor with equation 3.15.

$$R_{\text{ori}} = \frac{p_1^2 - p_2^2}{2 \cdot R_g \cdot T \cdot \dot{m}_{\text{ori}}} \quad (3.15)$$

With this the total flow resistance of the inlet for one actuator cell is  $R_i = R_{\text{ori}}/n$ . In figure 3.15 the flow resistance of the inlet for one actuator cell is shown when four orifice restrictors ( $n = 4$ ) are used. To show the influence of the orifice diameter, different diameters are modelled. One could model more than four orifices per actuator cell, but  $A_{\text{ori}}$  scales linear with  $n \cdot \pi \cdot d_{\text{ori}} \cdot h_p$ . The associated required pressure  $p_1$  is shown in figure 3.16, which is needed to get a pressure of  $p_2 = 3$  bar. When  $p_1 = 3.00 \text{ bar}/0.528 = 5.68 \text{ bar}$  the inlet becomes choked. This is indicated with an asterisk symbol in figures 3.15 to 3.18. The design operating film height between a dam and the substrate is  $10 \mu\text{m}$ . Therefore a diameter of  $0.1 \text{ mm}$  is invalid to use, because the orifices become sonic before  $p_2$  reaches  $3$  bar. A diameter of  $0.2 \text{ mm}$  could be valid, but if  $h_d$  increases to  $11.9 \mu\text{m}$  the inlet becomes sonic. So an orifice diameter of  $0.3 \text{ mm}$  is selected. At the operating fly height of  $10 \mu\text{m}$  a pressure of  $p_1 = 3.76 \text{ bar}$  is required to have a pressure of  $p_2 = 3$  bar. This results in a Mach number of  $0.577$  at  $p_2$  and a Reynolds number of  $4344$  in the inlet. The flow resistance graph in figure 3.14 can be added to the flow resistance graphs in figure 3.15 which results in the total flow resistance for one actuator cell  $R_{\text{act}} = R_i + R_f$ , which is shown in figure 3.17.

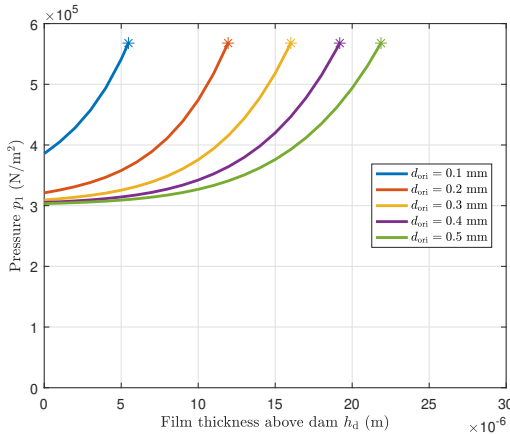


Figure 3.16: Required pressure  $p_1$  to get  $p_2 = 3$  bar. When  $\left(\frac{p_2}{p_1}\right)_{\text{crit}} = 0.528$  the flow reaches  $Ma = 1.0$ , which is indicated with an asterisk symbol. For  $h_d = 10 \mu\text{m}$  the pressure  $p_1 = 3.76 \cdot 10^5 \text{ N/m}^2$

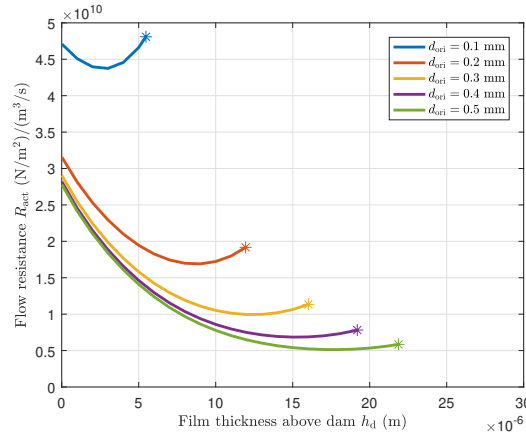


Figure 3.17: Total flow resistance of one actuator cell  $R_{\text{act}} = R_i + R_f$ . Here the design operating fly height is  $h_d = 10 \mu\text{m}$  where  $R_{\text{act}} = 1.05 \cdot 10^{10} \text{ (N/m}^2\text{) / (m}^3\text{/s)}$ .

At last, the vertical stiffness can be determined. By using equations 2.23 and 2.24 one can approximate the vertical stiffness. The stiffness is shown in figure 3.18. It is chosen to have a large stiffness as possible, because it is desired to suppress any unmodelled out-of-plane disturbances from substrate vibrations. No larger diameters than  $0.3 \text{ mm}$  are considered, because this would reduce the stiffness. With  $d_{\text{ori}} = 0.3 \text{ mm}$  the vertical stiffness is  $5.44 \cdot 10^9 \text{ (N/m) / m}^2$  per actuator cell at the operating point of  $h_d = 10 \mu\text{m}$ .

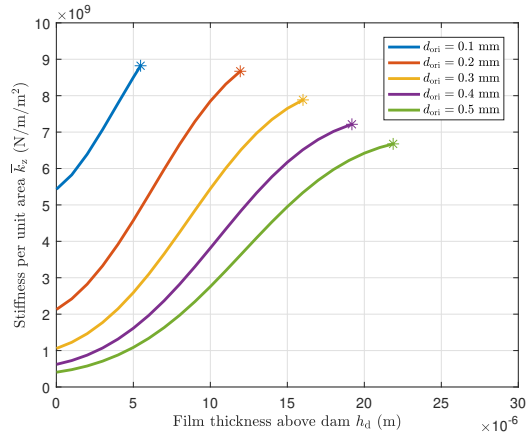


Figure 3.18: Stiffness per unit area per actuator cell. Here the design operating fly height is  $h_d = 10\mu\text{m}$  where  $\bar{k}_z = 5.44 \cdot 10^9 \text{ (N/m)/m}^2$  for  $d_{ori} = 0.3 \text{ mm}$ .

### 3.4.3. Manifold design

Now that the dimensions of the actuator cells are specified, the design of the manifold can be drawn. Using the concept described in section 3.3 and the design of the actuator cells of section 3.4.1, a three dimensional drawing is made in SOLIDWORKS 2016. The result of the bottom manifold is shown in figure 3.19.

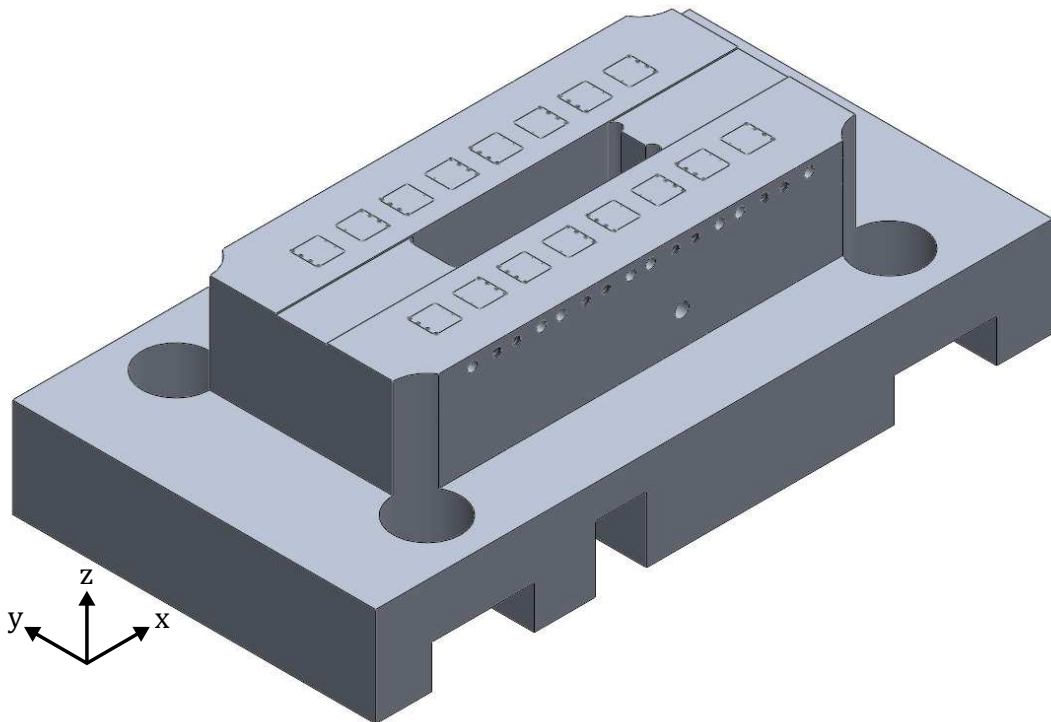


Figure 3.19: Three dimensional view of the bottom manifold made in SOLIDWORKS 2016.

Here it can be seen that a single manifold contains sixteen air film actuator cells. On the sides of the manifold are ducts where air can flow to the inlet or from the outlet of an actuator cell. Furthermore, the top view of the bottom manifold is shown in figure 3.20. As mentioned in sections 3.4.1 and 3.4.2 the pockets have a length and width of 8.5 mm and the inlets have orifice restrictors with a diameter of 0.3 mm. For the outlets it is chosen to have orifice restrictors with a diameter of 1 mm such that  $R_o \ll R_i$ . In each actuator cell at the inlet

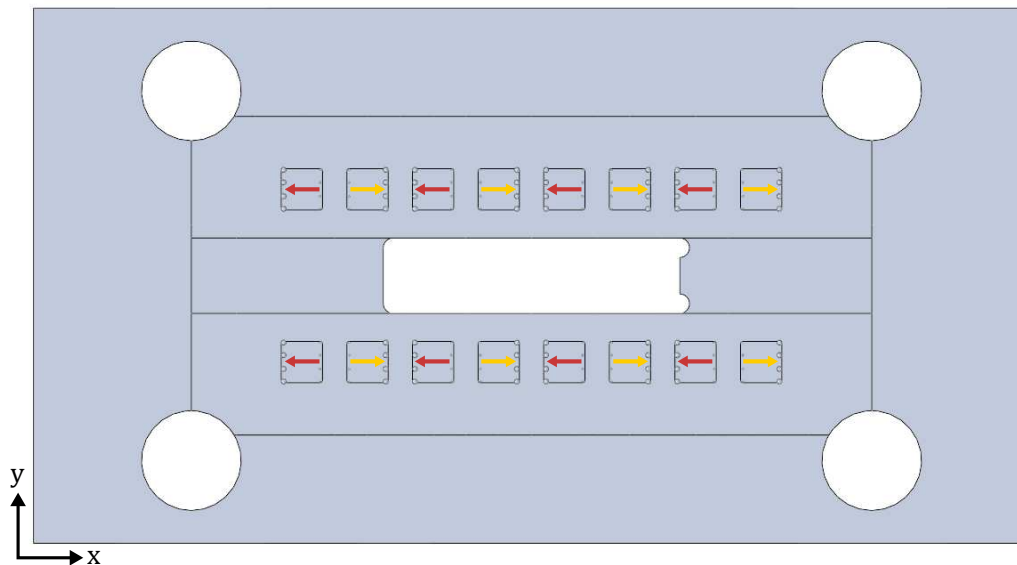


Figure 3.20: Top view of the bottom manifold made in SOLIDWORKS 2016. Here the yellow arrows indicate the actuator cells generating an actuation force to the right and the red arrows indicate the actuator cells generating a force to the left.

there are four orifice restrictors and at the outlet there are four orifice restrictors. In figure 3.20 the yellow arrows indicate the actuator cells generating an actuation force to the right and the red arrows indicate the actuator cells generating an actuation force to the left. The space between each actuator cell is 5 mm, because this is the smallest distance to place two fittings next to each other.

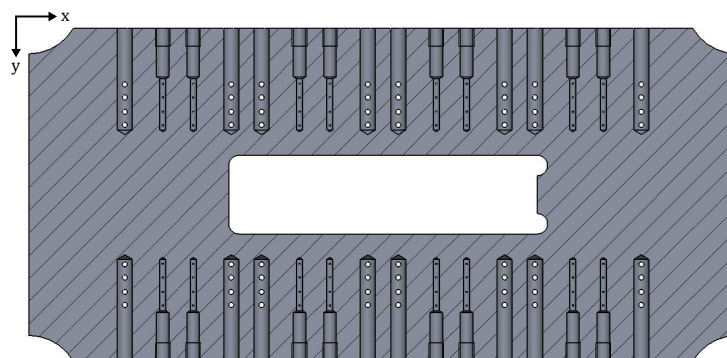


Figure 3.21: Cross section of the bottom manifold of the xy-plane. The manifold is viewed from below.

To show the routing of the ducts, a cross section of the bottom manifold of the xy-plane is made. This is shown in figure 3.21. The cross section is viewed from below. Here the entrances of the ducts for the inlets are tapped as is shown in the figure. With these tapped holes M3 fittings can be installed to connect these ducts to valves. In figure 3.22 a close up is made of the first three actuator cells of figure 3.20, counted from the left down corner. Here one can see more closely the placement of the orifice restrictors at the inlets and the orifice restrictors at the outlets. In figure 3.23 a cross section of the xz-plane is shown of the same three actuator cells. Here one can see how the ducts are connected to the actuator cells via inlet restrictors and outlet restrictors.

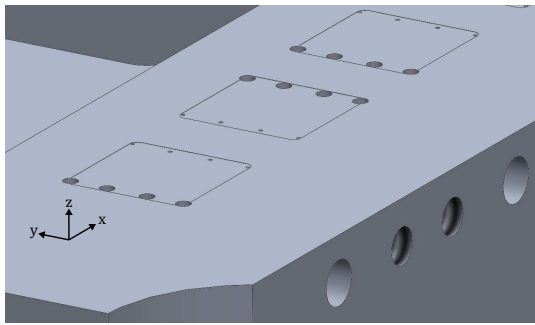


Figure 3.22: Close up of the first three actuators cells.

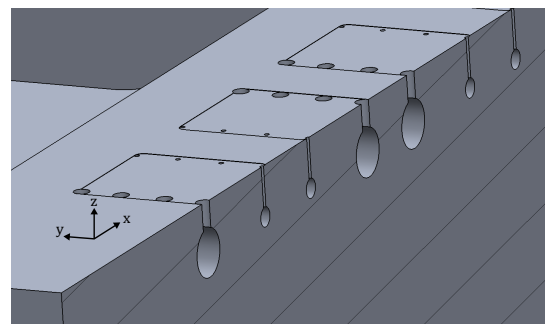


Figure 3.23: Cross section of the same three actuator cells as figure 3.22. The cross section is in the xz-plane.

### 3.5. Pneumatic management

In the previous section the design of an actuator cell was explained. Each actuator cell is controlled by air pressure. The management of the pneumatics in the motion system is described in this section. In subsection 3.5.1 the connections between a valve and the manifolds is explained. Thereafter, in subsection 3.5.2 the modelling of the pneumatic circuit is described. In the final subsection 3.5.3, the choice and modelling of a valve is explained.

#### 3.5.1. Tubing

In order to have a fast responsive system, the volume of air between the valve and an actuator cell has to be as small as possible. In section 3.5.2 it will be explained why it is beneficial to have as little volume of air in the connection between the valve and an actuator cell. The volume would be minimum if valves could be directly placed and connected to an inlet of an actuator cell. Unfortunately, such valves do not exist yet on the market. So for now plastic tubes (and fittings) are used to connect a valve to an actuator cell. In the design a single valve is connected to four actuator cells.

The smallest tubing found is the PUN-H-2x0,4 from Festo<sup>1</sup>. It has an inner diameter of 1.2 mm and an outer diameter of 2 mm. It has a minimum relevant-flow bending radius of 8 mm where it has no flow rate reduction. Lastly, it has an operating pressure between  $-0.95$  bar and 10 bar (gauge pressure).

Next to the tubing, also a fitting is needed to connect the tubes to the valve and manifold. The chosen fitting is the QSM-M3-2-I also from Festo. The outer diameter of the fitting is 5 mm. This means that the dam section between two actuator cells needs to be at least 5 mm in order to place two fittings next to each other. On one end of the fitting it has a push-in connecting for tubing with 2 mm outer diameter. On the other end it has a M3 external thread. On the inside of the thread it has an internal hex which can be used for a hex key to fasten the fitting to a threaded hole.

In the design the total volume of air between one valve and four actuator cells is  $V_t = 4.68 \cdot 10^{-7} \text{ m}^3$ . This is the volume which will be used in section 3.5.2 to model the capacitance behaviour of the compressible air.

#### 3.5.2. Pneumatic circuit model

A pneumatic circuit model with lumped components is used to describe the fluid flow in the system. The pneumatic circuit is similar to an electric circuit, but instead of charge conservation it needs to have mass conservation at each node.

The pneumatic circuit consists five components: a valve, plastic tubes (and fittings), inlet restrictors, thin film restrictors and outlet restrictors. To simplify the model the following assumptions are made:

1. When the **valve** is closed, the flow resistance over the valve is infinite. In this case no air can flow from the air supply through the valve. When the valve is open the resistance is negligible small compared to the resistances of the inlet restrictor and thin film restrictor.

<sup>1</sup><https://www.festo.com>

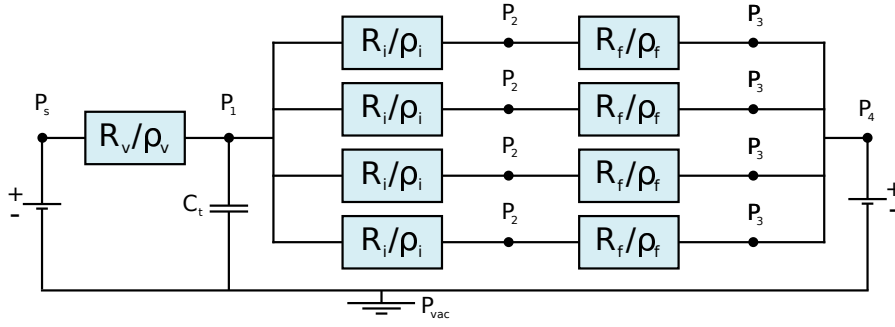


Figure 3.24: Pneumatic circuit for one valve configuration.

2. Each valve is connected to four actuator cells by plastic **tubes** (and fittings). The volume of air that can be stored in the tubes between one valve and four actuator cells is  $V_t = 4.68 \cdot 10^{-7} \text{ m}^3$ . This volume is much larger than the volume of air that can be stored in the other components. That is why it is assumed that the capacitance-effect is dominant in the tubes and negligible in the other components. However, the flow resistance through these tubes is negligible small compared to the resistance in the thin film restrictor.
3. Between each tube and each actuator cell is an **inlet restrictor** with  $R_i = 4.10 \cdot 10^9 \text{ (N/m}^2\text{)}/(\text{m}^3/\text{s})$ . Each inlet restrictor ( $R_i$ ) consists of four orifice restrictors ( $R_{\text{ori}}$ ) as explained in section 3.4.2. The combined volume of four orifice restrictors is  $V_i = 7.07 \cdot 10^{-10} \text{ m}^3$ , which is negligible to the volume in the tubes. Hence, the capacitance in the inlets are neglected.
4. After the inlet restrictors, the air flows to an actuator cell. The flow resistance over an actuator cell can be described by a **thin film restrictor** with  $R_f = 6.42 \cdot 10^9 \text{ (N/m}^2\text{)}/(\text{m}^3/\text{s})$ , as explained in section 3.4.1. Here it is assumed that the fluid film thickness above a dam is constant with a value of  $10 \mu\text{m}$ . The volume of the thin film restrictor is  $V_f = 5.50 \cdot 10^{-9} \text{ m}^3$ , which is negligible to the volume in the tubes. The capacitance in the air film is therefore neglected.
5. Finally, the air flows through **outlet restrictors** into ambient air. As explained in section 2.7 the flow resistance of the outlet restrictor is assumed to be  $R_o = 0 \frac{\text{(N/m}^2\text{)}}{\text{(m}^3/\text{s})}$ . So this component can be neglected in the model, which results in  $p_3 = p_4 = p_{\text{amb}}$ .

The dominant components are schematically drawn in figure 3.24. Here  $R_v$  is the flow resistance of the valve,  $C_t$  the total capacitance of the tubes,  $R_i$  is the total flow resistance of the inlet for one actuator cell and  $R_f$  is the total flow resistance of the thin film restrictor of a single actuator cell. From figure 3.24 three differential equations can be obtained, namely 3.16, 3.17 and 3.18. Equation 3.16 relates the flow between  $p_s$  and  $p_1$ . Equation 3.17 relates to the flow between  $p_1$  and  $p_3$ . Here  $R_{\text{eq}} = R_{\text{act}}/4 = (R_i + R_f)/4$  is the equivalent resistance of four actuator cells connected to one valve. Equation 3.18 relates to the flow difference between  $\dot{m}_{s1}$  and  $\dot{m}_{13}$  to the rate change of pressure  $\dot{p}_1$ . Here the capacitance in the tubing connected to one valve is defined as  $C_t = \frac{V_t}{\kappa \cdot p_1}$  [10] [11].

$$p_s^2 - p_1^2 = 2 \cdot R_g \cdot T \cdot R_v \cdot \dot{m}_{s1} \quad (3.16)$$

$$p_1^2 - p_3^2 = 2 \cdot R_g \cdot T \cdot R_{\text{eq}} \cdot \dot{m}_{13} \quad (3.17)$$

$$\dot{p}_1 = \frac{\kappa \cdot R_g \cdot T}{V_t} \cdot (\dot{m}_{s1} - \dot{m}_{13}) \quad (3.18)$$

Substituting  $\dot{m}_{s1}$  and  $\dot{m}_{13}$  of equations 3.16 and 3.17 in equation 3.18 results in equation 3.19.

$$\begin{aligned} \dot{p}_1 &= \frac{1}{R_v} \cdot \frac{\kappa \cdot (p_s + p_1)}{V_t \cdot 2} \cdot (p_s - p_1) + \frac{1}{R_{\text{eq}}} \cdot \frac{\kappa \cdot (p_1 + p_3)}{V_t \cdot 2} \cdot (-p_1 + p_3) \\ &= \frac{1}{R_v \cdot C_{s1}} \cdot (p_s - p_1) + \frac{1}{R_{\text{eq}} \cdot C_{13}} \cdot (-p_1 + p_3) \end{aligned} \quad (3.19)$$

Here  $C_{s1}$  is the capacitance between  $p_s$  and  $p_1$ . And  $C_{13}$  is the capacitance between  $p_1$  and  $p_3$ . The term  $\frac{1}{R_v \cdot C_{s1}} \cdot (p_s - p_1)$  determines how the pressure builds up between  $p_s$  and  $p_1$ . It is expected that its response is fast because it is assumed that  $R_v \ll R_{eq}$ . For the response of the actuator it is more relevant to determine the pressure build up between  $p_1$  and  $p_3$ , which is determined by the term  $\frac{1}{R_{eq} \cdot C_{13}} \cdot (-p_1 + p_3)$ . The transfer function between  $p_1$  and  $p_3$  in the Laplace domain is given in equation 3.20.

$$\frac{p_1}{p_3} = \frac{1}{R_{eq} \cdot C_{13} \cdot s + 1} \quad (3.20)$$

Equation 3.20 has the form of a passive first-order RC-filter. Here  $\tau_{RC} = R_{eq} \cdot C_{13} = 3.69$  ms is the time constant which determines the dynamic behaviour of a first-order system. In the time domain this time constant determines the rise time ( $t_r = 2.2 \cdot \tau_{RC}$ ) and the settling time ( $t_s = 4.6 \cdot \tau_{RC}$ ). And in the frequency domain it determines the cut-off frequency  $\omega_{cut} = \frac{1}{\tau_{RC}} = 2 \cdot \pi \cdot f_{cut}$  (not to be confused with the unity-gain cross-over frequency). The bode plot for this transfer function is shown in figure 3.25. Here the cut-off frequency is  $f_{cut} = 43.1$  Hz. With this the pressure build up in the system is determined. In section 3.6.2 this model will be used to determine the response of the plant.

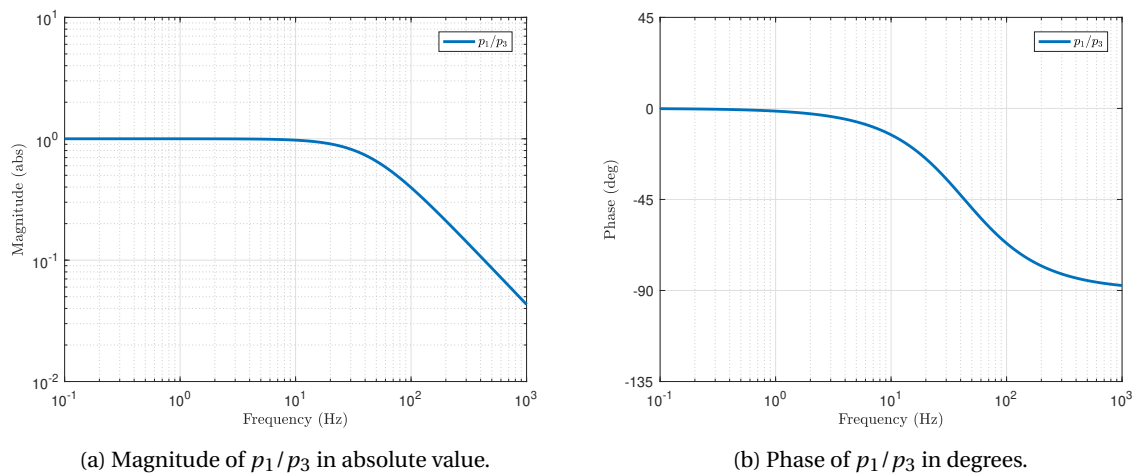


Figure 3.25: Bode plot of the transfer function of  $p_1/p_3$  which describes the pressure build up (due to the compressibility of the air) in the ducts. Here  $\tau_{RC} = 3.69$  ms.

### 3.5.3. Valves

Now we discuss why the valve from Staiger is chosen and explain how a valve influences the response of the plant. Generally speaking there are two different types of electric controlled valves: discrete on/off valves and proportional valves. With discrete on/off valves the flow passage can either be fully open or fully closed (often via a plunger). With a proportional valve the size of the flow passage can be varied by a current or voltage signal.

A proportional valve is chosen over a discrete on/off valve because of two reasons. The first reason is that it is desired to have accurate regulation of the pressure which can follow a triangular profile. It is believed that a proportional valve can follow such a profile more gradually than a discrete on/off valve. The second reason is that a proportional valve can adjust for variations in force between different actuator cells. This makes it easier to position the substrate within the accuracy range, because the force can be applied more subtle.

To compare different valves the following seven properties are taken into account:

1. **Operating pressure:** This is the range between the lowest required and highest permissible supply pressure for safe operation of a valve. Manufacturers give these ranges often in gauge pressure. In our test setup we are able to reach up to 6 bar gauge supply pressure (or 7 bar absolute pressure). Best is to choose a valve that has an operating pressure up to at least 6 bar gauge pressure.

2. **Flow range:** This is the minimum and maximum flow that can go through the valve expressed in litre per minute at atmospheric pressure and 20 °C. As is shown in figure 3.13 of section 3.4.2, the flow per actuator cell is at least 3.63 L/min. Each valve is connected to four actuator cells. Thus each valve should reach a flow of at least 14.5 L/min.
3. **Response time:** The response time of a valve is defined as the amount of time needed for a valve to go from a closed to an open position or vice versa. For the valve opening, the response time is defined as the duration between energizing the valve and reaching 90 % of the stabilized outlet pressure. The response time for closing the valve is defined as the duration from de-energizing the valve until the pressure drops to 10 % of the supply pressure. Here air is supplied to the valve with 6 bar and 20 °C. However, valve manufacturers may use alternative definitions or measurement procedures. For our design it is desired to have a low response time which results in a phase of more than -235° of the plant at 56 Hz (see equation 3.10 of section 3.2.2).
4. **Hysteresis:** This is the difference in motion that the plunger of a valve exhibit by opening and closing. Hysteresis is determined by the maximum difference between outlet pressure (or flow) for the same measured point, one point obtained while increasing from zero (fully closed valve) and the other while decreasing from full scale (fully open valve). The points are taken on the same continuous cycle. The hysteresis is defined as the percentage of the maximum hysteresis error compared to the full scale. This hysteresis is unfavourable for feedforward control, because the input signal to a valve gives a different output pressure for opening the valve compared to closing the valve. Such hysteresis effects can be compensated with feedback control to some extent. But it is desired to have a low hysteresis error for a fast responsive motion system.
5. **Lifetime:** The lifetime of a valve is indicated by the minimal number of switching cycles it can make before failure.
6. **Actuator type:** This is the type of actuator that is used to vary the size of the flow passage of the valve. The most common used type of actuator for electric controlled valves are solenoids.
7. **Input signal type:** This is the type of input signal that is used to control the valve. In general, there are three types input signals to control a valve. The first type of input signal is the use of DC current, which varies the flow passage of the valve proportionally to the current. The second type of input signal is the use of DC voltage, which varies the flow passage of the valve proportionally to the voltage. Lastly the third type of input signal is the use of a Pulse Width Modulation (PWM) technique. This technique consists of the generation of a square (current or voltage) wave of constant frequency and a variable pulse duration. By varying the pulse duration one can vary the flow proportionally. There are more modulation techniques, but these are out of the scope of this thesis. For our demonstrator it is desired to have DC current as input signal, because the used power amplifier can deliver controlled current directly to the coils or piezo element of a valve. It is believed this is the fastest way to electrically control a valve.

A field research was performed to find the most suitable valve for our application. We have limit our search to valves with an operating pressure up to at least 6 bar gauge pressure, a minimum flow range up to at least 14.5 L/min, a response time of 15 ms or lower and valves that were specified as proportional valves. The best performing valves (for our application) from the following six different companies were taken into account: BIBUS<sup>2</sup>, Burkert<sup>3</sup>, Festo, Kelly Pneumatics<sup>4</sup>, Parker<sup>5</sup> and Staiger<sup>6</sup>. The valves of these companies are listed in table 3.1 with their performances.

It is chosen to use the Spider  $\mu$ Prop valve from Staiger because of four reasons. The first reason is that the valve has one of the lowest response time. This is a crucial parameter for performing a 50 ms triangular pressure profile. Also the feedback controller benefits of a fast responding valve. The second reason is that the coils of the solenoid can directly be supplied with a current signal. This is beneficial for controlling the valve in the fastest way possible, as mentioned before. The third reason is that this valve can be placed in a custom

---

<sup>2</sup><https://www.bibus.uk>

<sup>3</sup><https://www.burkert.com>

<sup>4</sup><https://kellypneumatics.com>

<sup>5</sup><http://www.parker.com>

<sup>6</sup><https://www.staiger.de>

Table 3.1: Comparison between different high end performance proportional control valves which are commercially available on the market.

	BIBUS	Burkert	Festo	Kelly Pneumatics	Parker	Staiger
<b>Name valve</b>	Matrix 820	Type 2871	VEAB	Miniature Proportional Valve	VSO MAX HP	Spider $\mu$ Prop VP 204-503
<b>Operating gauge pressure (bar)</b>	0 to 8	0 to 12	0.03 to 6	0 to 6.8	0 to 8.28	0 to 10
<b>Flow range (L/min)</b>	0 to 180	-	0 to 20	0 to 32	0 to 200	0 to 80
<b>Response time (ms)</b>	1	<15	<10	3 to 5	10	<3
<b>Hysteresis (%)</b>	-	<5	0.25	6 to 10	7 to 15	<10
<b>Lifetime (million cycles)</b>	>500	-	>300	>100	>100	>100
<b>Actuator type</b>	solenoid	solenoid	piezo element	solenoid (non-spool)	solenoid	solenoid
<b>Input signal type</b>	PWM	DC voltage or PWM	DC voltage or DC current	DC voltage	DC voltage, DC current or PWM	DC current or PWM

mounting block, which allows for much freedom of the tube placement. Lastly, the fourth reason is that the maximum flow at 6 bar gauge pressure is about 48 L/min. This is beneficial in case the fly height becomes larger than 10  $\mu$ m. Then each valve is capable of dealing with flows up to about 48 L/min.

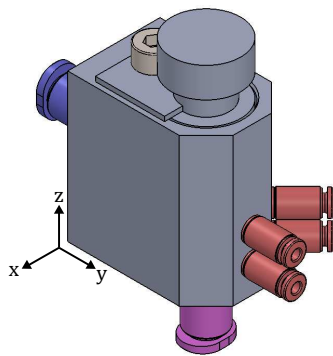


Figure 3.26: Design of the mounting block. Pressure is supplied at the blue fitting. A pressure sensor can be connected to the magenta fitting. By controlling the valve the flow through the reds fittings can be varied.

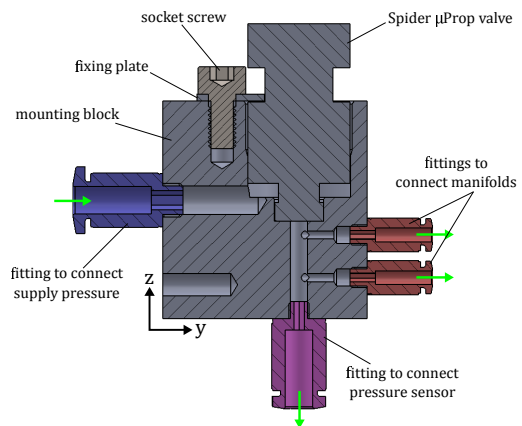


Figure 3.27: A cross section is shown of the mounting block. The flow directions through the mounting block are indicated by green arrows. Note that a cosmetic representation is given of the valve.

The design of the mounting block is shown in figure 3.26. A cross section is shown in figure 3.27. The flow directions through the mounting block are indicated by green arrows. This mounting block has one fitting (indicated in blue) to supply pressure. Also it has five outputs, one fitting (indicated in magenta) for a pressure sensor and four fittings (indicated in red) to connect to the manifolds. With this configuration each valve

can control up to four actuator cells actuating in the same direction.

Finally, the modelling of the valve will be explained. As mentioned in previous work [31] the electronic and mechanical parts of the valve contain delay effects. Furthermore, as mentioned in section 3.5.2 the time constant  $R_v \cdot C_{s1}$  is assumed to be much smaller than the time constant  $R_{eq} \cdot C_{13}$ . Thus aside from a pressure drop over the valve, the valve can be approximated as a pure time delay only. This is shown in equation 3.21. Here  $\tau_{\text{delay}}$  is the delay of the valve. Next to that,  $B$  is a conversion constant for converting the input current signal to an output pressure. This constant also accounts for the pressure drop over the valve. It is estimated that the delay of the valve is approximately 0.5 ms ( $\tau_{\text{delay}} = 0.5 \text{ ms}$ ). To show the effect of the delay, a bode plot is made from the transfer function of equation 3.21. This is shown in figure 3.28 where  $B = 1 \text{ (N/m}^2\text{)/(A)}$  and  $\tau_{\text{delay}} = 0.5 \text{ ms}$ . Here it can be seen that the magnitude is constant and that the phase (in degrees) scales linearly with the frequency by:  $\theta_{\text{delay}} = -360 \cdot \tau_{\text{delay}} \cdot f$ . In section 3.6.2 this model will be used in combination with the pressure build up model of section 3.5.2 to describe the response of the pneumatics of the plant.

$$\frac{p_1}{I} = B \cdot e^{(-\tau_{\text{delay}} \cdot s)} \quad (3.21)$$

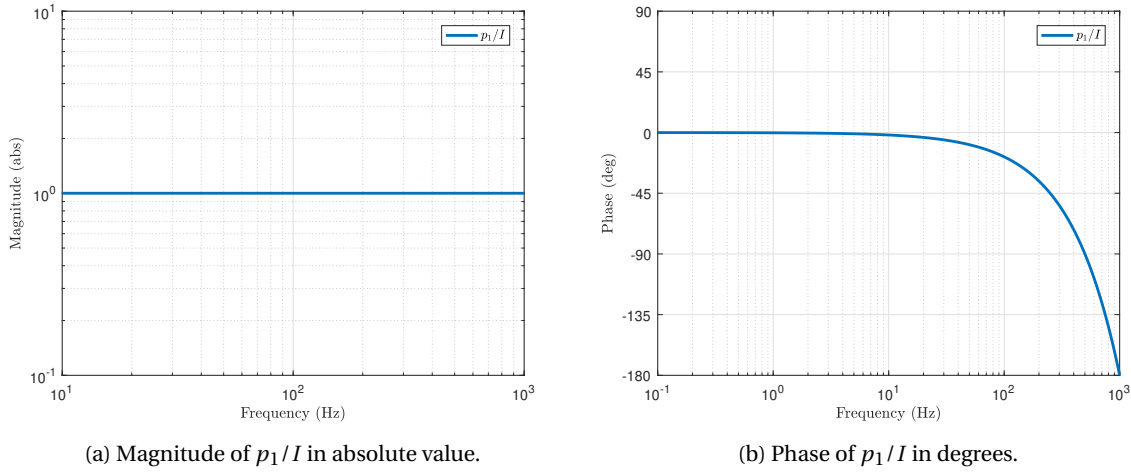


Figure 3.28: Bode plot of the transfer function of the valve  $p_1/I$  of a pure delay where  $B = 1 \text{ (N/m}^2\text{)/(A)}$  and  $\tau_{\text{delay}} = 0.5 \text{ ms}$ .

## 3.6. Control

In this section the control of the valves and the response of the plant are described. In section 3.6.1 the desired pressure profiles for the valves are described. After that, in section 3.6.2, the response of the transfer function of the plant is determined.

### 3.6.1. Valve pressure control

With the designed actuators cells we want to generate a triangular acceleration profile for the substrate. This triangular acceleration profile is already described in figure 3.1 of section 3.2.1 with a maximum acceleration of  $160 \text{ m/s}^2$ . To generate this acceleration profile, a triangular pressure profile for  $p_2$  should be generated at each inlet of the actuator cells. This is because the actuation force is linear dependent on the pressure difference over each actuator cell, and thus  $p_2$ . Also, as mentioned in section 3.3, half of the actuator cells generates a force in  $-x$ -direction (left) and the other half of the actuator cells generates a force in  $+x$ -direction (right). With this configuration it is chosen to generate a triangular pressure profile for both actuation directions. The actuation scheme will be explained by the graphs in figure 3.29. Here the yellow line indicates pressure  $p_2$  at the actuators cells generating a force to the right. This pressure is indicated by  $p_{2,R}$ . Furthermore, the red line indicates pressure  $p_2$  at the actuators cells generating a force to the left. This pressure is indicated by  $p_{2,L}$ . The actuation scheme in time will be explained here below. The five Roman numerals in figure 3.29 correspond to the five Roman numerals listed here below:

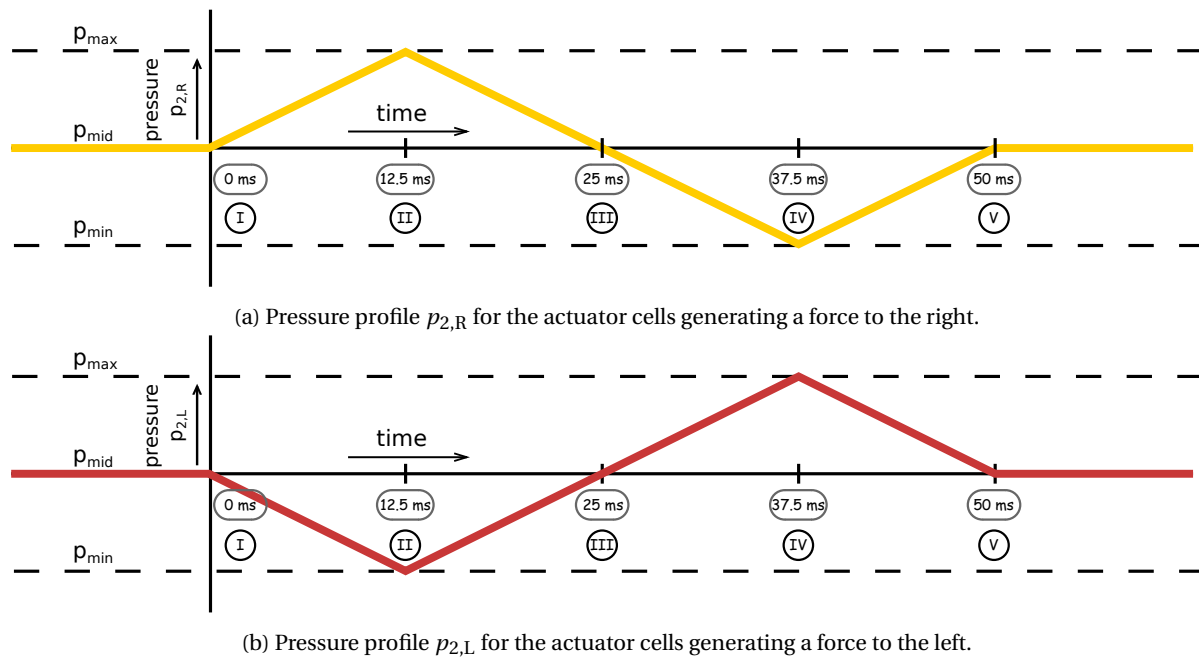


Figure 3.29: Pressure profiles  $p_{2,R}$  and  $p_{2,L}$  for the actuator cells generating a force to the right (a) or left (b) in time. Here  $p_{\max} = 3$  bar,  $p_{\text{mid}} = 2.25$  bar and  $p_{\min} = 1.5$  bar.

- I. At  $t = 0$  ms the substrate is at standstill at  $x = 0$  mm. All actuator cells generate mid their minimum and maximum actuation force at  $p_{2,R} = p_{2,L} = 2.25$  bar. This results in a net force of 0 N on the substrate and the substrate floating between the two manifolds. At  $t = 0$  ms a current signal is given to the valves such that  $p_{2,R}$  is gradually increased and  $p_{2,L}$  is gradually decreased.
- II. At  $t = 12.5$  ms the pressure  $p_{2,R}$  is maximum at 3 bar. Also pressure  $p_{2,L}$  is minimum at 1.5 bar. This results in a maximum acceleration of about  $160 \text{ m/s}^2$  and a velocity of 1 m/s of the substrate. After this point the pressure  $p_{2,R}$  and  $p_{2,L}$  are gradually changed towards the mid pressure of 2.25 bar.
- III. At  $t = 25$  ms pressures  $p_{2,R}$  and  $p_{2,L}$  are 2.25 bar. This results in a net force of 0 N. The substrate has an acceleration of  $0 \text{ m/s}^2$  and a velocity of 2 m/s. At  $t = 25$  ms a current signal is given to the valves such that  $p_{2,R}$  is gradually decreased and  $p_{2,L}$  is gradually increased.
- IV. At  $t = 37.5$  ms pressure  $p_{2,R}$  is minimum at 1.5 bar and pressure  $p_{2,L}$  is maximum at 3.0 bar. This results in a minimum acceleration of about  $-160 \text{ m/s}^2$  and a substrate velocity of 1 m/s. After this point pressures  $p_{2,R}$  and  $p_{2,L}$  are gradually changed towards the mid pressure of 2.25 bar.
- V. At  $t = 50$  ms pressure  $p_{2,R}$  and  $p_{2,L}$  are 2.25 bar. This results in a net force of 0 N. The substrate has an acceleration of  $0 \text{ m/s}^2$  and a velocity of 0 m/s. This results in the same conditions as at  $t = 0$  ms, except that the position of the substrate has moved from 0 mm to 50 mm.

With these pressure profiles the acceleration profile shown in figure 3.1 of section 3.2.1 can be produced. It depends mainly on the rise time and fall time characteristics of the plant in order for the motion system to achieve these pressure profiles.

### 3.6.2. Transfer function of the plant

In this subsection the transfer function of the plant  $x/I$  is described. The plant is modelled by two main blocks, as is shown in figure 3.33. The first block explains the pneumatics of the plant. Here the delay of the valve and the pressure build up at point  $p_2$  are described. This gives the transfer function between the input current of the valve to the output pressure  $p_2$ . The second block describes the substrate dynamics due to

pressure  $p_2$ . This gives the transfer function between the input pressure  $p_2$  to the output position  $x$  of the substrate.

The pneumatics consists of two parts. The first part is the valve time delay as described in section 3.5.3. This can be modelled as a pure delay of 0.5 ms. This is shown in figure 3.28. The second part is the pressure build up in the flow. As mentioned in section 3.5.2, the transient behaviour of the pressure in the ducts can be modelled as a passive first-order RC-filter with a dominant time constant of 3.69 ms. This is shown in figure 3.25. Thus the transfer function from input current  $I$  to output pressure  $p_2$  results in equation 3.22. Here the constant  $B$  accounts for the pressure difference between the initial pressure and the steady state final pressure for a step response. It also converts the input current signal to a pressure. The response of transfer function  $p_2/I$  is shown in figure 3.30.

$$\frac{p_2}{I} = \frac{B \cdot e^{(-\tau_{\text{delay}} \cdot s)}}{\tau_{\text{RC}} \cdot s + 1} \quad (3.22)$$

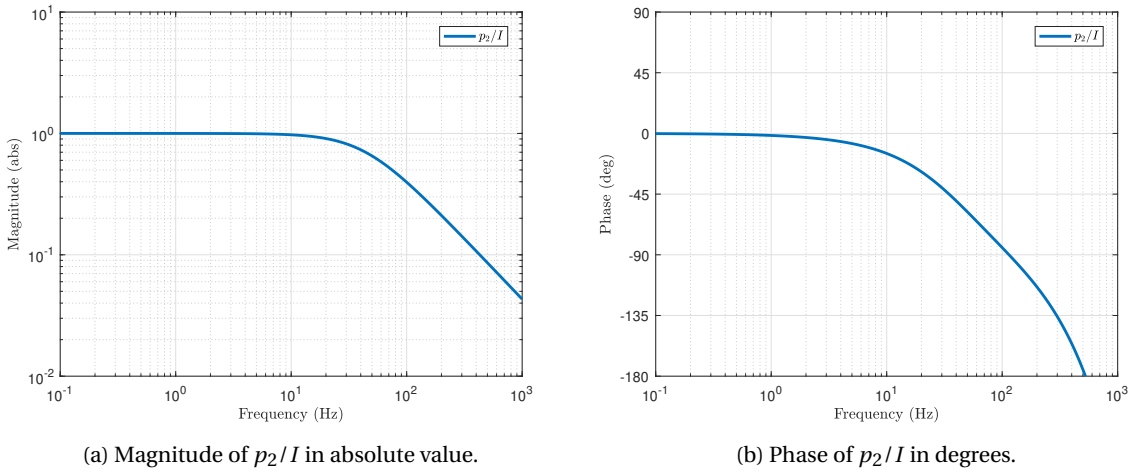


Figure 3.30: Bode plot of the transfer function  $p_2/I$  which describes pneumatics. Here  $B = 1 \text{ (N/m}^2\text{)}/(\text{A})$ ,  $\tau_{\text{delay}} = 0.5 \text{ ms}$  and  $\tau_{\text{RC}} = 3.69 \text{ ms}$ .

The motion of the substrate is determined by the applied force on the substrate as described in equation 2.31 of section 2.7. In this equation, the force in x-direction consists of an actuation constant  $f_a$  and a viscous damping constant  $c_{\text{visc}}$ . Together with the substrate mass ( $m_{\text{sub}}$ ) a mass-damper model can be made. With this model the motion of the substrate can be determined.

First let us determine  $f_a$ . The net force due to the actuator cells is  $F_a = 0.5 \cdot b_p \cdot (h_p - h_d) \cdot (n_R \cdot (p_{2,R} - p_3) - n_L \cdot (p_{2,L} - p_3))$ . Here  $n_R$  are the number of actuator cells generating an actuation force in positive x-direction with pressure  $p_2 = p_{2,R}$ . Furthermore,  $n_L$  are the number of actuator cells generating an actuation force in negative x-direction with pressure  $p_2 = p_{2,L}$ . In the design  $n_R = n_L = 16$ . This results in  $f_a = \frac{F_a}{p_{2,R} - p_{2,L}} = 0.5 \cdot b_p \cdot (h_p - h_d) \cdot n_R = 1.36 \cdot 10^{-6} \text{ N}/(\text{N/m}^2)$ . This is the actuation constant of the plant.

Secondly let us determine  $c_{\text{visc}}$ . The net force due to the viscous damping is  $F_{\text{visc}} = -u_{\text{sub}} \cdot \mu \cdot A/h$ . Here  $A$  is the surface area and  $h$  the local film thickness. Thus the viscous damping constant of the system is defined as  $c_{\text{visc}} = F_{\text{visc}}/u_{\text{sub}} = \mu \cdot A/h$ . This results in a total viscous damping constant of  $17.8 \cdot 10^{-3} \text{ N}/(\text{m/s})$  with both sides of the substrate included.

With these constants, one can determine the transfer function  $x/p_2$ . The substrate has a mass  $m_{\text{sub}} = 1.058 \text{ g}$ , the force on the substrate is driven by a Poiseuille flow with actuation constant  $f_a$  and the substrate is damped by a Couette flow with a viscous damping constant  $c_{\text{visc}}$ . This results in the transfer function  $x/p_2$  shown in

equation 3.23. The response of the transfer function  $x/p_2$  is shown in figure 3.31.

$$\frac{x}{p_2} = \frac{f_a}{m_{\text{sub}} \cdot s^2 + c_{\text{visc}} \cdot s} \quad (3.23)$$

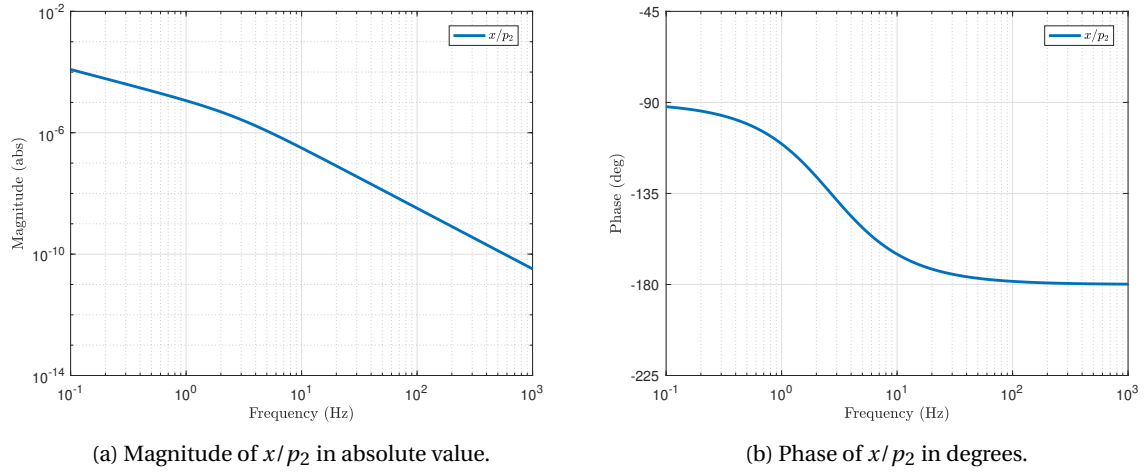


Figure 3.31: Bode plot of the transfer function  $x/p_2$  which describes the substrate dynamics. Here  $f_a = 1.36 \cdot 10^{-6} \text{ N}/(\text{N}/\text{m}^2)$ ,  $m_{\text{sub}} = 1.058 \text{ g}$  and  $c_{\text{visc}} = 17.8 \cdot 10^{-3} \text{ N}/(\text{m}/\text{s})$ .

With the pneumatics and the substrate dynamics described, one can determine the total transfer function of the plant from input current  $I$  to output position  $x$ . This transfer function can be obtained by multiplying equation 3.22 with equation 3.23. The result is shown in equation 3.24. The response of this transfer function is shown in figure 3.32. Here the frequency at a phase of  $-235^\circ$  is 49.8 Hz. Although the required bandwidth of 56 Hz is not achieved, the RC-effect of the valve is not taken into account. Measurements must show by how much the bandwidth increases due to the RC-effect of the valve.

$$\frac{x}{I} = \frac{B \cdot e^{(-\tau_{\text{delay}} \cdot s)}}{\tau_{\text{RC}} \cdot s + 1} \cdot \frac{f_a}{m_{\text{sub}} \cdot s^2 + c_{\text{visc}} \cdot s} \quad (3.24)$$

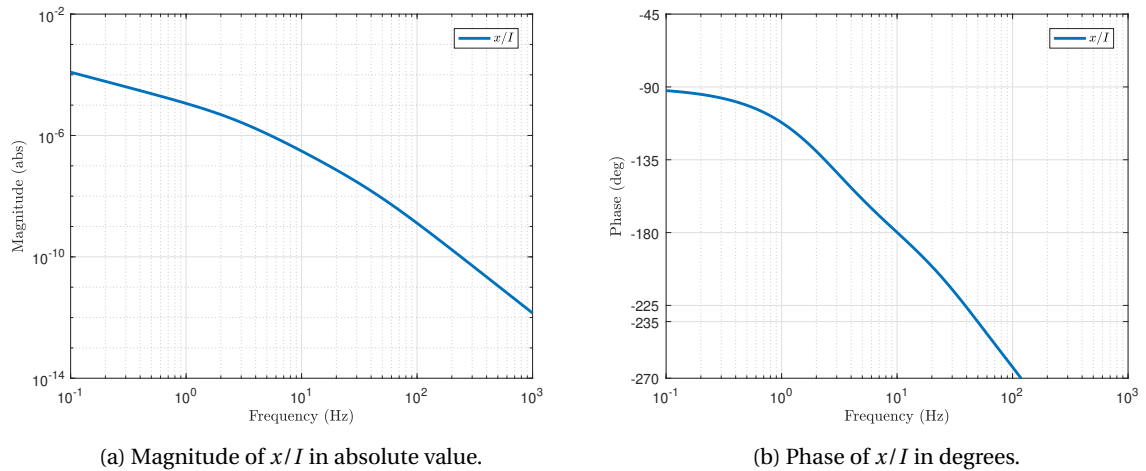


Figure 3.32: Bode plot of the transfer function  $x/I$  of the plant. Here  $B = 1 (\text{N}/\text{m}^2)/(\text{A})$ ,  $\tau_{\text{delay}} = 0.5 \text{ ms}$ ,  $\tau_{\text{RC}} = 3.69 \text{ ms}$ ,  $f_a = 1.36 \cdot 10^{-6} \text{ N}/(\text{N}/\text{m}^2)$ ,  $m_{\text{sub}} = 1.058 \text{ g}$  and  $c_{\text{visc}} = 17.8 \cdot 10^{-3} \text{ N}/(\text{m}/\text{s})$ .

Lastly an overview is given of the motion control system. In figure 3.33 a block diagram is shown of the motion control system, including feedforward and feedback control.

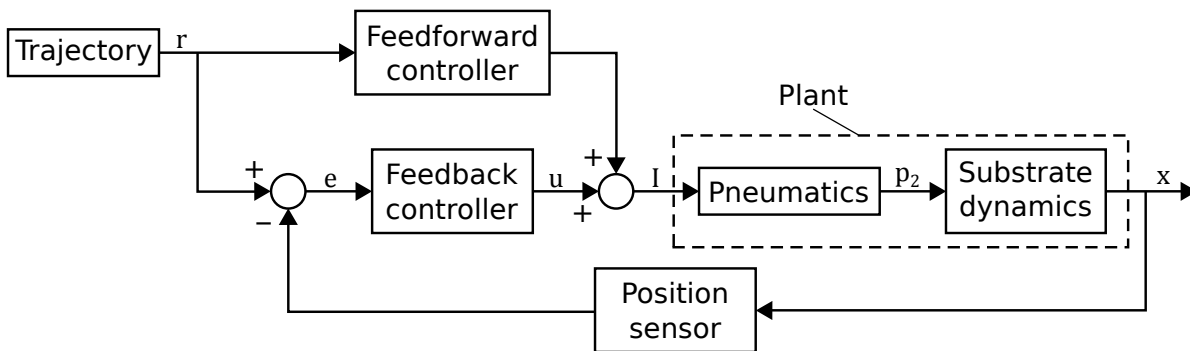


Figure 3.33: Block diagram of the motion control system, including feedforward and feedback control. Here the plant consists of a pneumatics block ( $p_2/I$ ) and a substrate dynamics block ( $x/p_2$ ).

### 3.7. Design overview

In the previous sections of this chapter the designs of different parts of the motion system were explained. In this section a brief overview is given of the final design. Furthermore, some references to the appendix are given for additional information about the design and the realisation of the motion system.

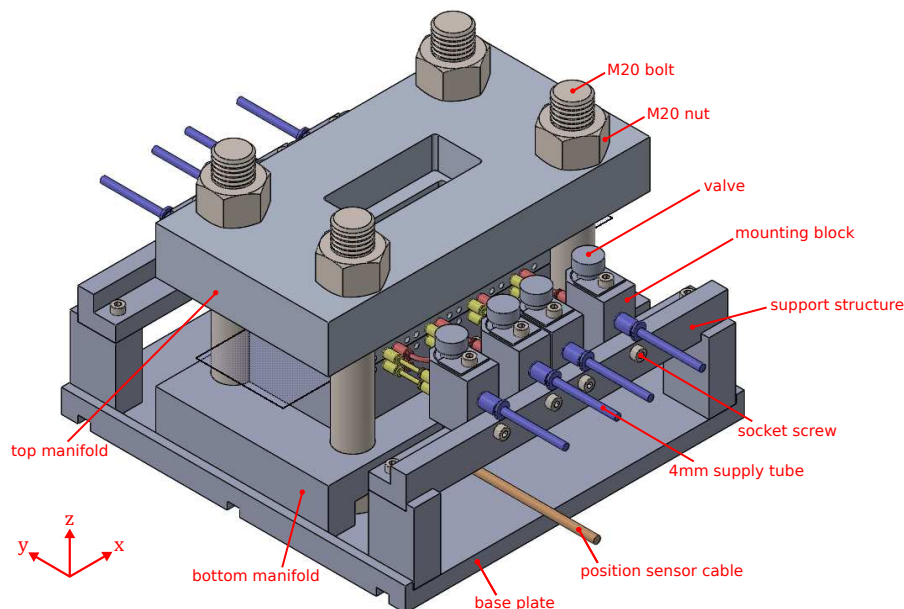


Figure 3.34: Overview of the assembly of the total design.

The assembly of the total design is shown in figure 3.34. The drawing is made in SOLIDWORKS 2016. Here the bottom manifold is mounted to the base plate. The top manifold is placed above the bottom manifold with the bearing surfaces facing each other. The two manifolds are separated by a fixed distance with the use two feeler gauges. These feeler gauges are shown in figure 3.35 where the top manifold is removed. The two manifolds are held together by four M20 bolts. More information about the function of the feeler gauges and the M20 bolts can be found in appendix C.2. Between the two manifolds a piece of flexible substrate is placed. The substrate is free to move in x-direction, but constrained in the other directions. Furthermore, eight proportional valves are mounted on support structures. With these valves air is supplied and controlled to the inlets of the air film actuators. This creates an air film on both sides of the substrate. By controlling the valves the substrate can be moved in positive or negative x-direction. The position of the substrate is measured with a position sensor. Also a pressure sensor and a flow sensor are used to measure the pressure downstream a valve and the flow through a valve. More information about the used sensors is described in appendix C.3.

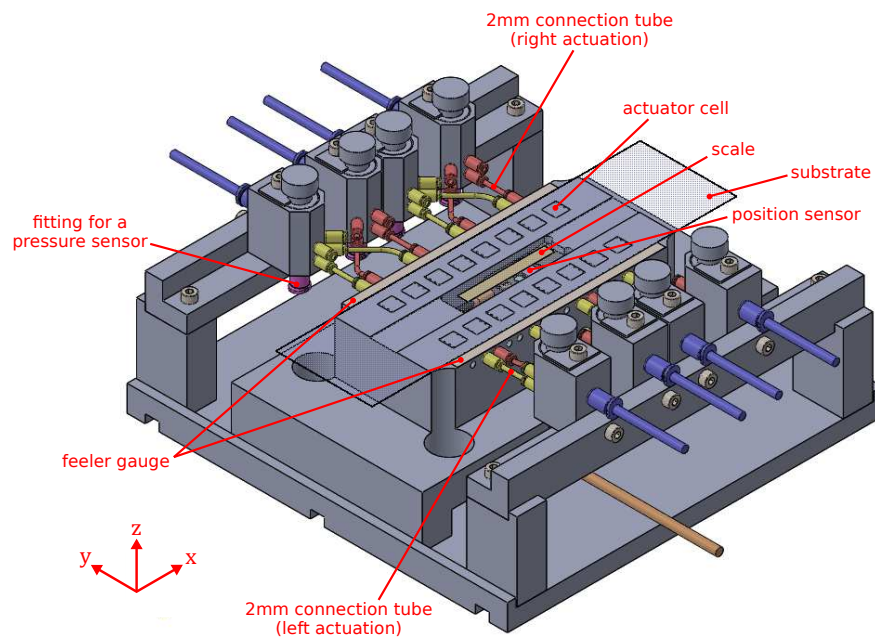


Figure 3.35: Overview of the assembly of the total design with the top manifold and bolts removed.

To compare the analytical analysis, a numerical analysis is performed on the bottom manifold. The numerical analysis and the boundary conditions are described in appendix C.4. The results of the analytical and numerical analysis are shown in table 3.2. Here it can be seen that there is a good resemblance between the analytical and numerical results. Finally, for more information about the working principle of the design and the realisation of the design, see appendix D.

Table 3.2: Comparison between analytical analysis and numerical analysis. Here the performances of the total system are shown when both manifolds are used.

	Analytical	Numerical	Description
$F_{fx}$	194 mN	171 mN	Total actuation force on substrate in x-direction
$F_{fy}$	0 mN	$8.97 \cdot 10^{-4}$ mN	Total actuation force on substrate in y-direction
$F_{fz}$	155 N	261 N	Net force in z-direction generated on a single manifold
$\dot{m}_{tot}$	$1.30 \cdot 10^{-3}$ kg/s	$1.27 \cdot 10^{-3}$ kg/s	Total mass flow of air
$q_{tot}$	63.7 L/min	62.2 L/min	Total volume flow of air
$k_z$	$9.31 \cdot 10^6$ N/m	$1.69 \cdot 10^7$ N/m	Total vertical stiffness applied on substrate
$\bar{k}_z$	$1.63 \cdot 10^9$ (N/m)/m <sup>2</sup>	$2.97 \cdot 10^9$ (N/m)/m <sup>2</sup>	Total vertical stiffness applied on substrate (per unit area)

# 4

## Experiments and results

In this chapter three different experiments are performed to measure different sections of the plant and compare this with the theoretical models. First in section 4.1 the flow and pressure for different inlets are measured. In this case no substrate is used. With this experiment one can compare the orifice restrictor model to the measurement results. Secondly in section 4.2 the flow, pressure and actuation force are measured in case a substrate is placed between the two manifolds. The measured values are compared with the numerical model. Lastly, in section 4.3 the substrate is pretensioned between two springs and actuated with step current signals on the valves. With this, one can obtain the open-loop response of the plant and determine the performance of the motion system.

### 4.1. Inlets measurement without substrate

The goal is to measure the flow through an inlet as function of  $p_1$  and compare the results with the orifice model. It is expected that the measurements comply with the orifice model. In figure 4.1 an illustration is given of the test setup. For this experiment the following components are used:

1. A flow sensor to measure the flow through the inlet of a single actuator cell.
2. One valve to regulate the flow.
3. A pressure sensor to measure pressure  $p_1$  located between the valve and the inlet.
4. Single actuator cell with no object covering it.

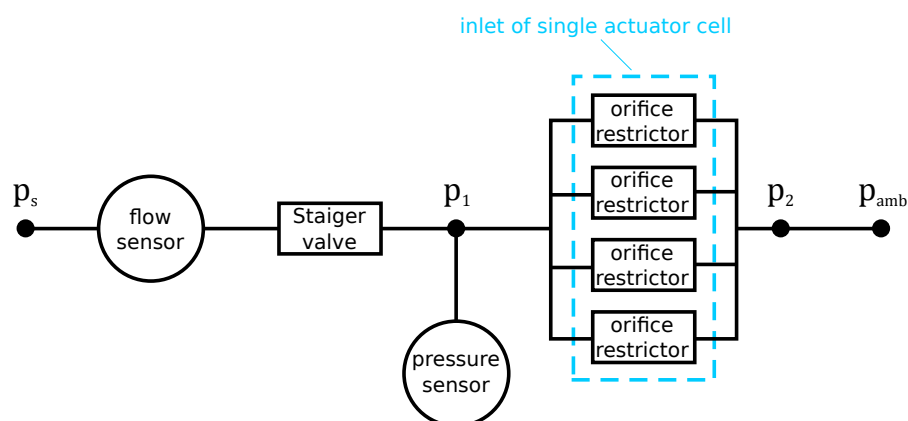


Figure 4.1: Schematic overview of experiment 1. Here the inlet of a single actuator cell is connected which consists of four orifice restrictors.

First pressure  $p_s$  is supplied to the valve. Next, current is applied to the valve with steps of 10 mA starting from 0 mA. At a certain current value the valve begins to open, depending on  $p_s$ . From this point the valve gradually opens by increasing the current. The consequence is that both  $q_{s1}$  (flow between  $p_s$  and  $p_1$ ) at the flow sensor and  $p_1$  at the pressure sensor increase. The actuator cell has an inlet which consists of four orifice restrictors with a diameter of 0.3 mm. Thus flow  $q_{s1}$  is divided over four orifice restrictors. Lastly the flow leaves the orifice restrictors at  $p_2$ . Because only one actuator cell is used and no substrate is placed over the actuator cell, the air flows into ambient air where the pressure is  $p_2 = p_{\text{amb}} = 1$  bar. By measuring  $q_{s1}$  and  $p_1$  one can compare the orifice model from equation 2.13 of section 2.5 to the measurement results and determine the values of  $C_d$  (coefficient of discharge). In literature the value of  $C_d$  is often between 0.7 and 0.9, but falls however at pressure ratios above  $p_2/p_1 > 0.8$  [24] [28].

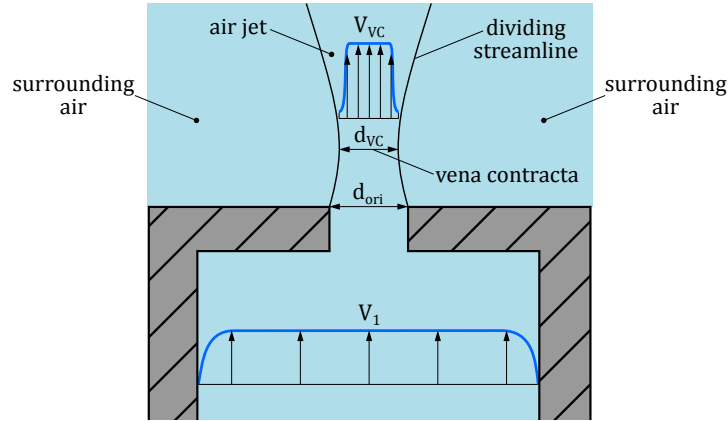


Figure 4.2: Illustration of the vena contracta effect at an orifice. Air is supplied with a velocity of  $V_1$  to the orifice and increases to  $V_{VC}$  at the vena contracta.

The coefficient of discharge accounts for two effects. The first effect is the vena contracta. This is the smallest flow passage, which takes place at a section slightly downstream of the orifice. This is shown in figure 4.2, where the dividing streamline separates the air jet from the surrounding air. In figure 4.2 the diameter of the orifice is  $d_{\text{ori}}$  and the diameter of the vena contracta is  $d_{VC}$ . Because  $d_{VC}$  is smaller than  $d_{\text{ori}}$ , the actual mass flow is also smaller. Instead of measuring  $d_{VC}$  one uses  $d_{\text{ori}}$  and corrects with  $C_d$  [32]. The second effect is the friction between the flowing air and the orifice wall. The consequence of friction is that a smaller exit velocity (and thus smaller mass flow) is realized than would have been obtained in an isentropic expansion to the same pressure [20]. Both the vena contracta effect and the friction losses are captured in  $C_d$ .

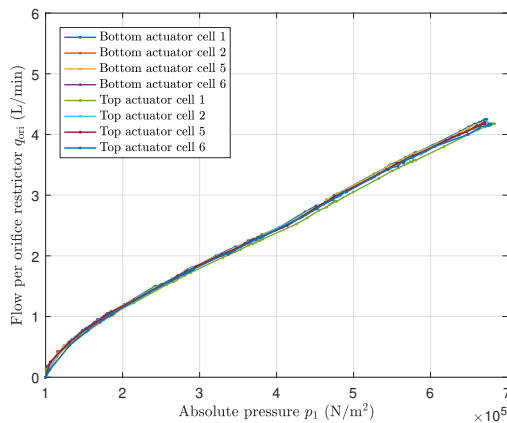


Figure 4.3: Measurement of inlets for eight different actuator cells. Here the flow-pressure relation is plotted per orifice restrictor, where  $q_{\text{ori}} = q_f/4$ .

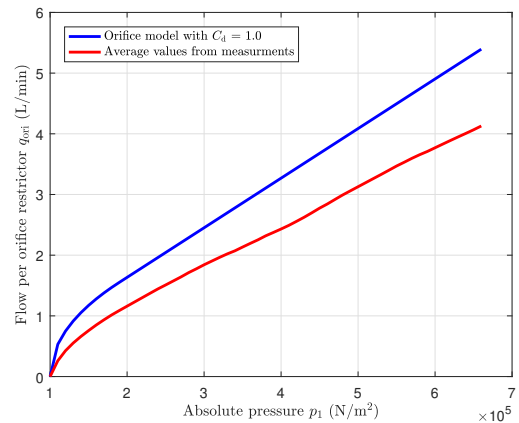


Figure 4.4: Comparison between measurements and orifice restrictor model. Here the blue line is the orifice restrictor of equation 2.13 with  $C_d = 1.0$ . The red line is the average of the eight lines of figure 4.3.

The measurement results for the flow and pressure of eight different actuator cells are plotted in figure 4.3. For this  $p_s$  is varied from 2 to 7 bar (absolute pressure) with increments of 1 bar. At each of these pressure values the current to the valve is varied from 0 to 200 mA with increments of 10 mA. For each measurement point the flow ( $q_{s1}$ ) at the flow sensor and the pressure ( $p_1$ ) at the pressure sensor are measured. Lastly the flow values for each actuator cell are sorted from low to high pressure as is shown in figure 4.3. The flow is expressed per orifice restrictor which is  $q_{ori} = q_{s1}/4$ . From figure 4.3 it can be seen that the graphs for different actuator cells show similar results. This indicates that the orifice restrictors perform equally and are produced well. Moreover, one can see that after  $p_1 = 1/0.528 = 1.89$  bar the flow becomes proportional to  $p_1$ . This complies with the theory that the flow is choked (reaches speed of sound) and becomes a function of  $p_1$  only.

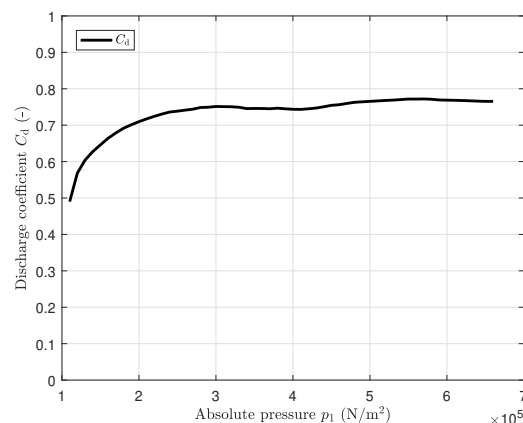


Figure 4.5: The coefficient of discharge ( $C_d$ ) obtained by dividing the values of the orifice model by the measured values of figure 4.4.

Furthermore, a graph is made of the orifice restrictor model with  $C_d = 1.0$  as is shown by the blue line in figure 4.4. The red line in figure 4.4 is the average of the eight lines of figure 4.3. With this, one can divide the values of the blue line by the values of the red line and determine the actual discharge coefficient of an orifice restrictor. The result is shown in figure 4.5. At large values of  $p_1$  the discharge coefficient is around 0.75. Also at pressure ratio's above  $p_2/p_1 > 0.8$  the discharge coefficient drops rapidly. The discharge coefficient at small and large values of  $p_1$  is consistent with theory. Thus the different orifice restrictors show similar flow performances and the results show behaviour which is consistent with theory.

## 4.2. Measurement with substrate

The goal of this second experiment is to observe how the flow, pressure and actuation force behave when a substrate is placed between the two manifolds. It is expected that the substrate would float contactless between the two manifolds. The substrate might vibrate at the edges, where the substrate is not supported. But experimentation should reveal how the substrate behaves between the two manifolds.

In figure 4.6 a schematic overview is given of the test setup for a single valve. For this experiment the following components are used:

1. One flow sensor to measure the flow through one valve. Here one valve is connected to four actuator cells.
2. Four valves to actuate the substrate in positive x-direction. In total 16 actuator cells are controlled. The valves are connected in parallel electronically.
3. Pressure sensor to measure pressure  $p_1$  located between one valve and the inlets of four actuator cells.
4. Both manifolds are used and separated by two feeler gauges. Feeler gauges with the following thicknesses are used: 60  $\mu\text{m}$ , 70  $\mu\text{m}$  or 80  $\mu\text{m}$ . Using a substrate with a thickness of 36  $\mu\text{m}$  (and a tolerance

of  $\pm 2$  mm) results respectively in film thicknesses ( $h_d$ ) of  $12\ \mu\text{m}$ ,  $17\ \mu\text{m}$  or  $22\ \mu\text{m}$  on either side of the substrate.

5. Between the two manifolds a substrate with thickness  $36\ \mu\text{m}$  is placed. The substrate is connected to a tension gauge by a steel wire and tape. With this the force acting on the substrate can be measured.

For this experiment  $p_s$  is varied from 2 to 6 bar (absolute pressure) with increments of 1 bar. The maximum supply pressure in this experiment is 6 bar instead of 7 bar, because at this time it was not possible to reach 7 bar consistently due to practical reasons. At each value of  $p_s$  the current to the four valves is varied from 0 to 760 mA with increments of 40 mA. One could increase the current up to 800 mA, but the valves become warm around 760 mA. So to prevent the valves from overheating we stopped at 760 mA. For each measurement point the flow ( $q_{s1}$ ) at the flow sensor, the pressure ( $p_1$ ) at the pressure sensor and the actuation force ( $F_a$ ) at the tension gauge are measured.

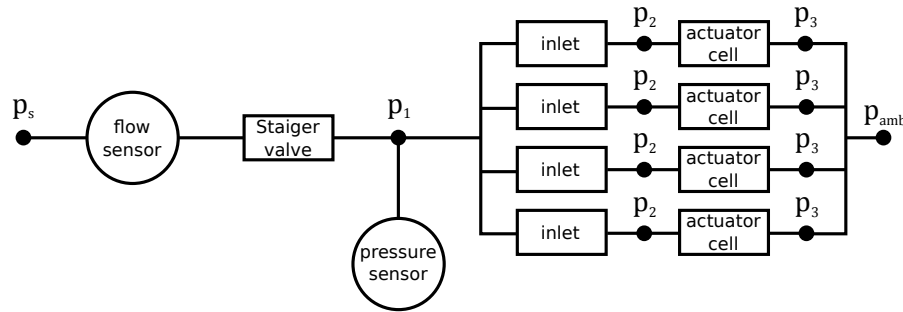


Figure 4.6: Schematic overview of a single valve for experiment 2. In total four valves are used to actuate in one direction. Note that each inlet consists of four orifice restrictors.

As a first observation, a high-pitched sound was noticeable at small and large values of  $p_1$ . When one puts the substrate under tension the sound is attenuated, but the sound is still there. By removing the substrate the high-pitched sound disappeared. This indicates that the source of the sound is due to vibrations of the substrate. No further analysis was performed on the substrate vibrations as this is out of the scope of this thesis. It is recommended to further research the interaction between the fluid films and the structural behaviour of a thin substrate to analyse these vibrations.

Another observation is that the substrate does not float fully contactless. One can experience this when the actuator cells generate about as much force in positive x-direction as in negative x-direction. One would expect that by the slightest deviation in net action force, the substrate would drift away. Instead the substrate stays in position. By pulling on the substrate one has to overcome some friction force before the substrate moves. The least amount of friction was experienced at  $h_d = 17\ \mu\text{m}$ . Therefore in this chapter a film height of  $h_d = 17\ \mu\text{m}$  is shown. Auxiliary measurements with  $h_d = 12\ \mu\text{m}$  and  $h_d = 22\ \mu\text{m}$  are shown in appendix E.

The flow  $q_{\text{ori}}$  as function of the current  $I$  for different supply pressures  $p_s$  is shown in figure 4.7. Here the flow is expressed per orifice restrictor, where  $q_{\text{ori}} = q_{s1}/16$ . This is because each valve is connected to four inlets with each inlet containing four orifice restrictors. The value  $I$  is the current applied to the four valves. From figure 4.7 it can be seen that for low currents the valve is closed with the flow being zero. At a certain current value the valve gradually opens by increasing  $I$ . The value of the current at which the valve starts opening is larger at higher supply pressures. From there the flow gradually increases up to a maximum value depending on  $p_s$ . Furthermore, the red areas indicate when a high-pitched sound was noticeable. The green area indicates when the high-pitched sound was significantly reduced in loudness, but still noticeable. Similar graphs can be obtained for pressure  $p_1$  and  $F_a$  (actuation force in x-direction on the substrate), which are shown in figures 4.8 and 4.9 respectively.

By combining the results from figures 4.7 and 4.8, one can obtain a graph of  $q_{\text{ori}}$  as function of  $p_1$ . The values  $q_{\text{ori}}$  are sorted from low to high pressure  $p_1$ . The result is shown in figure 4.10. Also the numerical result obtained from COMSOL is plotted in figure 4.10. From this it can be seen that the theoretical result shows good

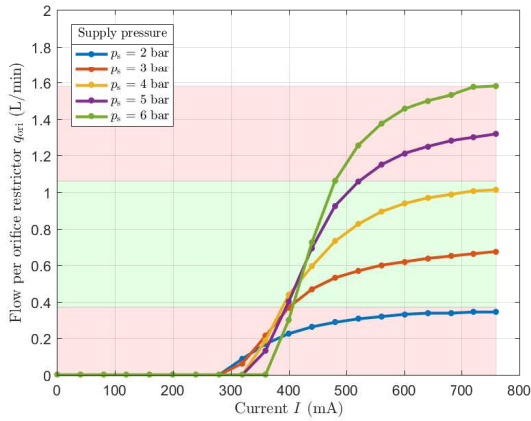


Figure 4.7: Measurement results of flow  $q_{ori}$  as function of current  $I$  for different supply pressures. Here  $h_d = 17\mu\text{m}$ .

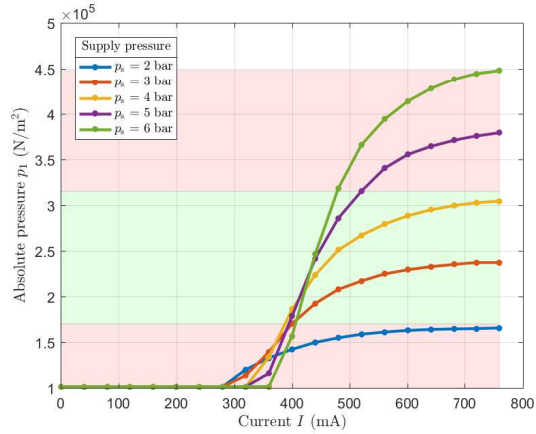


Figure 4.8: Measurement results of pressure  $p_1$  as function of current  $I$  for different supply pressures. Here  $h_d = 17\mu\text{m}$ .

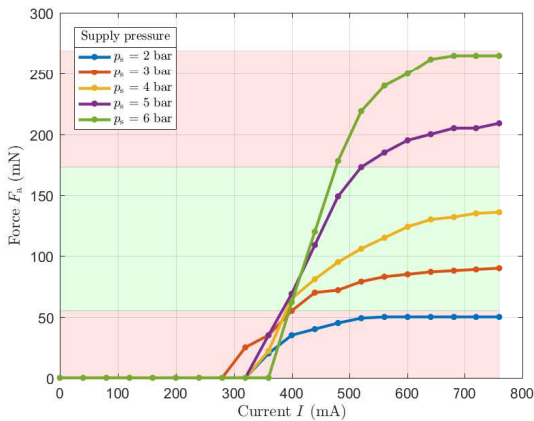


Figure 4.9: Measurement results of actuation force  $F_a$  as function of current  $I$  for different supply pressures. Here  $h_d = 17\mu\text{m}$ .

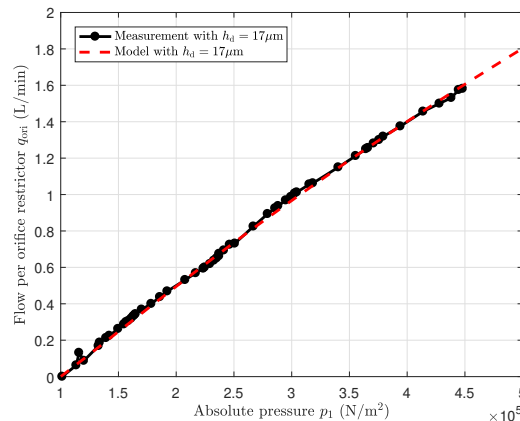


Figure 4.10: Comparison between measurement results and numerical model of flow  $q_{ori}$  as function of pressure  $p_1$ .

resemblance with the measurement results. Lastly, by comparing figure 4.10 with figure 4.3 one can observe that the flow is smaller at similar values of  $p_1$ . This shows that the flow through an orifice restrictor highly depends on what kind of flow restrictor is placed after the orifice restrictor.

Another graph can be made by combining the results from figures 4.8 and 4.9. With this one can obtain a graph of actuation force  $F_a$  as function of  $p_1$ . The values  $F_a$  are sorted from low to high pressure  $p_1$ . The result is shown in figure 4.11. In this figure also the numerical result obtained with COMSOL is plotted. As expected the actuation force increases as  $p_1$  increases. The numerical result does show some resemblance with the measurement results, but the lines do not fully coincide. For  $h_d = 17\mu\text{m}$  and  $p_s = 5\text{ bar}$  a maximum actuation force of  $F_a = 209\text{ mN}$  was measured with a total air consumption of  $84.4\text{ L/min}$ .

Next to that, one can make an estimation of  $p_2$ . Unfortunately it is not possible to measure  $p_2$  in the current setup. But from theory  $p_2$  cannot be larger than  $p_1$  and smaller than  $0.528 \cdot p_1$ . With measured  $q_{s1}$ ,  $p_1$  and assuming  $C_d = 0.9$ , one can estimate  $p_2$  with equation 2.13. Unfortunately  $C_d$  cannot be estimated by figure 4.5, as the test setup configurations of section 4.1 and section 4.2 are different. The result is shown in figure 4.12. Also,  $p_2$  can be plotted directly from the numerical model, as the orifice restrictor model is already incorporated in the numerical model. From figure 4.12 one can see that  $p_2$  increases as  $p_1$  increases. But  $p_2$  does not reach  $0.528 \cdot p_1$ , thus it can be assumed that the flow is not choked. Finally, similar results of figures 4.7 to 4.12 for  $h_d = 12\mu\text{m}$  and  $h_d = 22\mu\text{m}$  can be found in appendix E.

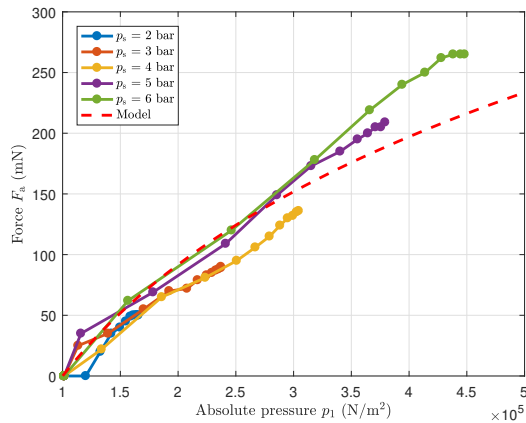


Figure 4.11: Comparison between measurement results and numerical model of actuation force  $F_a$  as function of pressure  $p_1$ .

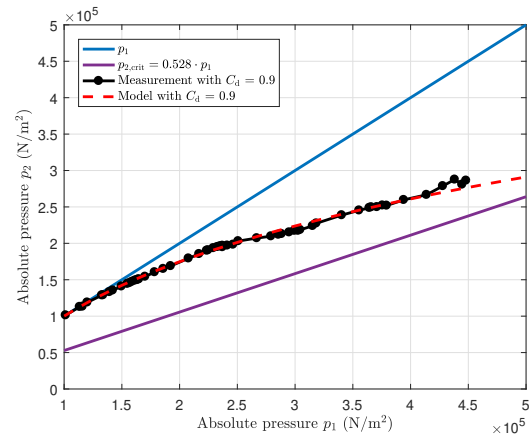


Figure 4.12: Pressure  $p_2$  as function of  $p_1$  determined with the orifice restrictor model. For comparison  $p_2$  is determined with either the use of the measurement data or the numerical data. In both situations is assumed that  $C_d = 0.9$ .

### 4.3. Open-loop response of the motion system

The goal of this last experiment is to determine the open-loop response of the system. With the open-loop response, the closed-loop performance can be determined. First in subsection 4.3.1 the test setup is explained and the results are compared with the theoretical model. Subsequently the theoretical model is used in subsection 4.3.2 to determine the performances for three different cases.

#### 4.3.1. Results

In this third experiment the step response of pressure  $p_1$  and position  $x$  of the substrate are measured in real time. With this, one can compare the theoretical model with the measured results. The top view of the used test setup is shown in figure 4.13. For this experiment the following components are used:

1. Four valves to actuate the substrate in positive x-direction and four valves to actuate the substrate in negative x-direction. In total 32 actuator cells are controlled.
2. Two pressure sensors to measure the pressure between a valve and the inlets of four actuator cells. One pressure sensor is used to measure  $p_{1,R}$ , which is the pressure for generating a force in positive x-direction. The other pressure sensor is used to measure  $p_{1,L}$ , which is the pressure for generating a force in negative x-direction.
3. Between the two manifolds a substrate is placed. On either ends the substrate is connected to a spring by a steel wire and tape. A close-up is shown in figure 4.14. With these springs the substrate is pre-tensioned. This straightens the substrate and reduces vibrations.
4. One readhead to measure the relative position from the scale and thus determine the displacement of the substrate.
5. The manifolds are separated by two feeler gauges with a thickness of  $70 \mu\text{m}$ . This results in a film height  $h_d$  of  $17 \mu\text{m}$  on either side of the substrate.

For this experiment a supply pressure of 5 bar (absolute pressure) is used, because at this pressure low friction was observed. The current to all valves is first set to 400 mA. At this current all valves are open at a minimum. Next  $I_R$ , the current for the valves generating a force to the right, is set to 680 mA. With this, one can observe the step response when the current is changing from 400 mA to 680 mA. After reaching a steady state,  $I_R$  is set back to 400 mA. Also the same current signal is performed for the valves generating a force to the left. This current is called  $I_L$ . The resulting block waves are shown in figure 4.15 and are performed simultaneously. During these current signals the pressure ( $p_1$ ) at the pressure sensor and the position of the substrate ( $x$ ) are measured in time.

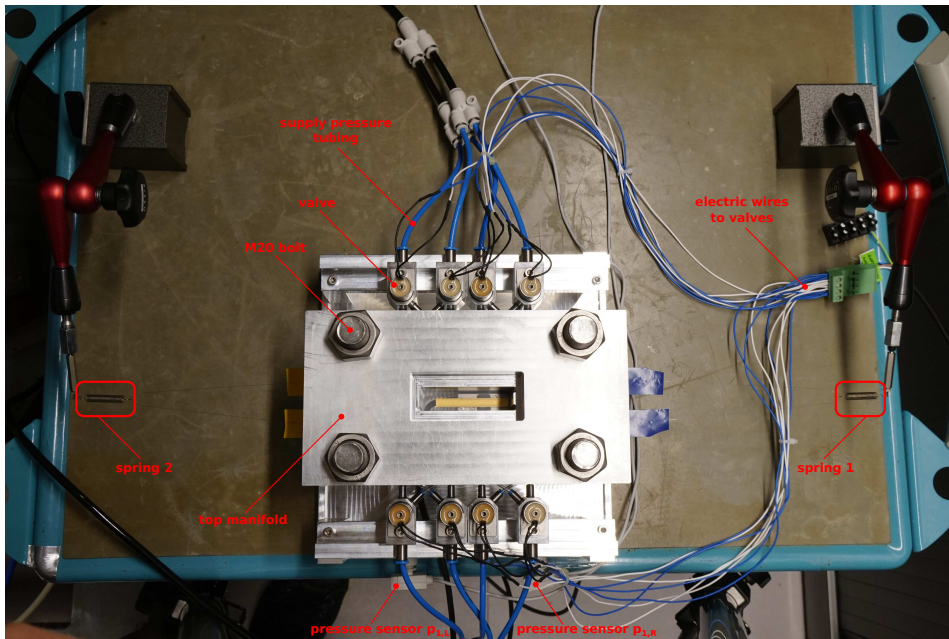


Figure 4.13: Top view of experiment 3. Here the substrate is between the two manifolds and is pretensioned by two springs. In total 8 valves are used to control 32 actuator cells. The valves are connected to electric wires through which current signals can be transmitted.

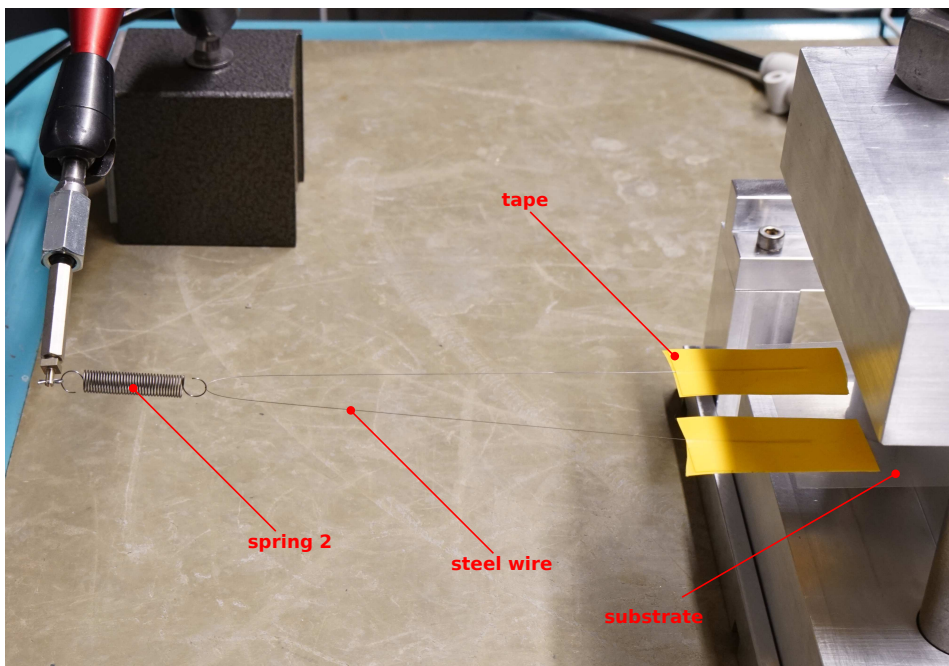


Figure 4.14: Close up of spring 2. Here it is shown how the substrate is attached to the spring by a steel wire and tape.

It is expected that the measured response corresponds to the theoretical response of equation 3.24. To simplify the relation between  $I$  and  $F_a$ ,  $I$  is normalized to  $I'$ . Here  $I'$  is non-dimensional and ranges between 0 and 1. With this, one can also define  $\Delta F_a = B \cdot f_a$ . Here  $\Delta F_a$  is the force difference between the initial and final state of the step response. Furthermore, because the substrate is attached to two springs, equation 3.24 is altered to equation 4.1. Here  $m_{\text{add}}$  is the additional mass by the tape, steel wires and springs. Because one end of a spring is fixed and the other end of a spring is moving with the same displacement of the substrate, only half the mass of each spring is included. Furthermore,  $c_{\text{visc}}$  is the viscous damping constant at  $h_d = 17 \mu\text{m}$ .

Next is  $c_{\text{spring}}$ , the damping constant of the springs. It is assumed that the springs contain 10 % damping. Any unmodelled damping is captured in  $c_{\text{unmod}}$ . Lastly, spring 1 and spring 2 have a spring stiffness  $k_1$  and  $k_2$  respectively. Each parameter is listed in table 4.1, which are either determined theoretically or determined by measurements.

$$G_1 = \frac{x}{I'} = \frac{e^{(-\tau_{\text{delay}} \cdot s)}}{\tau_{\text{RC}} \cdot s + 1} \cdot \frac{\Delta F_a}{(m_{\text{sub}} + m_{\text{add}}) \cdot s^2 + (c_{\text{visc}} + c_{\text{spring}} + c_{\text{unmod}}) \cdot s + (k_1 + k_2)} \quad (4.1)$$

Table 4.1: Used values of the parameters for describing the response of the plant when pressure  $p_{1,R}$  is rising.

Parameter	$\Delta F_a$	$\tau_{\text{delay}}$	$\tau_{\text{RC}}$	$m_{\text{sub}}$	$m_{\text{add}}$
<b>Value</b>	96.5 mN	0.375 ms	1.80 ms	1.005 g	1.635 g

Parameter	$c_{\text{visc}}$	$c_{\text{spring}}$	$c_{\text{unmod}}$	$k_1$	$k_2$
<b>Value</b>	$10.7 \cdot 10^{-3}$ N/(m/s)	$54.0 \cdot 10^{-3}$ N/(m/s)	$750 \cdot 10^{-3}$ N/(m/s)	13.8 N/m	13.8 N/m

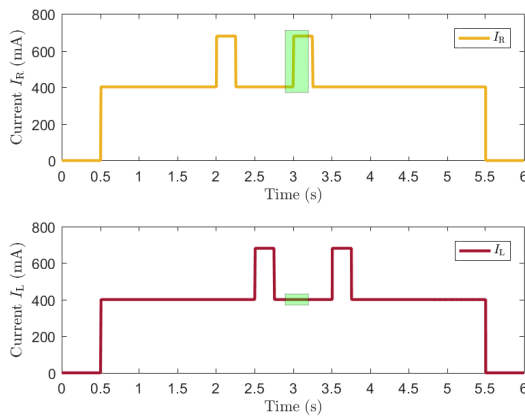


Figure 4.15: Signals  $I_R$  and  $I_L$  are the currents provided to the valves generating a force in positive and negative  $x$ -direction respectively.

The green areas indicate the time interval  $3.0\text{s} \leq t \leq 3.2\text{s}$ .

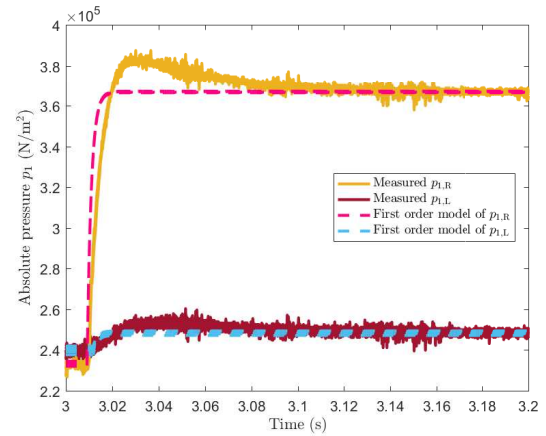


Figure 4.16: Pressures  $p_{1,R}$  and  $p_{1,L}$  measured by the pressure sensors. The results are shown for 10 measurements. The measured pressures are also approximated by a first order model.

Now that the measurement setup and theoretical model are explained, one can perform the measurement and look at the step response of the plant. Let us first look at pressures  $p_{1,R}$  and  $p_{1,L}$  as function of time. The results of 10 experiments are shown by the yellow lines ( $p_{1,R}$ ) and red lines ( $p_{1,L}$ ) in figure 4.16. Because of the high repeatability, one cannot distinguish 10 individual yellow lines or 10 individual red lines in figure 4.16. The pressure is observed in the interval  $3.0\text{s} \leq t \leq 3.2\text{s}$ , because this shows the rise time behaviour when the substrate is actuated in positive  $x$ -direction. This time interval is indicated by the green areas in figure 4.15. The rise time and fall time characteristics at other intervals are described in appendix F. In figure 4.16 it can be seen that  $p_{1,R}$  has a pressure of around 2.33 bar at  $t = 3.0\text{s}$  and a pressure of around 3.67 bar at  $t = 3.2\text{s}$ . Each individual yellow line in figure 4.16 can be approximated by a first order model of the form  $\Delta p \cdot e^{(-\tau_{\text{delay}} \cdot s)} / (\tau_{\text{RC}} \cdot s + 1) + p_{\text{offset}}$ , which are shown by the magenta dashed lines in figure 4.16. Here  $\Delta p$  describes the amplitude of the pressure and  $p_{\text{offset}}$  accounts for the pressure offset. The time constants  $\tau_{\text{delay}}$  and  $\tau_{\text{RC}}$  are determined by the position sensor instead of the pressure sensor, because the position sensor has the fastest response time. From table 4.1 it can be seen that  $\tau_{\text{RC}} = 1.80\text{ms}$ , which implies a rise time of  $\tau_r = 3.96\text{ms}$  and a settling time of about  $\tau_s = 8.28\text{ms}$  (see section 3.5.2). From figure 4.16 it is uncertain if the overshoot of the yellow lines is actually happening or if it is an internal characteristic of the pressure sensor itself, because this overshoot behaviour is not occurring in the displacement of the substrate.

Furthermore,  $p_{1,L}$  has a pressure of around 2.40 bar at  $t = 3.0\text{s}$  and a pressure of around 2.49 bar at  $t = 3.2\text{s}$ . So although the current is constant at 400 mA,  $p_{1,L}$  does increase with 0.09 bar. This is due to the increase of

$p_{1,R}$ , which has a slight effect on  $p_{1,L}$ . Each individual line of  $p_{1,L}$  is also approximated by a first order model, which are shown by the blue dashed lines in figure 4.16.

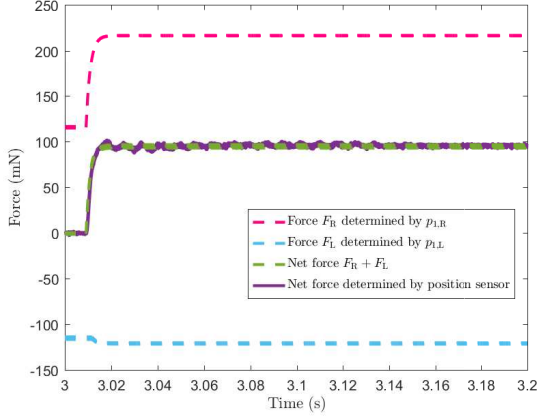


Figure 4.17: Forces in  $x$ -direction acting on the substrate. The actuation force is either determined with  $p_{1,R}$  and  $p_{1,L}$  or with the measured displacement.

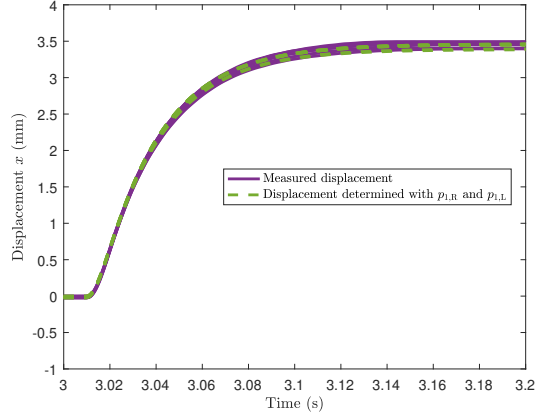


Figure 4.18: Displacement  $x$  of the substrate measured with the position sensor. The displacement is also determined with  $p_{1,R}$  and  $p_{1,L}$ .

Next, each approximated line in figure 4.16 is converted from pressure to force. The force can be determined with figure 4.11 of section 4.2 where we showed the relationship between  $F_a$  and  $p_1$ . The result is shown in figure 4.17. Here the magenta dashed lines have positive values as  $p_{1,R}$  generates a force in positive  $x$ -direction. In contrast to the blue dashed lines, which have negative values as  $p_{1,L}$  generates a force in negative  $x$ -direction. The net force on the substrate due to the magenta dashed lines and the blue dashed lines is given by the green dashed lines. Furthermore, the purple lines in figure 4.17 are also the net force on the substrate. Although these lines are determined by the position of the substrate and a mass-damper-spring model of the form  $F_a = (m_{\text{sub}} + m_{\text{add}}) \cdot \ddot{x} + (c_{\text{visc}} + c_{\text{spring}} + c_{\text{unmod}}) \cdot \dot{x} + (k_1 + k_2) \cdot x$ . Here  $\ddot{x}$  and  $\dot{x}$  are obtained by taking the derivatives of  $x$ . By comparing the green dashed lines with the purple lines, one can see that both approaches give similar results.

At last, the position of the substrate is shown in figure 4.18. The purple lines show the position of the substrate measured by the position sensor. From these lines it can be seen that the substrate makes a displacement of about 3.46 mm. The substrate comes at rest because the applied actuation force balances with the forces of the springs. Furthermore, the green dashed lines in figure 4.18 give also the position of the substrate. Although these lines are determined by the green dashed lines of figure 4.17 and a mass-damper-spring model with transfer function  $x/F_a = 1 / ((m_{\text{sub}} + m_{\text{add}}) \cdot s^2 + (c_{\text{visc}} + c_{\text{spring}} + c_{\text{unmod}}) \cdot s + (k_1 + k_2))$ . By comparing the green dashed lines with the purple lines, one can see that both approaches give similar results. Which is expected, because the green dashed lines and purple lines in figure 4.17 were already corresponding to one another.

### 4.3.2. Open-loop response

In subsection 4.3.1 we have found a good match between the theoretical model and measurement results. By modifying the theoretical model of equation 4.1 one can predict the performance in case no springs were used. Furthermore, one can determine the open-loop bandwidth for three different cases. The first case is with the substrate connected to the two springs. The transfer function for this case is  $G_1$  shown in equation 4.1. The second case is that the two springs are removed, but that  $c_{\text{unmod}}$  is still present. The transfer function in this case,  $G_2$ , is shown in equation 4.2. The third case is the same as transfer function  $G_2$ , but with  $c_{\text{unmod}}$  omitted. The transfer function for this case is  $G_3$  shown in equation 4.3.

$$G_2 = \frac{x}{I'} = \frac{e^{(-\tau_{\text{delay}} \cdot s)}}{\tau_{\text{RC}} \cdot s + 1} \cdot \frac{\Delta F_a}{m_{\text{sub}} \cdot s^2 + (c_{\text{visc}} + c_{\text{unmod}}) \cdot s} \quad (4.2)$$

$$G_3 = \frac{x}{I'} = \frac{e^{(-\tau_{\text{delay}} \cdot s)}}{\tau_{\text{RC}} \cdot s + 1} \cdot \frac{\Delta F_a}{m_{\text{sub}} \cdot s^2 + c_{\text{visc}} \cdot s} \quad (4.3)$$

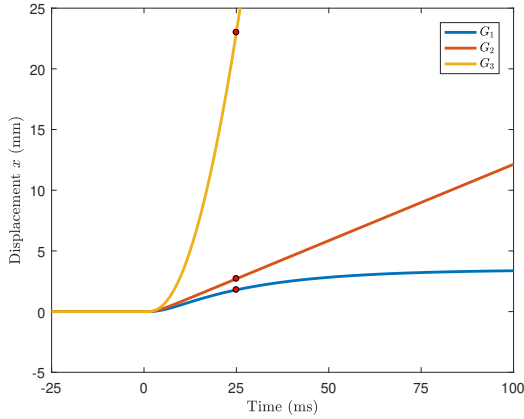


Figure 4.19: Position response of the transfer functions  $G_1$ ,  $G_2$  and  $G_3$  due to a unit step on the input. The red circles indicate the displacement for each model when  $t = 25$  ms.

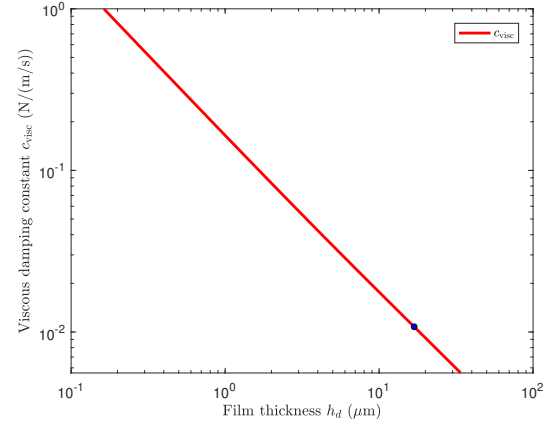


Figure 4.20: Viscous damping constant  $c_{\text{visc}}$  as function of the film height  $h_d$  on a log-log scale. As  $h_d$  approaches zero,  $c_{\text{visc}}$  becomes very large. The blue circle indicates where  $h_d = 17 \mu\text{m}$  with  $c_{\text{visc}} = 10.7 \cdot 10^{-3} \text{ N/(m/s)}$ .

With equations 4.1, 4.2 and 4.3 and the parameters from table 4.1 one can determine the step responses for the different cases. These step responses are shown in figure 4.19. The displacement after 25 ms is shown by the red circles in figure 4.19. The first graph to discuss is the step response of  $G_1$ . This graph corresponds to the graphs of figure 4.18, as expected. Remarkably, the step response does not show any oscillations. The corresponding damping ratio in  $G_1$  is  $\zeta = 1.50$ . This implies that the plant is overdamped. Next to discuss is the step response of  $G_2$ . This graph shows that the displacement of the substrate increases as it is no longer bounded by the springs. Here the maximum velocity of the substrate is 0.126 m/s and is mainly limited by  $c_{\text{unmod}}$ . This is an unexpected behaviour as one would expect that the only significant form of damping would be caused by  $c_{\text{visc}}$  as is shown by the step response of  $G_3$ . An explanation for this behaviour is that the vibrations in the substrate and the local contact of the substrate to the bearing surface induce an increased damping. This is due to the fact that the viscous damping constant is inversely proportional to the film height. In the analysis it is assumed that  $h_d = 17 \mu\text{m}$ . But when  $h_d$  approaches zero, the damping constant increases rapidly. This is shown in figure 4.20 on a log-log scale. So in case the substrate would make contact or near contact with one of the manifolds at some surface areas, this would increase the viscous damping constant. This could explain why the damping constant is much larger than initially expected. The large damping has considerable effect on the performance, resulting in a lower speed than initially expected. For model  $G_2$  it is not possible to move the substrate 50 mm within 50 ms. Instead it would take 405 ms to move the substrate 50 mm.

Finally, we can look at the transfer functions in the frequency domain. The bode plots for  $G_1$ ,  $G_2$  and  $G_3$  are shown in figure 4.21. These responses are similar to the response that was shown in figure 3.32 of section 3.6.2. The green circles in figure 4.21 point out at what frequencies the phase is  $-235^\circ$ . By using PID controllers  $C_1$ ,  $C_2$  and  $C_3$  one can optimize for maximum bandwidth while having a phase margin of  $35^\circ$ . The open-loop responses for the plants in combination with the controllers are shown in figure 4.22. Here the green circles indicate the unity-gain cross-over frequencies with a phase margin of  $35^\circ$ . For  $C_1 \cdot G_1$ ,  $C_2 \cdot G_2$  and  $C_3 \cdot G_3$  these are respectively 133.5 Hz, 182.1 Hz and 87.0 Hz. These bandwidths are indeed larger than 49.8 Hz as predicted in section 3.6.2, because the RC-effect of the valves are now taken into account. Also the bandwidths are larger than the design bandwidth of 56 Hz.

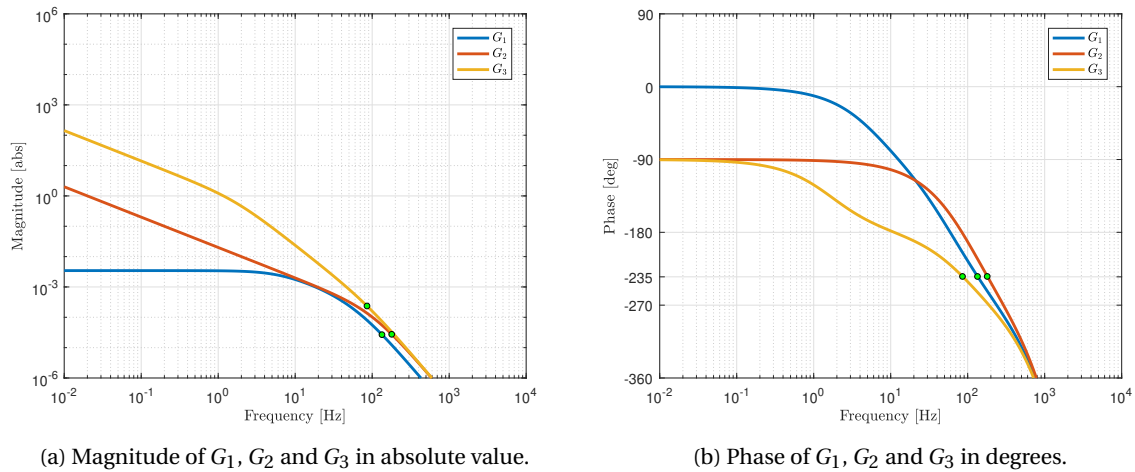


Figure 4.21: Bode plots of the open-loop transfer functions  $G_1$ ,  $G_2$  and  $G_3$ . Here the green circles indicate at what frequencies the phase is  $-235^\circ$ .

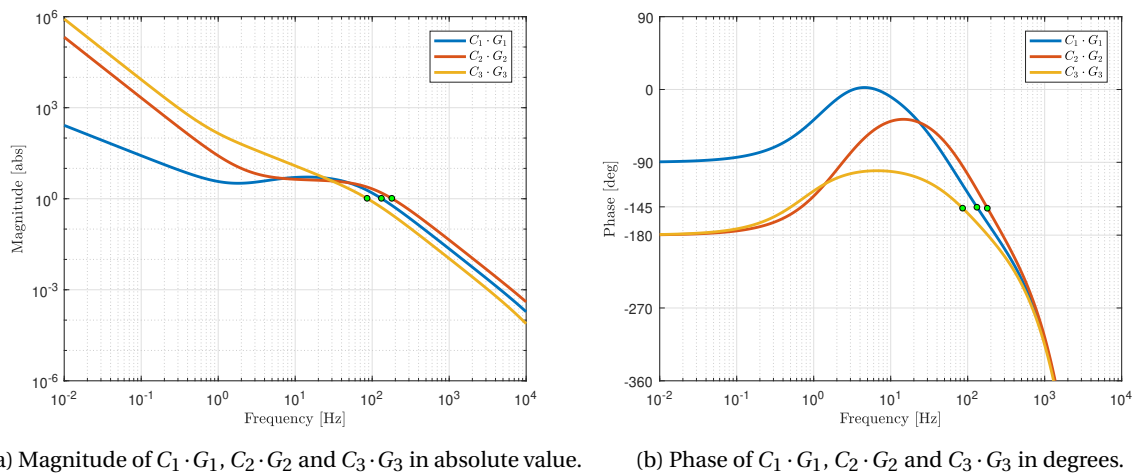


Figure 4.22: Bode plots of the open-loop transfer functions  $C_1 \cdot G_1$ ,  $C_2 \cdot G_2$  and  $C_3 \cdot G_3$ . Here the green circles indicate the unity-gain cross-over frequencies with a phase margin of  $35^\circ$ .

With this we can conclude that the theoretical model shows much resemblance with the measured results. The force applied on the substrate shows a rise time of  $\tau_r = 3.96$  ms and a settling time of about  $\tau_s = 8.28$  ms. However, the plant does contain a larger damping constant than initially expected. With this motion system it would take 405 ms to move the substrate 50 mm. One could either increase the actuation force or lower the damping in the plant to reach higher velocities with the substrate. Finally, the bandwidth of the motion system is about 87.0 Hz. This shows that the motion system is capable to actuate the substrate within the required accuracy range of  $\pm 1$  mm.



# 5

## Conclusions and recommendations

The main goal of this thesis was to make a demonstrator and validation of opposed air film actuators for contactless positioning of thin flexible substrates to be applied in the semiconductor industry. Such opposed air film actuators use pressurized air on both sides of the substrate to keep the substrate at a steady fly height. Additionally, the air film actuators are able to move the substrate by using the viscous shear from the generated air flow. The biggest advantage of using air film actuators is that the substrate is the only moving mass. In this chapter the conclusions and recommendations of this thesis are presented.

### 5.1. Conclusions

The main conclusions from this thesis are given below. These are divided into two categories: design aspects and measurement results.

#### 5.1.1. Conclusions regarding design aspects

From proposed design requirements and the theoretical analysis in this thesis a design was developed. The most important conclusions regarding the design of the motion system are:

- It was proposed to design air film actuators which could move a piece of flexible substrate with 50 mm in x-direction within 50 ms and with a positioning accuracy of  $\pm 1$  mm. With the use of a trajectory planner it was determined that a maximum acceleration of  $160 \text{ m/s}^2$  is needed to get the desired motion. Because the estimated mass of the substrate was 1.058 g, the required maximum force generated by the actuators needed to be at least 169 mN. Furthermore, for a positioning accuracy of  $\pm 1$  mm the motion system needs a bandwidth of at least 56 Hz. At this frequency the plant should have a phase larger than  $-235^\circ$  in order to have a stable system with a phase margin of  $35^\circ$ .
- For the substrate a PET based web was used with a rectangular shape of length 210 mm, a width of 55.5 mm and a thickness of  $36 \mu\text{m}$ . The substrate can be placed between two manifolds which are separated by two feeler gauges. Each manifold contained air film actuators in the bearing surface to levitate and actuate the substrate.
- The actuators consist of pockets with dimensions of 8.5 mm by 8.5 mm and a recess of  $20 \mu\text{m}$ . Each pocket has four inlets with diameters of 0.3 mm and four outlets with diameters of 1.0 mm. Via ducts each manifold connects the inlets to valves and connects the outlets to ambient air. A single manifold contains 16 air film actuators from which 8 are able to actuate the substrate in positive x-direction and the other 8 are able to actuate the substrate in negative x-direction.
- As air is a compressible fluid, the response of the viscous force on the substrate is determined by the pressure build up in the ducts. The pressure build up is primarily determined by the flow resistances of the actuators, the air volume in the ducts and the response time of the valves. Therefore the volumes of the ducts between the valves and the inlets are minimized. Furthermore the chosen valves have a low response time. However, the flow resistances of the actuators are not minimized as these are also responsible for a high stiffness and a low air consumption.

- The two most important features of the design are the flatness tolerance of the bearing surfaces and the diameter tolerance of the inlets. These tolerances need to be low as they are essential for the operation and performance of the air film actuators. Therefore each manifold is designed as a monolithic part as this is beneficial for producing a flat bearing surface. The aluminium manifolds are manufactured by milling and Electrical Discharge Machining (EDM) which resulted in a flatness tolerance of  $3\ \mu\text{m}$  of the bearing surfaces and a diameter tolerance of  $\pm 15\ \mu\text{m}$  of the inlets.

### 5.1.2. Conclusions regarding measurement results

In this thesis three different experiments were described to determine the performance of the motion system. From these experiments the following conclusions can be made:

- In the first experiment the behaviour of inlet restrictors were measured where no substrate was used yet. From this experiment it was shown that different inlet restrictors show comparable flow-pressure curves. This showed that the inlets were well produced and have similar performances. Also from these results it could be verified that the inlet restrictors behave as orifice restrictors, which agrees with literature.
- In the second experiment the behaviour of the air film actuators was measured. Here the substrate was placed between the two manifolds at different fly heights. From initial testing a high-pitched sound was noticeable at small and large values of pressure  $p_1$ . This sound was created by substrate vibrations as the sound disappeared when the substrate was removed between the two manifolds. Furthermore, the substrate did not float fully contactless, as one had to overcome some friction before the substrate moved. The least amount of friction was observed at a fly height of  $17\ \mu\text{m}$  and with a supply pressure of 5 bar. At this fly height and supply pressure a maximum actuation force of 209 mN was reached in one direction with a total air consumption of 84.4 L/min. Finally the modelled flow, pressure and actuation force showed good resemblance with the measurement results.
- In the third experiment the step response of pressure  $p_1$  and the position of the substrate were measured. It was possible to measure the position of the substrate with the encoder system. In this experiment it was shown that the theoretical model gives a good approximation of the measured response. However, the plant contained a larger damping constant than initially expected. An explanation for this higher damping is that the vibrations in the substrate and local contact of the substrate to the bearing surfaces induce an increased viscous damping constant, as the viscous damping constant is inversely proportional to the film height. Also when all air film actuators are used, a maximum net actuation force of 96.5 mN was reached. Therefore a lower speed was achieved than initially expected. With the theoretical model it was determined that the motion system is able to move the substrate 50 mm in 405 ms with a system bandwidth of around 87.0 Hz.

## 5.2. Recommendations

Several aspects of the current motion system can be further researched. In this section some directions are given for improving the performance of the motion system.

- The current configuration of the air film actuators in the bearing surface has each neighbouring actuator generating an actuation force in opposite direction (see figure 3.20 in section 3.4.3). A better configuration would be if each neighbouring actuator generates a force in the same direction as is shown in figure 5.1, because of two reasons. The first benefit is that this configuration inherently straightens the substrate, which reduces unwanted substrate deformations. This is because all actuators on the left side of the bearing surface generate a force to the left and all actuators on the right side of the bearing surface generate a force to the right. The second benefit is that there are less areas on the bearing surface with low pressure, which is beneficial for contactless levitation of the substrate.
- In the experiments the used substrate did make contact with the bearing surfaces. This gives unintentional friction and increases the damping constant of the system. This contact could be caused by insufficient stiffness provided by the air films. In this thesis the global stiffness over the bearing surface was determined. Although the global stiffness gave large values, local stiffnesses might be lower than expected and therefore should be investigated when working with flexible substrates in future research. At areas where the local stiffness is low one could implement auxiliary air bearings to support the substrate.

- During the measurements it was observed that the substrate vibrated, which was not expected. This vibration might be the reason for a higher damping constant in the system. Further research could be performed on the interaction between the fluid films and the structural behaviour of a thin substrate. With this, one could investigate the cause of the substrate vibrations and validate if the vibrations cause an increased damping constant. Possible solutions could be found to reduce the damping constant in the system.
- In experiment 3 the pressure sensor measured an overshoot of pressure  $p_1$  during the step response (see figure 4.16 in section 4.3). This overshoot behaviour was not the measured by the position sensor which has a smaller response time. The displacement of the substrate showed a smooth motion. To measure if this overshoot actually occurs, a pressure sensor with smaller response time could be used.
- The orifice restrictor model describes a flow which is dominated by inertial forces, while the Reynolds equation describes a flow which is dominated by viscous forces. The flow transition between an orifice restrictor and the air film could be further improved. In the current numerical model the velocities near the inlets and outlets are overestimated by the Reynolds equation due to large convective accelerations.
- In this thesis pressure  $p_2$  was estimated, but it would be better to measure  $p_2$  and the pressure in the air film at different locations. This could be achieved by holes in the manifold or holes in a rigid test substrate. With pressure sensors the pressure at the holes can be measured. With this, one could measure the actual pressure profile in the air film and compare this with the numerical model.

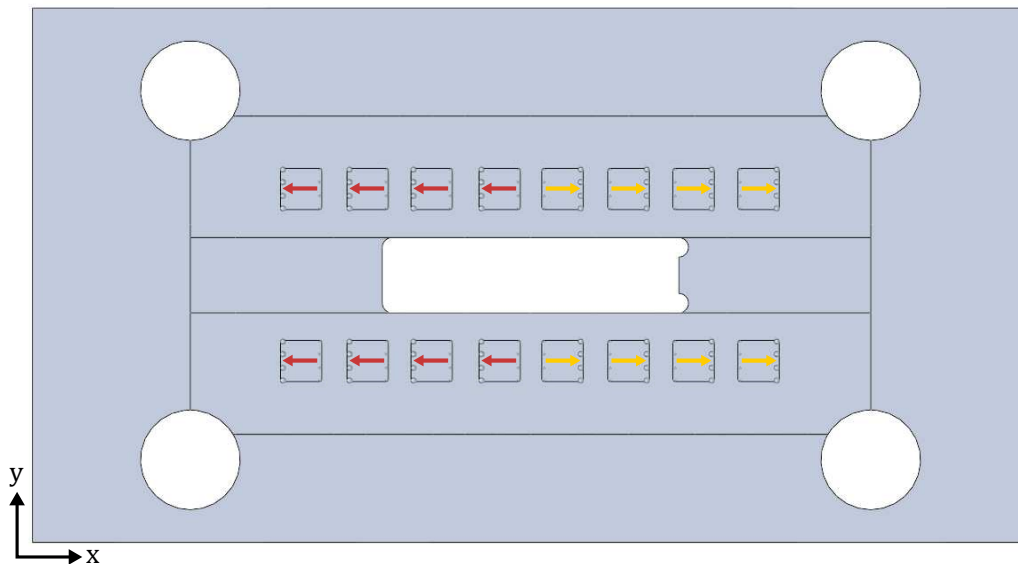
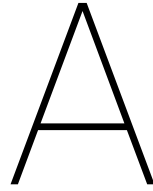


Figure 5.1: Recommendation for improving the placement of the actuators. Top view of the bottom manifold. Here the yellow arrows indicate the actuators generating an actuation force to right and the red arrows indicate the actuators generating a force to the left.





# Contactless substrate handling systems using air

In literature there are numerous techniques for contactless substrate handling systems with the use of air. In section 1.2 air film actuators were already discussed. In this appendix four different techniques are explained and some examples from literature are described. The survey of various air manipulation systems discussed in Laurent et al. [15] has been used as an inspiration. The four different techniques are: air bearings, tilted air jet actuators, squeeze film actuators and air flow actuators. These are described in sections A.1 to A.4 respectively.

## A.1. Air bearings

The first and most basic design to levitate an object is by an air bearing. An illustration of such a system is shown in figure A.1. Here the lower surface is the stationary part called the bearing surface. The moving part is called the substrate or object. In the bearing surface are holes with diameter  $d$  from which air can be supplied. By applying gauge pressure at the holes, air flows and impinges against the substrate. With this an air film is created between the bearing surface and the substrate. A pressure field is generated in the air film which is larger than the ambient pressure. Therefore the substrate is levitated from the bearing surface until an equilibrium fly height  $h$  is reached. An air hockey table that lifts a puck is a common example of an air bearing. The air bearing only levitates the substrate. In order to move the substrate an in-plane actuation force is needed, as is shown by  $F_{act}$  in figure A.1. Common solutions use a gravity force, an electromagnetic force or an electrostatic force to transport an object. An example of contactless actuation was shown in Pister et al. [21]. Here air nozzles were used to levitate objects of 1 mm by 1 mm on an air film of about 20  $\mu\text{m}$  thick. Conductive plates were used to generate an electrostatic field to apply a force on the levitated object. With this, actuation forces up to 0.01 mN were reached.

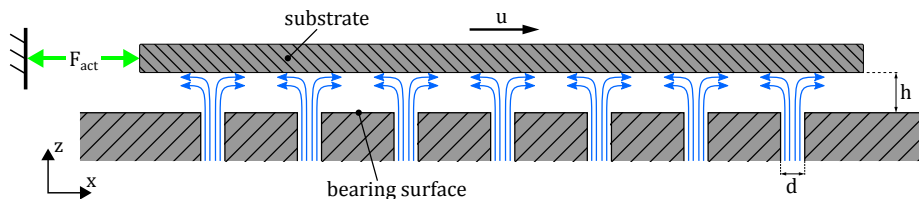


Figure A.1: Air bearing.

## A.2. Tilted air jet actuators

The second kind of contactless handling systems by air are tilted air jet actuators. An illustration of a tilted air jet actuator is shown in figure A.2. The configuration of this system is similar to a conventional air bearing. However the inlet holes with diameter  $d$  are all at an angle  $\phi$  with the vertical. By applying a gauge pressure

at the holes, the pressure field underneath the substrate becomes larger than the ambient pressure. This causes the substrate to levitate to an equilibrium fly height  $h$ . Furthermore, the pressure field also induces an air flow. This flow has a net contribution in one direction. The linear momentum transfer from the jets to the substrate gives an in-plane traction force. By using multiple tilted air jets in different directions, one can position the substrate to the desired location.

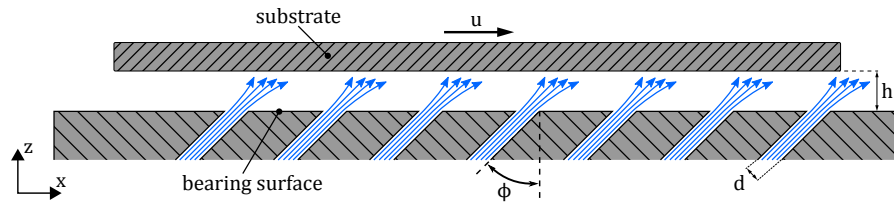


Figure A.2: Air jet actuator.

Several researches have been conducted with such actuators. Examples of researches and the performances of tilted air jet actuators are listed below:

- In Biegelsen et al. [2][3][6] a system was used to transport sheets by actuating on both sides of the sheet. Measurements were performed on a 15 cm by 13 cm flexible plastic sheet with a mass of 3 g. The film thickness was about 2 mm on either side of the sheet. It was measured that a single jet could generate 0.17 mN with an air consumption of 1.2 L/min.
- In Moon et al. [19] a 2 m long track was developed to transport a 300 mm wafer of 127 g. Here the air film thickness was 400  $\mu\text{m}$ . With this system a maximum wafer velocity of 0.56 m/s was achieved.
- Guelpa et al. [7] developed modular square blocks that could lift and push the substrate in a single direction. Multiple blocks were used to transport and position a 150 mm glass wafer. Measurements showed a maximum wafer velocity of 0.3 m/s. The maximum measured in-plane force was about 11 mN with an air consumption of about 27 L/min.

### A.3. Squeeze film actuators

A third way to generate a pressure field to position a substrate is to change the film thickness actively. When the gap between the bearing surface and the substrate is oscillated with sufficient high frequency, the air between the bearing surface and the substrate can be considered to be trapped. Because air is a compressible fluid, the pressure to volume relationship can be described as an isothermal ideal gas. In figure A.3 it can be seen that during compression the pressure difference ( $\Delta p^+$ ) is larger than the pressure difference during expansion ( $\Delta p^-$ ). This results in an average pressure ( $p_{\text{avg}}$ ) which is larger than the atmospheric pressure ( $p_{\text{atm}}$ ). With this a pressure distribution can be created which levitates the substrate. This phenomenon is called the 'squeeze film effect' [22][23].

Furthermore, the vibrating bearing surface can be made up of different vibrating surfaces which is shown in figure A.4. When increasing the vibration amplitude of the next vibrating surface, the pressure there is increased ( $p^{++}$  in figure A.4). Note that the pressure can only increase when a vibrating surface is covered by the substrate. Due to the generated pressure field a flow is induced. Subsequently this flow generates a viscous traction force which shifts the substrate to the next vibrating surface and holds it there. With this principle the substrate can be transported to the desired location.

Several researches have been conducted on vibrating surfaces to transport and position a substrate. Examples of researches and the performances of such systems are listed below:

- In Ueha et al. [27] a vibrating plate of 609 mm long was used to levitate and transport an object. By applying travelling waves in the plate a flow is generated. This flow induces a viscous traction which can move the object in the desired direction. The plate was vibrated at a resonant frequency of 19 kHz with a wavelength of 38.06 mm. With this a 90 mm by 65 mm Bakelite plate of 8.6 g could be lifted and transported with a maximum velocity of 0.7 m/s. In this case the vibration amplitude of the plate was 20  $\mu\text{m}$ .

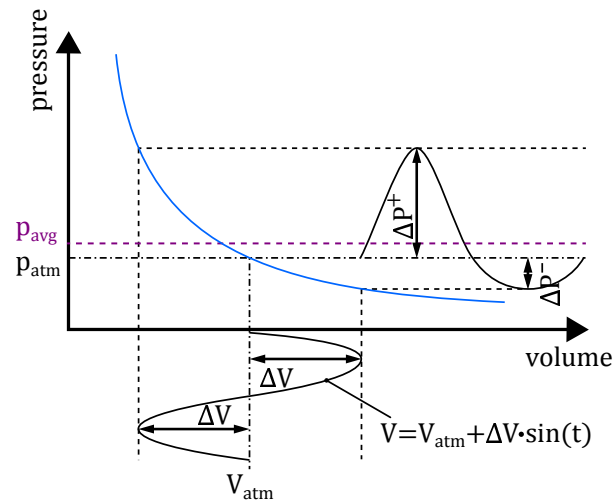


Figure A.3: Expansion and compression of air on a constant temperature line.

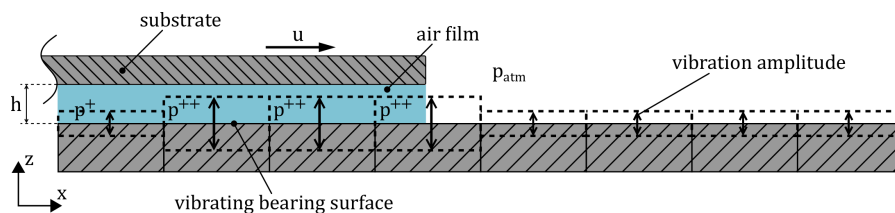


Figure A.4: Squeeze film actuator.

- In Yano et al. [34] a demonstrator was developed to levitate and transport an object. The system contained three 35 mm by 15 mm steel plates placed next to each other. The plates have a resonance frequency of about 22.5 kHz. A 10 mm by 17.5 mm acrylic object could be levitated at a film height between 25  $\mu\text{m}$  and 45  $\mu\text{m}$ . The largest measured in-plane force on the object was 0.15 mN.

## A.4. Air flow actuators

A fourth way to position a substrate contactless using air, is by creating an induced flow at the edge of the substrate. This is done by having a bearing surface consisting of a pattern of nozzles. There are two different nozzles: levitation nozzles and traction nozzles (as is shown in figure A.5). The levitation nozzles are used to create an air cushion between the substrate and the actuator surface. By this the substrate maintains a constant fly height  $h$  above the bearing surface (same principle as regular air bearings). The substrate can be moved by generating strong vertical air jets through the traction nozzles (as is shown in figure A.5). This is done by applying high pressure at the traction nozzles which are located at the leading edge of the substrate. The air jets create an induced air flow in the surrounding fluid that pulls the object toward the nozzle by viscous traction. By consistently applying pressure at the leading edge of the substrate, the substrate can be positioned at the desired location. The induced flow can also be generated by applying a vacuum pressure instead of a gauge pressure.

Examples of researches and the performances of air flow actuators are shown below:

- In Moon et al. [18][29] a demonstrator was developed to position small plexiglass objects. An air hockey table was used to lift the object. A cover plate with holes was placed 1 cm above the object. The holes used vacuum pressure with an air flow of 114 L/min. By moving the cover plate, the object could be positioned in-plane to a desired location.
- In Laurent et al. [5] [16] a table was used consisting of levitation nozzles and traction nozzles to position an object in-plane (see figure A.5). Visual feedback was used such that the traction nozzles at leading

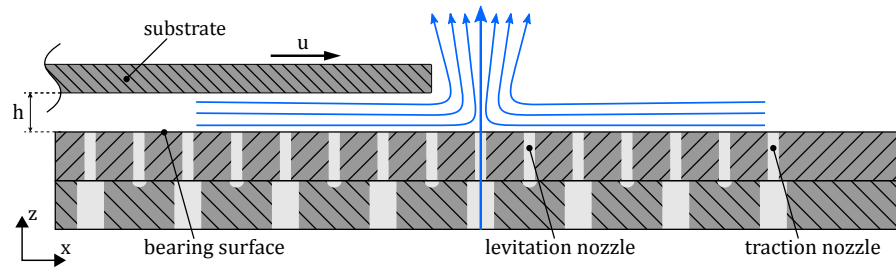


Figure A.5: Air flow actuator.

edge of the object were activated. With this the object could be moved in the desired direction. The system was able to achieve a maximum traction force of 20.81 mN on a H-shaped object of 32.38 g.

# B

## Derivation Reynolds equation

As mentioned in section 2.1 the conservation laws describe the fundamental principles a flow has to satisfy. The differential forms of the conservation laws are quite difficult to solve and analytical techniques are limited to simple geometries and uniform boundary conditions. In this appendix the conservation of mass and momentum equations are combined and simplified which results in the so called 'Reynolds equation', shown in equation 2.1. From this equation the pressure field in the air film can be calculated. During the derivation of the Reynolds equation a description for the associated velocity field is also derived. This velocity field is crucial for determining the performance of the air film actuator.

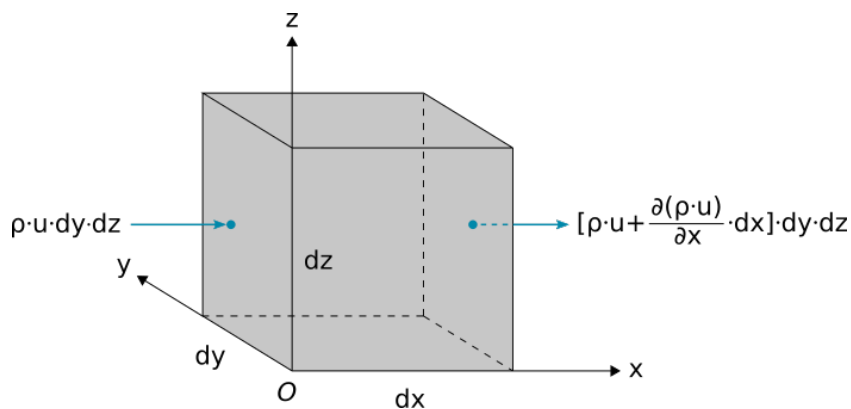


Figure B.1: Mass flow in  $x$ -direction entering and leaving boundaries of an infinitesimal small control volume element.

### B.1. Conservation of mass

The first conservation law to explain is the conservation of mass. This conservation law states that the fluid mass cannot change. This concept is applied to a fixed infinitesimal small control volume element (Eulerian approach) as is shown in figure B.1. Mass can be stored within the volume by a change in density. The rate of storage is  $\frac{\partial \rho}{\partial t} \cdot dx \cdot dy \cdot dz$ . Mass can flow across the control volume boundaries. For mass conservation if the mass flow at the left face is known by  $\rho \cdot u \cdot dy \cdot dz$ , the value on the right face is given by  $\left[ \rho \cdot u + \frac{\partial(\rho \cdot u)}{\partial x} \cdot dx \right] \cdot dy \cdot dz$ . These mass flows in  $x$ -direction are shown in figure B.1 on the left and right faces respectively. The flows in  $y$ -direction (front and back faces) and  $z$ -direction (bottom and top faces) are omitted to avoid cluttering up the drawing. The six flows are listed in table B.1.

By convention, flow that enters the control volume across a surface is denoted negative, because the outward normal and velocity vector are in opposite direction. While the flow that leaves the control volume across a surface is denoted positive, because the outward normal and velocity vector are in the same direction.

Table B.1: Mass flows in and out across boundaries of an infinitesimal small control volume element

Face	Inlet mass flow	Outlet mass flow
$x$	$\rho \cdot u \cdot dy \cdot dz$	$\left[ \rho \cdot u + \frac{\partial(\rho \cdot u)}{\partial x} \cdot dx \right] \cdot dy \cdot dz$
$y$	$\rho \cdot v \cdot dx \cdot dz$	$\left[ \rho \cdot v + \frac{\partial(\rho \cdot v)}{\partial y} \cdot dy \right] \cdot dx \cdot dz$
$z$	$\rho \cdot w \cdot dx \cdot dy$	$\left[ \rho \cdot w + \frac{\partial(\rho \cdot w)}{\partial z} \cdot dz \right] \cdot dx \cdot dy$

Summing the flows gives mass conservation relation as shown in equation B.1.

$$\frac{\partial \rho}{\partial t} \cdot dx \cdot dy \cdot dz + \frac{\partial(\rho \cdot u)}{\partial x} \cdot dx \cdot dy \cdot dz + \frac{\partial(\rho \cdot v)}{\partial y} \cdot dx \cdot dy \cdot dz + \frac{\partial(\rho \cdot w)}{\partial z} \cdot dx \cdot dy \cdot dz = 0 \quad (\text{B.1})$$

By dividing equation B.1 by the element volume ( $dx \cdot dy \cdot dz$ ), leaves the partial differential equation shown in equation B.2.

$$\frac{\partial \rho}{\partial t} + \frac{\partial(\rho \cdot u)}{\partial x} + \frac{\partial(\rho \cdot v)}{\partial y} + \frac{\partial(\rho \cdot w)}{\partial z} = 0 \quad (\text{B.2})$$

Using index notation, equation B.2 can be rewritten in more compact form as is shown in equation B.3.

$$\frac{\partial \rho}{\partial t} + \frac{\partial(\rho \cdot u_i)}{\partial x_i} = 0 \quad (\text{B.3})$$

Equation B.3 states that mass is conserved for an infinitesimal control volume. It is often called the equation of continuity because it requires no assumptions except that the density and velocity are continuum functions. In words, the second term in equation B.3  $\left( \frac{\partial(\rho \cdot u_i)}{\partial x_i} \right)$  is the divergence of the mass flux  $\rho \cdot u_i$ . This flux divergence gives the net loss of density per unit time at each point of the fluid. For example, if  $\frac{\partial(\rho \cdot u_i)}{\partial x_i}$  is positive the local density will decrease with time. For more details about conservation of mass and information about the Reynolds transport theorem see [13] [17] [32].

## B.2. Conservation of momentum

The second conservation law to explain is the conservation of momentum. This conservation law states that the time rate of change of momentum equals the sum of forces acting on the control volume. For analysis the same control volume is used as in section B.1, except instead of a fixed control volume (Eulerian approach) the control volume moves with the fluid flow (Lagrangian approach). Since the control volume moves with the fluid, the time rate of change of momentum is the elemental mass times its acceleration. By doing so the conservation of momentum results in equation B.4 which is equivalent to Newton's second law of motion.

$$\rho \cdot \frac{D\mathbf{u}}{Dt} \cdot dx \cdot dy \cdot dz = \sum d\mathbf{F} \quad (\text{B.4})$$

Here  $\frac{D\mathbf{u}}{Dt} = \frac{\partial \mathbf{u}}{\partial t} + \mathbf{u} \cdot (\nabla \mathbf{u})$  defines the material derivative of the velocity. Equation B.4 points out that the net force on the control volume must be of differential size and proportional to the element volume. These forces are divided in two types of forces: body forces and surface forces. The first one, body forces, are forces which are applied to the entire mass by an external field. In this thesis only gravity is considered as a force field, other force fields (such as magnetism, electric potential) are omitted. The differential gravity force applied on the control volume is stated by equation B.5. Here  $\mathbf{g} = [g_x \quad g_y \quad g_z]^T$ , depending on the orientation of the gravity field.

$$d\mathbf{F}_{\text{body}} = \rho \cdot \mathbf{g} \cdot dx \cdot dy \cdot dz \quad (\text{B.5})$$

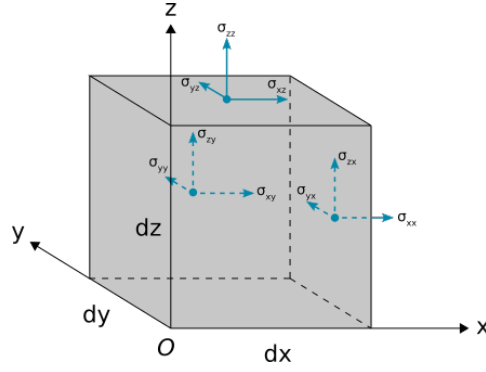


Figure B.2: Stress components on the sides of an infinitesimal small control volume element.

The second type of forces, the surface forces, are stresses which are applied to the surfaces of the control volume. These are shown in figure B.2. The surface forces arise from hydrostatic pressure and viscous stresses. The hydrostatic pressure ( $p$ ) is defined as the compressive stress at a point in a static fluid. By convention the hydrostatic pressure is taken positive for compression. The viscous stresses arise from a velocity gradient across the fluid denoted in the viscous stress tensor ( $\tau_{ij}$ ). Each stress component on each plane can be presented in a second order tensor ( $\sigma_{ij}$ ) shown in equation B.6.

$$\sigma_{ij} = -p \cdot \delta_{ij} + \tau_{ij} = \begin{bmatrix} -p + \tau_{xx} & \tau_{xy} & \tau_{xz} \\ \tau_{yx} & -p + \tau_{yy} & \tau_{yz} \\ \tau_{zx} & \tau_{zy} & -p + \tau_{zz} \end{bmatrix} \quad (B.6)$$

Here ( $\sigma_{ij}$ ) denotes a symmetric tensor called the Cauchy stress tensor. Where the first index ( $i$ ) of  $\sigma_{ij}$  indicates the direction in which the stress acts on its plane. While the second index ( $j$ ) indicates the direction of the outward normal of the surface on which the stress is acting on [8]. Lets now observe the stresses applied in the  $x$ -direction which are drawn in figure B.3. The net force in  $x$ -direction on the  $yz$ -plane is  $\frac{\partial \sigma_{xx}}{\partial x} \cdot dx \cdot dy \cdot dz$ . The same happens for the other faces, which results in a net differential surface force in the  $x$ -direction shown in equation B.7.

$$dF_{x,surf} = \left[ \frac{\partial \sigma_{xx}}{\partial x} + \frac{\partial \sigma_{xy}}{\partial y} + \frac{\partial \sigma_{xz}}{\partial z} \right] \cdot dx \cdot dy \cdot dz \quad (B.7)$$

From equation B.7 it can be seen that the force is proportional to the element volume. Furthermore, not the stresses but their gradients cause a net force on the surfaces. Each stress term in equation B.7 can be substituted by the terms on the first row of equation B.6. This results in equation B.8.

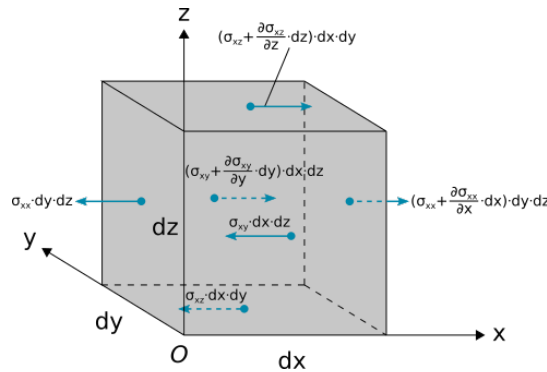


Figure B.3: Stresses applied in the  $x$ -direction on an infinitesimal small control volume element.

$$dF_{x,surf} = \left[ -\frac{\partial p}{\partial x} + \frac{\partial \tau_{xx}}{\partial x} + \frac{\partial \tau_{xy}}{\partial y} + \frac{\partial \tau_{xz}}{\partial z} \right] \cdot dx \cdot dy \cdot dz \quad (B.8)$$

With the same reasoning the forces in  $y$ -direction and  $z$ -direction can be derived. These net differential surface forces are shown in equations B.9 and B.10.

$$dF_{y,\text{surf}} = \left[ -\frac{\partial p}{\partial y} + \frac{\partial \tau_{yx}}{\partial x} + \frac{\partial \tau_{yy}}{\partial y} + \frac{\partial \tau_{yz}}{\partial z} \right] \cdot dx \cdot dy \cdot dz \quad (\text{B.9})$$

$$dF_{z,\text{surf}} = \left[ -\frac{\partial p}{\partial z} + \frac{\partial \tau_{zx}}{\partial x} + \frac{\partial \tau_{zy}}{\partial y} + \frac{\partial \tau_{zz}}{\partial z} \right] \cdot dx \cdot dy \cdot dz \quad (\text{B.10})$$

With these differential forces, Newton's second law (equation B.4) can be filled in where  $\sum d\mathbf{F} = d\mathbf{F}_{\text{surf}} + d\mathbf{F}_{\text{body}}$ . The result is shown in equation B.11.

$$\rho \cdot \frac{D\mathbf{u}}{Dt} \cdot dx \cdot dy \cdot dz = [-\nabla p + \text{div}(\tau_{ij}) + \rho \cdot \mathbf{g}] \cdot dx \cdot dy \cdot dz \quad (\text{B.11})$$

Furthermore, one can divide the element volume ( $dx \cdot dy \cdot dz$ ). This leaves the basic differential momentum equation for an infinitesimal element shown in equation B.12 in index notation.

$$\rho \cdot \frac{Du_i}{Dt} = -\frac{\partial p}{\partial x_i} + \frac{\partial \tau_{ij}}{\partial x_j} + \rho \cdot g_i \quad (\text{B.12})$$

In words equation B.4 states:

$$\begin{aligned} &\text{density} \cdot \text{acceleration} = - \text{pressure force per unit volume} \\ &+ \text{viscous force per unit volume} + \text{gravity force per unit volume} \end{aligned}$$

Finally, to fully define the momentum equation the viscous stress tensor  $\tau_{ij}$  has to be determined. By analogy with Hookean elasticity, the simplest assumption for the variation of viscous stress with strain rate is a linear law. These considerations were first made by Stokes (1845). Fluids that obey these conditions are said to be a 'Newtonian' fluid. The resulting deformation law is satisfied by all gases and most common fluids [33]. These assumptions are:

1. The fluid is continuous and its viscous stress tensor ( $\tau_{ij}$ ) is a linear function of the strain rates from dilating and shearing of the body.
2. The fluid is assumed isotropic where its properties are independent of direction. Therefore the state of stress does not depend on how the fluid body is oriented with respect to the direction of deformation.
3. When the strain rates are zero the viscous stresses vanish whereby the remaining stresses reduce to the hydrostatic pressure ( $\sigma_{ij} = -p \cdot \delta_{ij}$ ).

With these statements the deformation of a fluid element can be related to viscous stresses that act on it. By definition a viscous stress is one that is generated due to relative motion between different parts of a fluid. The motions which a fluid element can have are: translation, rotation, normal strain and shear strain. These motions are shown in figure B.4. It is clear from figure B.4 that only normal strain and shear strain involve motions in which parts of the fluid element move relative to one another, resulting in a deformation of the fluid element. Therefore only normal strain and shear strain are expected to be responsible for the generation

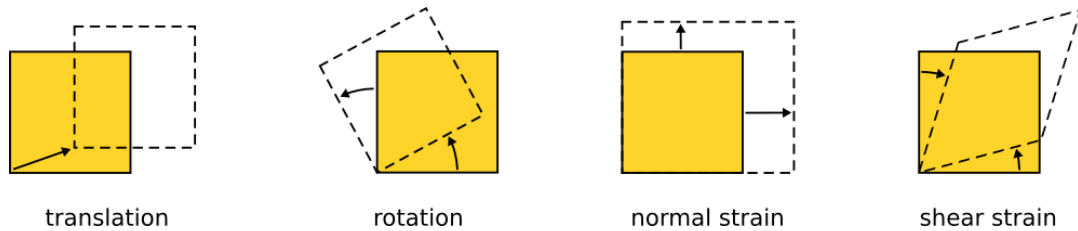


Figure B.4: Illustration of possible motions of a fluid element.

of viscous stress in a flowing fluid. In fluid kinematics the ‘strain rate tensor’ ( $S_{ij}$ ) describes the symmetric part of the velocity gradient  $\left(\frac{\partial u_i}{\partial x_j}\right)$  which embodies fluid element deformation. The strain rate tensor is given in equation B.13.

$$S_{ij} = \frac{1}{2} \cdot \left( \frac{\partial u_i}{\partial x_j} + \frac{\partial u_j}{\partial x_i} \right) \quad (\text{B.13})$$

When  $i = j$  then  $S_{11} = \frac{\partial u_1}{\partial x_1}$ ,  $S_{22} = \frac{\partial u_2}{\partial x_2}$  and  $S_{33} = \frac{\partial u_3}{\partial x_3}$ , which equals the rate of normal strain in  $x$ -,  $y$ - and  $z$ -direction respectively. While if  $i \neq j$  then  $S_{ij}$  equals one half the rate of shear strain in the  $xy$ -,  $xz$ - or  $yz$ -plane. As described in [13] the relation between the viscous stresses and the strain rate tensor is given as in equation B.14.

$$\tau_{ij} = 2 \cdot \mu \cdot S_{ij} + \lambda \cdot S_{mm} \cdot \delta_{ij} \quad (\text{B.14})$$

Here  $\mu$  is called the dynamic viscosity coefficient which relates normal strain or shear strain to a viscous stress. Whereas the term  $\lambda$  is called the second coefficient of viscosity which relates volume change of the fluid to a viscous stress. Filling in equation B.6 by equation B.14 results in equation B.15 which gives the stresses in a Newtonian fluid.

$$\sigma_{ij} = -p \cdot \delta_{ij} + 2 \cdot \mu \cdot S_{ij} + \lambda \cdot S_{mm} \cdot \delta_{ij} \quad (\text{B.15})$$

By substituting equation B.15 in equation B.12 the momentum equation is obtained as is shown in equation B.16. This equation is also known as the ‘Navier-Stokes’ equations which expresses the equations of motion for compressible Newtonian fluids.

$$\rho \cdot \left( \frac{\partial u_i}{\partial t} + u_j \cdot \frac{\partial u_i}{\partial x_j} \right) = -\frac{\partial p}{\partial x_i} + \frac{\partial}{\partial x_j} \cdot \left[ \mu \cdot \left( \frac{\partial u_i}{\partial x_j} + \frac{\partial u_j}{\partial x_i} \right) + \lambda \cdot \frac{\partial u_m}{\partial x_m} \cdot \delta_{ij} \right] + \rho \cdot g_i \quad (\text{B.16})$$

Lastly Stokes noted an interesting consequence of equation B.15. By taking the negative average of the three normal stresses, one obtains the average compression stress on the element. This is shown in equation B.17.

$$\bar{p} = -\frac{1}{3} \cdot (\sigma_{xx} + \sigma_{yy} + \sigma_{zz}) = p - \left( \lambda + \frac{2}{3} \cdot \mu \right) \cdot \frac{\partial u_m}{\partial x_m} \quad (\text{B.17})$$

Here  $\bar{p}$  is defined as the ‘mechanical pressure’ which the fluid experiences. And where  $\frac{\partial u_m}{\partial x_m} = \text{div}(u_i)$  describes the dilatation of the fluid. Equation B.17 states that the mean pressure in a deforming viscous fluid is not equal to the thermodynamic property called pressure ( $p$ ). This difference is due to the time lag with which the thermodynamic equilibrium condition is reached in a motion that implies an isotropic dilatation of a fluid element [4]. Stokes simply resolved the issue by assuming the relation stated in equation B.18.

$$\lambda + \frac{2}{3} \cdot \mu = 0 \quad (\text{B.18})$$

This statement is also known as ‘Stokes’ hypothesis’. With this assumption isotropic dilatations by the fluid do not produce viscous stresses. This statement is found to be accurate in many situations because either the term  $\left(\lambda + \frac{2}{3} \cdot \mu\right)$  or the term  $\frac{\partial u_m}{\partial x_m}$  is often very small [13] [33]. Only in special situations does the distinction between  $p$  and  $\bar{p}$  play an important role. For example in shock waves or explosions where the volume of a fluid element rapidly changes. Throughout this thesis it is assumed that Stokes hypothesis is valid (see assumption 6 from section 2.2). Substituting equation B.18 in equation B.16 results in equation B.19 which will be the momentum equation used throughout this thesis.

$$\rho \cdot \left( \frac{\partial u_i}{\partial t} + u_j \cdot \frac{\partial u_i}{\partial x_j} \right) = -\frac{\partial p}{\partial x_i} + \frac{\partial}{\partial x_j} \cdot \left[ \mu \cdot \left( \frac{\partial u_i}{\partial x_j} + \frac{\partial u_j}{\partial x_i} \right) - \frac{2}{3} \cdot \mu \cdot \frac{\partial u_m}{\partial x_m} \cdot \delta_{ij} \right] + \rho \cdot g_i \quad (\text{B.19})$$

### B.3. Nondimensionalization: conservation of mass

By writing conservation laws in nondimensional form, one can determine which terms are negligible. This simplifies the differential equations significantly. Let us first analyse the conservation of mass shown in equation B.3 in index notation.

$$\frac{\partial \rho}{\partial t} + \frac{\partial (\rho \cdot u_i)}{\partial x_i} = 0 \quad (\text{B.3})$$

To determine which terms are important and which may be neglected, the differential equation will be nondimensionalized. There are eight independent and dependent variables, namely:  $u, v, w, x, y, z, t$  and  $\rho$ . These variables can be expressed by a characteristic scaling unit (denoted with a subscript 's') and a nondimensionalized quantity (expressed with an asterisk above the quantity):

$$\begin{aligned} u &= u_s \cdot u^* & v &= v_s \cdot v^* & w &= w_s \cdot w^* \\ x &= L_s \cdot x^* & y &= L_s \cdot y^* & z &= H_s \cdot z^* \\ t &= t_s \cdot t^* & \rho &= \rho_s \cdot \rho^* \end{aligned}$$

Here is  $u_s$  the characteristic velocity of the flow in  $x$ -direction,  $v_s$  the characteristic velocity of the flow in  $y$ -direction,  $w_s$  the characteristic velocity in  $z$ -direction. It is given that the dimensions in  $x$ - and  $y$ -direction are in the same order (see assumption 10 from section 2.2). Therefore  $L_s$  represents the characteristic length of the fluid film in  $x$ - or  $y$ -direction.  $H_s$  is the characteristic length of the fluid film in  $z$ -direction,  $t_s$  the characteristic time scale and  $\rho_s$  the characteristic density of the fluid. Substitute these variables in equation B.3 gives equation B.20.

$$\frac{\rho_s}{t_s} \cdot \frac{\partial \rho^*}{\partial t^*} + \frac{\rho_s \cdot u_s}{L_s} \cdot \frac{\partial (\rho^* \cdot u^*)}{\partial x^*} + \frac{\rho_s \cdot v_s}{L_s} \cdot \frac{\partial (\rho^* \cdot v^*)}{\partial y^*} + \frac{\rho_s \cdot w_s}{H_s} \cdot \frac{\partial (\rho^* \cdot w^*)}{\partial z^*} = 0 \quad (\text{B.20})$$

This equation is not yet dimensionless. Therefore by dividing this equation by the coefficient of the highest ordered derivative term  $\frac{\partial (\rho^* \cdot u^*)}{\partial x^*}$ , this equation becomes dimensionless as is shown in equation B.21.

$$\frac{L_s}{t_s \cdot u_s} \cdot \frac{\partial \rho^*}{\partial t^*} + \frac{\partial (\rho^* \cdot u^*)}{\partial x^*} + \frac{v_s}{u_s} \cdot \frac{\partial (\rho^* \cdot v^*)}{\partial y^*} + \frac{L_s}{H_s} \cdot \frac{w_s}{u_s} \cdot \frac{\partial (\rho^* \cdot w^*)}{\partial z^*} = 0 \quad (\text{B.21})$$

Now the continuity equation is dimensionless, some insight can be obtained about the relation between different scaling quantities. For that the coefficients in front of the terms  $\frac{\partial \rho^*}{\partial t^*}$ ,  $\frac{\partial (\rho^* \cdot v^*)}{\partial y^*}$  and  $\frac{\partial (\rho^* \cdot w^*)}{\partial z^*}$  are set to unity. With this, one can observe the relevance of these terms with respect to the highest order derivative term  $\frac{\partial (\rho^* \cdot u^*)}{\partial x^*}$ , which coefficient is already unity. From this results the following relations shown in equations B.22, B.23 and B.24.

$$\frac{L_s}{t_s \cdot u_s} = 1 \Rightarrow t_s = \frac{L_s}{u_s} \quad (\text{B.22})$$

$$\frac{v_s}{u_s} = 1 \Rightarrow v_s = u_s \quad (\text{B.23})$$

$$\frac{L_s}{H_s} \cdot \frac{w_s}{u_s} = 1 \Rightarrow w_s = \frac{H_s}{L_s} \cdot u_s \quad (\text{B.24})$$

### B.4. Nondimensionalization: Navier-Stokes momentum equations

Secondly, the Navier-Stokes equations will be nondimensionalized. As described in section B.2 these equations describe the momentum balance in the fluid in each direction ( $x, y$  and  $z$ ). In equation B.19 the Navier-Stokes equations are given.

$$\rho \cdot \left( \frac{\partial u_i}{\partial t} + u_j \cdot \frac{\partial u_i}{\partial x_j} \right) = - \frac{\partial P}{\partial x_i} + \frac{\partial}{\partial x_j} \cdot \left[ \mu \cdot \left( \frac{\partial u_i}{\partial x_j} + \frac{\partial u_j}{\partial x_i} \right) - \frac{2}{3} \cdot \mu \cdot \frac{\partial u_m}{\partial x_m} \cdot \delta_{ij} \right] + \rho \cdot g_i \quad (\text{B.19})$$

In this case there are nine independent and dependent variables, namely:  $u, v, w, x, y, z, t, p$  and  $\rho$ . Now equations B.22, B.23 and B.24 are substituted:

$$\begin{aligned}
u &= u_s \cdot u^* & v &= v_s \cdot v^* = u_s \cdot v^* & w &= w_s \cdot w^* = \frac{H_s}{L_s} \cdot u_s \cdot w^* \\
x &= L_s \cdot x^* & y &= L_s \cdot y^* & z &= H_s \cdot z^* \\
t &= t_s \cdot t^* = \frac{L_s}{u_s} \cdot t^* & p &= p_s \cdot p^* & \rho &= \rho_s \cdot \rho^*
\end{aligned}$$

Here  $p_s$  is the characteristic pressure scale in the fluid. With these the variables in the Navier-Stokes equations can be substituted. There are three momentum equations, one for every direction. These equations will be discussed individually in the following sections.

#### B.4.1. Conservation of momentum in $x$ -direction

From equation B.19 the momentum balance in  $x$ -direction can be given. This is shown in equation B.25. Note that  $\mu$  is brought out of the partial derivatives because this parameter is assumed constant (see assumption 8 from section 2.2).

$$\begin{aligned}
\rho \cdot \left( \frac{\partial u}{\partial t} + u \cdot \frac{\partial u}{\partial x} + v \cdot \frac{\partial u}{\partial y} + w \cdot \frac{\partial u}{\partial z} \right) &= -\frac{\partial p}{\partial x} \\
+\mu \cdot \left[ \frac{\partial^2 u}{\partial x^2} + \frac{\partial^2 u}{\partial y^2} + \frac{\partial^2 u}{\partial z^2} + \frac{1}{3} \cdot \left( \frac{\partial^2 u}{\partial x^2} + \frac{\partial^2 v}{\partial x \cdot \partial y} + \frac{\partial^2 w}{\partial x \cdot \partial z} \right) \right] &+ \rho \cdot g_x
\end{aligned} \tag{B.25}$$

Now the variables are substituted in equation B.25 as is shown in equation B.26. In equation B.27 the coefficients are grouped together. And lastly in equation B.28 the equation is divided by the coefficient of the highest order derivative term  $\frac{\partial^2 u^*}{\partial z^{*2}}$ , which makes each coefficient term dimensionless.

$$\begin{aligned}
\rho_s \cdot \rho^* \cdot \left( \frac{u_s^2}{L_s} \cdot \frac{\partial u^*}{\partial t^*} + \frac{u_s^2}{L_s} \cdot u^* \cdot \frac{\partial u^*}{\partial x^*} + \frac{u_s^2}{L_s} \cdot v^* \cdot \frac{\partial u^*}{\partial y^*} + \frac{H_s \cdot u_s^2}{L_s \cdot H_s} \cdot w^* \cdot \frac{\partial u^*}{\partial z^*} \right) &= -\frac{p_s}{L_s} \cdot \frac{\partial p^*}{\partial x^*} \\
+\mu \cdot \left[ \frac{u_s}{L_s^2} \cdot \frac{\partial^2 u^*}{\partial x^{*2}} + \frac{u_s}{L_s^2} \cdot \frac{\partial^2 u^*}{\partial y^{*2}} + \frac{u_s}{H_s^2} \cdot \frac{\partial^2 u^*}{\partial z^{*2}} + \frac{1}{3} \cdot \left( \frac{u_s}{L_s^2} \cdot \frac{\partial^2 u^*}{\partial x^{*2}} + \frac{u_s}{L_s^2} \cdot \frac{\partial^2 v^*}{\partial x^* \cdot \partial y^*} + \frac{H_s \cdot u_s}{L_s \cdot L_s \cdot H_s} \cdot \frac{\partial^2 w^*}{\partial x^* \cdot \partial z^*} \right) \right] &+ \rho_s \cdot \rho^* \cdot g_x
\end{aligned} \tag{B.26}$$

$$\begin{aligned}
\frac{\rho_s \cdot u_s \cdot L_s}{\mu} \cdot \rho^* \cdot \left( \frac{\partial u^*}{\partial t^*} + u^* \cdot \frac{\partial u^*}{\partial x^*} + v^* \cdot \frac{\partial u^*}{\partial y^*} + w^* \cdot \frac{\partial u^*}{\partial z^*} \right) &= -\frac{p_s \cdot L_s}{\mu \cdot u_s} \cdot \frac{\partial p^*}{\partial x^*} \\
+\frac{\partial^2 u^*}{\partial x^{*2}} + \frac{\partial^2 u^*}{\partial y^{*2}} + \frac{L_s^2}{H_s^2} \cdot \frac{\partial^2 u^*}{\partial z^{*2}} + \frac{1}{3} \cdot \left( \frac{\partial^2 u^*}{\partial x^{*2}} + \frac{\partial^2 v^*}{\partial x^* \cdot \partial y^*} + \frac{\partial^2 w^*}{\partial x^* \cdot \partial z^*} \right) &+ \frac{\rho_s \cdot L_s^2}{\mu \cdot u_s} \cdot g_x \cdot \rho^*
\end{aligned} \tag{B.27}$$

$$\begin{aligned}
\frac{H_s}{L_s} \cdot \frac{\rho_s \cdot u_s \cdot H_s}{\mu} \cdot \rho^* \cdot \left( \frac{\partial u^*}{\partial t^*} + u^* \cdot \frac{\partial u^*}{\partial x^*} + v^* \cdot \frac{\partial u^*}{\partial y^*} + w^* \cdot \frac{\partial u^*}{\partial z^*} \right) &= -\frac{H_s}{L_s} \cdot \frac{p_s \cdot H_s}{\mu \cdot u_s} \cdot \frac{\partial p^*}{\partial x^*} \\
+\frac{\partial^2 u^*}{\partial z^{*2}} + \frac{H_s^2}{L_s^2} \cdot \left[ \frac{\partial^2 u^*}{\partial x^{*2}} + \frac{\partial^2 u^*}{\partial y^{*2}} + \frac{1}{3} \cdot \left( \frac{\partial^2 u^*}{\partial x^{*2}} + \frac{\partial^2 v^*}{\partial x^* \cdot \partial y^*} + \frac{\partial^2 w^*}{\partial x^* \cdot \partial z^*} \right) \right] &+ \frac{\rho_s \cdot H_s^2}{\mu \cdot u_s} \cdot g_x \cdot \rho^*
\end{aligned} \tag{B.28}$$

#### B.4.2. Conservation of momentum in $y$ -direction

In equation B.29 the momentum balance in  $y$ -direction is given.

$$\begin{aligned}
\rho \cdot \left( \frac{\partial v}{\partial t} + u \cdot \frac{\partial v}{\partial x} + v \cdot \frac{\partial v}{\partial y} + w \cdot \frac{\partial v}{\partial z} \right) &= -\frac{\partial p}{\partial y} \\
+\mu \cdot \left[ \frac{\partial^2 v}{\partial x^2} + \frac{\partial^2 v}{\partial y^2} + \frac{\partial^2 v}{\partial z^2} + \frac{1}{3} \cdot \left( \frac{\partial^2 u}{\partial x \cdot \partial y} + \frac{\partial^2 v}{\partial y^2} + \frac{\partial^2 w}{\partial y \cdot \partial z} \right) \right] &+ \rho \cdot g_y
\end{aligned} \tag{B.29}$$

Yet again, the variables are filled in as is shown in equation B.30. In equation B.31 the coefficients are grouped together. And lastly in equation B.32 the equation is divided by the coefficient of the highest order derivative term  $\frac{\partial^2 v^*}{\partial z^{*2}}$ , which makes each coefficient term dimensionless.

$$\begin{aligned}
\rho_s \cdot \rho^* \cdot \left( \frac{u_s^2}{L_s} \cdot \frac{\partial v^*}{\partial t^*} + \frac{u_s^2}{L_s} \cdot u^* \cdot \frac{\partial v^*}{\partial x^*} + \frac{u_s^2}{L_s} \cdot v^* \cdot \frac{\partial v^*}{\partial y^*} + \frac{H_s \cdot u_s^2}{L_s \cdot H_s} \cdot w^* \cdot \frac{\partial v^*}{\partial z^*} \right) &= -\frac{p_s}{L_s} \cdot \frac{\partial p^*}{\partial y^*} \\
+\mu \cdot \left[ \frac{u_s}{L_s^2} \cdot \frac{\partial^2 v^*}{\partial x^{*2}} + \frac{u_s}{L_s^2} \cdot \frac{\partial^2 v^*}{\partial y^{*2}} + \frac{u_s}{H_s^2} \cdot \frac{\partial^2 v^*}{\partial z^{*2}} + \frac{1}{3} \cdot \left( \frac{u_s}{L_s^2} \cdot \frac{\partial^2 u^*}{\partial x^* \cdot \partial y^*} + \frac{u_s}{L_s^2} \cdot \frac{\partial^2 v^*}{\partial y^{*2}} + \frac{H_s \cdot u_s}{L_s \cdot L_s \cdot H_s} \cdot \frac{\partial^2 w^*}{\partial y^* \cdot \partial z^*} \right) \right] &+ \rho_s \cdot \rho^* \cdot g_y
\end{aligned} \tag{B.30}$$

$$\begin{aligned} & \frac{\rho_s \cdot u_s \cdot L_s}{\mu} \cdot \rho^* \cdot \left( \frac{\partial v^*}{\partial t^*} + u^* \cdot \frac{\partial v^*}{\partial x^*} + v^* \cdot \frac{\partial v^*}{\partial y^*} + w^* \cdot \frac{\partial v^*}{\partial z^*} \right) = - \frac{\rho_s \cdot L_s}{\mu \cdot u_s} \cdot \frac{\partial p^*}{\partial y^*} \\ & + \frac{\partial^2 v^*}{\partial x^{*2}} + \frac{\partial^2 v^*}{\partial y^{*2}} + \frac{L_s^2}{H_s^2} \cdot \frac{\partial^2 v^*}{\partial z^{*2}} + \frac{1}{3} \cdot \left( \frac{\partial^2 u^*}{\partial x^* \cdot \partial y^*} + \frac{\partial^2 v^*}{\partial y^{*2}} + \frac{\partial^2 w^*}{\partial y^* \cdot \partial z^*} \right) + \frac{\rho_s \cdot L_s^2}{\mu \cdot u_s} \cdot g_y \cdot \rho^* \end{aligned} \quad (\text{B.31})$$

$$\begin{aligned} & \frac{H_s}{L_s} \cdot \frac{\rho_s \cdot u_s \cdot H_s}{\mu} \cdot \rho^* \cdot \left( \frac{\partial v^*}{\partial t^*} + u^* \cdot \frac{\partial v^*}{\partial x^*} + v^* \cdot \frac{\partial v^*}{\partial y^*} + w^* \cdot \frac{\partial v^*}{\partial z^*} \right) = - \frac{H_s}{L_s} \cdot \frac{\rho_s \cdot H_s}{\mu \cdot u_s} \cdot \frac{\partial p^*}{\partial y^*} \\ & + \frac{\partial^2 v^*}{\partial z^{*2}} + \frac{H_s^2}{L_s^2} \cdot \left[ \frac{\partial^2 v^*}{\partial x^{*2}} + \frac{\partial^2 v^*}{\partial y^{*2}} + \frac{1}{3} \cdot \left( \frac{\partial^2 u^*}{\partial x^* \cdot \partial y^*} + \frac{\partial^2 v^*}{\partial y^{*2}} + \frac{\partial^2 w^*}{\partial y^* \cdot \partial z^*} \right) \right] + \frac{\rho_s \cdot H_s^2}{\mu \cdot u_s} \cdot g_y \cdot \rho^* \end{aligned} \quad (\text{B.32})$$

### B.4.3. Conservation of momentum in z-direction

In equation B.33 the momentum balance in z-direction is given.

$$\begin{aligned} & \rho \cdot \left( \frac{\partial w}{\partial t} + u \cdot \frac{\partial w}{\partial x} + v \cdot \frac{\partial w}{\partial y} + w \cdot \frac{\partial w}{\partial z} \right) = - \frac{\partial p}{\partial z} \\ & + \mu \cdot \left[ \frac{\partial^2 w}{\partial x^2} + \frac{\partial^2 w}{\partial y^2} + \frac{\partial^2 w}{\partial z^2} + \frac{1}{3} \cdot \left( \frac{\partial^2 u}{\partial x \cdot \partial z} + \frac{\partial^2 v}{\partial y \cdot \partial z} + \frac{\partial^2 w}{\partial z^2} \right) \right] + \rho \cdot g_z \end{aligned} \quad (\text{B.33})$$

As previous, the variables are filled in as is shown in equation B.34. In equation B.35 the coefficients are grouped together. Furthermore in equation B.36 the equation is divided by the coefficient of the highest order derivative term  $\frac{\partial^2 w^*}{\partial z^{*2}}$ , which makes each coefficient term dimensionless. Additionally the equation is multiplied by  $\frac{H_s^2}{L_s^2}$  in order to have the coefficient term  $-\frac{H_s}{L_s} \cdot \frac{\rho_s \cdot H_s}{\mu \cdot u_s}$  in front of  $\frac{\partial p^*}{\partial z^*}$ . This is done in preparation of the next section. Because in that section it will be explained that the pressure gradient is the dominant term in this differential equation.

$$\begin{aligned} & \rho_s \cdot \rho^* \cdot \left( \frac{H_s \cdot u_s^2}{L_s^2} \cdot \frac{\partial w^*}{\partial t^*} + \frac{H_s \cdot u_s^2}{L_s^2} \cdot u^* \cdot \frac{\partial w^*}{\partial x^*} + \frac{H_s \cdot u_s^2}{L_s^2} \cdot v^* \cdot \frac{\partial w^*}{\partial y^*} + \frac{H_s^2 \cdot u_s^2}{L_s^2 \cdot H_s} \cdot w^* \cdot \frac{\partial w^*}{\partial z^*} \right) = - \frac{\rho_s}{H_s} \cdot \frac{\partial p^*}{\partial z^*} \\ & + \mu \cdot \left[ \frac{H_s \cdot u_s}{L_s \cdot L_s^2} \cdot \frac{\partial^2 w^*}{\partial x^{*2}} + \frac{H_s \cdot u_s}{L_s \cdot L_s^2} \cdot \frac{\partial^2 w^*}{\partial y^{*2}} + \frac{H_s \cdot u_s}{L_s \cdot H_s^2} \cdot \frac{\partial^2 w^*}{\partial z^{*2}} + \frac{1}{3} \cdot \left( \frac{u_s}{L_s \cdot H_s} \cdot \frac{\partial^2 u^*}{\partial x^* \cdot \partial z^*} + \frac{u_s}{L_s \cdot H_s} \cdot \frac{\partial^2 v^*}{\partial y^* \cdot \partial z^*} + \frac{H_s \cdot u_s}{L_s \cdot H_s \cdot H_s} \cdot \frac{\partial^2 w^*}{\partial z^{*2}} \right) \right] \\ & + \rho_s \cdot \rho^* \cdot g_z \end{aligned} \quad (\text{B.34})$$

$$\begin{aligned} & \frac{\rho_s \cdot u_s \cdot L_s}{\mu} \cdot \rho^* \cdot \left( \frac{\partial w^*}{\partial t^*} + u^* \cdot \frac{\partial w^*}{\partial x^*} + v^* \cdot \frac{\partial w^*}{\partial y^*} + w^* \cdot \frac{\partial w^*}{\partial z^*} \right) = - \frac{L_s^2}{H_s^2} \cdot \frac{\rho_s \cdot L_s}{\mu \cdot u_s} \cdot \frac{\partial p^*}{\partial z^*} \\ & + \frac{\partial^2 w^*}{\partial x^{*2}} + \frac{\partial^2 w^*}{\partial y^{*2}} + \frac{L_s^2}{H_s^2} \cdot \frac{\partial^2 w^*}{\partial z^{*2}} + \frac{1}{3} \cdot \frac{L_s^2}{H_s^2} \cdot \left( \frac{\partial^2 u^*}{\partial x^* \cdot \partial z^*} + \frac{\partial^2 v^*}{\partial y^* \cdot \partial z^*} + \frac{\partial^2 w^*}{\partial z^{*2}} \right) + \frac{L_s}{H_s} \cdot \frac{\rho_s \cdot L_s^2}{\mu \cdot u_s} \cdot g_z \cdot \rho^* \end{aligned} \quad (\text{B.35})$$

$$\begin{aligned} & \frac{H_s^3}{L_s^3} \cdot \frac{\rho_s \cdot u_s \cdot H_s}{\mu} \cdot \rho^* \cdot \left( \frac{\partial w^*}{\partial t^*} + u^* \cdot \frac{\partial w^*}{\partial x^*} + v^* \cdot \frac{\partial w^*}{\partial y^*} + w^* \cdot \frac{\partial w^*}{\partial z^*} \right) = - \frac{H_s}{L_s} \cdot \frac{\rho_s \cdot H_s}{\mu \cdot u_s} \cdot \frac{\partial p^*}{\partial z^*} \\ & + \frac{H_s^4}{L_s^4} \cdot \frac{\partial^2 w^*}{\partial x^{*2}} + \frac{H_s^4}{L_s^4} \cdot \frac{\partial^2 w^*}{\partial y^{*2}} + \frac{H_s^2}{L_s^2} \cdot \frac{\partial^2 w^*}{\partial z^{*2}} + \frac{1}{3} \cdot \frac{H_s^2}{L_s^2} \cdot \left( \frac{\partial^2 u^*}{\partial x^* \cdot \partial z^*} + \frac{\partial^2 v^*}{\partial y^* \cdot \partial z^*} + \frac{\partial^2 w^*}{\partial z^{*2}} \right) + \frac{H_s}{L_s} \cdot \frac{\rho_s \cdot H_s^2}{\mu \cdot u_s} \cdot g_z \cdot \rho^* \end{aligned} \quad (\text{B.36})$$

At this point one can compare equations B.28, B.32 and B.36 with each other. From these it can be seen that equations B.28 and B.32 have identical coefficient groups. While equation B.36 is similar to these equations, some coefficient groups contain extra  $\frac{H_s}{L_s}$  terms.

### B.4.4. Dominant terms

In the previous sections the Navier-Stokes equations are nondimensionalized and simplified. In this section the characteristic scaling units and constants of equations B.28, B.32 and B.36 are evaluated. These equations contain four distinct groups, namely:

1.  $\frac{H_s}{L_s}$ , this is the ratio between the characteristic length in  $z$ -direction and characteristic length in  $x$ - or  $y$ -direction.
2.  $\frac{\rho_s \cdot u_s \cdot H_s}{\mu}$ , this dimensionless group is known as the Reynolds number which describes the ratio between inertial forces and viscous forces in the fluid.
3.  $\frac{p_s \cdot H_s}{\mu \cdot u_s}$ , note that this group is the Euler number multiplied by the Reynolds number (Eu·Re). The Euler number represents the ratio between the pressure forces and the inertial forces in the fluid.
4.  $\frac{\rho_s \cdot H_s^2}{\mu \cdot u_s} \cdot g_i$  (where  $i$  is  $x, y$  or  $z$ ), note that this group is the Reynolds number divided by the Froude number squared (Re/Fr<sup>2</sup>). The Froude number is the ratio between the inertial forces and the gravity forces in the fluid.

First discuss the constants  $\mu$  and  $g_i$ . As stated in assumption 8 from section 2.2, it is assumed that the fluid has a constant viscosity. For air this is valid assumption because the viscosity of air is only slightly dependent on temperature [28]. The viscosity of air is  $1.81 \cdot 10^{-5} \text{ kg}/(\text{m} \cdot \text{s})$ .

Furthermore, the gravity constant  $g_i$  has three components in  $x$ -,  $y$ - and  $z$ -direction. For the  $x$ - and  $y$ -direction the gravity is  $0 \text{ m/s}^2$ . Only in  $z$ -direction the gravity has a value of  $-9.81 \text{ m/s}^2$ .

Next discuss the characteristic scaling units  $H_s$ ,  $L_s$ ,  $\rho_s$ ,  $u_s$  and  $p_s$ . Here the  $H_s$  is the characteristic length in the  $z$ -direction. This represents the film thickness of the fluid. For typical air bearings this thickness is often in the order of  $5 \mu\text{m}$  to  $50 \mu\text{m}$  [28]. Throughout this thesis, values of the film thickness around  $10 \mu\text{m}$  or  $30 \mu\text{m}$  are most common.

The following variable is  $L_s$ , which represents the characteristic length of the fluid in  $x$ - or  $y$ -direction. This variable depends on the dimensions in  $x$ - or  $y$ -direction of the pocket or dam of an actuator cell. The smallest dimensions of the actuator design are in the order of around  $10 \text{ mm}$ .

Next is  $\rho_s$  which is the characteristic scaling of the density of the fluid. The density of air depends on the local pressure and temperature. As stated in assumption 7 from section 2.2, the temperature in the fluid is assumed not to change much. So the density only depends on the fluid pressure. In the final design the pressure in an actuator cell varies between 1 and 3 bar. Therefore the density in an actuator cell varies between  $1.225$  and  $3.675 \text{ kg/m}^3$ .

The following characteristic scaling unit is  $u_s$ , which is the fluid speed in  $x$ -direction. The fluid velocity is largest in the pocket during actuation when the pressure gradient is largest. The average velocity during actuation in the pocket is around  $138 \text{ m/s}$ .

Lastly, the characteristic scaling unit  $p_s$  represents the pressure in the fluid. As mentioned previously the pressure in the final design varies between 1 and 3 bar.

Now that the order of magnitudes of the characteristic scaling units and constants are known, the four distinct groups can be evaluated:

1.  $\frac{H_s}{L_s} \approx \frac{10^{-5}}{10^{-2}} = 10^{-3}$
2.  $\frac{\rho_s \cdot u_s \cdot H_s}{\mu} \approx \frac{10^0 \cdot 10^2 \cdot 10^{-5}}{10^{-5}} = 10^2$
3.  $\frac{p_s \cdot H_s}{\mu \cdot u_s} \approx \frac{10^5 \cdot 10^{-5}}{10^{-5} \cdot 10^2} = 10^3$
4.  $\frac{\rho_s \cdot H_s^2}{\mu \cdot u_s} \cdot g_z \approx \frac{10^0 \cdot (10^{-5})^2}{10^{-5} \cdot 10^2} \cdot 10^1 = 10^{-6}$

Finally with these groups known equations B.28, B.32 and B.36 can be filled in. These are shown in equations B.37, B.38 and B.39.

$$10^{-1} \cdot \rho^* \cdot \left( \frac{\partial u^*}{\partial t^*} + u^* \cdot \frac{\partial u^*}{\partial x^*} + v^* \cdot \frac{\partial u^*}{\partial y^*} + w^* \cdot \frac{\partial u^*}{\partial z^*} \right) = -10^0 \cdot \frac{\partial p^*}{\partial x^*} + \frac{\partial^2 u^*}{\partial z^{*2}} + 10^{-6} \cdot \left[ \frac{\partial^2 u^*}{\partial x^{*2}} + \frac{\partial^2 u^*}{\partial y^{*2}} + \frac{1}{3} \cdot \left( \frac{\partial^2 u^*}{\partial x^{*2}} + \frac{\partial^2 v^*}{\partial x^* \cdot \partial y^*} + \frac{\partial^2 w^*}{\partial x^* \cdot \partial z^*} \right) \right] + 0 \cdot \rho^* \quad (\text{B.37})$$

$$10^{-1} \cdot \rho^* \cdot \left( \frac{\partial v^*}{\partial t^*} + u^* \cdot \frac{\partial v^*}{\partial x^*} + v^* \cdot \frac{\partial v^*}{\partial y^*} + w^* \cdot \frac{\partial v^*}{\partial z^*} \right) = -10^0 \cdot \frac{\partial p^*}{\partial y^*} + \frac{\partial^2 v^*}{\partial z^{*2}} + 10^{-6} \cdot \left[ \frac{\partial^2 v^*}{\partial x^{*2}} + \frac{\partial^2 v^*}{\partial y^{*2}} + \frac{1}{3} \cdot \left( \frac{\partial^2 u^*}{\partial x^* \cdot \partial y^*} + \frac{\partial^2 v^*}{\partial y^{*2}} + \frac{\partial^2 w^*}{\partial y^* \cdot \partial z^*} \right) \right] + 0 \cdot \rho^* \quad (\text{B.38})$$

$$10^{-7} \cdot \rho^* \cdot \left( \frac{\partial w^*}{\partial t^*} + u^* \cdot \frac{\partial w^*}{\partial x^*} + v^* \cdot \frac{\partial w^*}{\partial y^*} + w^* \cdot \frac{\partial w^*}{\partial z^*} \right) = -10^0 \cdot \frac{\partial p^*}{\partial z^*} + 10^{-12} \cdot \frac{\partial^2 w^*}{\partial x^{*2}} + 10^{-12} \cdot \frac{\partial^2 w^*}{\partial y^{*2}} + 10^{-6} \cdot \frac{\partial^2 w^*}{\partial z^{*2}} + \frac{1}{3} \cdot 10^{-6} \cdot \left( \frac{\partial^2 u^*}{\partial x^* \cdot \partial z^*} + \frac{\partial^2 v^*}{\partial y^* \cdot \partial z^*} + \frac{\partial^2 w^*}{\partial z^{*2}} \right) + 10^{-9} \cdot \rho^* \quad (\text{B.39})$$

By neglecting terms smaller than unity, equations B.37, B.38 and B.39 become equations B.40, B.41 and B.42 respectively.

$$0 = -\frac{\partial p^*}{\partial x^*} + \frac{\partial^2 u^*}{\partial z^{*2}} \quad (\text{B.40})$$

$$0 = -\frac{\partial p^*}{\partial y^*} + \frac{\partial^2 v^*}{\partial z^{*2}} \quad (\text{B.41})$$

$$0 = -\frac{\partial p^*}{\partial z^*} \quad (\text{B.42})$$

In order to return to dimensional form, one can substitute the nondimensional quantities. Furthermore, from equations B.28 and B.32 one can choose  $p_s = \frac{L_s}{H_s} \cdot \frac{\mu \cdot u_s}{H_s}$ , such that the coefficient in front of the pressure gradient term is unity [1]. Lastly one can divide the equation by the term in front of the pressure gradient. These steps are shown in equations B.43, B.44 and B.45, resulting in the dimensional form of the dominant terms. This greatly reduces the complexity of the momentum equations. It also shows that pressure forces and viscous forces are the dominant driving forces in lubrication theory.

$$0 = -\frac{L_s}{p_s} \cdot \frac{\partial p}{\partial x} + \frac{H_s^2}{u_s} \cdot \frac{\partial^2 u}{\partial z^2} \Rightarrow 0 = -\frac{H_s^2}{\mu \cdot u_s} \cdot \frac{\partial p}{\partial x} + \frac{H_s^2}{u_s} \cdot \frac{\partial^2 u}{\partial z^2} \Rightarrow 0 = -\frac{\partial p}{\partial x} + \mu \cdot \frac{\partial^2 u}{\partial z^2} \quad (\text{B.43})$$

$$0 = -\frac{L_s}{p_s} \cdot \frac{\partial p}{\partial y} + \frac{H_s^2}{u_s} \cdot \frac{\partial^2 v}{\partial z^2} \Rightarrow 0 = -\frac{H_s^2}{\mu \cdot u_s} \cdot \frac{\partial p}{\partial y} + \frac{H_s^2}{u_s} \cdot \frac{\partial^2 v}{\partial z^2} \Rightarrow 0 = -\frac{\partial p}{\partial y} + \mu \cdot \frac{\partial^2 v}{\partial z^2} \quad (\text{B.44})$$

$$0 = -\frac{H_s}{p_s} \cdot \frac{\partial p}{\partial z} \Rightarrow 0 = -\frac{\partial p}{\partial z} \quad (\text{B.45})$$

## B.5. Reynolds equation

The simplified momentum equations and continuity equation can be combined into one equation named the 'Reynolds equation' shown in equation 2.1. First the momentum equations and continuity equation are integrated across a fluid film between two parallel surfaces in order to substitute the boundary conditions. By doing so, the results of the momentum equations and continuity equation can be substituted as will be shown.

### B.5.1. Integrating momentum equations

Equations B.43, B.44 and B.45 can be applied on a fluid film. As is shown in figure B.5 the fluid is between two parallel surfaces. In the model a right handed coordinate system is applied where to the right denotes the positive  $x$ -axis, into the paper the positive  $y$ -axis (not drawn) and up the positive  $z$ -axis. The distance between the two parallel surfaces is  $H_2 - H_1$ . Here  $H_1$  describes the vertical distance between surface 1 and the origin. While  $H_2$  describes the vertical distance between surface 2 and the origin. Lastly surface 1 has a velocity  $u_1$  in  $x$ -direction and a velocity  $v_1$  in  $y$ -direction. Whereas surface 2 has a velocity  $u_2$  in  $x$ -direction and a velocity  $v_2$  in  $y$ -direction.

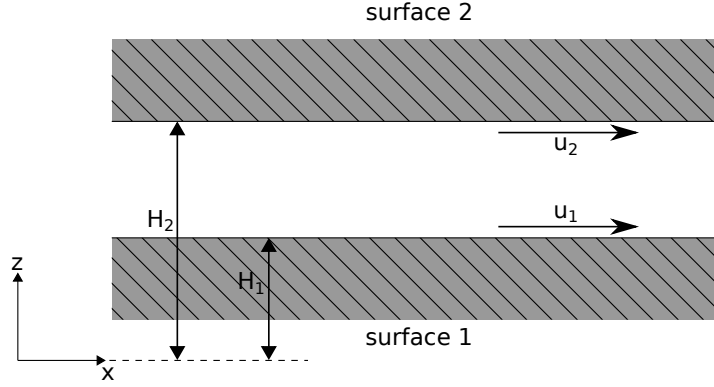


Figure B.5: Fluid film between two parallel surfaces.

Now with this model the boundary conditions of the velocities at the surfaces are specified which can be applied to the differential equation B.43, B.44 and B.45. Lets first begin with equation B.43 and integrate it twice with respect to  $z$ . By rearranging this results in equation B.46.

$$\mu \cdot u = \frac{1}{2} \cdot \frac{\partial p}{\partial x} \cdot z^2 + C_1 \cdot z + C_2 \quad (\text{B.46})$$

Here  $C_1$  and  $C_2$  are two integration constants. These constants can be solved by substituting the boundary conditions:  $u(H_1) = u_1$  and  $u(H_2) = u_2$ . Here 'no slip' assumptions are applied where the fluid and boundary surface have the same velocity at the interface. Substitution results in equation B.47.

$$C_1 = \frac{\mu \cdot u_2 - \frac{1}{2} \cdot \frac{\partial p}{\partial x} \cdot H_2^2 - C_2}{H_2} \quad (\text{B.47a})$$

$$C_2 = \mu \cdot u_1 - \frac{1}{2} \cdot \frac{\partial p}{\partial x} \cdot H_1^2 - C_1 \cdot H_1 \quad (\text{B.47b})$$

Now assume  $H_1 = 0$ , which states that the coordinate system coincides with surface 1. This simplifies the algebra. The results are shown in equation B.48.

$$C_1 = -\frac{1}{2} \cdot \frac{\partial p}{\partial x} \cdot H_2 + \frac{\mu \cdot (u_2 - u_1)}{H_2} \quad (\text{B.48a})$$

$$C_2 = \mu \cdot u_1 \quad (\text{B.48b})$$

Substituting equation B.48 in B.46 results in the total velocity profile in  $x$ -direction as is shown in equation B.49.

$$u = \frac{1}{2} \cdot \frac{1}{\mu} \cdot (z^2 - H_2 \cdot z) \cdot \frac{\partial p}{\partial x} + (u_2 - u_1) \cdot \frac{z}{H_2} + u_1 \quad (\text{B.49})$$

The same procedure can be used to find the velocity profile in  $y$ -direction. This can be obtained by integrating equation B.44 and using the boundary conditions  $v(H_1) = v_1$  and  $v(H_2) = v_2$ . The result is shown in equation B.50.

$$v = \frac{1}{2} \cdot \frac{1}{\mu} \cdot (z^2 - H_2 \cdot z) \cdot \frac{\partial p}{\partial y} + (v_2 - v_1) \cdot \frac{z}{H_2} + v_1 \quad (\text{B.50})$$

One can visualise the shape of the velocity profiles in  $x$ -direction by plotting equation B.49. This is shown in figure B.6 for four different cases. Figure B.6 (a) represents a flow where only a negative pressure gradient is present. This creates a flow with a parabolic velocity profile which is called a 'Poiseuille flow'. Whereas in figure B.6 (b) only the upper surface has a velocity in  $x$ -direction. This creates a linear velocity profile which is called a 'Couette flow'. Figures B.6 (c) and (d) show two combinations of Poiseuille and Couette flows.

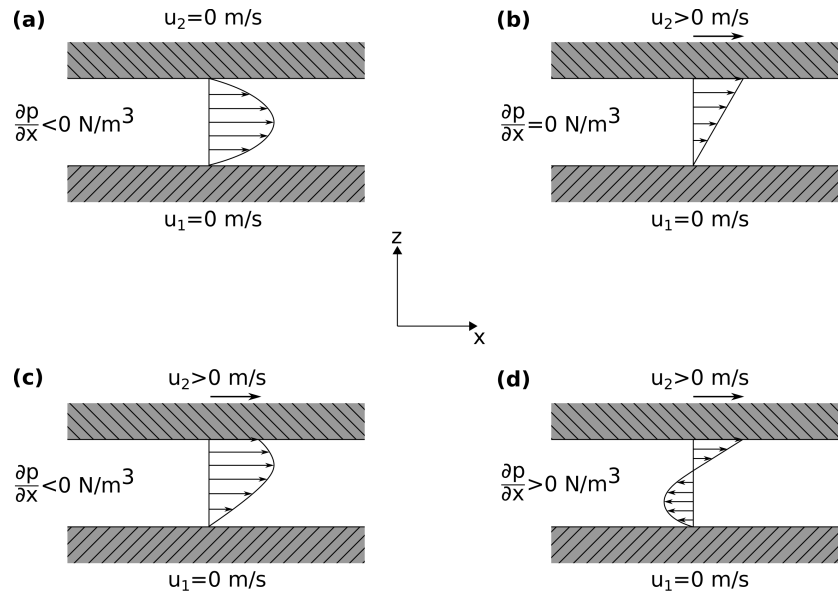


Figure B.6: Various flow cases between two parallel surfaces: (a)  $\frac{\partial p}{\partial x} < 0 \text{ N/m}^3$  and  $u_2 = 0 \text{ m/s}$  known as a Poiseuille flow, (b)  $\frac{\partial p}{\partial x} = 0 \text{ N/m}^3$  and  $u_2 > 0 \text{ m/s}$  known as a Couette flow, (c)  $\frac{\partial p}{\partial x} < 0 \text{ N/m}^3$  and  $u_2 > 0 \text{ m/s}$  and (d)  $\frac{\partial p}{\partial x} > 0 \text{ N/m}^3$  and  $u_2 > 0 \text{ m/s}$

Lastly, also equation B.45 can be integrated. This results in equation B.51. From equation B.51 it can be stated that the pressure is constant across the film height. Thus the pressure is not a function of  $z$ .

$$p(z) = \text{constant} \implies p = p(t, x, y) \quad (\text{B.51})$$

### B.5.2. Integrating continuity equation

As with integrating the momentum equations across the film height, one can also integrate the continuity equation across the film height. Yet again one can use the same terminology as is used in figure B.5. With this equation B.2 is integrated in  $z$ -direction between  $H_1$  and  $H_2$  as is shown in equation B.52.

$$\int_{H_1}^{H_2} \frac{\partial \rho}{\partial t} \cdot dz + \int_{H_1}^{H_2} \frac{\partial(\rho \cdot u)}{\partial x} \cdot dz + \int_{H_1}^{H_2} \frac{\partial(\rho \cdot v)}{\partial y} \cdot dz + \int_{H_1}^{H_2} \frac{\partial(\rho \cdot w)}{\partial z} \cdot dz = 0 \quad (\text{B.52})$$

Each partial derivative can be put out of the integral by using Leibniz's integral rule. This is shown in equation B.53.

$$\begin{aligned}
& \frac{\partial}{\partial t} \cdot \int_{H_1}^{H_2} \rho \cdot dz + \rho(t, H_1) \cdot \frac{\partial H_1}{\partial t} - \rho(t, H_2) \cdot \frac{\partial H_2}{\partial t} \\
& + \frac{\partial}{\partial x} \cdot \int_{H_1}^{H_2} \rho \cdot u \cdot dz + \rho(x, H_1) \cdot u(x, H_1) \cdot \frac{\partial H_1}{\partial x} - \rho(x, H_2) \cdot u(x, H_2) \cdot \frac{\partial H_2}{\partial x} \\
& + \frac{\partial}{\partial y} \cdot \int_{H_1}^{H_2} \rho \cdot v \cdot dz + \rho(y, H_1) \cdot v(y, H_1) \cdot \frac{\partial H_1}{\partial y} - \rho(y, H_2) \cdot v(y, H_2) \cdot \frac{\partial H_2}{\partial y} \\
& \quad + \int_{H_1}^{H_2} \frac{\partial(\rho \cdot w)}{\partial z} \cdot dz = 0
\end{aligned} \tag{B.53}$$

In section B.5.1 it was pointed out that the pressure in  $z$ -direction is constant ( $p = p(t, x, y)$ ). Thereby the pressure is not a function of  $z$ . Also note that the density can be expressed by pressure through the ideal gas law ( $\rho = \frac{p}{R_g \cdot T}$ ). Because temperature is assumed constant through the fluid, the density is a function of pressure only. Thus  $\rho = \rho(t, x, y)$  and  $\rho \neq \rho(z)$ . Applying this to equation B.53 and working out the integrals leads to equation B.54.

$$\begin{aligned}
& \frac{\partial(\rho \cdot (H_2 - H_1))}{\partial t} - \rho(t) \cdot \left[ \frac{\partial H_2}{\partial t} - \frac{\partial H_1}{\partial t} \right] \\
& + \frac{\partial(\rho \cdot q_{x,y})}{\partial x} - \rho(x) \cdot \left[ u(x, H_2) \cdot \frac{\partial H_2}{\partial x} - u(x, H_1) \cdot \frac{\partial H_1}{\partial x} \right] \\
& + \frac{\partial(\rho \cdot q_{y,x})}{\partial y} - \rho(y) \cdot \left[ v(y, H_2) \cdot \frac{\partial H_2}{\partial y} - v(y, H_1) \cdot \frac{\partial H_1}{\partial y} \right] \\
& \quad + \rho \cdot [w(H_2) - w(H_1)] = 0
\end{aligned} \tag{B.54}$$

Here  $q_{x,y} = \frac{\partial q_x}{\partial y}$ , where  $q_x = \int_{y_1}^{y_2} \int_{z_1}^{z_2} u(z) \cdot dz \cdot dy$  is the volume flow in  $x$ -direction. The same analogy can be used for the volume flow in  $y$ -direction ( $q_y$ ). Further, note that  $w = \frac{dz}{dt} = \frac{\partial z}{\partial t} + \frac{\partial x}{\partial t} \cdot \frac{\partial z}{\partial x} + \frac{\partial y}{\partial t} \cdot \frac{\partial z}{\partial y}$ . Filling this in equation B.54 gives equation B.55.

$$\begin{aligned}
& \frac{\partial(\rho \cdot (H_2 - H_1))}{\partial t} - \rho(t) \cdot \left[ \frac{\partial H_2}{\partial t} - \frac{\partial H_1}{\partial t} \right] \\
& + \frac{\partial(\rho \cdot q_{x,y})}{\partial x} - \rho(x) \cdot \left[ u(x, H_2) \cdot \frac{\partial H_2}{\partial x} - u(x, H_1) \cdot \frac{\partial H_1}{\partial x} \right] \\
& + \frac{\partial(\rho \cdot q_{y,x})}{\partial y} - \rho(y) \cdot \left[ v(y, H_2) \cdot \frac{\partial H_2}{\partial y} - v(y, H_1) \cdot \frac{\partial H_1}{\partial y} \right] \\
& + \rho \cdot \left[ \frac{\partial H_2}{\partial t} + u(H_2) \cdot \frac{\partial H_2}{\partial x} + v(H_2) \cdot \frac{\partial H_2}{\partial y} - \frac{\partial H_1}{\partial t} - u(H_1) \cdot \frac{\partial H_1}{\partial x} - v(H_1) \cdot \frac{\partial H_1}{\partial y} \right] = 0
\end{aligned} \tag{B.55}$$

Lastly equation B.55 can be simplified which results in equation B.56.

$$\frac{\partial(\rho \cdot (H_2 - H_1))}{\partial t} + \frac{\partial(\rho \cdot q_{x,y})}{\partial x} + \frac{\partial(\rho \cdot q_{y,x})}{\partial y} = 0 \tag{B.56}$$

Lets now stop and think about what we have just done. By integrating the mass continuity equation across the fluid film height, any derivative term of  $z$  has disappeared. Furthermore, each remaining term is integrated with respect to  $z$ , for  $z$  between  $H_1$  and  $H_2$ . An illustration is shown figure B.7. The vertical yellow line represents the film height over which is integrated at an arbitrary position in the fluid. A physical interpretation can be given for equation B.56. In words, the terms  $\frac{\partial(\rho \cdot q_{x,y})}{\partial x}$  and  $\frac{\partial(\rho \cdot q_{y,x})}{\partial y}$  in equation B.56 are the gradients of the mass flows per unit length in  $x$ - or  $y$ -direction respectively across the film height. The sum of these terms gives the net loss of the term  $\rho \cdot (H_2 - H_1)$  per unit time at each point of the fluid. For example if  $\frac{\partial(\rho \cdot q_{x,y})}{\partial x} + \frac{\partial(\rho \cdot q_{y,x})}{\partial y}$  is positive and the film height is hold constant, then the local density will decrease with time. The balance in equation B.56 must be satisfied at every point in the fluid film.

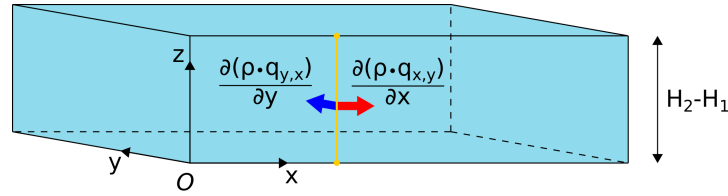


Figure B.7: Part of the fluid film with height  $H_2 - H_1$ . Here the red arrow indicates the gradient of the mass flow per unit length in  $x$ -direction. While, the blue arrow indicates the gradient of the mass flow per unit length in  $y$ -direction. Both mass flow gradients are across the fluid film height, indicated by a yellow line with length  $H_2 - H_1$ .

### B.5.3. Volume flow gradients

Equation B.56 can be further expressed by substituting the terms  $q_{x,y}$  and  $q_{y,x}$ . These gradients of the volume flows can be derived by integrating the velocity profiles from section B.5.1. By definition  $q_{x,y} = \int_{H_1}^{H_2} u(z) \cdot dz$ , is the flow of fluid in  $x$ -direction between  $H_1$  and  $H_2$  per unit length in  $y$ -direction. Has mentioned before, one can choose  $H_1 = 0$  for simplifying the algebra. Integrating the velocity profile of equation B.49 results in equation B.57.

$$\begin{aligned} q_{x,y} &= \int_0^{H_2} u(z) \cdot dz \\ &= \left[ \frac{1}{2} \cdot \frac{1}{\mu} \cdot \left( \frac{1}{3} \cdot z^3 - \frac{H_2}{2} \cdot z^2 \right) \cdot \frac{\partial p}{\partial x} + (u_2 - u_1) \cdot \frac{z^2}{2 \cdot H_2} + u_1 \cdot z \right]_0^{H_2} \\ &= -\frac{H_2^3}{12 \cdot \mu} \cdot \frac{\partial p}{\partial x} + \frac{u_1 + u_2}{2} \cdot H_2 \end{aligned} \quad (\text{B.57})$$

The same procedure can be used to find the  $q_{y,x}$ . This can be obtained by integrating equation B.50 with respect to  $z$ , for  $z$  between  $H_1 = 0$  and  $H_2$ . The result is show in equation B.58.

$$\begin{aligned} q_{y,x} &= \int_0^{H_2} v(z) \cdot dz \\ &= \left[ \frac{1}{2} \cdot \frac{1}{\mu} \cdot \left( \frac{1}{3} \cdot z^3 - \frac{H_2}{2} \cdot z^2 \right) \cdot \frac{\partial p}{\partial y} + (v_2 - v_1) \cdot \frac{z^2}{2 \cdot H_2} + v_1 \cdot z \right]_0^{H_2} \\ &= -\frac{H_2^3}{12 \cdot \mu} \cdot \frac{\partial p}{\partial y} + \frac{v_1 + v_2}{2} \cdot H_2 \end{aligned} \quad (\text{B.58})$$

### B.5.4. Substituting volume flow gradients

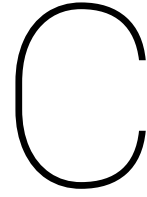
Finally, the terms  $q_{x,y}$  and  $q_{y,x}$  of equation B.56 can be substituted by equations B.57 and B.58. This is shown in equation B.59.

$$\frac{\partial(\rho \cdot (H_2 - H_1))}{\partial t} + \frac{\partial\left(\rho \cdot \left(-\frac{H_2^3}{12 \cdot \mu} \cdot \frac{\partial p}{\partial x} + (u_1 + u_2) \cdot \frac{H_2}{2}\right)\right)}{\partial x} + \frac{\partial\left(\rho \cdot \left(-\frac{H_2^3}{12 \cdot \mu} \cdot \frac{\partial p}{\partial y} + (v_1 + v_2) \cdot \frac{H_2}{2}\right)\right)}{\partial y} = 0 \quad (\text{B.59})$$

Lastly, equation B.59 can be rearranged and for terminology  $H_2 = h$  is used to describe the height of the fluid film. This results in equation 2.1.

$$\frac{\partial\left(\frac{\rho \cdot h^3}{12 \cdot \mu} \cdot \frac{\partial p}{\partial x}\right)}{\partial x} + \frac{\partial\left(\frac{\rho \cdot h^3}{12 \cdot \mu} \cdot \frac{\partial p}{\partial y}\right)}{\partial y} - \frac{\partial\left(\frac{\rho \cdot h \cdot (u_1 + u_2)}{2}\right)}{\partial x} - \frac{\partial\left(\frac{\rho \cdot h \cdot (v_1 + v_2)}{2}\right)}{\partial y} = \frac{\partial(\rho \cdot h)}{\partial t} \quad (2.1)$$

Equation 2.1 is called the 'Reynolds equation'. It was presented by Osborne Reynolds in 1886 to describe the pressure build up in self-acting bearings [28] [32].



## Additional design considerations

In this appendix additional design considerations are described in four different sections. First in section C.1 the design of the substrate is explained. Secondly in section C.2 is explained how the distance between the two manifolds is prescribed. In section C.3 the used sensors are described. Lastly, in section C.4 a numerical analysis is performed to validate the analytical analysis from chapter 3.

### C.1. Substrate

The substrate is the moving mass of the system that is desired to be actuated. The substrate consists of a web (also called foil or film) and a scale for the position sensor. The total mass of the substrate is 1.058 g. The design of the substrate is shown in figure C.1. The choices that are made for the web and scale are explained in subsections C.1.1 and C.1.2.

#### C.1.1. Web

The web is a carrier on which dies can be placed. Also, conducting material can be laminated on the web by the foil manufacturer. Through printing and etching antennas can be produced out of the conducting material which then allows it to receive radio-frequency signals. For these applications most common webs are made from PET (polyethylene terephthalate). The thickness of these webs range typically from 23  $\mu\text{m}$  to 100  $\mu\text{m}$  and typically have a width in the range of 40 mm to 400 mm. The laminated conducting material often consists of aluminium or copper with typically a thickness of about 10  $\mu\text{m}$  or 20  $\mu\text{m}$ .

To prove if it is possible to actuate a flexible substrate, a small piece of web is used for the demonstrator. The following four considerations are made:

1. The web has an uniform **thickness** of 36  $\mu\text{m}$  with a tolerance of  $\pm 2 \mu\text{m}$ . This is one of the thinnest webs used, which is beneficial for a low mass substrate. Furthermore, the low thickness tolerance ensures that the height of the air film beneath and above the web will only vary  $\pm 2 \mu\text{m}$  due to the web. Because of this small tolerance, no aluminium layer is laminated on the web.
2. It is chosen that the web has a **width** of 55.5 mm, so that two air film actuators and a position sensor can be placed next to each other.
3. A **length** of 210 mm for the web is selected so that the web can make a trajectory of 50 mm while the air film actuators are covered by the web at all time.
4. Finally, the web is made of PET with a density of 1420  $\text{kg}/\text{m}^3$ . Therefore the estimated **web mass** is 0.596 g.

#### C.1.2. Scale

In order to measure the position of the substrate a linear encoder from Renishaw is used (for more information see section C.3). For this sensor a (RGSZ20) scale is used to read out the relative position. This scale has a width of 6 mm and a thickness of 0.2 mm. It is supplied on a reel for 'cut-to-suit' convenience. Because the

substrate has to make a trajectory of 50 mm, the length of the scale is also 50 mm. When cut, the scale can be placed on the web by its adhesive backing tape. The scale is made from steel with a golden coating for protection. Taking a density of  $7700 \text{ kg/m}^3$  this results in a **scale mass** of 0.462 g. The **combined mass** of the web and the scale is 1.058 g. This is the moving mass that needs to be accelerated by the motion system. The scale is used for the proof of principle of the motion system, but for end use application a different solution is needed.

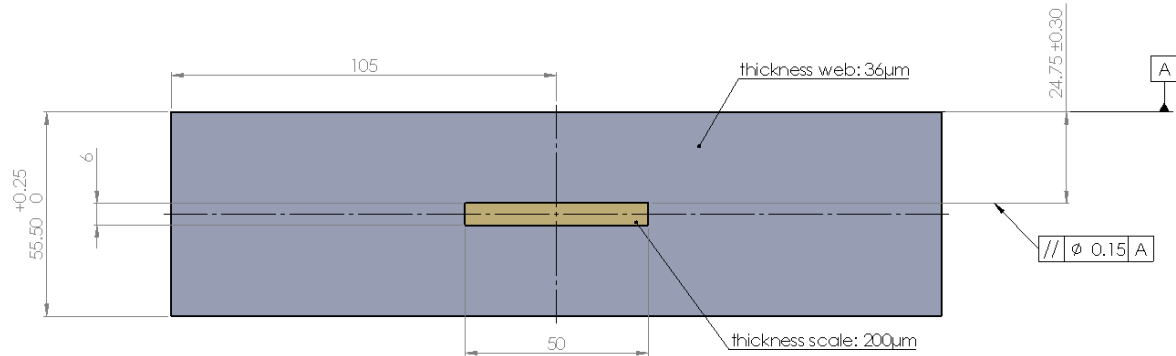


Figure C.1: Substrate design drawn in SOLIDWORKS 2016. Dimensions are in millimetres unless otherwise specified.

## C.2. Support structure

In the assembly the top manifold is placed on top of the bottom manifold. This is shown in figure C.2. Between the two manifolds is a substrate which can move freely in x-direction. In order to have a consistent performance of the actuator cells, the film height between the dams and the substrate should be uniform. Therefore it is desired to have parallel surfaces and a fixed distance between the two manifolds. In order to achieve this, the distance between the two manifolds should be prescribed. It is chosen to use two feeler gauges between the two manifold surfaces to adjust and fix the distance between the two manifolds. The placement of the two feeler gauges is shown in figure C.3. The biggest benefits for this solution is that it gives a precise defined distance between the two manifolds and it is easy to implement in the design.

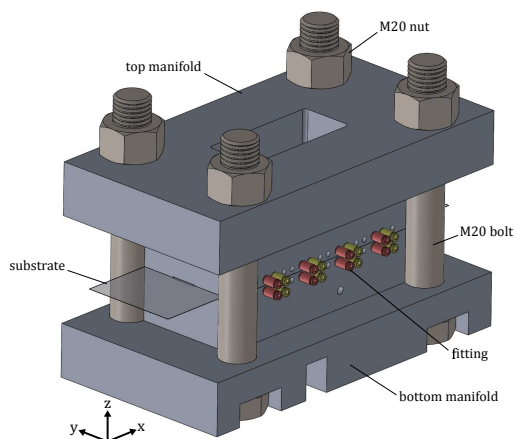


Figure C.2: Top manifold clamped on bottom manifold by four M20 bolts.

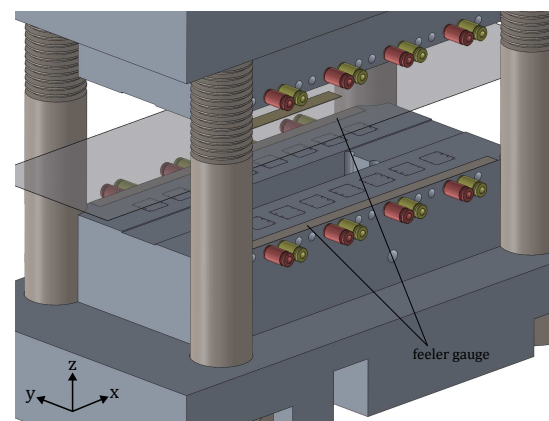


Figure C.3: Exploded view of figure C.2. Here one can see the placement of the two feeler gauges.

Because there is a gauge pressure between the substrate and the manifolds, a net vertical force is generated. This vertical force is directed downwards on the bottom manifold and directed upwards on the top manifold. During actuation the net vertical force on a manifold is 261 N (see section C.4). It is chosen to use four bolts

which have the additional function to guide the substrate. These bolts need to be at least 130 mm long to go through both manifolds. As mentioned before, the distance between the two manifolds should be as homogeneous as possible. That is why the bolts may not elongate more than  $0.2 \mu\text{m}$ . This condition also ensures that the elongation of the bolts is in the sub-micrometre range for load cases larger than 261 N. For steel bolts the minimum cross section for each bolt needs to be  $A_{\text{bolt}} = \frac{(F_{\text{p2}})/4 \cdot L_{\text{bolt}}}{d_{\text{bolt}} \cdot E_{\text{bolt}}} = \frac{(261)/4 \cdot 0.130}{0.2 \cdot 10^{-6} \cdot 200 \cdot 10^9} = 212 \text{ mm}^2$ . Rounded up, this is equivalent to a M20 bolt. The integration of the bolts in the design is shown in figure C.2. Note that not much pretension can be used by the bolts because the steel feeler gauges could damage the softer aluminium manifolds.

## C.3. Sensors

In this section the sensors in the design are described. In the design three different types of sensors are used: position sensor, pressure sensor and flow sensor.

### C.3.1. Position sensor

For measuring the position, the TONiC encoder system (T1000-10A) with a dual output interface (DOP0400A08A) from Renishaw<sup>1</sup> is selected. This encoder uses a (RGSZ20) scale to read out the relative position, as mentioned in section C.1.2. The readhead can measure with a speed up to 10 m/s and has a 50 nm resolution. The dimensions of the readhead are 35 x 13.5 x 10 mm. The readhead is placed in the bottom manifold, beneath the substrate. In order for the readhead to read out the scale on the substrate, the scale has to be within the specified tolerances with respect to the readhead. Special care should be taken for the tolerances in z-direction ( $\pm 0.15 \text{ mm}$ ) and yaw direction ( $\pm 0.4^\circ$ ), because these are the smallest tolerances. To meet the tolerance in z-direction any substrate vibrations should be minimized below an amplitude of 0.15 mm. For the tolerance in yaw direction the cutting of the substrate width and the placement of the scale should be done carefully. The tolerances for this are indicated in figure C.1.

### C.3.2. Pressure sensor

For measuring pressure  $p_1$  the PSE510 pressure sensor from SMC<sup>2</sup> is chosen. This sensor has an operating pressure range between 0 bar and 10 bar (gauge pressure) and a repeatability of  $\pm 0.03 \text{ bar}$ . The sensor is placed downstream the valve beneath the mounting block. The fitting to connect this pressure sensor is indicated in figure 3.26 by the magenta coloured fitting.

### C.3.3. Flow sensor

For measuring the flow through a single valve it is chosen to use a PFM725 flow sensor from SMC. This sensor has an operating pressure range between  $-0.7 \text{ bar}$  and  $7.5 \text{ bar}$  (gauge pressure), a flow range between 0 L/min and 25 L/min and a repeatability of less than  $\pm 0.75 \text{ L/min}$ . The flow sensor is located upstream a valve. The fitting to connect this flow sensor is indicated in figure 3.26 by the blue coloured fitting. Here it measures the flow of air through a single valve.

## C.4. Numerical analysis

To compare the analytical analysis, a numerical analysis is performed for the bottom manifold. The numerical analysis is implemented in COMSOL Multiphysics 5.4 with the general form PDE (Partial Differential Equation) package. With this, one can solve equation 2.1 numerically for the steady state pressure where  $\frac{\partial}{\partial t}(\rho \cdot h) = 0 \text{ kg}/(\text{s} \cdot \text{m}^2)$ . The geometry of the bottom manifold from section 3.4.3 is used. Furthermore, because the top manifold has an identical geometry as the bottom manifold, the pressure profile is mirrored across the substrate. So, when one determines the pressure profile for the bottom manifold, one also knows the pressure profile for the top manifold. The following boundary conditions are used, which are identical to the boundary conditions described in sections 3.4.1 and 3.6.1.

- The pressure at the inlet restrictors generating a force to the right is  $p_{2,R} = 3 \text{ bar}$ .
- The pressure at the inlet restrictors generating a force to the left is  $p_{2,L} = 1.5 \text{ bar}$ .

<sup>1</sup><https://www.renishaw.com>

<sup>2</sup><https://www.smc-pneumatics.com>

- The pressure at all outlet restrictors is  $p_3 = 1$  bar.
- The pressure of the outer perimeter of the dams is 1 bar.
- The film height between the dams and the substrate is  $10 \mu\text{m}$ .
- The film height between the pockets and the substrate is  $30 \mu\text{m}$ .
- The substrate has a velocity of  $1 \text{ m/s}$  in positive x-direction

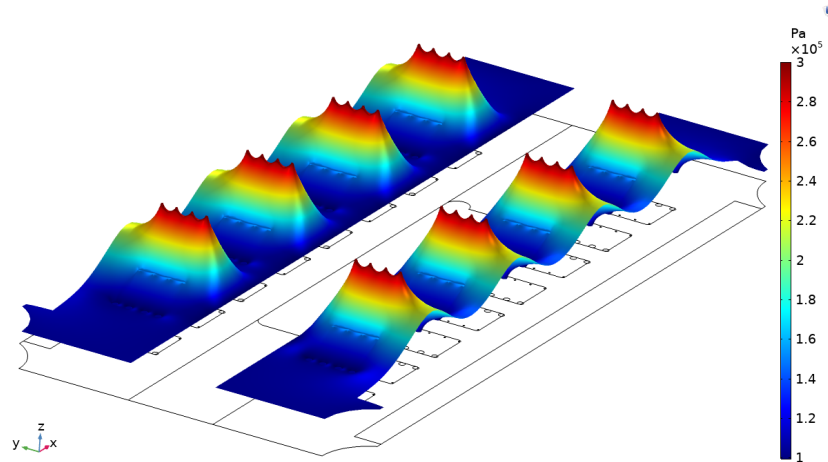


Figure C.4: Scalar field of the pressure on the bottom manifold during actuation in positive x-direction. Here  $p_{2,R} = 3$  bar,  $p_{2,L} = 1.5$  bar,  $p_3 = 1$  bar and  $h_d = 10 \mu\text{m}$ .

The resulting pressure profile for the bottom manifold is shown in figure C.4. With this, one can determine the performance when both manifolds are used to actuate the substrate. The results for the analytical analysis and numerical analysis are shown in table C.1. Here one can see that there is a good resemblance between the analytical and numerical results. Although there are some differences. These differences are mainly due to the fact that the numerical model embraces the exact geometry of the bottom manifold in contrast to the analytical model which consists of an approximation of the manifold geometry.

Table C.1: Comparison between analytical analysis and numerical analysis. Here the performances of the total system are shown when both manifolds are used.

	Analytical	Numerical	Description
$F_{fx}$	194 mN	171 mN	Total actuation force on substrate in x-direction
$F_{fy}$	0 mN	$8.97 \cdot 10^{-4}$ mN	Total actuation force on substrate in y-direction
$F_{fz}$	155 N	261 N	Net force in z-direction generated on a single manifold
$\dot{m}_{tot}$	$1.30 \cdot 10^{-3}$ kg/s	$1.27 \cdot 10^{-3}$ kg/s	Total mass flow of air
$q_{tot}$	63.7 L/min	62.2 L/min	Total volume flow of air
$k_z$	$9.31 \cdot 10^6$ N/m	$1.69 \cdot 10^7$ N/m	Total vertical stiffness applied on substrate
$\bar{k}_z$	$1.63 \cdot 10^9$ (N/m)/m <sup>2</sup>	$2.97 \cdot 10^9$ (N/m)/m <sup>2</sup>	Total vertical stiffness applied on substrate (per unit area)

To show more detail of the flow, a close up is taken of a single actuator cell. In figure C.5 the scalar field of the pressure is shown within one actuator cell. Here it can be seen that  $p_{2,R} = 3$  bar at the inlet gradually decreases

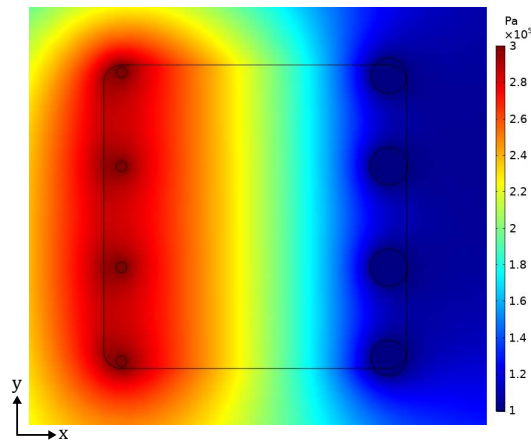


Figure C.5: Scalar field of the pressure at a single air film actuator cell. Here  $p_{2,R} = 3 \text{ bar}$ ,  $p_3 = 1 \text{ bar}$  and  $h_d = 10 \mu\text{m}$ .

to  $p_3 = 1 \text{ bar}$  at the outlet. Furthermore, in figure C.6 the scalar field of the average velocity of the air is shown. Here the arrows indicate the direction of the velocity. From this figure one can see that the majority of the flow in the pocket has a velocity around  $100 \text{ m/s}$ . Except near the inlet and outlet where the velocity is larger than  $343 \text{ m/s}$  (speed of sound). This contradicts with the orifice model of section 3.4.2 which stated that the sonic conditions are not reached. An explanation for this result is that the Reynolds equation only includes viscous effects and does not include inertial effects. This is one of the limitations of the Reynolds equation. Lastly in figure C.7 the scalar field of the Reynolds number is plotted. Figure C.7 shows that the majority of the flow in the pocket has a Reynolds number of around 450. This is similar to the Reynolds number of equation 3.14a, which has a value of 384. This indicates that viscous effects are dominant over the inertial effects. In the vicinity of the inlet the Reynolds number is over 1000 and near the outlet the Reynolds number is around 800. This indicates that inertial effects do play a significant role near the inlet and outlet. This confirms that the Reynolds equation gives realistic results in the majority of the actuator cell where the Reynolds number is small, but it does not give realistic results in the neighbourhood of the inlet and outlet restrictors where the Reynolds number is large.

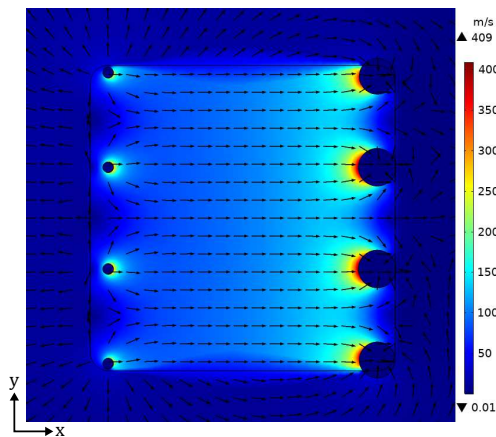


Figure C.6: Scalar field of the average velocity of the air flow. The arrows indicate the direction of the velocity. The air flow is observed at a single air film actuator cell. Here  $p_{2,R} = 3 \text{ bar}$ ,  $p_3 = 1 \text{ bar}$  and  $h_d = 10 \mu\text{m}$ .

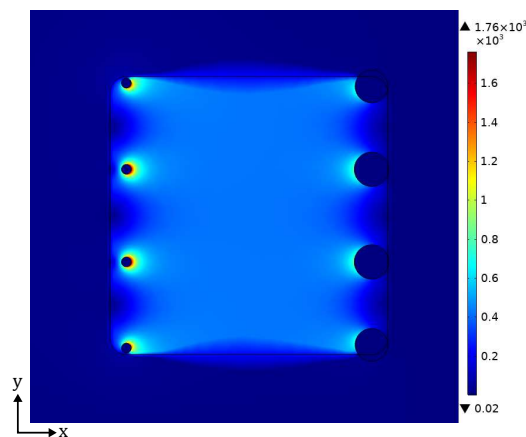


Figure C.7: Scalar field of the Reynolds number at a single air film actuator cell. Here  $p_{2,R} = 3 \text{ bar}$ ,  $p_3 = 1 \text{ bar}$  and  $h_d = 10 \mu\text{m}$ .



# D

## Realisation

In this appendix the realisation of the motion system is described. First in section D.1 an overview is given of the total design assembly. Secondly in section D.2 the manufacturing process and realisation of the manifolds is described. Lastly, in section D.3 the end result of the total motion system is shown.

### D.1. Overview design

Before discussing the manufacturing process of the manifolds, let us first show the total design. In figure D.1 an overview is given of the total design made in SOLIDWORKS 2016. The top manifold is placed on top of the bottom manifold with a substrate placed between them. The manifolds are separated from each other by two feeler gauges. Air can be supplied to the valves by the supply tubes (indicated in blue) which have an outer diameter of 4 mm. The valves are placed in aluminium mounting blocks which are placed on aluminium support structures.

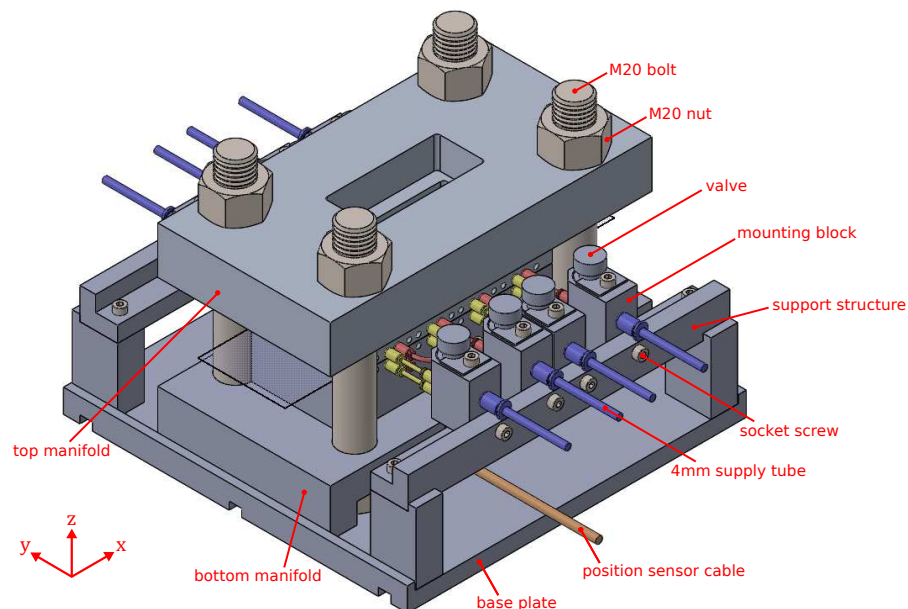


Figure D.1: Overview of the assembly of the total design.

In figure D.2 the exact same design is shown but now with the bolts and top manifold removed, to show the inner design. Each valve is connected to four actuator cells by connection tubes which have an outer diameter of 2 mm. The red tubes and fittings indicate the flow lines which are connected to actuator cells that generate an actuation force in positive x-direction (right). The yellow tubes and fittings indicate the flow lines which

are connected to actuator cells that generate an actuation force in negative x-direction (left). The net force generated by the actuator cells translates the substrate in x-direction.

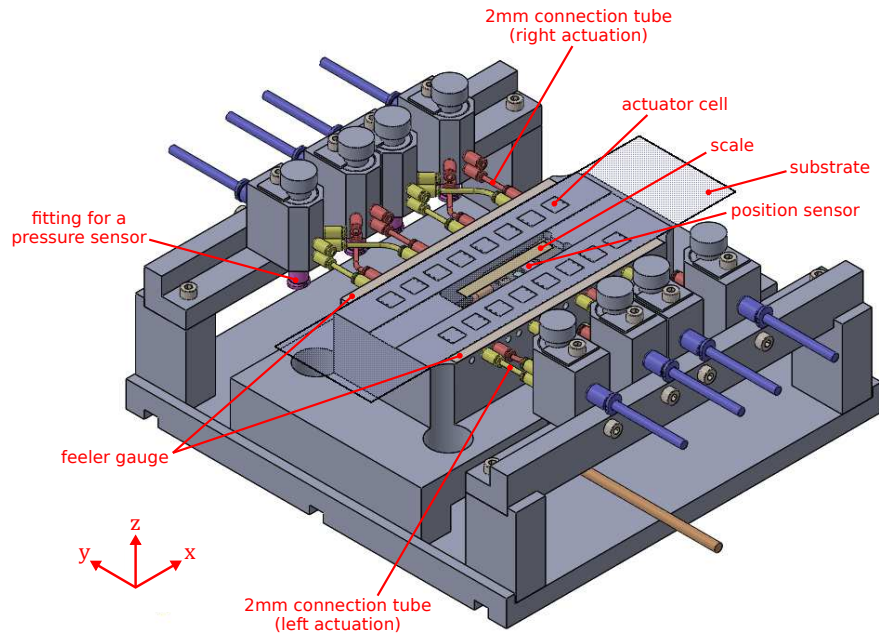


Figure D.2: Overview of assembly of the total design with the top manifold and bolts removed.

## D.2. Production of the manifolds

In this section the manufacturing process of top manifold and bottom manifold are described. As has been encountered in the work of Snieder [25], after the production process the bearing surface (manifold surface containing the dams) may contain significant curvatures. These curvatures can be formed during the manufacturing process, by stacking different plates and by gluing different layers. These curvatures cause height differences along the bearing surface. Snieder encountered curvatures that induced peak to peak height differences ranging from  $30\ \mu\text{m}$  to  $110\ \mu\text{m}$ , depending on the measurement line and assembly configuration. In order to place two manifolds on top of each other, it is essential that the flatness of the bearing surface of each manifold is well defined. Otherwise the air film thickness could vary significantly. An illustration of the influence of curvatures in the manifolds is given in figure D.3, in contrast to manifolds without curvatures shown in figure D.4. The increase in film thickness could reduce the performance of the actuator cells resulting in an increase of air flow, a reduction of the pressure and a reduction of the bearing stiffness. In order to limit the curvatures in the bearing surfaces, it is chosen to produce each manifold as a single part.

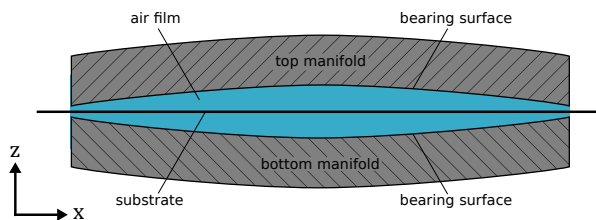


Figure D.3: Both top manifold and bottom manifold contain a curved bearing surface. This increases the air film thickness at different locations, which decrease the performance of individual actuator cells.

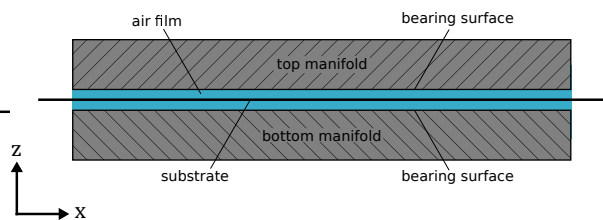


Figure D.4: Both top manifold and bottom manifold contain a flat bearing surface. This provides a homogeneous thickness of the air film over the whole bearing surface, which results in predictable and optimal performance of the actuator cells.

### Manufacturing process

In order to produce each manifold as a single part a suitable manufacturing process should be selected. Therefore the following three manufacturing processes are discussed:

### 1. Chemical Etching

Chemical etching is a material process in which a workpiece is covered by a mask and is exposed to a chemical aggressive fluid. The areas of the workpiece that are not covered by the mask are dissolved with a specified rate. With this the workpiece is uniformly processed at different exposed areas. In previous work (Snieder [25] and Wesselingh [31]) it has been seen that this technique is a possible solution for creating the bearing surface on a thin plate. Although creating a flat surface in the assembly has been challenging. Also for creating the inlets and outlets a different technique is necessary (for example: drilling with a bore, drilling with a laser or using tubes with predefined inner diameters).

### 2. Electroforming

Electroforming is an additive manufacturing process in which a workpiece is covered by a non-conductive mask and is inserted in a bath. An electrical current dissolves a desired metal (often copper, chrome, nickel, cadmium or zinc) at the anode. The metal galvanically bonds at the conductive areas of the workpiece at the cathode. This technique has seen promising results in previous work (Wesselingh [31]) on thin plates as it does not induce internal stresses. Although this technique becomes more challenging to work with on thick objects. Also for creating the inlets and outlets a different technique is necessary.

### 3. Electrical Discharge Machining (EDM)

EDM is a manufacturing technique in which an electrical voltage is applied between a workpiece and an electrode. With this, small sparks are generated that melt small bits of material of the workpiece. With this material process it is possible to mill the pockets and drill the inlets and outlets. In previous work (Wesselingh [31]) this technique has been applied on thin plates with poor results due to internal stresses which bend the plates (see figure D.5). But because the object is not a thin plate but a thick object, these internal stresses no longer result in a bended object.

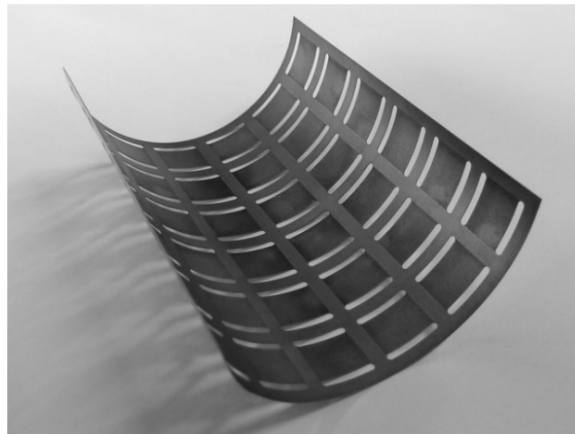


Figure D.5: Wesselingh experimented with EDM on a thin steel plate. Because material is only removed on one side, internal stress in the steel plate caused it to bend. The writer wants to emphasise that such curvatures may occur when working with thin plates, but not necessary when working with stiff objects.

It is chosen to use EDM to manufacture the pockets, inlets and outlets of the manifolds for three main reasons. The first reason is that a manifold can be produced from a single part. This prevents the bearing surface of having significant curvatures compared to bearing surfaces produced on a thin plate as encountered in previous work. The second reason is that the pockets can be produced with a tolerance a few micrometres. With these tight tolerances the flow resistances of the pockets can be predicted accurately. The third reason is that with EDM one can also drill the inlets and outlets with small tolerances. With these the flow resistances of the holes can be predicted accurately.

The manufacturing of the manifolds using EDM was in collaboration with Ter Hoek<sup>1</sup>. The tolerances of the manifolds were chosen such that the bearing surface has a tolerance of a few micrometres. The flatness toler-

<sup>1</sup><https://terhoek.com>

ance of the bearing surface was chosen to be  $3\ \mu\text{m}$  with a surface roughness of  $R_a = 0.3\ \mu\text{m}$  which are achieved with mirror milling. The pockets in the bearing surface were chosen to have a depth of  $20\ \mu\text{m}$  with a tolerance of  $\pm 1.5\ \mu\text{m}$  and manufactured by micro EDM milling. With these tolerances the maximum possible variation of the film thickness on one side of the substrate is  $\pm 4.5\ \mu\text{m}$ . In case of  $h_d = 17\ \mu\text{m}$ , this results in a maximum variation of the flow resistance of around  $\pm 40\%$  in the pocket. The inlets were chosen with a diameter of  $300\ \mu\text{m} \pm 15\ \mu\text{m}$  and the outlets with a diameter of  $500\ \mu\text{m} \pm 50\ \mu\text{m}$ . These holes were manufactured by hole-drilling EDM. The chosen material for the manifolds was aluminium, because it is easier to manufacture than steel and it gives protection against oxidation.

To check the manufactured manifold an image is taken of a single actuator cell in the bottom manifold, as is shown in figure D.6. The image is produced with a digital microscope. A detailed representation of the inlet in the bottom left corner of the pocket is shown in figure D.7. The measured diameter of the inlet is  $306\ \mu\text{m}$ , well within the specified tolerance of  $\pm 15\ \mu\text{m}$ . A similar image is made for the outlet in the bottom right corner of the pocket, as is shown in figure D.8. The measured diameter of the outlet is  $536\ \mu\text{m}$ , well within the specified tolerance of  $\pm 50\ \mu\text{m}$ .

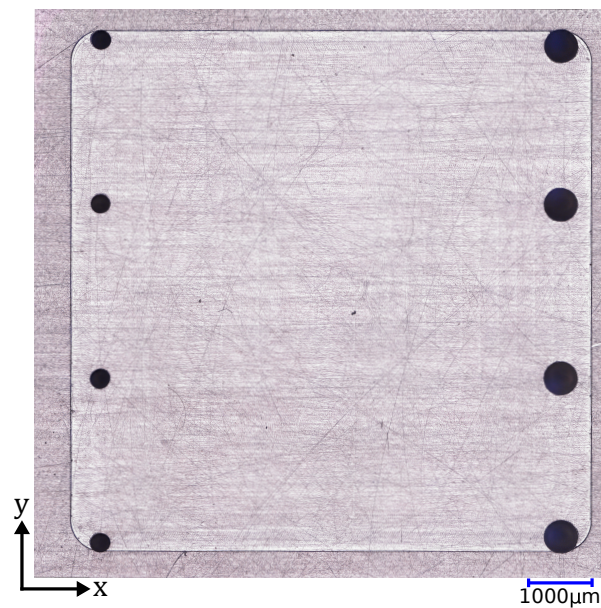


Figure D.6: Image of a single actuator cell made with a digital microscope.

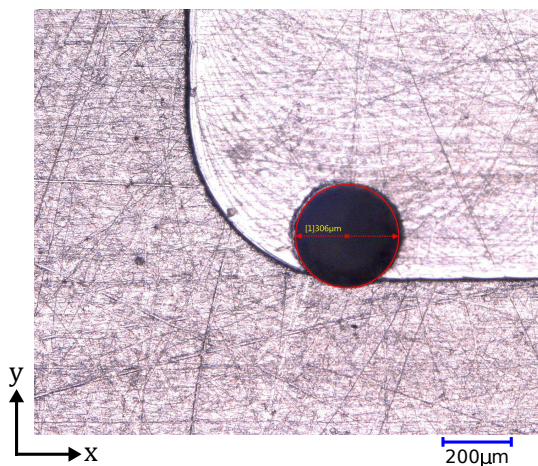


Figure D.7: Detailed view of the inlet in the left down corner of the pocket. The inlet has a diameter of  $306\ \mu\text{m}$ .

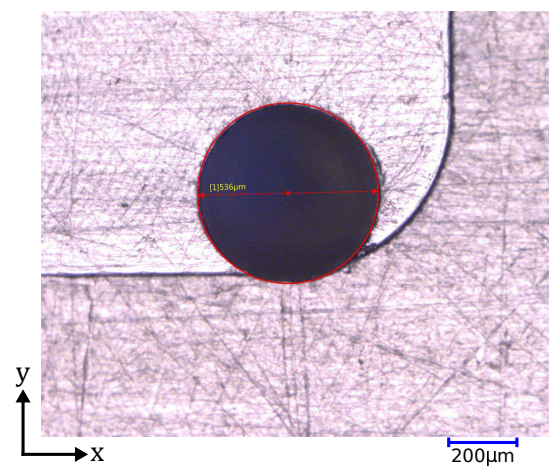


Figure D.8: Detailed view of the outlet in the right down corner of the pocket. The outlet has a diameter of  $536\ \mu\text{m}$ .

### Enlargement of the outlets

During the initial experiments it was noticeable that the substrate was vibrating. To reduce the amplitude of the vibrations it was chosen to increase the vertical stiffness. One way to increase the vertical stiffness is to enlarge the outlets. Therefore it was chosen to drill the outlets from 0.5 mm to 1.0 mm. All 64 outlets were enlarged manually with a 1.0 mm bore. An example of an enlarged outlet is shown in figure D.9. The red encirclements indicate areas where the edge of the hole contains some burrs. Most burrs can be removed by polishing the holes. Such a result is shown in figure D.10. The experiments described in this thesis were performed with both manifolds containing outlets with a diameter of 1.0 mm. A top view of the bottom manifold is shown in figure D.11 with the inlets having a diameter of 0.3 mm and the outlets having a diameter of 1.0 mm.

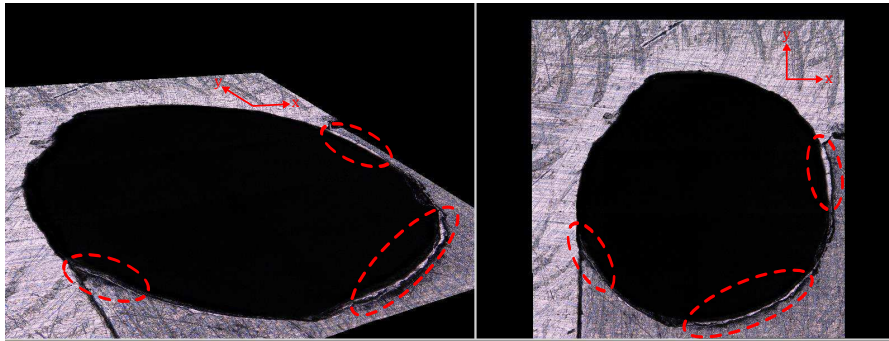


Figure D.9: Outlet diameter enlarged to 1.0 mm performed manually with a bore. The red encirclements indicate areas where the edge of the hole contains some burrs due to the drilling process.

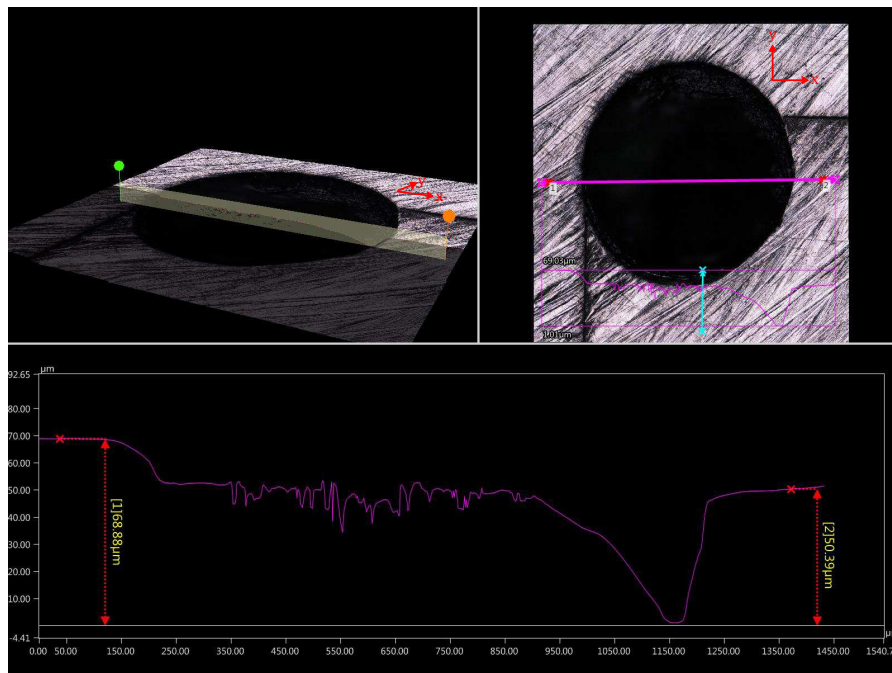


Figure D.10: Polished outlet with most burrs removed. The height difference between point 1 and point 2 is 18.49  $\mu\text{m}$ .

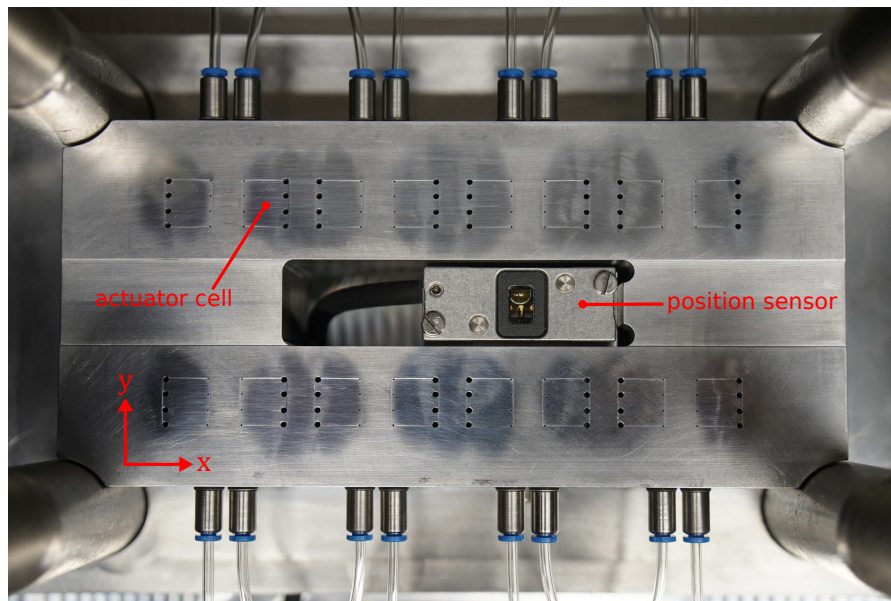


Figure D.11: Top view of the bottom manifold with all outlets enlarged to 1.0 mm.

### D.3. End result

Now that the manifolds are produced, one can put together the different components. The total assembly is shown in figure D.12. The base plate, the two support structures and the eight mounting blocks are made of aluminium and manufactured by CNC milling. Figure D.12 is comparable to the drawing in figure D.1. This is also the configuration used in experiment 3 of section 4.3. In figure D.13 the top manifold and support structures are disassembled to show the components between the two manifolds. Figure D.13 is comparable to the drawing in figure D.2.

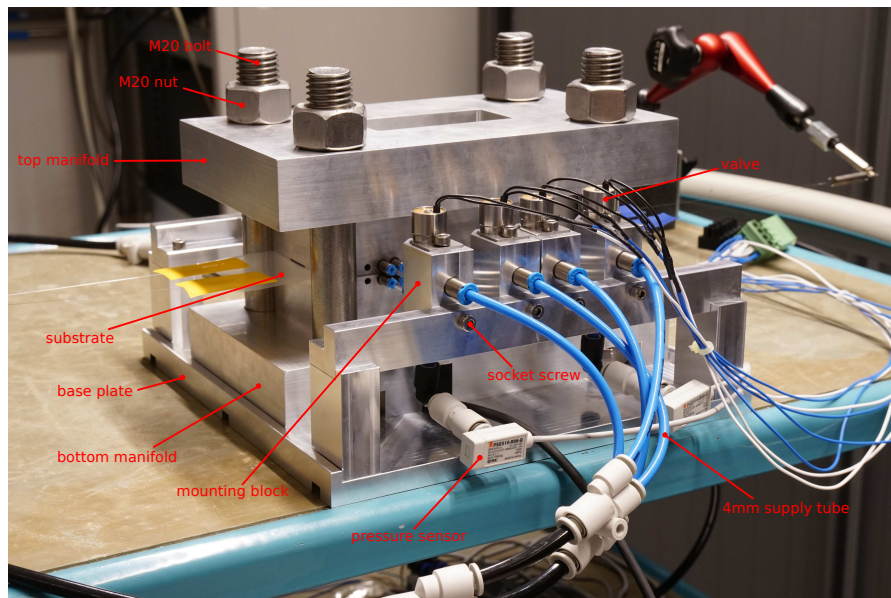


Figure D.12: Overview of total motion system.

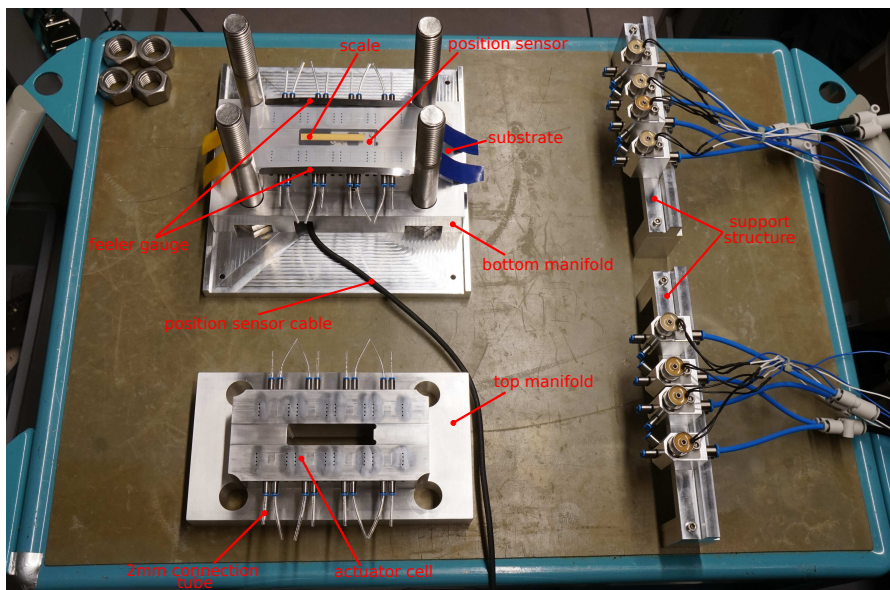
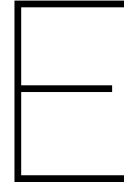


Figure D.13: Overview of total motion system with top manifold and support structures removed.





# Measurement results for different film thicknesses

This appendix contains additional results for experiment 2 of section 4.2. Measurements were also performed at a film height of  $12\ \mu\text{m}$  and  $22\ \mu\text{m}$  which are shown in sections E.1 and E.2 respectively.

## E.1. Results with $h_d = 12\ \mu\text{m}$

In this section the same measurements were performed as in section 4.2. Except instead of  $h_d = 17\ \mu\text{m}$  as was shown in figures 4.7 to 4.12 the film height is now  $h_d = 12\ \mu\text{m}$  with the results shown in figures E.1 to E.6. The consequence of a smaller film height is that the flow passage for the orifice restrictors decreases, as  $A_{\text{ori}}$  scales linearly with  $h_d$ . This increases the flow resistance of the orifice restrictors. Also the flow resistance of the air film increases, as  $R_f$  scales by  $h_d^3$ . With this the flow  $q_{\text{ori}}$  reduces and  $p_2$  increases. That is why the flow in figure E.4 is smaller than in figure 4.10 for similar values of  $p_1$ . This also explains why the actuation force in figure E.5 is larger than in figure 4.11, because  $p_2$  has increased for similar values of  $p_1$ . Finally, the least amount of friction was experienced at  $h_d = 17\ \mu\text{m}$ , therefore it was decided to use  $h_d = 17\ \mu\text{m}$  instead of  $h_d = 12\ \mu\text{m}$  for the measurements in section 4.3.

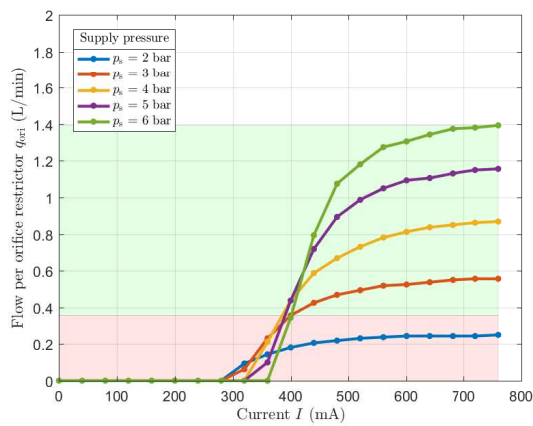


Figure E.1: Measurement results of flow  $q_{\text{ori}}$  as function of current  $I$  for different supply pressures. Here  $h_d = 12\ \mu\text{m}$ .

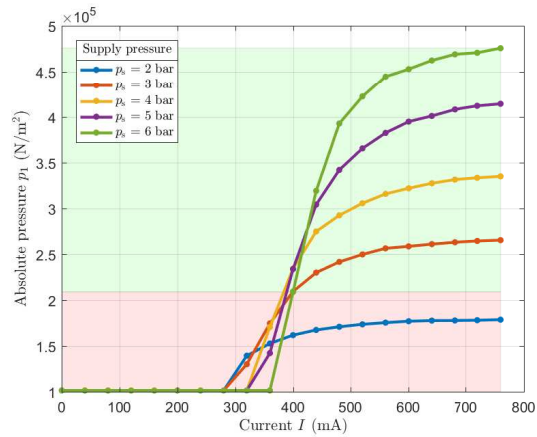


Figure E.2: Measurement results of pressure  $p_1$  as function of current  $I$  for different supply pressures. Here  $h_d = 12\ \mu\text{m}$ .

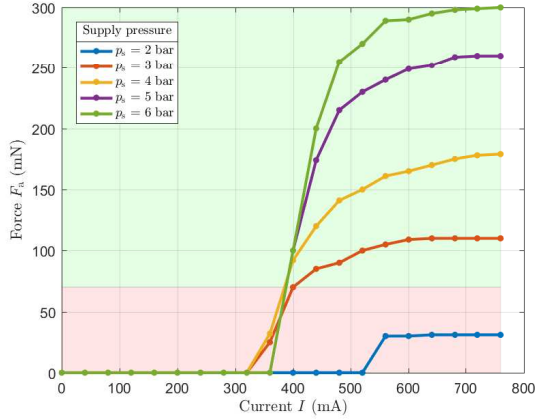


Figure E.3: Measurement results of actuation force  $F_a$  as function of current  $I$  for different supply pressures. Here  $h_d = 12\mu\text{m}$ .

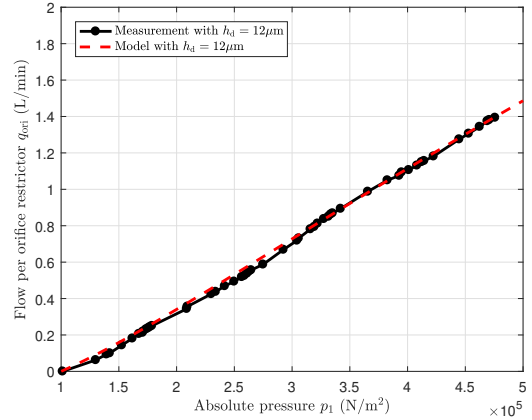


Figure E.4: Comparison between measurement results and numerical model of flow  $q_{ori}$  as function of pressure  $p_1$ .

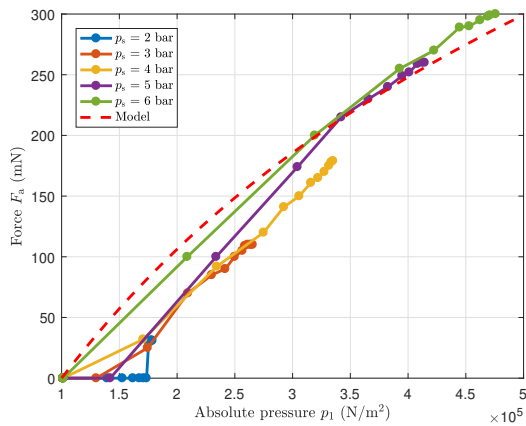


Figure E.5: Comparison between measurement results and numerical model of actuation force  $F_a$  as function of pressure  $p_1$ .

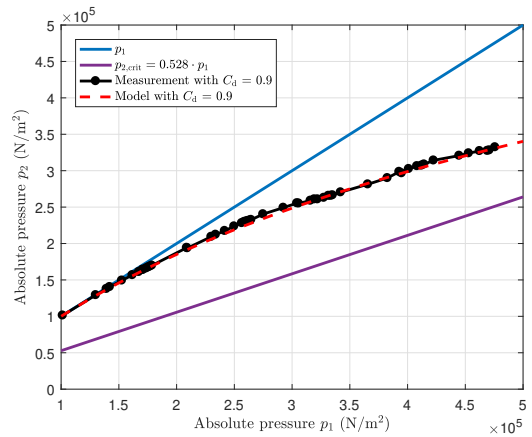


Figure E.6: Pressure  $p_2$  as function of  $p_1$  determined with the orifice restrictor model. For comparison  $p_2$  is determined with either the use of the measurement data or the numerical data. In both situations is assumed that  $C_d = 0.9$ .

### E.2. Results with $h_d = 22\mu\text{m}$

In this section the same measurements were performed as in section 4.2. Except instead of  $h_d = 17\mu\text{m}$ , as was shown in figures 4.7 to 4.12, the film height is now  $h_d = 22\mu\text{m}$  with the results shown in figures E.7 to E.12. The consequence of a larger film height is that the flow passage for the orifice restrictors increases, as  $A_{\text{ori}}$  scales linearly with  $h_d$ . This decreases the flow resistance of the orifice restrictors. Also the flow resistance of the air film decreases, as  $R_f$  scales by  $h_d^3$ . With this the flow  $q_{\text{ori}}$  increases and  $p_2$  decreases. That is why the flow in figure E.10 is larger than in figure 4.10 for similar values of  $p_1$ . This also explains why the actuation force in figure E.11 is smaller than in figure 4.11, because  $p_2$  has decreased for similar values of  $p_1$ . Finally, the least amount of friction was experienced at  $h_d = 17\mu\text{m}$ , therefore it was decided to use  $h_d = 17\mu\text{m}$  instead of  $h_d = 22\mu\text{m}$  for the measurements in section 4.3.

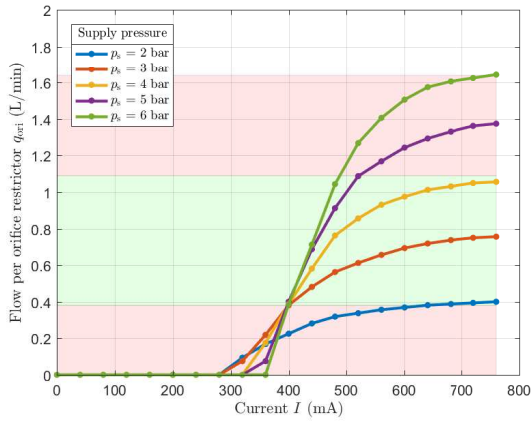


Figure E.7: Measurement results of flow  $q_{\text{ori}}$  as function of current  $I$  for different supply pressures. Here  $h_d = 22\mu\text{m}$ .

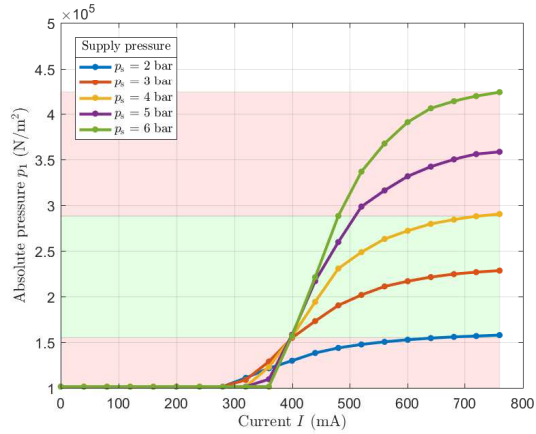


Figure E.8: Measurement results of pressure  $p_1$  as function of current  $I$  for different supply pressures. Here  $h_d = 22\mu\text{m}$ .

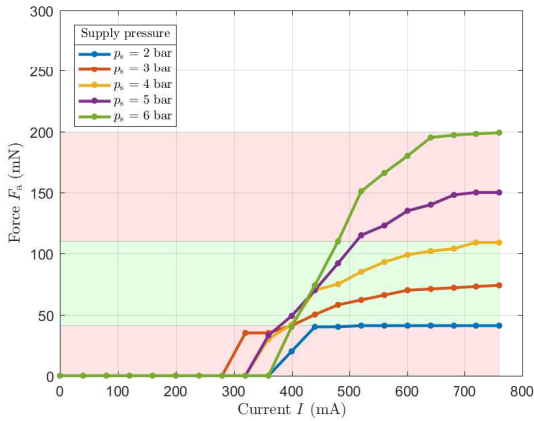


Figure E.9: Measurement results of actuation force  $F_a$  as function of current  $I$  for different supply pressures. Here  $h_d = 22\mu\text{m}$ .

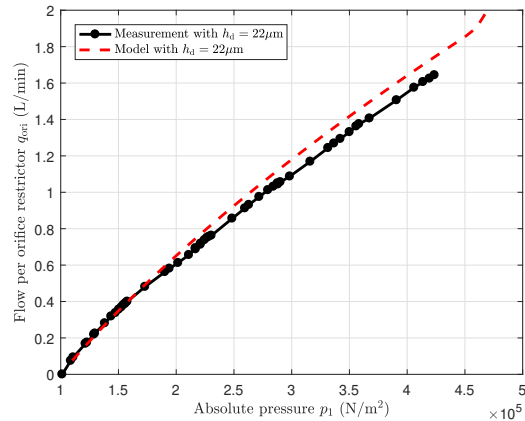


Figure E.10: Comparison between measurement results and numerical model of flow  $q_{\text{ori}}$  as function of pressure  $p_1$ .

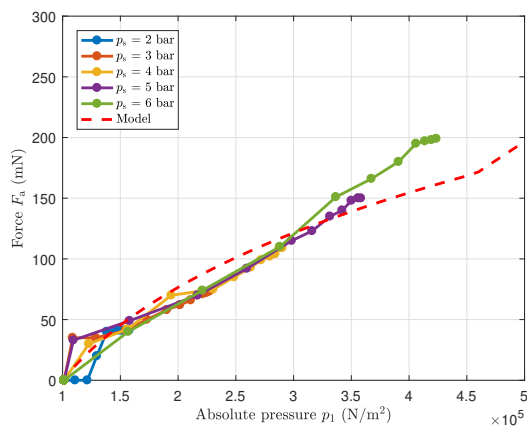


Figure E.11: Comparison between measurement results and numerical model of actuation force  $F_a$  as function of pressure  $p_1$ .

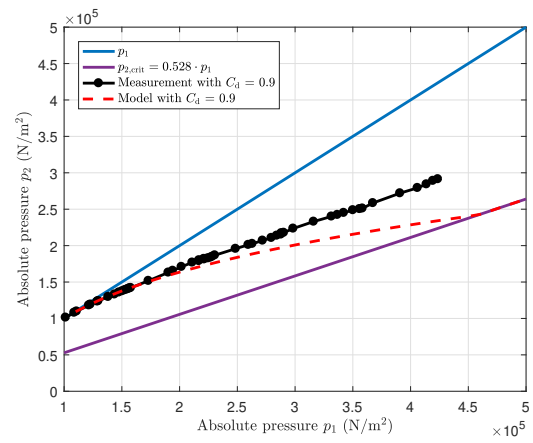
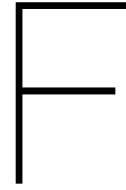


Figure E.12: Pressure  $p_2$  as function of  $p_1$  determined with the orifice restrictor model. For comparison  $p_2$  is determined with either the use of the measurement data or the numerical data. In both situations is assumed that  $C_d = 0.9$ .



# Step responses during pressure rise and pressure fall

This appendix contains additional graphs for experiment 3 of section 4.3. In section 4.3 the pressure was observed in the interval  $3.0\text{ s} \leq t \leq 3.2\text{ s}$ , because this showed the rise time behaviour when the substrate was actuated in positive x-direction. In this appendix the pressure rise and pressure fall at different intervals are observed. With this the rise time and fall time characteristics can be determined when actuating in positive or negative x-direction. The pressure rise of  $p_{1,L}$ , the pressure fall of  $p_{1,R}$  and the pressure fall of  $p_{1,L}$  are shown in sections F.1, F.2 and F.3 respectively.

## F.1. Pressure rise of $p_{1,L}$

In this section the same measurement results are used as in section 4.3. Except in this section the pressure rise of  $p_{1,L}$  in the interval  $3.5\text{ s} \leq t \leq 3.7\text{ s}$  is observed. During this interval a step signal is given to the valves generating a force in negative x-direction. This interval is shown by the green areas in figure F.1. The same models are used as in section 4.3, but now with slightly different values for the parameters which are shown in table F.1. By comparing table F.1 with table 4.1 from section 4.3, one can see that the value of  $\Delta F_a$  has reduced from 96.5 mN to 86.7 mN and  $c_{\text{unmod}}$  has reduced from  $750 \cdot 10^{-3}\text{ N/(m/s)}$  to  $600 \cdot 10^{-3}\text{ N/(m/s)}$ . The other parameters remained the same.

Table F.1: Used values of the parameters for describing the response of the plant when pressure  $p_{1,L}$  is rising.

Parameter	$\Delta F_a$	$\tau_{\text{delay}}$	$\tau_{\text{RC}}$	$m_{\text{sub}}$	$m_{\text{add}}$
Value	86.7 mN	0.375 ms	1.80 ms	1.005 g	1.635 g

Parameter	$c_{\text{visc}}$	$c_{\text{spring}}$	$c_{\text{unmod}}$	$k_1$	$k_2$
Value	$10.7 \cdot 10^{-3}\text{ N/(m/s)}$	$54.0 \cdot 10^{-3}\text{ N/(m/s)}$	$600 \cdot 10^{-3}\text{ N/(m/s)}$	13.8 N/m	13.8 N/m

In figure F.2 pressures  $p_{1,R}$  and  $p_{1,L}$  are shown as function of time. Here it can be seen that  $p_{1,L}$  has a pressure of around 2.40 bar at  $t = 3.5\text{ s}$  and a pressure of around 3.71 bar at  $t = 3.7\text{ s}$ . Furthermore,  $p_{1,R}$  has a pressure of around 2.33 bar at  $t = 3.5\text{ s}$  and a pressure of around 2.37 bar at  $t = 3.7\text{ s}$ . Both  $p_{1,R}$  and  $p_{1,L}$  can again be approximated by first order models as is shown in figure F.2. The force generated by these pressures are shown in figure F.3. In this case the net force is negative, because the substrate is actuated in negative x-direction. Although the magnitude of the actuation force is slightly lower, compared to figure 4.17,  $\tau_{\text{delay}}$  and  $\tau_{\text{RC}}$  remain the same. Also  $c_{\text{unmod}}$  is slightly lower, which indicates that this parameter is varying under different working conditions. The position of the substrate is shown in figure F.4. Here it can be seen that the substrate is moving in negative x-direction as expected, with a displacement of about 3.22 mm. In figure F.4 it can be seen that the model shows a small mismatch between the measurement and the model in the interval  $3.55\text{ s} \leq t \leq 3.60\text{ s}$ , but overall the graphs show good resemblance. Finally, the open-loop responses for the plant in combinations with controllers are shown in figure F.5. Here the green circles indicate the unity-gain

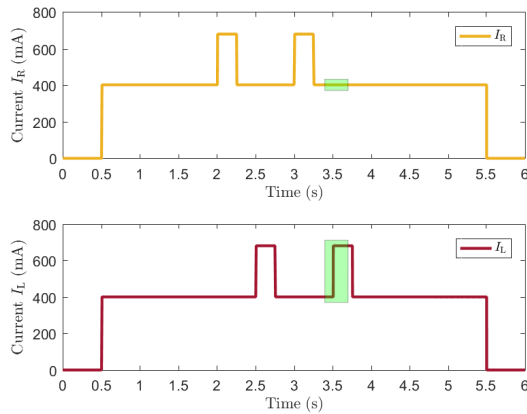


Figure E1: Signals  $I_R$  and  $I_L$  are the currents provided to the valves generating a force in positive and negative  $x$ -direction respectively. The green areas indicate the time interval  $3.5\text{ s} \leq t \leq 3.7\text{ s}$ .

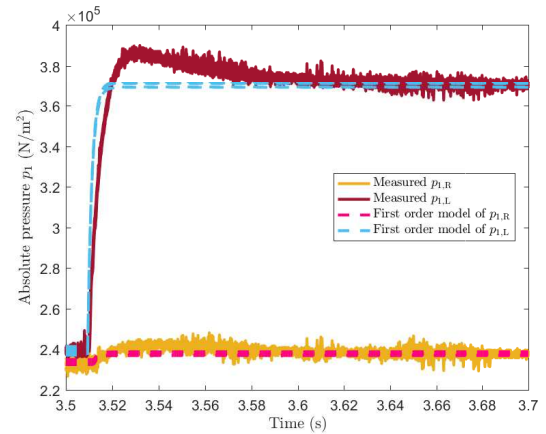


Figure E2: Pressures  $p_{1,R}$  and  $p_{1,L}$  measured by the pressure sensors. The results are shown for 10 measurements. The measured pressures are also approximated by a first order model.

cross-over frequency with a phase margin of  $35^\circ$ . For  $C_1 \cdot G_1$ ,  $C_2 \cdot G_2$  and  $C_3 \cdot G_3$  these are respectively 125.8 Hz, 168.6 Hz and 87.0 Hz.

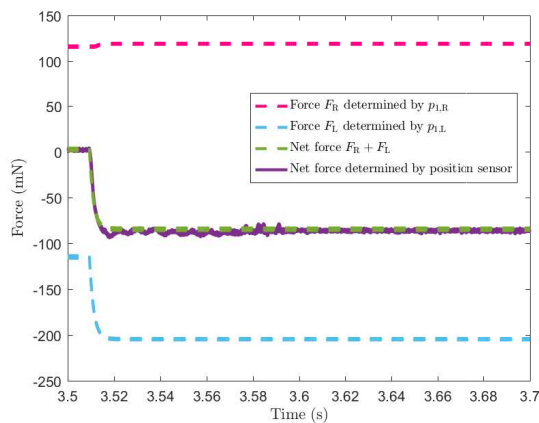


Figure E3: Forces in  $x$ -direction acting on the substrate. The actuation force is either determined with  $p_{1,R}$  and  $p_{1,L}$  or with the measured displacement.

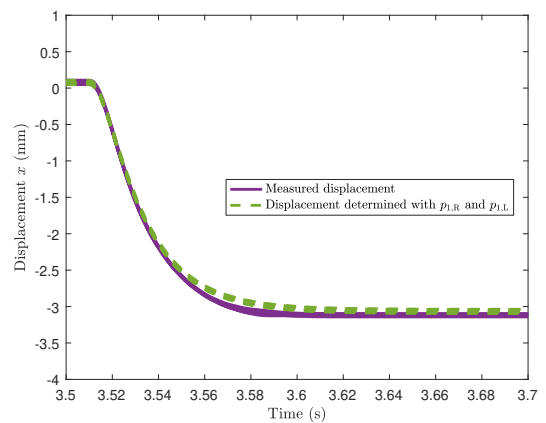
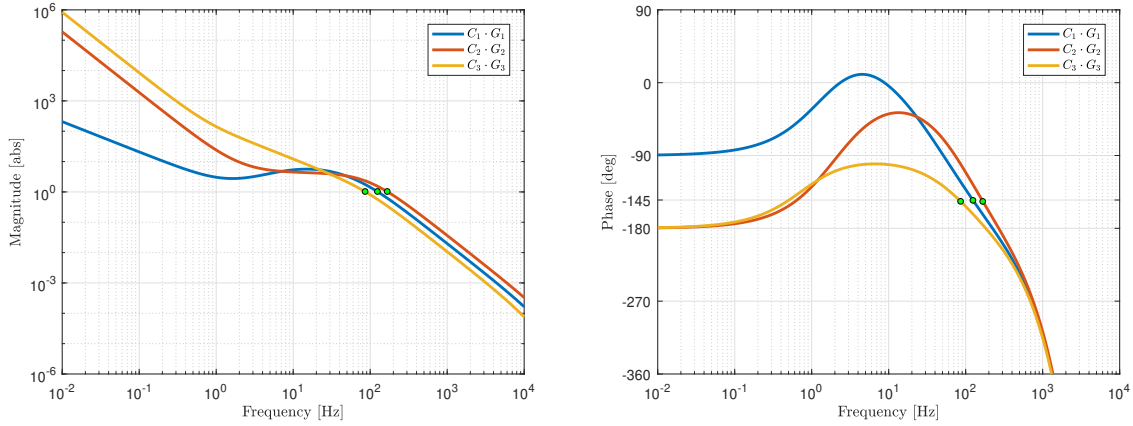


Figure E4: Displacement  $x$  of the substrate measured with the position sensor. The displacement is also determined with  $p_{1,R}$  and  $p_{1,L}$ .

With this we can conclude that actuating in positive  $x$ -direction (section 4.3) and actuating in negative  $x$ -direction (this section) give similar results. Although  $\Delta F_a$  is lower, also  $c_{unmod}$  is lower in this situation. Because of the lower damping the maximum speed becomes  $0.142\text{ m/s}$  with which it can move the substrate  $50\text{ mm}$  in  $360\text{ ms}$  in negative  $x$ -direction. The time constants remain the same, resulting in a rise time of  $\tau_r = 3.96\text{ ms}$  and a settling time of about  $\tau_s = 8.28\text{ ms}$ . Finally, the bandwidth of the motion system is about  $87.0\text{ Hz}$ . This is sufficient enough to actuate the substrate within the required accuracy range of  $\pm 1\text{ mm}$ .



(a) Magnitude of  $C_1 \cdot G_1$ ,  $C_2 \cdot G_2$  and  $C_3 \cdot G_3$  in absolute value. (b) Phase of  $C_1 \cdot G_1$ ,  $C_2 \cdot G_2$  and  $C_3 \cdot G_3$  in degrees.

Figure E5: Bode plots of the open-loop transfer functions  $C_1 \cdot G_1$ ,  $C_2 \cdot G_2$  and  $C_3 \cdot G_3$ . Here the green circles indicate the unity-gain cross-over frequencies with a phase margin of  $35^\circ$ .

## F.2. Pressure fall of $p_{1,R}$

In this section the same measurement results are used as in section 4.3. Except in this section the pressure fall of  $p_{1,R}$  in the interval  $3.25\text{ s} \leq t \leq 3.45\text{ s}$  is observed. During this interval a step signal is given to the valves generating a force in positive  $x$ -direction. This interval is shown by the green areas in figure F6. The same models are used as in section 4.3, but now with some different values for the parameters which are shown in table E.2. By comparing table E.2 with table 4.1 of section 4.3, one can see that the value of  $\Delta F_a$  has reduced from  $96.5\text{ mN}$  to  $94.9\text{ mN}$ ,  $\tau_{RC}$  has increased from  $1.80\text{ ms}$  to  $4.20\text{ ms}$  and  $c_{unmod}$  has reduced from  $750 \cdot 10^{-3}\text{ N/(m/s)}$  to  $400 \cdot 10^{-3}\text{ N/(m/s)}$ . The other parameters remained the same.

Table E.2: Used values of the parameters for describing the response of the plant when pressure  $p_{1,R}$  is falling.

Parameter	$\Delta F_a$	$\tau_{\text{delay}}$	$\tau_{RC}$	$m_{\text{sub}}$	$m_{\text{add}}$
Value	$94.9\text{ mN}$	$0.375\text{ ms}$	$4.20\text{ ms}$	$1.005\text{ g}$	$1.635\text{ g}$

Parameter	$c_{\text{visc}}$	$c_{\text{spring}}$	$c_{\text{unmod}}$	$k_1$	$k_2$
Value	$10.7 \cdot 10^{-3}\text{ N/(m/s)}$	$54.0 \cdot 10^{-3}\text{ N/(m/s)}$	$400 \cdot 10^{-3}\text{ N/(m/s)}$	$13.8\text{ N/m}$	$13.8\text{ N/m}$

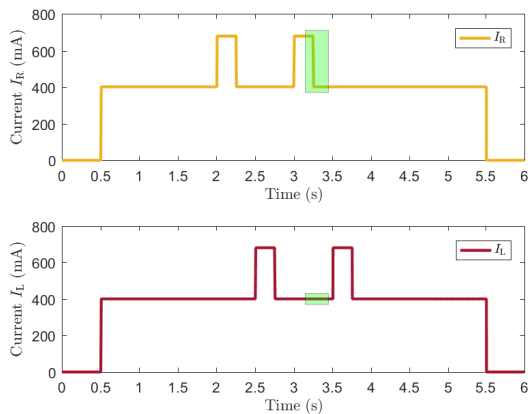


Figure F6: Signals  $I_R$  and  $I_L$  which are the currents provided to the valves generating a force in positive and negative  $x$ -direction respectively.

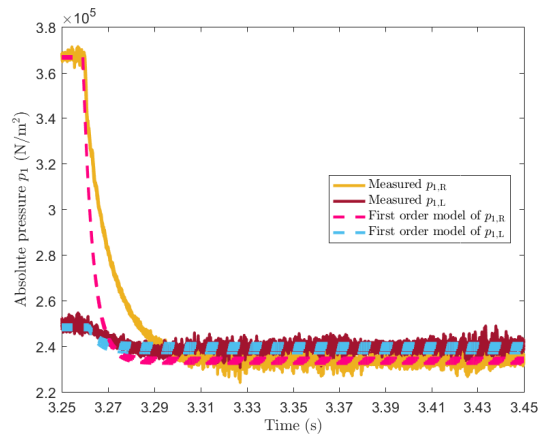


Figure E7: Pressures  $p_{1,R}$  and  $p_{1,L}$  measured by the pressure sensors. The results are shown for 10 measurements. The measured pressures are also approximated by a first order model.

In figure E7 pressures  $p_{1,R}$  and  $p_{1,L}$  are shown as function of time. Here it can be seen that  $p_{1,R}$  has a pressure of around 3.67 bar at  $t = 3.25$  s and a pressure of around 2.34 bar at  $t = 3.45$  s. Furthermore,  $p_{1,L}$  has a pressure of around 2.49 bar at  $t = 3.25$  s and a pressure of around 2.39 bar at  $t = 3.45$  s. Both  $p_{1,R}$  and  $p_{1,L}$  can again be approximated by first order models as is shown in figure E7. The force generated by these pressures are shown in figure E8. In this case the net force decreases from a positive value to zero. Here  $\tau_{RC} = 4.20$  ms which shows that the response is slower during pressure fall compared to pressure rise. This is because the air in the ducts can only leave through the actuators, which takes time. One could use a different configuration of the valves to decrease  $\tau_{RC}$ , but it would make the system more complex. Therefore this is not further investigated in this thesis. Furthermore,  $c_{unmod}$  is lower which indicates that this parameter is varying under different working conditions. The position of the substrate is shown in figure E9. Here it can be seen that the substrate is moving in negative  $x$ -direction as expected, with a displacement of about 3.44 mm. In figure E9 it can be seen that the model shows a small mismatch between the measurement and the model in the interval  $3.30 \text{ s} \leq t \leq 3.36 \text{ s}$ , but overall the graphs show good resemblance. Finally, the open-loop responses for the plant in combinations with controllers are shown in figure E.10. Here the green circles indicate the unity-gain cross-over frequency with a phase margin of  $35^\circ$ . For  $C_1 \cdot G_1$ ,  $C_2 \cdot G_2$  and  $C_3 \cdot G_3$  these are respectively 77.2 Hz, 110.0 Hz and 46.8 Hz.

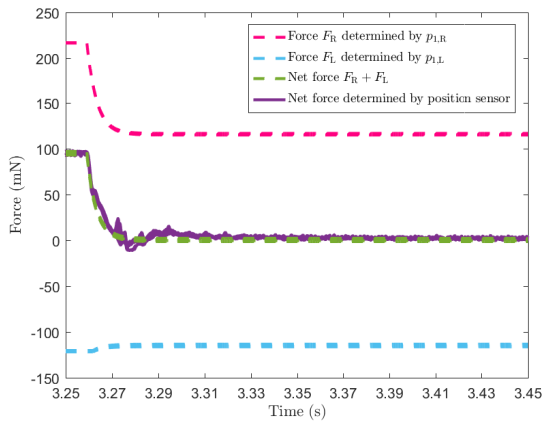


Figure E8: Forces in  $x$ -direction acting on the substrate. The actuation force is either determined with  $p_{1,R}$  and  $p_{1,L}$  or with the measured displacement.

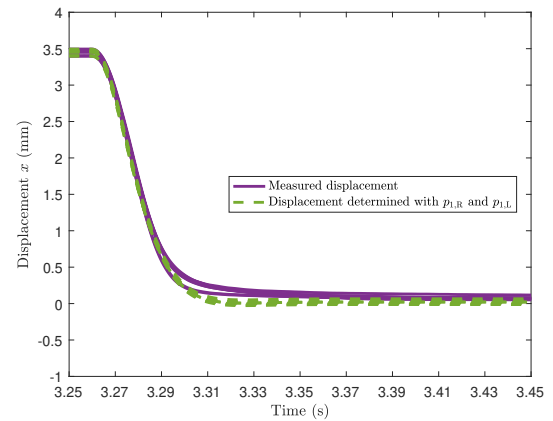
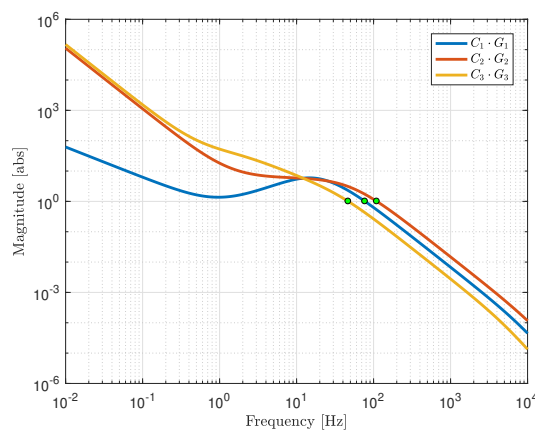
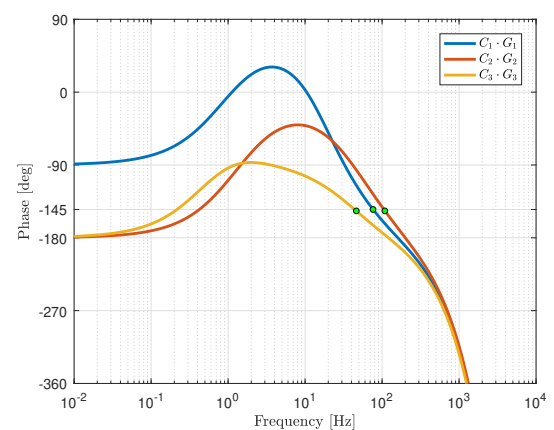


Figure E9: Displacement  $x$  of the substrate measured with the position sensor. The displacement is also determined with  $p_{1,R}$  and  $p_{1,L}$ .



(a) Magnitude of  $C_1 \cdot G_1$ ,  $C_2 \cdot G_2$  and  $C_3 \cdot G_3$  in absolute value.



(b) Phase of  $C_1 \cdot G_1$ ,  $C_2 \cdot G_2$  and  $C_3 \cdot G_3$  in degrees.

Figure F10: Bode plots of the open-loop transfer functions  $C_1 \cdot G_1$ ,  $C_2 \cdot G_2$  and  $C_3 \cdot G_3$ . Here the green circles indicate the unity-gain cross-over frequencies with a phase margin of  $35^\circ$ .

With this we can conclude that the pressure fall of  $p_{1,R}$  is slower than the pressure rise of  $p_{1,R}$ . The response

has a fall time of  $\tau_f = 9.24$  ms and a settling time of about  $\tau_s = 19.32$  ms. Resulting in a system bandwidth of about 46.8 Hz. This could be improved by using a different valve configuration, such that the air can leave the ducts more rapidly. Although such a configuration is more complex to implement.

### E.3. Pressure fall of $p_{1,L}$

In this section the same measurement results are used as in section 4.3. Except in this section the pressure fall of  $p_{1,L}$  in the interval  $3.75 \text{ s} \leq t \leq 3.95 \text{ s}$  is observed. During this interval a step signal is given to the valves generating a force in negative  $x$ -direction. This interval is shown by the green areas in figure F.11. The same models are used as in section 4.3, but now with some different values for the parameters which are shown in table E.3. By comparing table E.3 with table 4.1 of section 4.3, one can see that the value of  $\Delta F_a$  has reduced from 96.5 mN to 86.0 mN,  $\tau_{RC}$  has increased from 1.80 ms to 4.20 ms and  $c_{unmod}$  has reduced from  $750 \cdot 10^{-3} \text{ N/(m/s)}$  to  $400 \cdot 10^{-3} \text{ N/(m/s)}$ . The other parameters remained the same.

Table E.3: Used values of the parameters for describing the response of the plant when pressure  $p_{1,L}$  is falling.

Parameter	$\Delta F_a$	$\tau_{\text{delay}}$	$\tau_{RC}$	$m_{\text{sub}}$	$m_{\text{add}}$
Value	86.0 mN	0.375 ms	4.20 ms	1.005 g	1.635 g

Parameter	$c_{\text{visc}}$	$c_{\text{spring}}$	$c_{\text{unmod}}$	$k_1$	$k_2$
Value	$10.7 \cdot 10^{-3} \text{ N/(m/s)}$	$54.0 \cdot 10^{-3} \text{ N/(m/s)}$	$400 \cdot 10^{-3} \text{ N/(m/s)}$	13.8 N/m	13.8 N/m

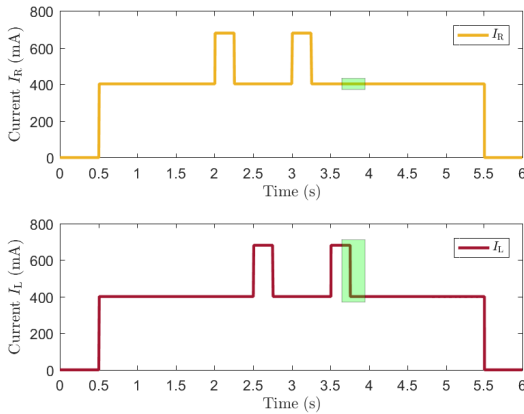


Figure F.11: Signals  $I_R$  and  $I_L$  which are the currents provided to the valves generating a force in positive and negative  $x$ -direction respectively.

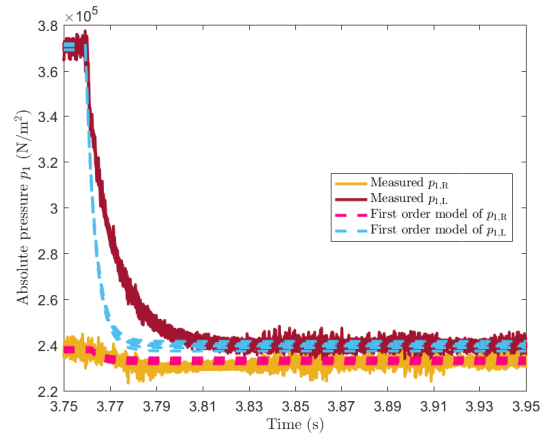


Figure F.12: Pressures  $p_{1,R}$  and  $p_{1,L}$  measured by the pressure sensors. The results are shown for 10 measurements. The measured pressures are also approximated by a first order model.

In figure F.12 pressures  $p_{1,R}$  and  $p_{1,L}$  are shown as function of time. Here it can be seen that  $p_{1,L}$  has a pressure of around 3.71 bar at  $t = 3.75$  s and a pressure of around 2.40 bar at  $t = 3.95$  s. Furthermore,  $p_{1,R}$  has a pressure of around 2.38 bar at  $t = 3.75$  s and a pressure of around 2.33 bar at  $t = 3.95$  s. Both  $p_{1,R}$  and  $p_{1,L}$  can again be approximated by first order models as is shown in figure F.12. The force generated by these pressures are shown in figure F.13. In this case the net force increases from a negative value to zero. Here  $\tau_{RC} = 4.20$  ms which shows that the response is slower during pressure fall compared to pressure rise. This is because the air in the ducts can only leave through the actuators, which takes time. One could use a different configuration of the valves to decrease  $\tau_{RC}$ , but it would make the system more complex. Therefore this is not further investigated in this thesis. Furthermore,  $c_{unmod}$  is lower which indicates that this parameter is varying under different working conditions. The position of the substrate is shown in figure F.14. Here it can be seen that the substrate is moving in positive  $x$ -direction as expected, with a displacement of about 3.12 mm. In figure F.14 it can be seen that the model shows a small mismatch between the measurement and the model in the interval  $3.79 \text{ s} \leq t \leq 3.84 \text{ s}$ , but overall the graphs show good resemblance. Finally, the open-loop responses for the plant in combinations with controllers are shown in figure F.15. Here the green circles indicate the unity-gain cross-over frequency with a phase margin of  $35^\circ$ . For  $C_1 \cdot G_1$ ,  $C_2 \cdot G_2$  and  $C_3 \cdot G_3$  these are respectively 77.2 Hz,

110.0 Hz and 46.8 Hz.

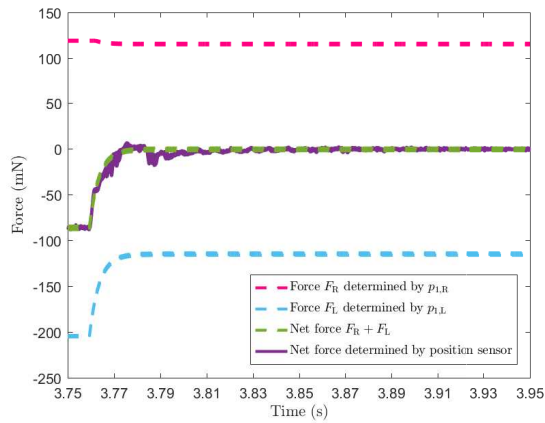


Figure E13: Forces in  $x$ -direction acting on the substrate. The actuation force is either determined with  $p_{1,R}$  and  $p_{1,L}$  or with the measured displacement.

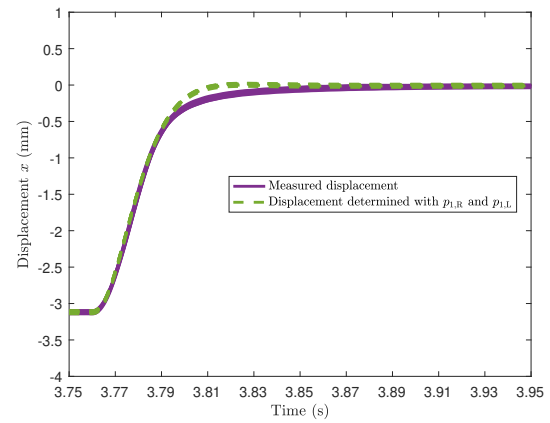
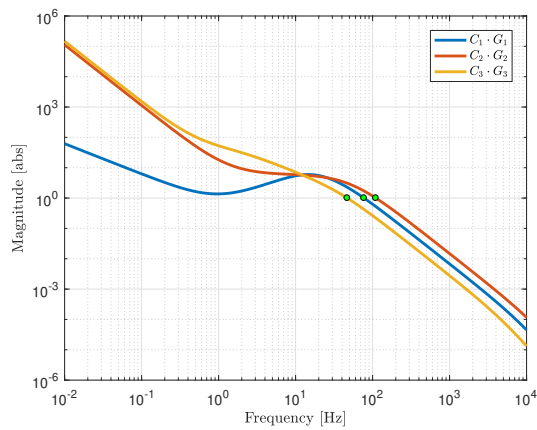
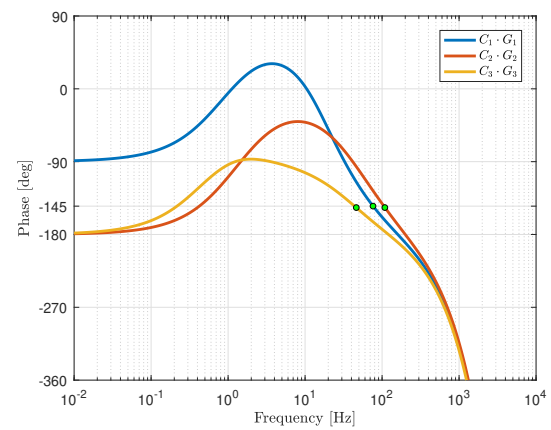


Figure E14: Displacement  $x$  of the substrate measured with the position sensor. The displacement is also determined with  $p_{1,R}$  and  $p_{1,L}$ .



(a) Magnitude of  $C_1 \cdot G_1$ ,  $C_2 \cdot G_2$  and  $C_3 \cdot G_3$  in absolute value.



(b) Phase of  $C_1 \cdot G_1$ ,  $C_2 \cdot G_2$  and  $C_3 \cdot G_3$  in degrees.

Figure E15: Bode plots of the open-loop transfer functions  $C_1 \cdot G_1$ ,  $C_2 \cdot G_2$  and  $C_3 \cdot G_3$ . Here the green circles indicate the unity-gain cross-over frequencies with a phase margin of  $35^\circ$ .

With this we can conclude that the pressure fall of  $p_{1,L}$  is slower than the pressure rise of  $p_{1,R}$  (and the pressure rise of  $p_{1,L}$ ). The response has a fall time of  $\tau_f = 9.24$  ms and a settling time of about  $\tau_s = 19.32$  ms. Resulting in a system bandwidth of about 46.8 Hz. This could be improved by using a different valve configuration, such that the air can leave the ducts more rapidly. Although such a configuration is more complex to implement.

# Bibliography

- [1] Suresh G Advani and E Murat Sozer. *Process modeling in composites manufacturing*, volume 6. Marcel Dekker New York, 2003.
- [2] Andrew Berlin, David Biegelsen, Patrick Cheung, Markus Fromherz, David Goldberg, Warren Jackson, Bryan Preas, James Reich, and Lars-Erik Swartz. Motion control of planar objects using large-area arrays of mems-like distributed manipulators. In *Micromechatronics*, 2000.
- [3] David K Biegelsen, Andrew A Berlin, Patrick Cheung, Markus PJ Fromherz, David Goldberg, Warren B Jackson, Bryan Preas, James Reich, and Lars E Swartz. Airjet paper mover: An example of mesoscale mems. In *Micromachined Devices and Components VI*, volume 4176, pages 122–130. International Society for Optics and Photonics, 2000.
- [4] Guido Buresti. A note on Stokes' hypothesis. *Acta Mechanica*, 226(10):3555–3559, 2015.
- [5] Anne Delettre, Guillaume J Laurent, Yassine Haddab, and Nadine Le Fort-Piat. Robust control of a planar manipulator for flexible and contactless handling. *Mechatronics*, 22(6):852–861, 2012.
- [6] Markus PJ Fromherz and Warren B Jackson. Force allocation in a large-scale distributed active surface. *IEEE transactions on control systems technology*, 11(5):641–655, 2003.
- [7] Valérian Guelpa, Guillaume J Laurent, Bassem Dahroug, and Nadine Le Fort-Piat. Modular contact-free conveyors for handling planar fragile objects. *IEEE Transactions on Robotics*, 33(1):92–101, 2017.
- [8] A Gerhard Holzapfel. *Nonlinear Solid Mechanics II*. John Wiley & Sons, Inc., 2000.
- [9] RP Hoogeboom. Design and experimental validation of low stiffness aerostatic thrust bearings. Master's thesis, Delft University of Technology, 2016.
- [10] Charles Maxwell Hunt, JC King, and Heinz R Trechsel. *Building air change rate and infiltration measurements*, volume 719. ASTM International, 1980.
- [11] Zbigniew Kamiński. A simplified lumped parameter model for pneumatic tubes. *Mathematical and Computer Modelling of Dynamical Systems*, 23(5):523–535, 2017.
- [12] ME Krijnen. Control system design for a contactless actuation system. Master's thesis, Delft University of Technology, 2016.
- [13] PK Kundu and IM Cohen. *Fluid mechanics*. Elsevier, 6th edition, 2016.
- [14] Paul Lambrechts, Matthijs Boerlage, and Maarten Steinbuch. Trajectory planning and feedforward design for electromechanical motion systems. *Control Engineering Practice*, 13(2):145–157, 2005.
- [15] Guillaume J Laurent and Hyungpil Moon. A survey of non-prehensile pneumatic manipulation surfaces: principles, models and control. *Intelligent Service Robotics*, 8(3):151–163, 2015.
- [16] Guillaume J Laurent, Anne Delettre, and Nadine Le Fort-Piat. A new aerodynamic-traction principle for handling products on an air cushion. *IEEE Transactions on robotics*, 27(2):379–384, 2011.
- [17] Anthony F Mills. *Basic heat and mass transfer*. Pearson Education, 2nd edition, 2014.
- [18] Hyungpil Moon and Jonathan Luntz. Prediction of equilibria of lifted logarithmic radial potential fields. *The International Journal of Robotics Research*, 23(7-8):747–762, 2004.
- [19] In-Ho Moon and Young-Kyu Hwang. Evaluation of a wafer transportation speed for propulsion nozzle array on air levitation system. *Journal of mechanical science and technology*, 20(9):1492–1501, 2006.

- [20] Michael J Moran, Howard N Shapiro, Daisie D Boettner, and Margaret B Bailey. *Principles of engineering thermodynamics*. John Wiley & Sons, 7th edition, 2015.
- [21] Kristopher SJ Pister, Ronald S Fearing, and Roger T Howe. A planar air levitated electrostatic actuator system. In *Micro Electro Mechanical Systems, 1990. Proceedings, An Investigation of Micro Structures, Sensors, Actuators, Machines and Robots. IEEE*, pages 67–71. IEEE, 1990.
- [22] G Reinhart and J Hoepfner. Non-contact handling using high-intensity ultrasonics. *CIRP Annals-Manufacturing Technology*, 49(1):5–8, 2000.
- [23] Gunther Reinhart, Michael Heinz, Johannes Stock, Josef Zimmermann, Michael Schilp, Adolf Zitzmann, and Jens Hellwig. Non-contact handling and transportation for substrates and microassembly using ultrasound-air-film-technology. In *Advanced Semiconductor Manufacturing Conference (ASMC), 2011 22nd Annual IEEE/SEMI*, pages 1–6. IEEE, 2011.
- [24] Alexander H Slocum. *Precision machine design*. Society of Manufacturing Engineers, 1992.
- [25] Jelle Snieder. Development of an air-based contactless transport demonstrator. Master's thesis, Delft University of Technology, 2017.
- [26] Jelle Snieder. Feasibility study into the application of a contactless handling stage in the ADAT3-XF. Feasibility study, 2017.
- [27] Sadayuki Ueha, Yoshiki Hashimoto, and Yoshikazu Koike. Non-contact transportation using near-field acoustic levitation. *Ultrasonics*, 38(1-8):26–32, 2000.
- [28] A van Beek. *Advanced Engineering Design: Lifetime Performance and Reliability. 2012*. TU Delft, 5th edition, 2012.
- [29] Konstantinos Varsos, Hyungpil Moon, and Jonathan Luntz. Generation of quadratic potential force fields from flow fields for distributed manipulation. *IEEE Transactions on robotics*, 22(1):108–118, 2006.
- [30] Phuc Hong Vuong. *Air-based contactless actuation system for thin substrates*. PhD thesis, Delft University of Technology, 2016.
- [31] Jasper Wesselingh. *Contactless positioning using an active air film*. PhD thesis, Delft University of Technology, 2011.
- [32] Frank M White. *Fluid mechanics, in SI units*. McGraw-Hill, 7th edition, 2011.
- [33] Frank M White and Isla Corfield. *Viscous fluid flow*. McGraw-Hill New York, 3rd edition, 2006.
- [34] Ryuto Yano, Manabu Aoyagi, Hideki Tamura, and Takehiro Takano. Novel transfer method using near-field acoustic levitation and its application. *Japanese Journal of Applied Physics*, 50(7S):07HE29, 2011.